

Karol Miller *Editor*

# Biomechanics of the Brain

BIOLOGICAL AND MEDICAL PHYSICS,  
BIOMEDICAL ENGINEERING

---

# BIOLOGICAL AND MEDICAL PHYSICS, BIOMEDICAL ENGINEERING

---

The fields of biological and medical physics and biomedical engineering are broad, multidisciplinary and dynamic. They lie at the crossroads of frontier research in physics, biology, chemistry, and medicine. The Biological and Medical Physics, Biomedical Engineering Series is intended to be comprehensive, covering a broad range of topics important to the study of the physical, chemical and biological sciences. Its goal is to provide scientists and engineers with textbooks, monographs, and reference works to address the growing need for information.

Books in the series emphasize established and emergent areas of science including molecular, membrane, and mathematical biophysics; photosynthetic energy harvesting and conversion; information processing; physical principles of genetics; sensory communications; automata networks, neural networks, and cellular automata. Equally important will be coverage of applied aspects of biological and medical physics and biomedical engineering such as molecular electronic components and devices, biosensors, medicine, imaging, physical principles of renewable energy production, advanced prostheses, and environmental control and engineering.

## Editor-in-Chief:

Elias Greenbaum, Oak Ridge National Laboratory, Oak Ridge, Tennessee, USA

## Editorial Board:

Masuo Aizawa, Department of Bioengineering,  
Tokyo Institute of Technology, Yokohama, Japan

Olaf S. Andersen, Department of Physiology,  
Biophysics & Molecular Medicine,  
Cornell University, New York, USA

Robert H. Austin, Department of Physics,  
Princeton University, Princeton, New Jersey, USA

James Barber, Department of Biochemistry,  
Imperial College of Science, Technology  
and Medicine, London, England

Howard C. Berg, Department of Molecular and Cellular  
Biology, Harvard University, Cambridge, Massachusetts,  
USA

Victor Bloomfield, Department of Biochemistry,  
University of Minnesota, St. Paul, Minnesota, USA

Robert Callender, Department of Biochemistry, Albert  
Einstein College of Medicine, Bronx, New York, USA

Steven Chu, Lawrence Berkeley National Laboratory,  
Berkeley, California, USA

Louis J. DeFelice, Department of Pharmacology,  
Vanderbilt University, Nashville, Tennessee, USA

Johann Deisenhofer, Howard Hughes Medical Institute,  
The University of Texas, Dallas, Texas, USA

George Feher, Department of Physics, University of  
California, San Diego, La Jolla, California, USA

Hans Frauenfelder, Los Alamos National Laboratory,  
Los Alamos, New Mexico, USA

Ivar Giaever, Rensselaer Polytechnic Institute, Troy,  
New York, USA

Sol M. Gruner, Cornell University, Ithaca,  
New York, USA

Judith Herzfeld, Department of Chemistry,  
Brandeis University, Waltham, Massachusetts, USA

Mark S. Humayun, Doheny Eye Institute,  
Los Angeles, California, USA

Pierre Joliot, Institute de Biologie Physico-Chimique,  
Fondation Edmond de Rothschild, Paris, France

Lajos Keszthelyi, Institute of Biophysics, Hungarian  
Academy of Sciences, Szeged, Hungary

Robert S. Knox, Department of Physics and Astronomy,  
University of Rochester, Rochester, New York, USA

Aaron Lewis, Department of Applied Physics,  
Hebrew University, Jerusalem, Israel

Stuart M. Lindsay, Department of Physics and  
Astronomy, Arizona State University, Tempe,  
Arizona, USA

David Mauzerall, Rockefeller University, New York,  
New York, USA

Eugenie V. Mielczarek, Department of Physics  
and Astronomy, George Mason University,  
Fairfax, Virginia, USA

Markolf H. Niemz, Medical Faculty Mannheim,  
University of Heidelberg, Mannheim, Germany

V. Adrian Parsegian, Physical Science Laboratory,  
National Institutes of Health, Bethesda,  
Maryland, USA

Linda S. Powers, University of Arizona, Tucson,  
Arizona, USA

Earl W. Prohofsky, Department of Physics, Purdue  
University, West Lafayette, Indiana, USA

Andrew Rubin, Department of Biophysics, Moscow  
State University, Moscow, Russia

Michael Seibert, National Renewable Energy  
Laboratory, Golden, Colorado, USA

David D. Thomas, Department of Biochemistry,  
University of Minnesota Medical School,  
Minneapolis, Minnesota, USA

## For further volumes:

<http://www.springer.com/series/3740>

Karol Miller  
Editor

# Biomechanics of the Brain



Springer

*Editor*

Karol Miller  
Intelligent Systems for Medicine Laboratory  
School of Mechanical and Chemical Engineering  
The University of Western Australia  
35 Stirling Highway, Crawley/Perth, WA 6009, Australia  
kmiller@mech.uwa.edu.au

ISSN 1618-7210

ISBN 978-1-4419-9996-2

e-ISBN 978-1-4419-9997-9

DOI 10.1007/978-1-4419-9997-9

Springer New York Dordrecht Heidelberg London

Library of Congress Control Number: 2011932175

© Springer Science+Business Media, LLC 2011

All rights reserved. This work may not be translated or copied in whole or in part without the written permission of the publisher (Springer Science+Business Media, LLC, 233 Spring Street, New York, NY 10013, USA), except for brief excerpts in connection with reviews or scholarly analysis. Use in connection with any form of information storage and retrieval, electronic adaptation, computer software, or by similar or dissimilar methodology now known or hereafter developed is forbidden.

The use in this publication of trade names, trademarks, service marks, and similar terms, even if they are not identified as such, is not to be taken as an expression of opinion as to whether or not they are subject to proprietary rights.

Printed on acid-free paper

Springer is part of Springer Science+Business Media ([www.springer.com](http://www.springer.com))

# Contents

<b>1</b>	<b>Introduction.....</b>	1
	Karol Miller	
<b>2</b>	<b>Introduction to Brain Anatomy.....</b>	5
	Wieslaw L. Nowinski	
<b>3</b>	<b>Introduction to Brain Imaging .....</b>	41
	Einat Liebenthal	
<b>4</b>	<b>Brain Tissue Mechanical Properties .....</b>	69
	Lynne E. Bilston	
<b>5</b>	<b>Modeling of the Brain for Injury Simulation and Prevention.....</b>	91
	King H. Yang and Albert I. King	
<b>6</b>	<b>Biomechanical Modeling of the Brain for Computer-Assisted Neurosurgery .....</b>	111
	K. Miller, A. Wittek, and G. Joldes	
<b>7</b>	<b>Dynamics of Cerebrospinal Fluid: From Theoretical Models to Clinical Applications .....</b>	137
	Marek Czosnyka, Zofia Czosnyka, Olivier Baledent, Ruwan Weerakkody, Magdalena Kasprowicz, Piotr Smielewski, and John D. Pickard	
<b>8</b>	<b>Computational Fluid Dynamics for the Assessment of Cerebrospinal Fluid Flow and Its Coupling with Cerebral Blood Flow .....</b>	169
	Vartan Kurtcuoglu	
<b>9</b>	<b>Algorithms for Computational Biomechanics of the Brain .....</b>	189
	A. Wittek, G. Joldes, and K. Miller	
<b>Index.....</b>	221	



# Contributors

**Olivier Baledent** Department of Imaging and Biophysics,  
University Hospital Amiens, Amiens Cedex, France

**Lynne E. Bilston** Neuroscience Research Australia  
and University of New South Wales, Randwick, Sydney, NSW 2031, Australia

**Marek Czosnyka** Neurosurgical Unit, Department of Clinical Neurosciences,  
University of Cambridge, Cambridge, UK

**Zofia Czosnyka** Neurosurgical Unit, Department of Clinical Neurosciences,  
University of Cambridge, Cambridge, UK

**G. Joldes** Intelligent Systems for Medicine Laboratory,  
School of Mechanical and Chemical Engineering, The University of Western  
Australia, Crawley/Perth, WA 6009, Australia

**Magdalena Kasprowicz** Institute of Biomedical Engineering  
and Instrumentation, Wroclaw University of Technology, Wroclaw, Poland

**Albert I. King** Wayne State University, Detroit, MI 48201, USA

**Vartan Kurteoglu** Laboratory of Thermodynamics in Emerging Technologies,  
Department of Mechanical and Process Engineering, ETH Zurich, Switzerland

**Einat Liebenthal** Neuroscience, University of Manitoba, Winnipeg,  
Canada & Neurology, Medical College of Wisconsin, Milwaukee, USA

**Karol Miller** Intelligent Systems for Medicine Laboratory, School of  
Mechanical and Chemical Engineering, The University of Western Australia,  
Crawley/Perth, WA 6009, Australia

**Wieslaw L. Nowinski** Biomedical Imaging Lab, ASTAR, Singapore

**John D. Pickard** Neurosurgical Unit, Department of Clinical Neurosciences,  
University of Cambridge, Cambridge, UK

**Piotr Smielewski** Neurosurgical Unit, Department of Clinical Neurosciences,  
University of Cambridge, Cambridge, UK

**Ruhan Weerakkody** Neurosurgical Unit, Department of Clinical Neurosciences,  
University of Cambridge, Cambridge, UK

**A. Wittek** Intelligent Systems for Medicine Laboratory, School of Mechanical  
and Chemical Engineering, The University of Western Australia,  
Crawley/Perth, WA 6009, Australia

**King H. Yang** Wayne State University, Detroit, MI 48201, USA

# Chapter 1

## Introduction

**Karol Miller**

The mechanical properties of living tissues continue to be the major topic of biomechanical investigations. Over the years, a vast amount of knowledge about load-bearing tissues, such as bones, ligaments, muscles and other components of the musculoskeletal system, blood vessels (and blood), lungs, skin and hair, has been published in journals and books. The very soft tissues of organs whose role has little or nothing to do with transmitting mechanical loads had been, until recently, outside the scope of the mainstream biomechanical research. Extremely important organs such as the liver, kidneys, prostate and other abdominal organs, and especially the brain, had been largely neglected by biomechanics.

Investigation of the mechanical properties of the brain began in the late 1960s. Ommaya described mammalian brain as a “soft, yielding structure, not as stiff as a gel, nor as plastic as a paste” [1]. These first studies were motivated by the increasing number of traumatic brain injuries resulting from automotive accidents. The first finite element models of the brain appeared in the early 1980s. Since then, the biomechanics of the brain for injury analysis and prevention has been a very active area of research.

There is wide international concern about the cost of meeting rising expectations for health care, particularly if large numbers of people require currently expensive procedures such as brain surgery. Costs can be reduced by using improved machinery to help surgeons perform these procedures quickly and accurately, with minimal side effects. A novel partnership between surgeons and machines, made possible by advances in computing and engineering technology, could overcome many of the limitations of traditional surgery. By extending surgeons’ ability to plan and carry out surgical interventions more accurately and with less trauma, Computer-Integrated Surgery (CIS) systems could help to improve clinical outcomes and the efficiency of

---

K. Miller (✉)

Intelligent Systems for Medicine Laboratory, School of Mechanical and Chemical Engineering, The University of Western Australia,  
35 Stirling Highway, Crawley/Perth, WA 6009, Australia  
e-mail: kmiller@mech.uwa.edu.au

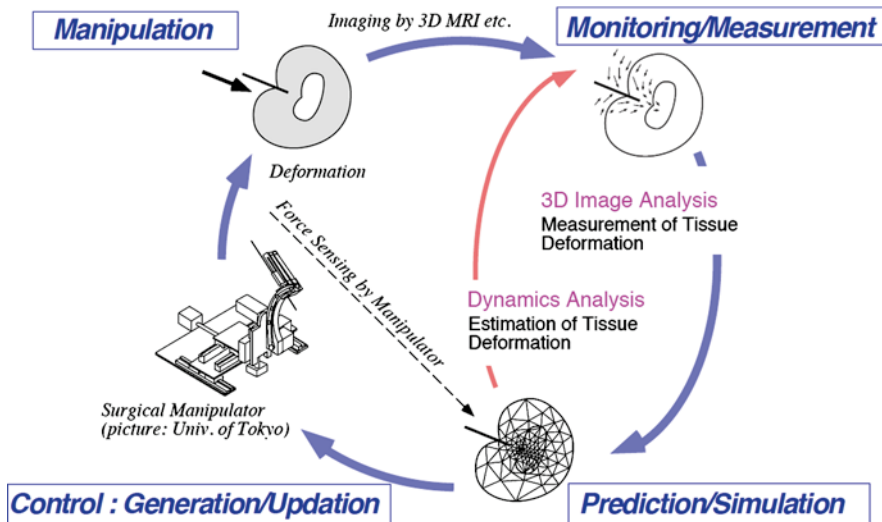


**Fig. 1.1** A concept of the image-guided neurosurgical robot with the feed-forward loop based on the biomechanical model in the control system [2, 3]. The concept has not been realized in its entirety; however, it provided a strong stimulus for brain biomechanics research (image courtesy of Dr Kiyoyuki Chinzei, AIST, Tsukuba, Japan)

health care delivery. CIS systems could have a similar impact on surgery to that long since realized in Computer-Integrated Manufacturing (CIM). Recent developments in robotics technology, especially the emergence of automatic surgical tools and robots and advances in virtual reality techniques, have motivated the latest interest in the biomechanics of the brain. An understanding of the brain biomechanics can be used for surgical simulation, computer-integrated and image-guided neurosurgery, and as a supporting tool for diagnosis and prognosis of brain disease.

The initial stimulus for this line of research was provided by the visionary project aiming at designing an image-guided neurosurgical robot. This project was conducted in 1995–1996 at Biomechanics Division of Mechanical Engineering Laboratory, AIST, in Tsukuba, Japan. Figure 1.1 provides the overview of that project.

Significantly increased interest in the biomechanics of soft tissues, and in particular the brain, as evidenced by the increased number of publications in this area, warrants an attempt to summarise recent developments in the form of a book. This book brings the current state of the art in the biomechanics of the brain to the reader. I have attempted to include all relevant aspects of biomechanical modeling that have progressed beyond initial investigations and attained a certain level of maturity, as well as the fields of their application. I have insisted that chapter contributors present the current state of the art in their specific fields in an authoritative way. Therefore, some of the newest, and still tentative developments (e.g. the biomechanics of cortical folding), have been intentionally omitted.

Biomechanics researchers new to the field often come with an engineering or physics background. I hope these readers will benefit from the introductory chapters on brain anatomy (Chap. 2) and brain imaging (Chap. 3). The information contained

in these primers should be easily digestible by readers with no medical background and save them a considerable amount of time spent studying the specialized literature in these fields.

Chapter 4 discusses mechanical properties of brain tissues. The knowledge of these properties is a prerequisite for the development of biomechanical models of the brain.

Chapter 5 describes mathematical modeling and computer simulation of the brain for injury prevention, and Chap. 6 considers brain-modeling issues for applications in image-guided surgery and surgical simulation. Mathematical modeling and computer simulation have proven tremendously successful in engineering. Computational mechanics has enabled technological developments in virtually every area of our lives. One of the greatest challenges for mechanists is to extend the success of computational mechanics to fields outside traditional engineering, in particular to biology, biomedical sciences, and medicine [4]. These two chapters demonstrate that in computational sciences, the most critical step in the solution of the problem is the selection of the physical and mathematical model of the phenomenon to be investigated. Model selection is a heuristic process, based on the analyst's judgment and experience. Often, model selection is a subjective endeavor; different modelers may choose different models to describe the same reality. Nevertheless, the selection of the model is the single most important step in obtaining valid computer simulations of any investigated reality [4].

Chapter 7 discusses the biomechanics of blood and cerebrospinal fluid flow through the brain and the dynamics of intracranial pressure. Unlike the results presented in Chaps. 5 and 6, the findings described in Chap. 7 have already found their way into the clinical practice and care of brain injury and disease sufferers.

Chapter 8 describes the most recent developments in computational fluid dynamics of cerebrospinal fluid and blood flow. This field will very soon strengthen the more heuristic, clinically applicable methods described in Chap. 7.

Often very large and complicated computations are required to extract reliable information from comprehensive, highly non-linear biomechanical models of the brain. Chapter 9 describes current best practice in selection of computational methods for solving models described in Chaps. 5 and 6. This is probably the most technical part of the book. The reader will require a sound understanding of the finite element method to fully appreciate this chapter.

## References

1. Ommaya, A.K.: Mechanical properties of tissues of the nervous system. *J. Biomech.* **1**, 127–138 (1968)
2. Miller, K., Chinzei, K.: Modeling of soft tissues deformation. *J. Comput. Aided Surg.* **1** (Suppl., Proceedings of Second International Symposium on Computer Aided Surgery, Tokyo Women's Medical College, Shinjuku, Tokyo), 62–63 (1995)
3. Miller, K., Chinzei, K.: Modeling of soft tissues. *Mech. Eng. Lab. News* **11**, 5–7 (1995)
4. Oden, J.T., Belytschko, T., Babuska, I., et al.: Research directions in computational mechanics. *Comput. Meth. Appl. Mech. Engg.* **192**, 913–922 (2003)



# Chapter 2

## Introduction to Brain Anatomy

Wieslaw L. Nowinski

### 2.1 Introduction

The human central nervous system (CNS), having been evolved over the last 600 million years, is the most complex living organ in the known universe. It has been extensively investigated over centuries, and a vast body of materials has been gathered in the print form and more recently also in electronic format. Neuroanatomy is presented in numerous textbooks [1–22], print brain atlases [23–51], and electronic brain atlases [52–74]. Several textbooks combine text with atlases [14, 15, 43, 44], and some provide neuroanatomy for various specialties including neurosurgery [1, 19, 22], neuroradiology [8, 17, 20], neurology [2], and neuroscience [18].

The comprehension of neuroanatomy is crucial in any neurosurgical, neuroradiological, neuro-oncological, or neurological procedure. Therefore, CNS anatomy has been intensively studied by generations of neuroanatomists, neurosurgeons, neurologists, neuroradiologists, neurobiologists, and psychologists, among others, including Renaissance artists. This resulted, however, in neuroanatomy discrepancies, inconsistencies, and even controversies among various communities in terms of parcellation, demarcation, grouping, terminology, and presentation.

The present work differs from existing neuroanatomy primers. Our overall objective is to make the presentation of brain anatomy easy. To achieve this objective:

- The presentation of neuroanatomy is in three dimensions (3D) with additional supportive planar images in the orthogonal (axial, coronal, and sagittal) planes.
- The brain is subdivided into structure, vasculature, and connections (white matter tracts); consequently, we consider structural, vascular, and connectional neuroanatomies.

---

W.L. Nowinski (✉)  
Biomedical Imaging Lab, ASTAR, Singapore  
e-mail: wieslaw@sbic.a-star.edu.sg

- 3D cerebral models of structure, vasculature, and tracts are mutually consistent because they were derived from the same brain specimen.
- 3D cerebral models and the planar images are fully parcellated; each parcellated object is uniquely colored.
- 3D cerebral models and the planar images are completely labeled; as a terminology, we use the *Terminologia Anatomica* [75].
- 3D cerebral models are electronically dissectible into groups and individual components.

In this work, we use the digital brain atlases developed in our laboratory for nearly 2 decades [63–69]. The 3D cerebral models have been created from multiple 3 and 7 Tesla magnetic resonance scans of the same brain specimen (WLN) [69]. The development of the atlases is addressed in [76–80], tools for their development in [81], techniques for modeling of cerebral structures in [76, 82, 83], and atlas-based applications in [77–80, 84–92].

## 2.2 Structural (Gross) Neuroanatomy

We present parcellation of the brain in 3D followed by sectional neuroanatomy. The stereotactic target structures and functional (Brodmann's) areas also are outlined.

### 2.2.1 Brain Parcellation

The CNS consists of the **brain** and the **spinal cord**. The brain encases the fluid-filled **ventricular system** and is parcellated into three main components (Fig. 2.1a):

- **Cerebrum**
- **Cerebellum (the little brain)**
- **Brainstem**

The cerebrum comprises:

- Left and right **cerebral hemispheres**
- Interbrain between the cerebrum and the brainstem termed the **diencephalon**
- **Deep gray nuclei**

The cerebral hemispheres are the largest compartment of the brain and are interconnected by white matter fibers (see Sect. 2.4.2). The hemispheres are composed of:

- Outer **gray matter** termed the **cerebral cortex**
- Inner **white matter** encompassing the deep gray nuclei

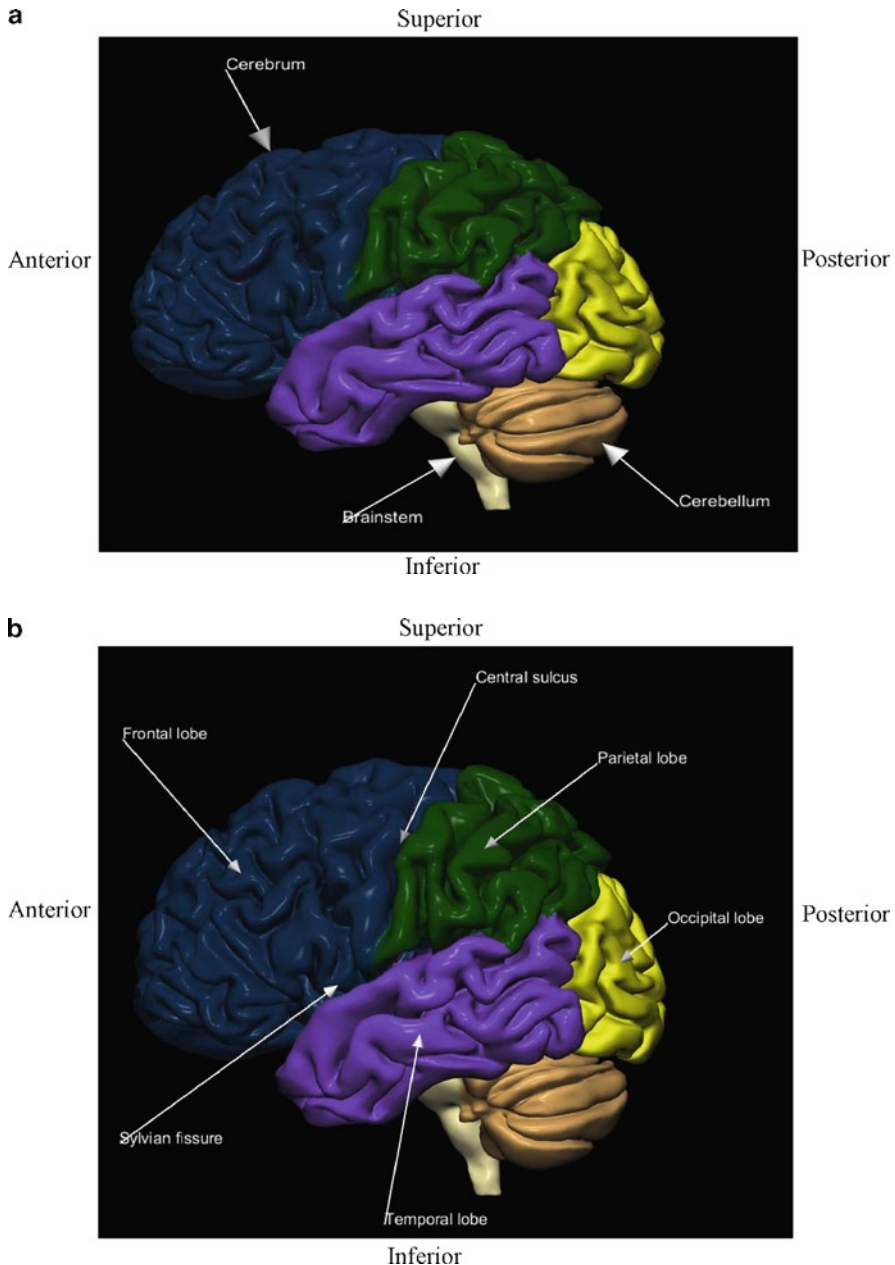


**Fig. 2.1** Gross anatomy of the left cerebral hemisphere: (a) brain parcellation; (b) lobes: lateral view; (c) lobes: medial view

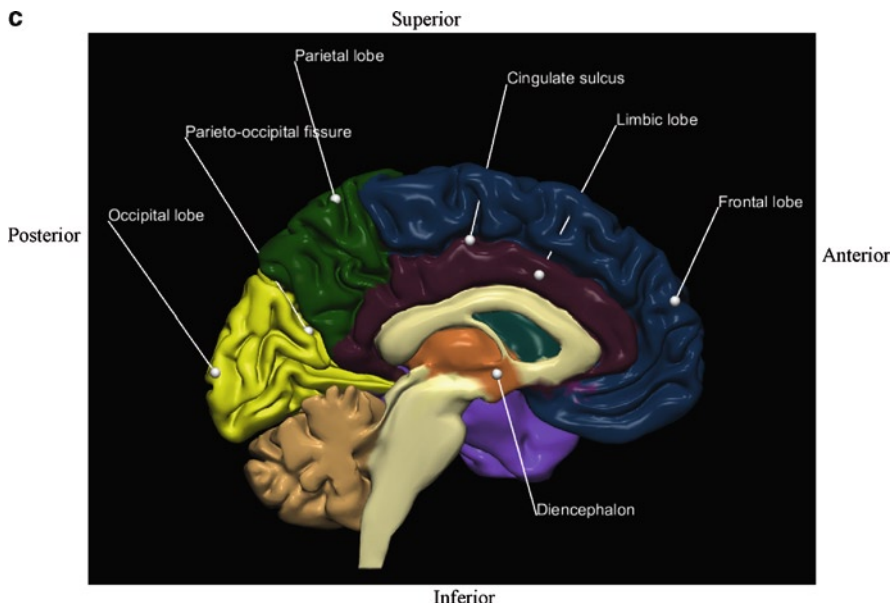


**Fig. 2.1** (continued)

The gray matter contains mainly nerve cell bodies, while the white matter is made up predominantly of nerve fibers (axons). The cerebral cortex is highly convoluted. The folds form *gyri* that are separated by grooves called *sulci* or *fissures* (deep sulci). The cerebral hemispheres are parcellated into five *lobes* (Fig. 2.1b, c):

- **Frontal lobe**
- **Temporal lobe**
- **Parietal lobe**
- **Occipital lobe**
- **Limbic lobe**

The **insula** is sometimes classified as the *central* or *insular lobe*. The lobes are partly demarcated by the sulci/fissures, Fig. 2.1. The **central sulcus** separates the frontal lobe anterior from the parietal lobe posterior, Fig. 2.1b. The **Sylvian (lateral) fissure** demarcates the temporal lobe below from the frontal and parietal lobes above, Fig. 2.1b. The **parieto-occipital fissure** separates the parietal lobe anterior from the occipital lobe posterior, Fig. 2.1c. The **cingulate sulcus** separates the frontal lobe above from the limbic lobe below, Fig. 2.1c.

The diencephalon contains (Fig. 2.1c):

- **Thalamus** (see also Fig. 2.6)
- **Subthalamus** including the *subthalamic nucleus* (see Sect. 2.2.6)
- **Hypothalamus** (see also Fig. 2.10a)

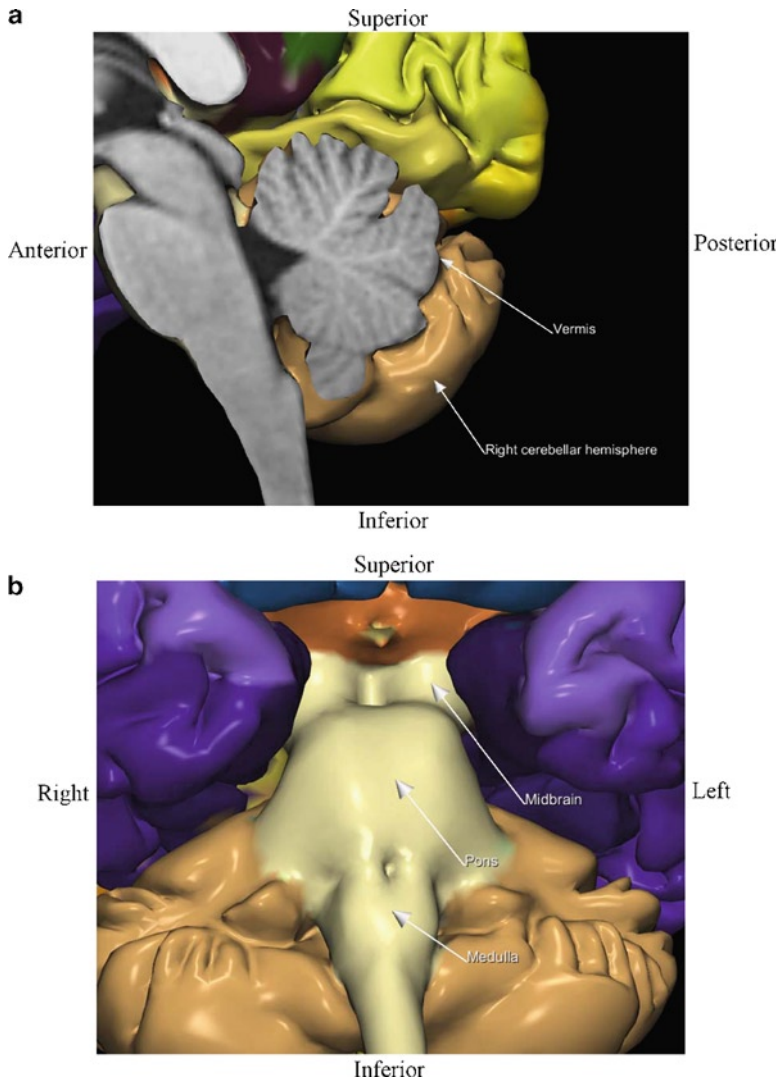


**Fig. 2.2** Cerebellum and brainstem: (a) cerebellum (medial view); (b) midbrain, pons, and medulla of the brainstem (infero-anterior view)

The cerebellum is composed of (Fig. 2.2a):

- Left and right **cerebellar hemispheres**
- Midline **vermis** which unites them

The brainstem is subdivided into (Fig. 2.2b):

- **Midbrain**
- **Pons**
- **Medulla**

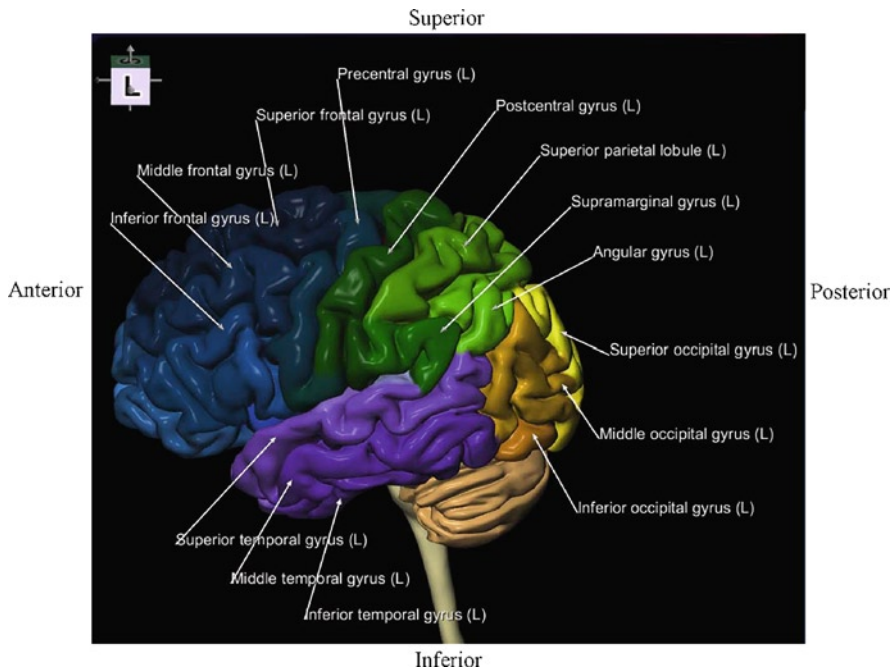


**Fig. 2.3** Cortical areas of the left (L) hemisphere: lateral view. The orientation cube in the *top-left corner* indicates the viewing direction (*L* left; *R* right; *S* superior (dorsal); *I* inferior (ventral); *A* anterior; *P* posterior). Each gyrus is assigned a unique color

### 2.2.2 *Cortical Areas*

The cortex has three surfaces: lateral, medial, and inferior (also called basal or ventral). Moreover, the transitional areas form the *frontal*, *temporal*, and *occipital poles* (see, e.g., Figs. 2.5 and 2.27).

#### 2.2.2.1 *Lateral Surface*

Four lobes are present on the lateral surface: frontal, temporal, parietal, and occipital, Fig. 2.1b. The lateral surface of the frontal lobe is subdivided by three sulci (superior frontal sulcus, inferior frontal sulcus, and precentral sulcus) into four gyri (Fig. 2.3):

- *Superior frontal gyrus*
- *Middle frontal gyrus*
- *Inferior frontal gyrus*
- *Precentral gyrus*

The lateral surface of the temporal lobe is subdivided by two sulci (superior temporal sulcus and inferior temporal sulcus) into three gyri (Fig. 2.3):

- *Superior temporal gyrus*
- *Middle temporal gyrus*
- *Inferior temporal gyrus*

The lateral surface of the parietal lobe is subdivided by the intraparietal sulcus into three gyri (Fig. 2.3):

- *Postcentral gyrus*
- *Superior parietal gyrus (lobule)*
- *Inferior parietal gyrus (lobule)*
  - *Supramarginal gyrus*
  - *Angular gyrus*

The lateral surface of the occipital lobe is subdivided by two sulci (superior occipital sulcus and inferior occipital sulcus) into three gyri (Fig. 2.3):

- *Superior occipital gyrus*
- *Middle occipital gyrus*
- *Inferior occipital gyrus*

### 2.2.2.2 Medial Surface

The frontal, parietal, occipital, and limbic lobes are present on the medial surface, Fig. 2.1c. The limbic lobe contains the gyri located at the inner edge (or *limbus*) of the hemisphere including (Fig. 2.4):

- *Subcallosal gyrus (areas)*
- *Cingulate gyrus*
- *Isthmus (of cingulate gyrus)*
- *Parahippocampal gyrus*

The superior frontal gyrus (separated from the limbic lobe by the cingulate sulcus, Fig. 2.1c) occupies most of the medial surface of the frontal lobe, Fig. 2.4. The parietal lobe includes the *precuneus*, Fig. 2.4 (separated from the occipital lobe by the parieto-occipital fissure, Fig. 2.1c). The occipital lobe comprises the *cuneus* and the *lingual gyrus*, Fig. 2.4.

### 2.2.2.3 Inferior Surface

The inferior surface includes the frontal, temporal, and occipital lobes. The frontal lobe comprises (Fig. 2.5):

- *Straight gyrus*
- *Orbital gyri* parcellated by the approximately *H-shape sulcus* into the *anterior, medial, lateral, and posterior orbital gyri*

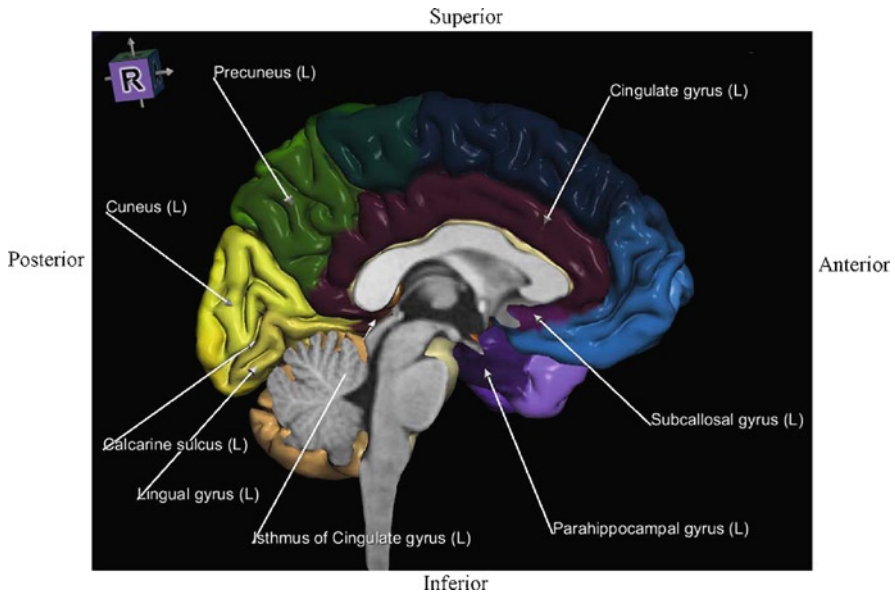


**Fig. 2.4** Cortical areas of the left hemisphere: medial view

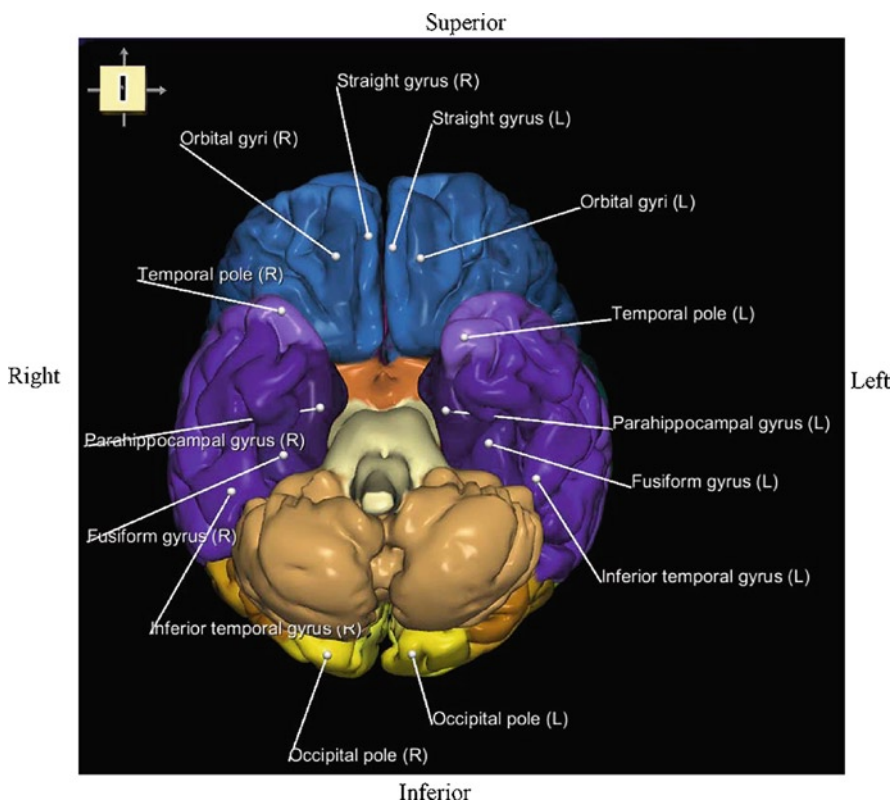


**Fig. 2.5** Cortical areas: inferior view

The temporal and occipital lobes are subdivided by two sulci (lateral occipitotemporal sulcus and medial occipitotemporal (collateral) sulcus) into three gyri, Fig. 2.5:

- **Medial occipitotemporal gyrus** whose temporal part constitutes the **parahippocampal gyrus** and the occipital part the **lingual gyrus**
- **Lateral occipitotemporal gyrus** (called also the **fusiform gyrus**)
- **Inferior temporal gyrus**

The lingual gyrus is separated from the cuneus by the **calcarine sulcus (fissure)**.

### 2.2.3 Deep Gray Nuclei

The deep gray nuclei are paired gray matter structures. The main deep gray nuclei are (Fig. 2.6):

- **Basal ganglia (nuclei)**
  - **Caudate nucleus**
  - **Lentiform nuclei**
    - **Putamen**
    - **Globus pallidus**
      - **Lateral (or outer) segment**
      - **Medial (or inner) segment** (see also Sect. 2.2.6)
- **Thalamus**
- **Hippocampus**
- **Amygdala (amygdaloid body)**

The lentiform nuclei and the caudate nucleus form the **striatum**.

### 2.2.4 Ventricular System

The ventricular system contains four interconnected cerebral ventricles (cavities) filled with cerebrospinal fluid (CSF) (Fig. 2.7a):

- Left and right **lateral ventricles**
- **Third ventricle**
- **Fourth ventricle**

CSF is secreted mainly in the *choroid plexus* (a network of vessels) and circulates from the lateral ventricles through the paired **interventricular foramina** (of Monro) to the third ventricle, and then via the  **aqueduct** to the fourth ventricle, Fig. 2.7a. The lateral ventricles are the largest and each contains (Fig. 2.7b):

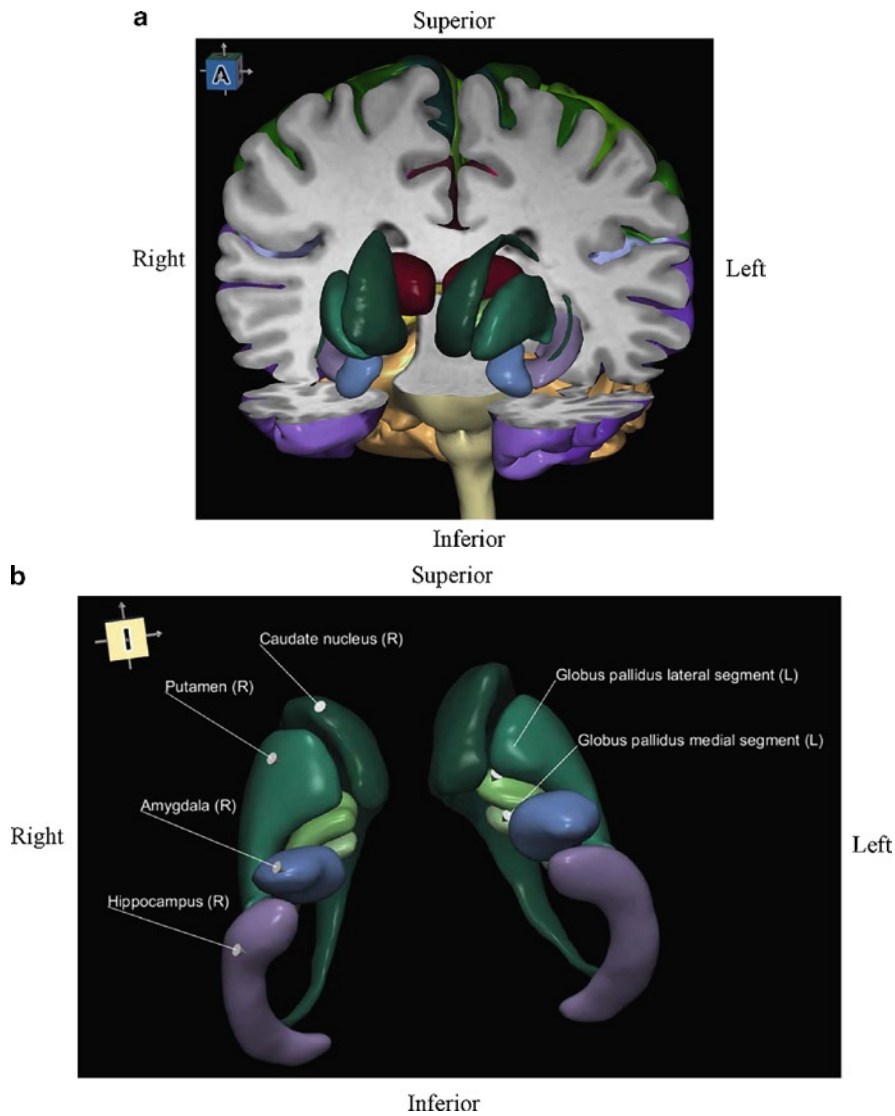


**Fig. 2.6** Deep gray nuclei: (a) embedded into the brain; (b) shown in isolation

- **Body** (or *central portion*)
- **Atrium** (or *trigon*)
- **Horns**
  - **Frontal** (*anterior*)
  - **Occipital** (*posterior*)
  - **Temporal** (*inferior*)

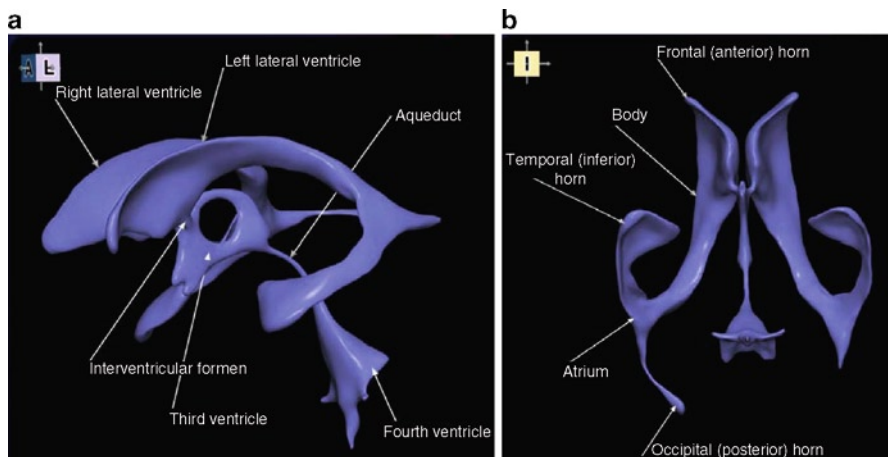


**Fig. 2.7** Ventricular system: (a) interconnected ventricles; (b) components of the lateral ventricle

### 2.2.5 Sectional Neuroanatomy

Sectional (planar) neuroanatomy is typically presented on orthogonal (axial, coronal, and sagittal) images. To spatially locate the orthogonal images, we place them in the Talairach coordinate system [48], which is a stereotactic reference system based on the anterior and posterior commissures (see also Fig. 2.28a) with the origin at the center of the anterior commissure (see also Figs. 2.8–2.10).

Four axial images located at  $-12$ ,  $+1$ ,  $+12$ , and  $+24$  mm (where “ $-$ ” denotes the level below and “ $+$ ” above the anterior commissure) with the cortical areas and deep gray nuclei segmented and labeled are shown in Fig. 2.8.

Two coronal images passing through the anterior and posterior commissures are presented in Fig. 2.9.

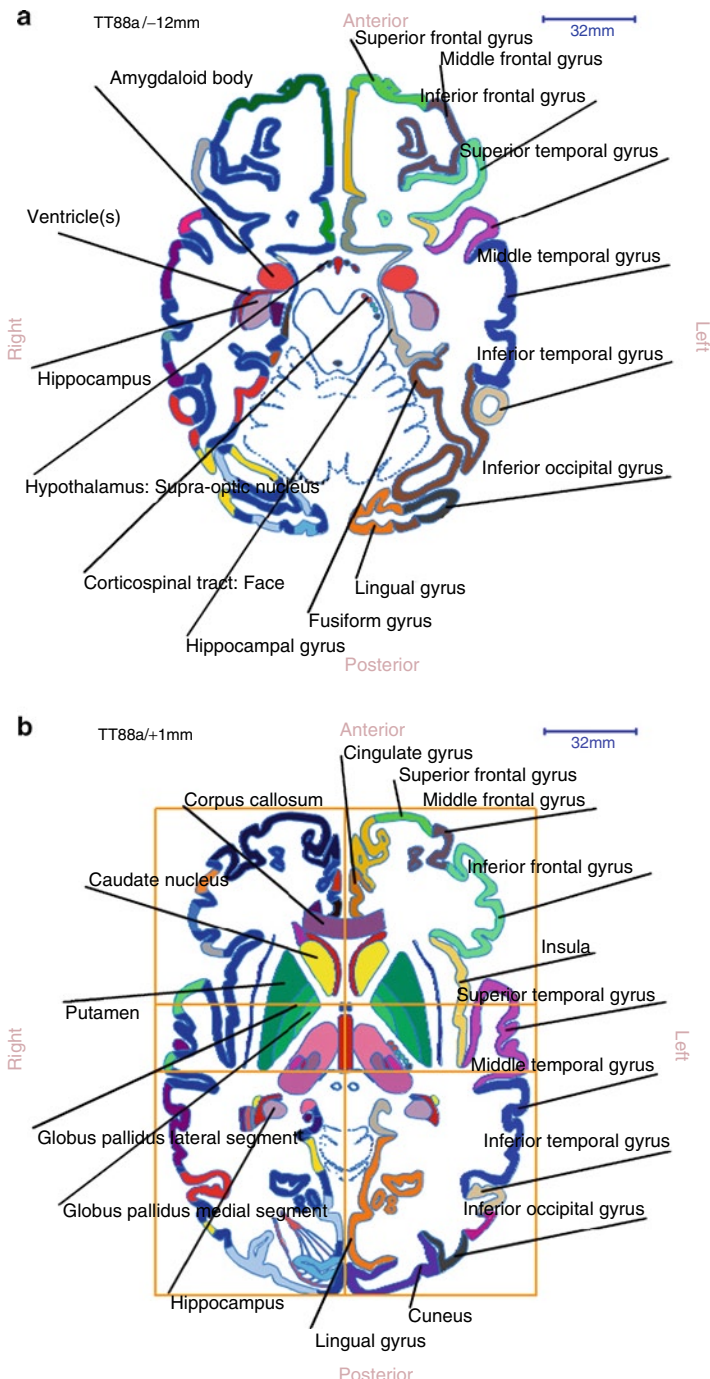
Two sagittal images located at 3 and 21 mm from the midline are shown in Fig. 2.10.

### 2.2.6 Main Stereotactic Target Structures

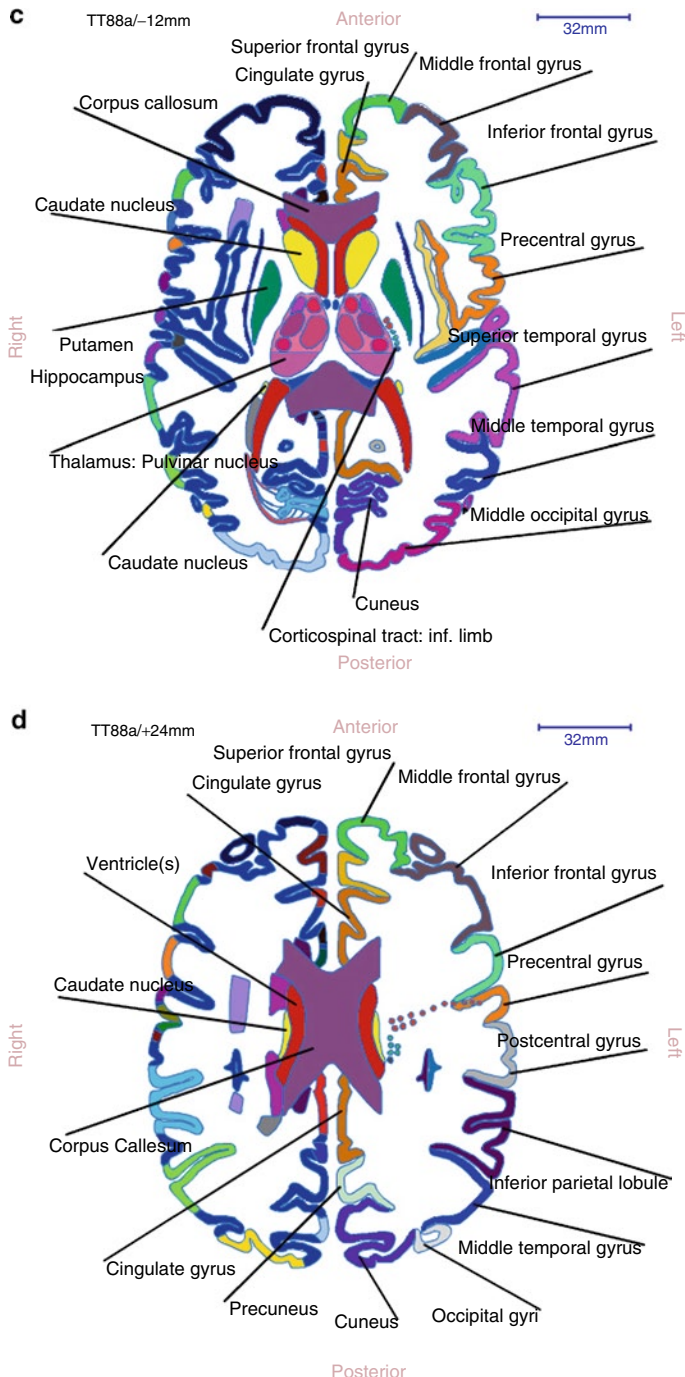
Several subcortical structures (and more recently also cortical areas) are therapeutic stimulation targets in stereotactic and functional neurosurgery [84] to treat movement disorders (mainly Parkinson’s disease), epilepsy, pain, and mental disorders (psychosurgery). The main stereotactic target structures are:

- **Subthalamic nucleus**, Fig. 2.11
- **Ventrointermediate nucleus of the thalamus**, Fig. 2.12
- **Globus pallidus interna** (medial segment), Fig. 2.13

The subthalamic nucleus presented on the triplanar (the axial, coronal, and sagittal planes) is shown in Fig. 2.11.



**Fig. 2.8** Planar neuroanatomy in axial orientation at: (a) -12 mm; (b) +1 mm (along with the Talairach grid); (c) +12 mm; (d) +24 mm (“-” denotes the level below and “+” the level above the anterior commissure)

**Fig. 2.8** (continued)

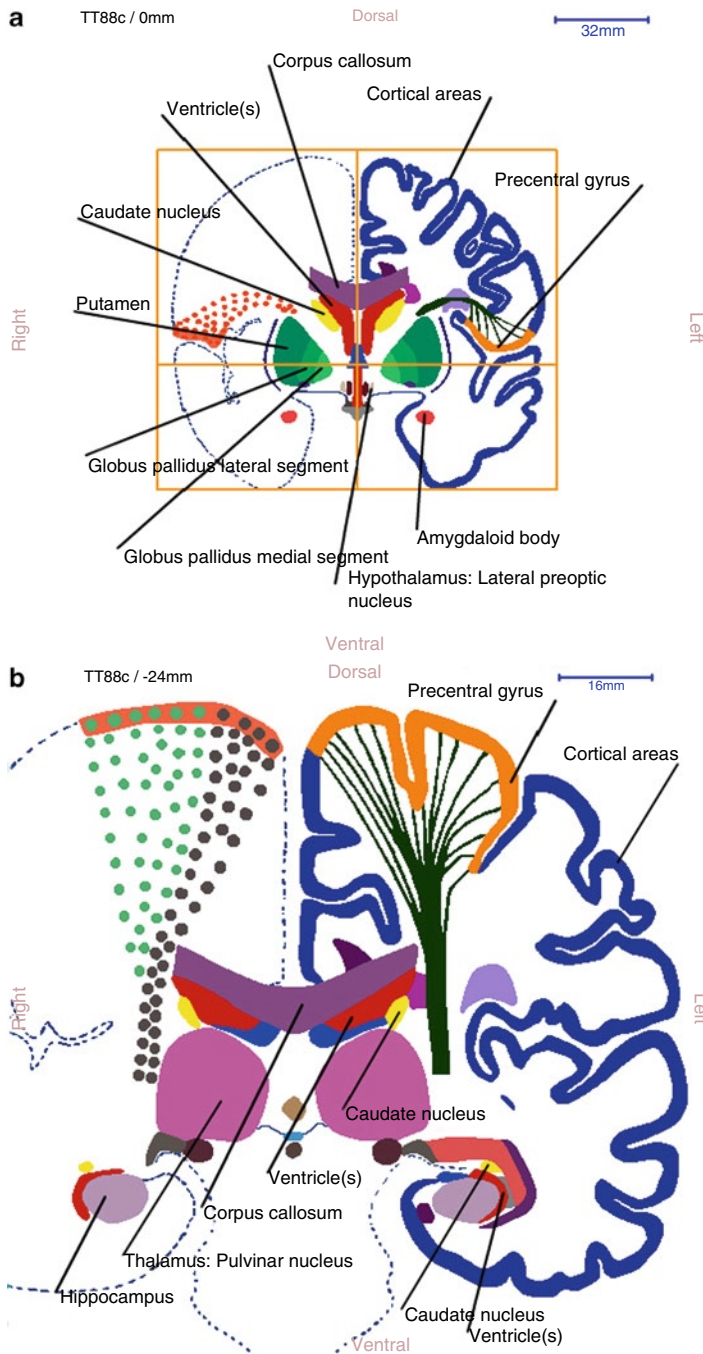


**Fig. 2.9** Planar neuroanatomy in coronal orientation at: (a) 0 mm passing through the anterior commissure (point), i.e., the location on the coronal plane where the horizontal and vertical planes of the Talairach system intersect; (b) -24 mm passing through the posterior commissure (point)

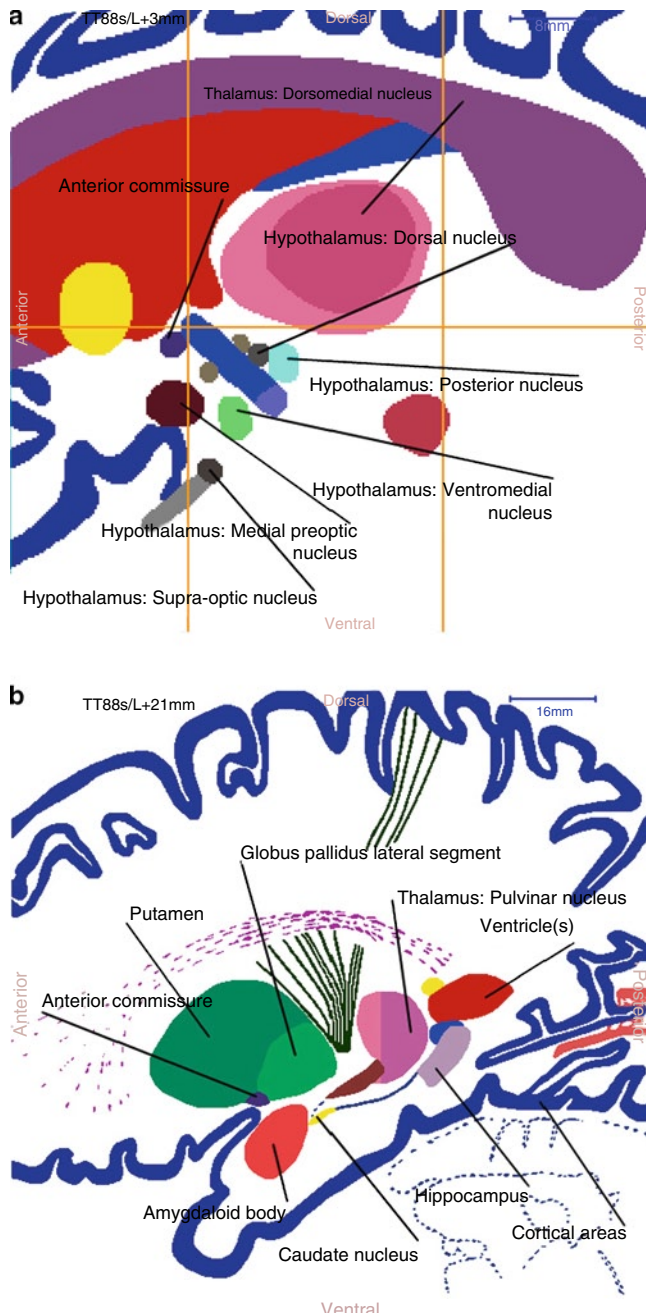


**Fig. 2.10** Planar neuroanatomy in sagittal orientation at: (a) 3 mm (along with the Talairach grid); (b) 21 mm from the midline

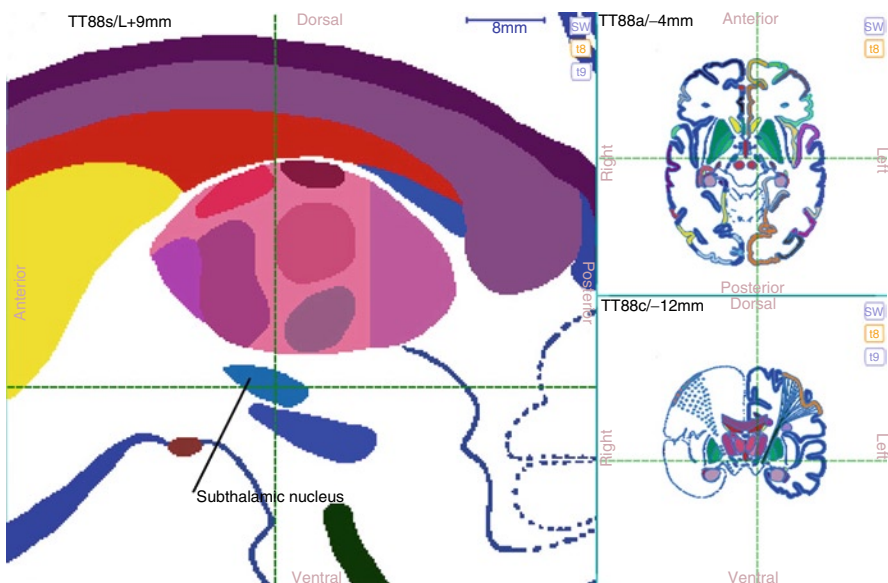


**Fig. 2.11** Subthalamic nucleus on sagittal, axial, and coronal planes (the location of the triplanar is marked by the green dashed lines)

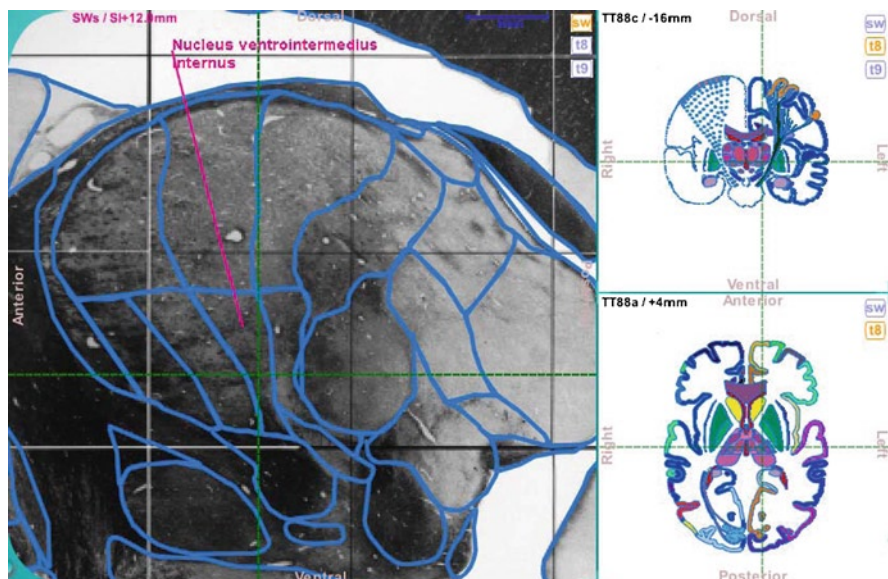


**Fig. 2.12** Ventrointermediate nucleus of the thalamus: sagittal, coronal, and axial planes

The ventrointermediate nucleus of the thalamus on the triplanar is presented in Fig. 2.12.

The globus pallidus interna is illustrated in Fig. 2.13.

All three structures in 3D placed in the Talairach stereotactic coordinate system are shown in Fig. 2.14.

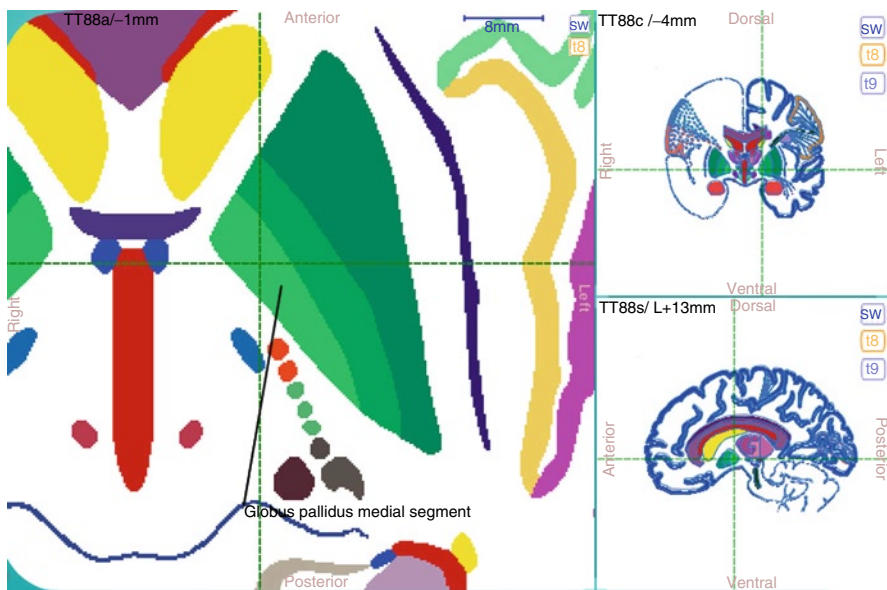


**Fig. 2.13** Globus pallidus interna (medial segment): axial, coronal, and sagittal planes

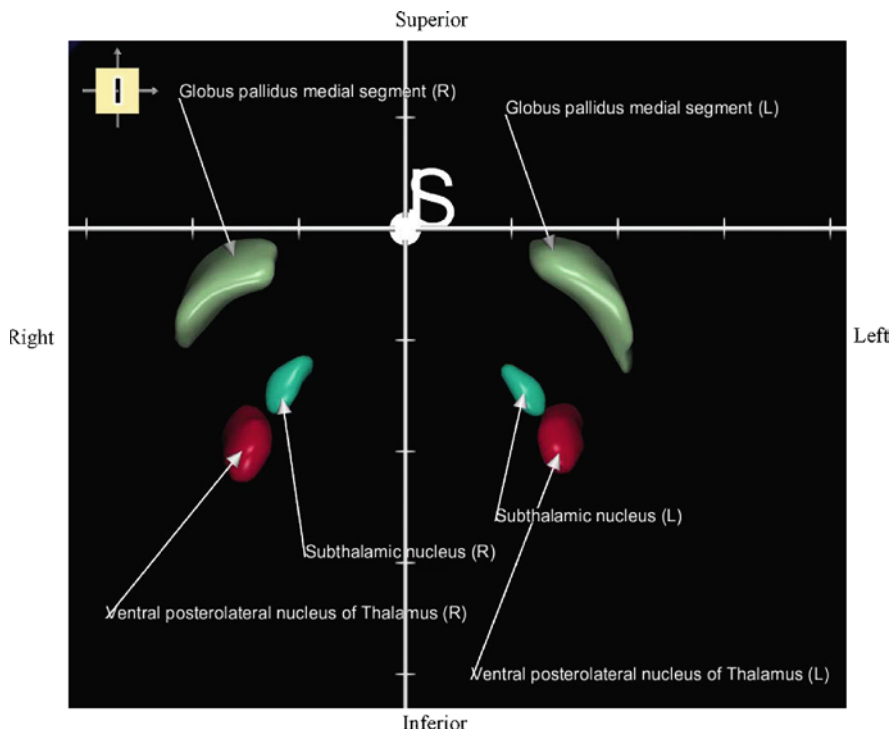


**Fig. 2.14** Stereotactic target structures in 3D. The marks on the axes are placed at 10-mm intervals

## 2.2.7 Functional Areas

Several parcellations are introduced to subdivide the cortical regions into functional areas [16]. Brodmann's parcellation based on histology is the most widely used and it is illustrated in axial orientation in Fig. 2.15. **Brodmann's areas** are useful in neuroscience and functional studies.

## 2.3 Vascular Neuroanatomy

The knowledge of cerebrovasculature is crucial in stroke, vascular and tumor surgery as well as interventional neuroradiology. The complete cerebrovasculature is highly complex and variable, Fig. 2.16. It is subdivided into:

- **Arterial system**
- **Venous system** with the **cerebral veins** and **dural sinuses**

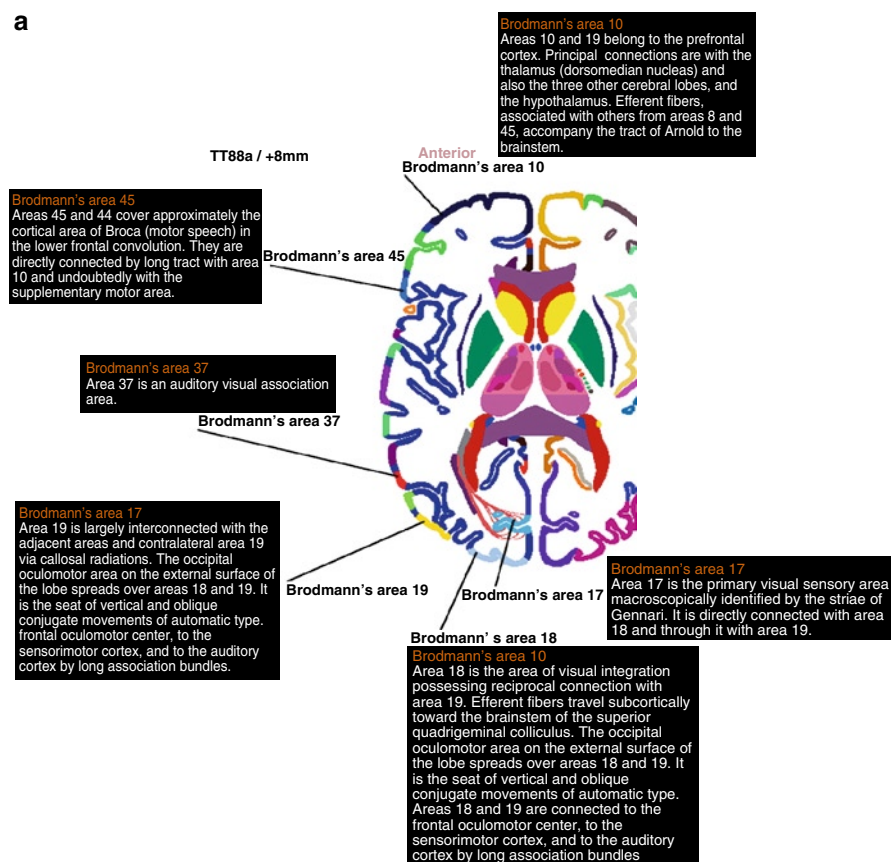


**Fig. 2.15** Brodmann's areas in axial orientation: (a) vision and speech areas (+8 mm); (b) motor and sensory areas (+40 mm). The areas are uniquely color-coded

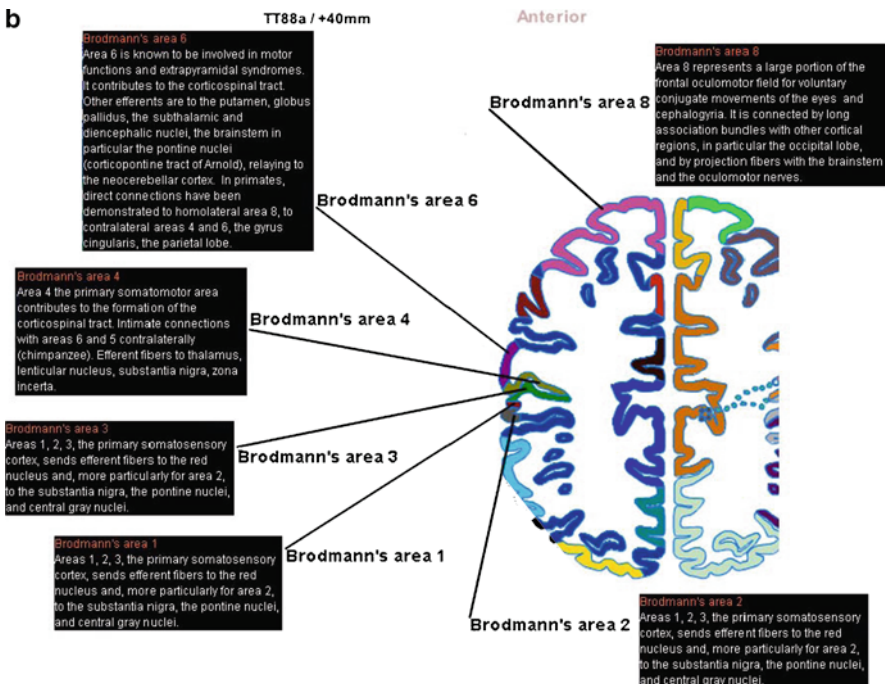


**Fig. 2.15** (continued)

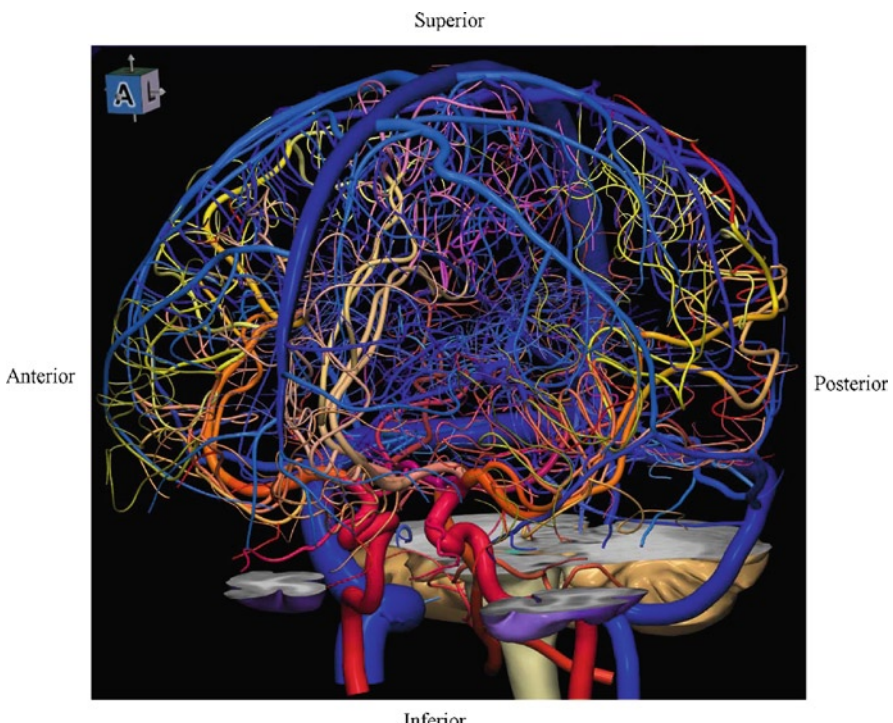


**Fig. 2.16** The cerebral vasculature with arteries, veins, and dural sinuses. The vessels are uniquely color-coded such that all vessels with the same name have the same color

### 2.3.1 Arterial System

#### 2.3.1.1 Parcellation of Arterial System

The brain is supplied by two pairs of arteries:

- Left and right ***internal carotid arteries*** anteriorly
- Left and right ***vertebral arteries*** posteriorly forming the ***basilar artery*** (Fig. 2.17a) interconnected by the ***circle of Willis*** (Fig. 2.21).

The internal carotid artery (ICA) branches into the ***anterior cerebral artery*** (Fig. 2.17c) and the ***middle cerebral artery*** (Fig. 2.17d). The left and right ***posterior cerebral arteries*** originate from the basilar artery (Fig. 2.17e).

#### 2.3.1.2 Anterior Cerebral Artery

The anterior cerebral artery has the following main branches (Fig. 2.18):

- ***A1 segment (precommunicating part)***
- ***A2 segment (postcommunicating part)***
  - ***Pericallosal artery***
  - ***Callosomarginal artery***

#### 2.3.1.3 Middle Cerebral Artery

The middle cerebral artery is subdivided into four segments (Fig. 2.19a):

- ***M1 segment (sphenoid part)***
- ***M2 segment (insular part)***
- ***M3 segment (opercular part)***
- ***M4 segment (terminal part)***

Its main branches for the left hemisphere are shown in Fig. 2.19b.

#### 2.3.1.4 Posterior Cerebral Artery

The posterior cerebral artery is parcelled into four segments (Fig. 2.20):

- ***P1 segment (precommunicating part)***
- ***P2 segment (postcommunicating part)***
- ***P3 segment (lateral occipital artery)***
- ***P4 segment (medial occipital artery)***

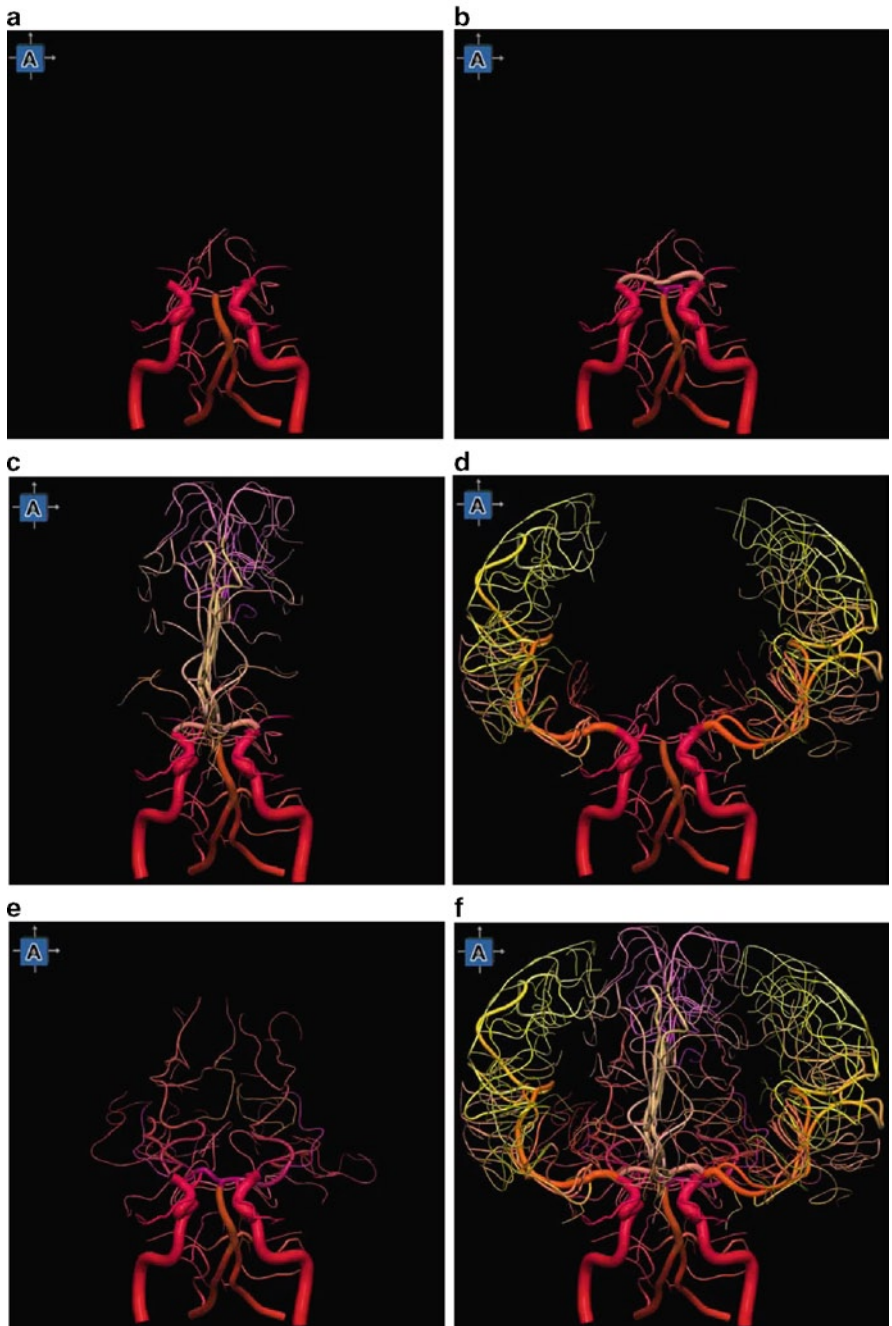


**Fig. 2.17** The cerebral arteries: (a) blood supply to the brain by the internal carotid artery (ICA) anteriorly, and the vertebral artery (VA) and the basilar artery (BA) posteriorly; (b) ICA and VA connected by the circle of Willis; (c) anterior cerebral artery along with the ICA, VA, and BA; (d) middle cerebral artery along with the ICA, VA, and BA; (e) posterior cerebral artery along with the ICA, VA, and BA; (f) complete arterial system

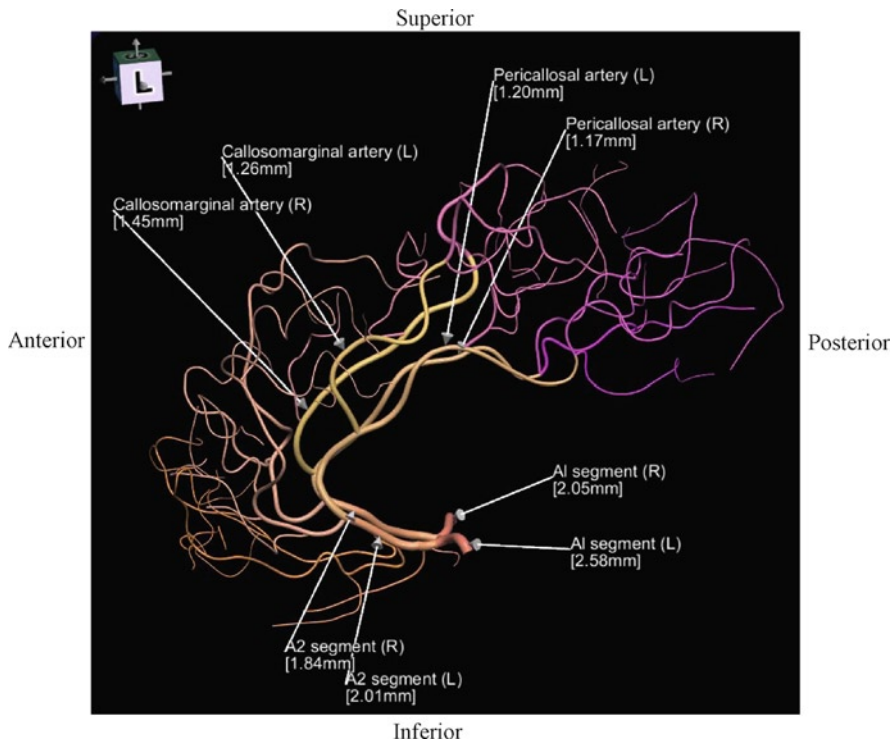


**Fig. 2.18** Anterior cerebral artery

### 2.3.1.5 Circle of Willis

The circle of Willis connects the anterior and posterior circulations. It includes the following vessels (Fig. 2.21):

- ***Anterior communicating artery***
- Left and right ***posterior communicating arteries***
- Part of the left and right ***internal carotid arteries***
- Left and right ***A1 segments*** of the anterior cerebral arteries
- Left and right ***P1 segments*** of the posterior cerebral arteries

### 2.3.2 Venous System

#### 2.3.2.1 Parcellation of Venous System

The main components of the venous system are, Fig. 2.22:

- ***Dural sinuses***

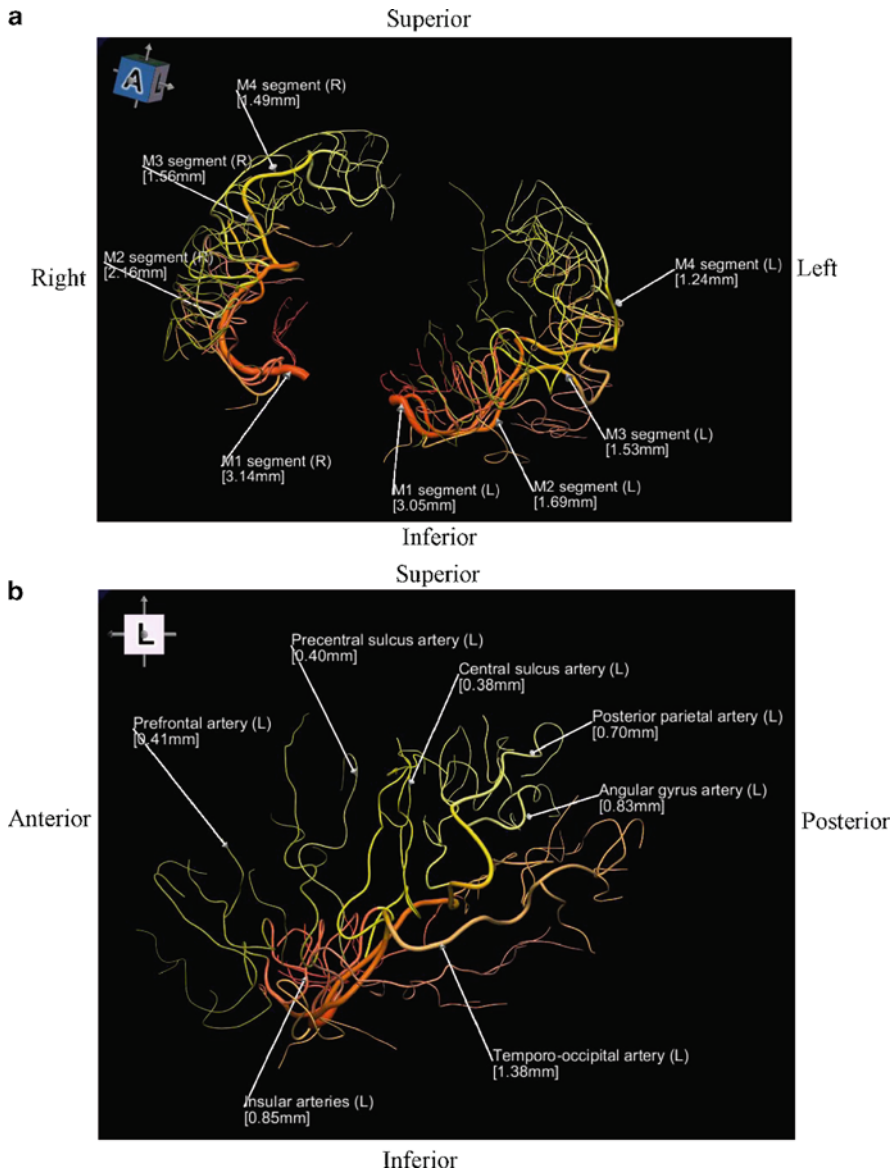


**Fig. 2.19** Middle cerebral artery: (a) M1, M2, M3, and M4 segments; (b) main branches of the left hemisphere

- **Cerebral veins**
  - *Superficial veins*
  - *Deep veins*

The cerebral veins empty into the dural sinuses.

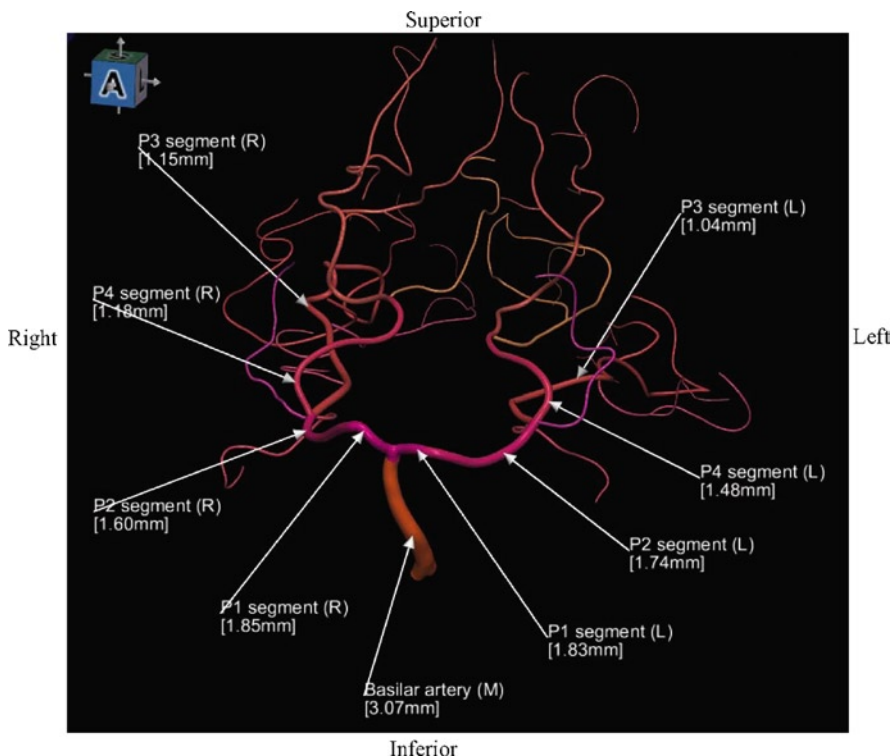


**Fig. 2.20** Posterior cerebral artery

### 2.3.2.2 Dural sinuses

The main dural sinuses are (Fig. 2.23):

- ***Superior sagittal sinus***
- ***Inferior sagittal sinus***
- ***Straight sinus***
- Left and right ***transverse sinuses***
- Left and right ***sigmoid sinuses***

### 2.3.2.3 Cerebral Veins

The main superficial cerebral veins are (Fig. 2.24):

- ***Frontopolar veins***
- ***Prefrontal veins***
- ***Frontal veins***
- ***Parietal veins***
- ***Occipital veins***

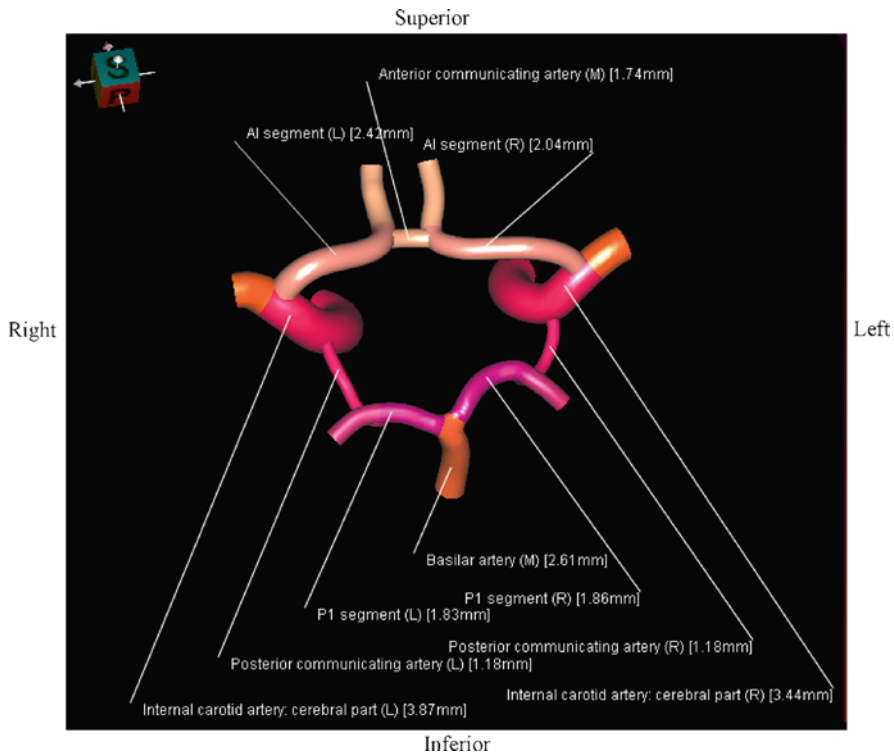


**Fig. 2.21** The circle of Willis

Other important superficial veins include **superior** and **inferior anastomotic veins**, and **superficial middle cerebral vein**.

The main deep cerebral veins are (Fig. 2.25):

- **Great vein** (of Galen)
- Left and right **basal vein** (of Rosenthal)
- Left and right **internal cerebral veins**

### 2.3.3 Vascular Variants

The human cerebrovasculature is highly variable and vascular variants have been extensively studied, see e.g., [6, 10, 13, 22]. Variations exist in terms of origin, location, shape, size, course, branching patterns as well as surrounding vessels and structures. The knowledge of cerebrovascular variants is central in diagnosis, treatment, and medical education.

Main variants in 3D in the circle of Willis are show in Fig. 2.26 (more 3D variants are presented in [70]).

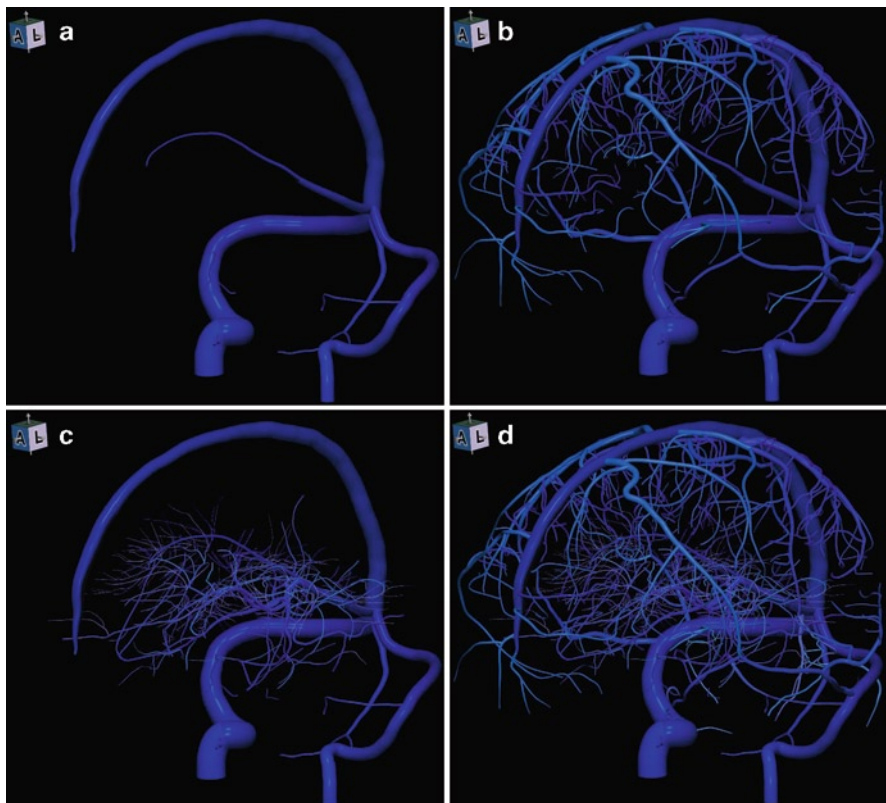


**Fig. 2.22** Parcellation of the venous system: (a) dural sinuses (DS); (b) superficial veins with the DS; (c) deep veins with the DS; (d) complete venous system

## 2.4 Connectional Neuroanatomy

Three types of white matter connections (or tracts, fibers, bundles, fiber pathways, fascicles) are distinguished in the cerebral hemispheres (Fig. 2.27):

- **Commissural tracts**
- **Association tracts**
- **Projection tracts**

In addition, three cerebellar paired peduncles:

- **Superior peduncle**
- **Middle peduncle**
- **Inferior peduncle**

connect the cerebellum to the midbrain, pons and medulla of the brainstem, respectively.

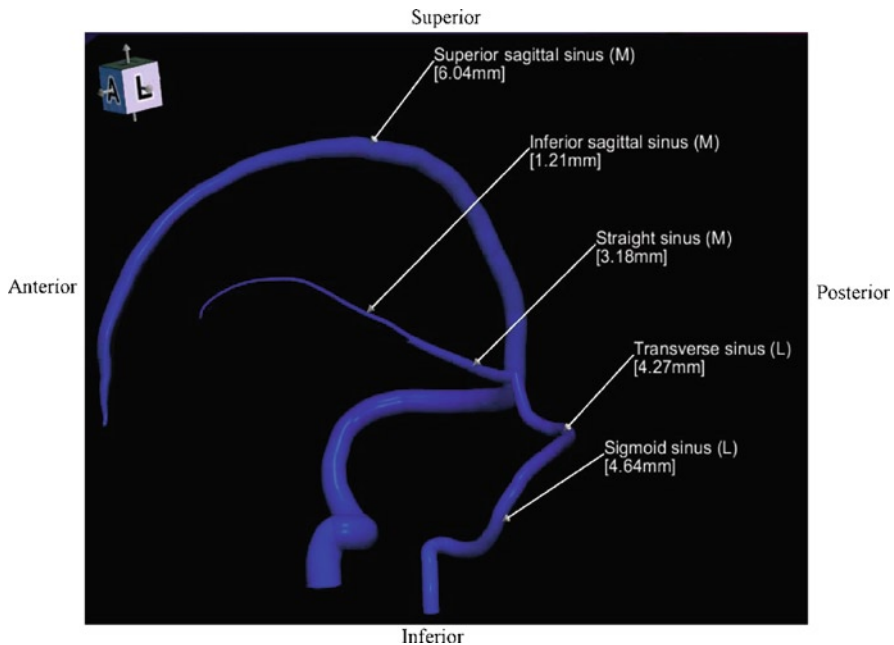


**Fig. 2.23** Dural sinuses (the left hemisphere is labeled)

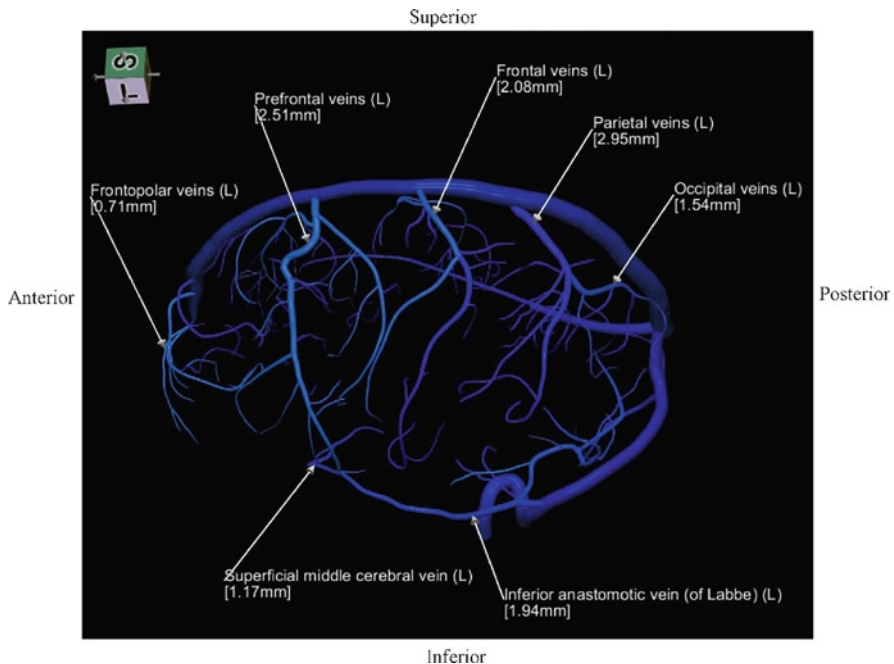


**Fig. 2.24** Superficial cerebral veins of the left hemisphere

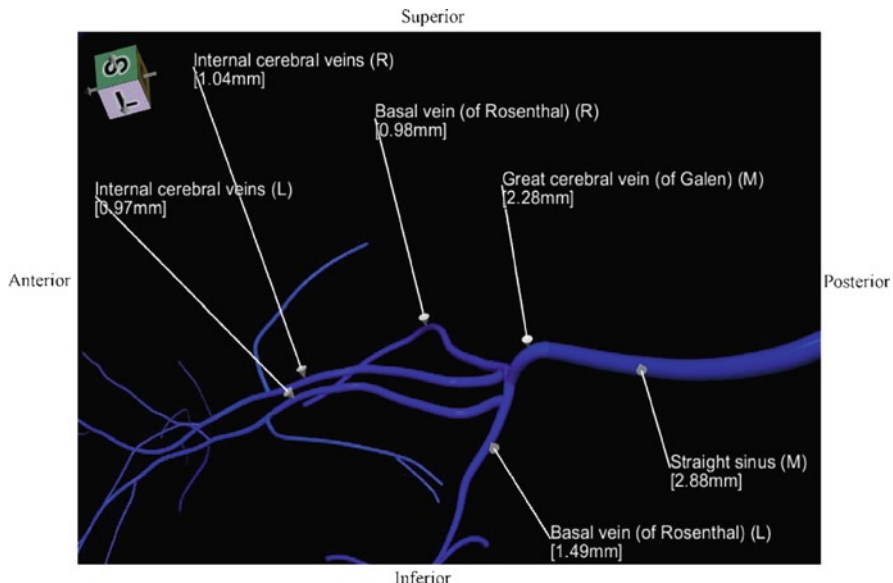


**Fig. 2.25** Deep cerebral veins



**Fig. 2.26** Vascular variants of the circle of Willis: (a) double anterior communicating artery; (b) absent left posterior communicating artery; (c) absent left P1 segment (the variants are in white)

#### 2.4.1 Commissural Tracts

The commissural tracts interconnect both hemispheres across the median plane. The main commissural tracts are, Fig. 2.28:

- **Corpus callosum**
- **Anterior commissure**
- **Posterior commissure**

The corpus callosum (the great commissure) is the largest commissure. Its three main parts, **genu** (knee), **body**, and **splenium**, connect the frontal lobes, wide areas of hemispheres, and the occipital lobes, respectively.

The anterior commissure connects the temporal lobes, while the posterior commissure the midbrain, thalamus, and hypothalamus on both sides.

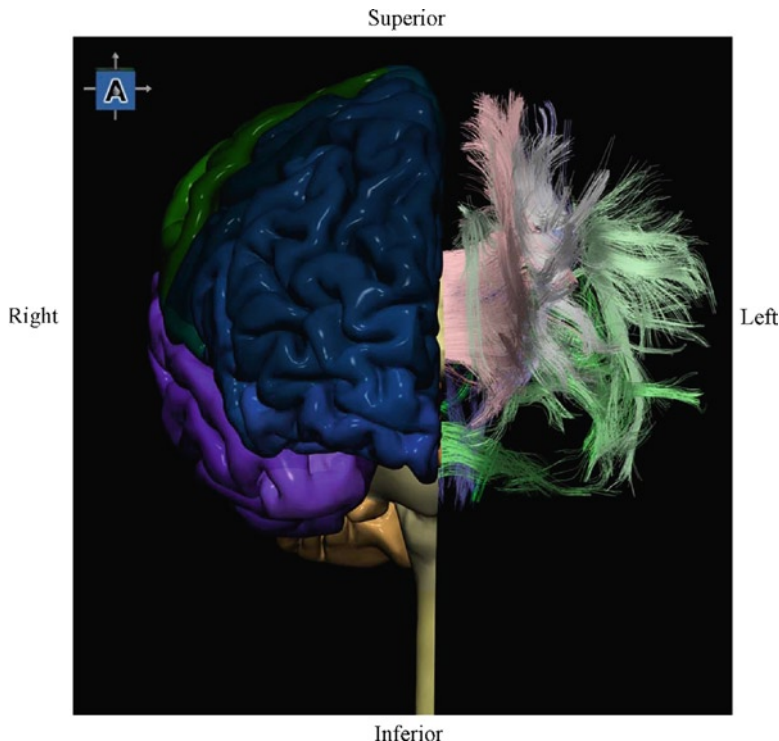


**Fig. 2.27** White matter tracts on the left and for comparison the brain on the right

#### 2.4.2 Association Tracts

The association tracts interconnect different cortical regions of the same hemisphere. There are two types of the association tracts:

- *Short arcuate* fibers that connect adjacent gyri (U fibers)
- *Long arcuate* fibers interconnecting widely separated gyri

The main association tracts are (Fig. 2.29):

- *Superior longitudinal fasciculus*
- *Middle longitudinal fasciculus*
- *Inferior longitudinal fasciculus*
- *Superior occipito-frontal fasciculus*
- *Inferior occipito-frontal fasciculus*
- *Cingulum*
- *Uncinate fasciculus*

The superior longitudinal fasciculus connects the frontal lobe with the temporal, parietal, and occipital lobes. The inferior longitudinal fasciculus links the temporal lobe with the occipital lobe. The cingulum deep to the cingulated gyrus interconnects

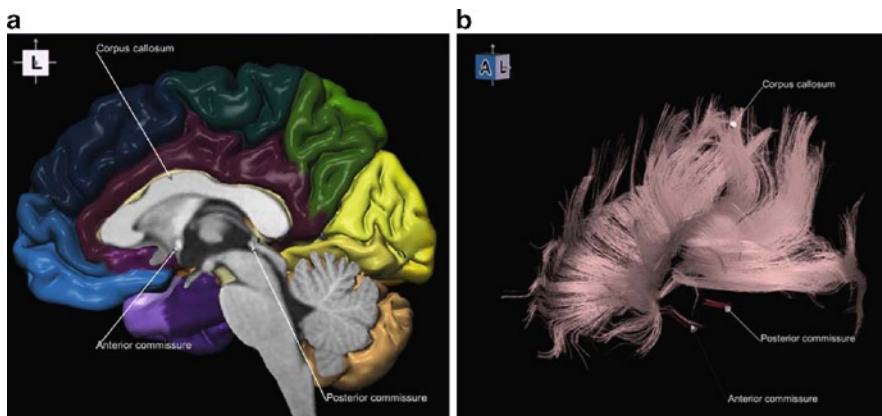


**Fig. 2.28** Commissural tracts with the corpus callosum, anterior commissure, and posterior commissure: (a) on the midsagittal plane; (b) in 3D

parts of the temporal, parietal, and occipital lobes. The uncinate fasciculus connects the frontal lobe (orbital gyri and motor speech area) with the temporal lobe.

### 2.4.3 Projection Tracts

The projection tracts connect the cortex with the subcortical structures in the diencephalon, brainstem, and spinal cord. The main projection tracts are (Fig. 2.30):

- **Cortico-spinal (pyramidal) tract**
- **Cortico-thalamic tract** including the *anterior*, *posterior (optic)*, and *superior thalamic radiations*
- **Cortico-bulbar tract** (connecting to the brainstem)
- **Cortico-pontine tract** (projecting to the cerebellum)
- **Auditory radiations**

The projection fibers between the striatum and thalamus form the **internal capsule** consisting of the **anterior limb** (containing the cortico-thalamic tract), **genus** (comprising the cortico-bulbar tract), and **posterior limb** (containing the cortico-spinal tract). The fibers radiating from the internal capsule to various parts of the cerebral cortex form the **corona radiata**.

## 2.5 Summary

The brain contains the cerebrum, cerebellum, and brainstem, and it encases the ventricular system. The cerebrum comprises the paired cerebral hemispheres and deep gray matter nuclei including the caudate nucleus, putamen, lateral and medial globus

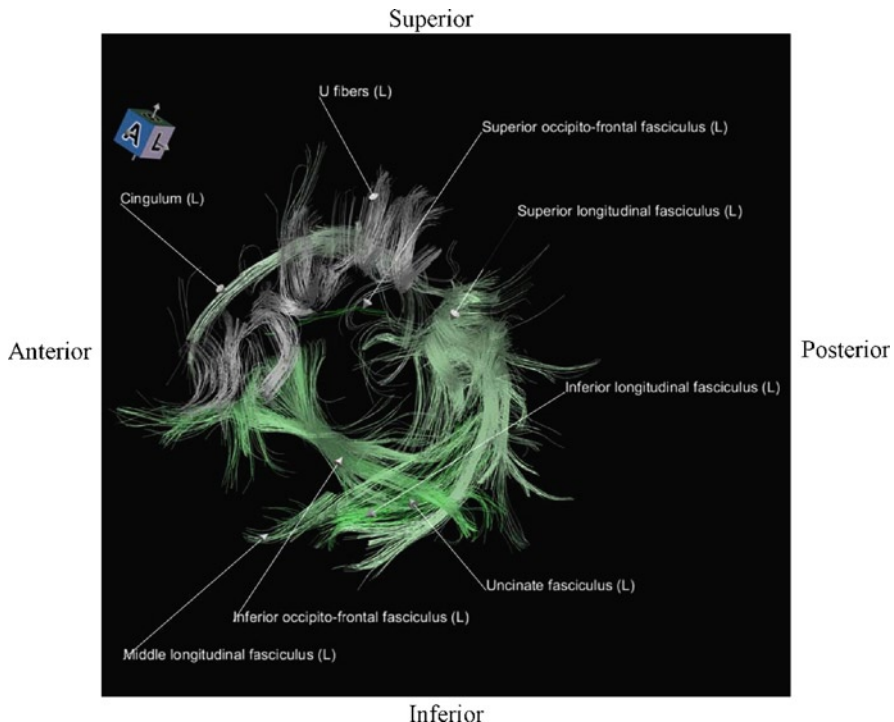


**Fig. 2.29** Association tracts of the left hemisphere

pallidus, thalamus, hypothalamus, hippocampus, and amygdala. The hemispheres are parcellated into frontal, temporal, parietal, occipital, and limbic lobes. The cerebellum contains the paired cerebellar hemispheres united by the midline vermis. The brainstem is subdivided into midbrain, pons, and medulla. The ventricular system contains the paired lateral and midline third and fourth ventricles.

The cerebral vasculature comprises the arterial and venous systems. The brain is supplied by two pairs of arteries: internal carotid artery anteriorly and vertebral artery posteriorly. The anterior and posterior circulations are connected by the circle of Willis, from which originate three paired branches: anterior cerebral, middle cerebral, and posterior cerebral arteries. The venous system contains dural sinuses, and cerebral superficial and deep veins.

The brain is connected by commissural, association, and projection tracts. The main commissural tracts (interconnecting both hemispheres) are: corpus callosum, and anterior and posterior commissures. The major association tracts (interconnecting different regions of the same hemisphere) are: superior longitudinal, middle longitudinal, inferior longitudinal, superior occipito-frontal, inferior occipito-frontal, and uncinate fascicles. The main projection tracts (connecting the cortex with subcortical structures) contain: cortico-spinal, cortico-thalamic (including optic radiation), cortico-bulbar, and cortico-pontine tracts as well as auditory radiation.

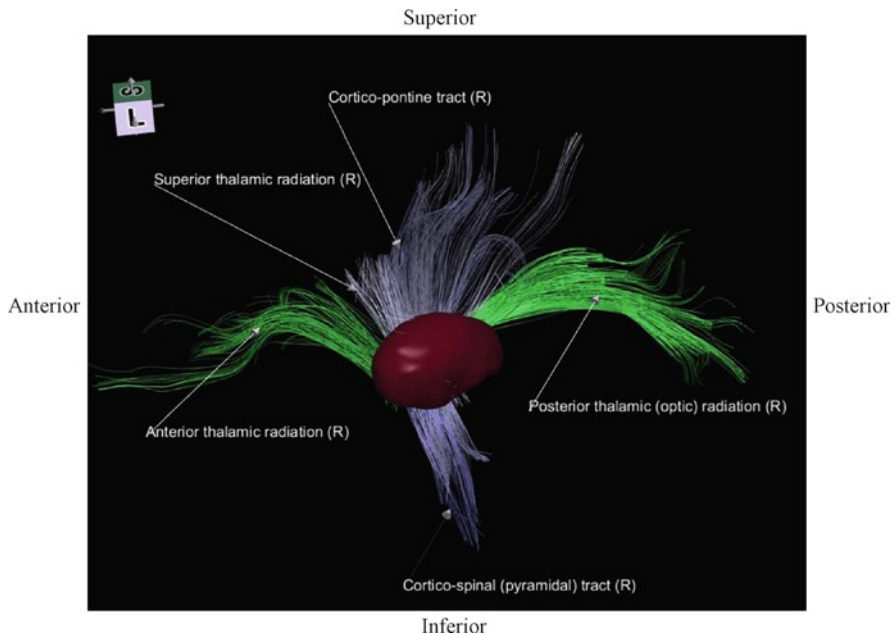


**Fig. 2.30** Projection tracts of the right hemisphere along with the thalamus

This introduction covers basic neuroanatomy. For further study, the reader is referred to the existing literature and electronic atlases.

**Acknowledgments** I am deeply grateful to Drs. J Talairach and P Tournoux for the insightful discussions about their atlases.

Numerous persons from our Biomedical Imaging Lab, A\*STAR, Singapore, have contributed to the development of tools for atlas construction and atlas-assisted applications. The key contributors are BC Chua, A Thirunavuukarasu, Y Marchenko, GY Qian, and I Volkau (the references [64–70, 76–80, 83–92] provide a more complete list of contributors). I thank Aminah Bivi for her editorial assistance.

I am also grateful to the reviewers: an anonymous reviewer and Dr. Joseph M. Corless, MD, PhD, Duke University Medical Center, for their valuable comments.

This work has been funded by A\*STAR, Singapore.

## References

### *Neuroanatomy Textbooks*

1. Apuzzo, M.L.J., Todd, E.M., Trent Jr., H.W.: *Surgery of the Human Cerebrum*. Lippincott Williams & Wilkins, Philadelphia (2009)
2. Arslan, O.: *Neuroanatomical Basis of Clinical Neurology*. Parthenon, Lancaster (2001)

3. Blumenfeld, H.: *Neuroanatomy Through Clinical Cases*. Sinauer Associates, Sunderland (2002)
4. Borden, N.M.: *3D Angiographic Atlas of Neurovascular Anatomy and Pathology*. Cambridge University Press, Cambridge (2007)
5. Carpenter, M.B., Sutin, J.: *Human Neuroanatomy*. Williams and Wilkins, Baltimore (1983)
6. Grand, W., Hopkins, L.N.: *Vasculature of the Brain and Cranial Base: Variations in Clinical Anatomy*. Thieme, Stuttgart (1999)
7. Gray, H., Bannister, L.H., Berry, M.M., et al.: *Gray's Anatomy: The Anatomical Basis of Medicine and Surgery*, 38th edn. Churchill Livingstone, Oxford (1995)
8. Harnsberger, H.R., Osborn, A.G., Ross, J., et al.: *Diagnostic and Surgical Imaging Anatomy: Brain, Head and Neck, Spine*. Amirsry, Salt Lake City (2006)
9. Hendelman, W.J.: *Atlas of Functional Neuroanatomy*. CRC Press LLC, Boca Raton (2000)
10. Huber, P.: *Cerebral Angiography*, 2nd edn. Thieme, Stuttgart (1982)
11. Kretschmann, H.J., Weinrich, W.: *Neurofunctional Systems. 3D Reconstructions with Correlated Neuroimaging*. Thieme, Stuttgart (1998)
12. Kretschmann, H.J., Weinrich, W.: *Cranial Neuroimaging and Clinical Neuroanatomy*, 3rd edn. Thieme, Stuttgart (2004)
13. Lasjaunias, P., Berenstein, A., ter Brugge, K.G.: *Surgical Neuroangiography: Clinical Vascular Anatomy and Variations*, 2nd edn. Springer, Berlin (2001)
14. Martin, J.: *Neuroanatomy. Text and Atlas*. Appleton & Lange, Norwalk (1989)
15. Netter, F.H.: *The Ciba Collection of Medical Illustrations, Volume 1: Nervous System, Part 1: Anatomy and Physiology*. Ciba-Geigy, New Jersey (1991)
16. Nieuwennhuys, R., Voogd, J., van Huijzen, C.: *The Human Central Nervous System. A Synopsis and Atlas*, 4th edn. Springer, Berlin (2008)
17. Osborn, A.G., Ross, J., Crim, J., et al.: *Expert Differential Diagnoses: Brain and Spine*. Amirsry, Salt Lake City (2008)
18. Purves, D., Augustine, G.J., Fitzpatrick, D., et al.: *Neuroscience*, 4th edn. Sinauer Associates, Sunderland (2007)
19. Rhiton, A.L.: *Cranial Anatomy and Surgical Approaches. The Congress of Neurological Surgeons*, Schaumburg (2003)
20. Salamon, G., Huang, Y.P.: *Radiological Anatomy of the Brain*. Springer, Berlin (1976)
21. Stephens, R.B., Stilwell, D.L.: *Arteries and Veins of the Human Brain*. CC Thomas, Springfield (1969)
22. Yasargil, M.G.: *Microneurosurgery*, vol. 1. Thieme, Stuttgart (1984)

## **Print Brain Atlases**

23. Afshar, E., Watkins, E.S., Yap, J.C.: *Stereotactic Atlas of the Human Brainstem and Cerebellar Nuclei*. Raven, New York (1978)
24. Andrew, J., Watkins, E.S.: *A Stereotaxic Atlas of the Human Thalamus and Adjacent Structures. A Variability Study*. Williams and Wilkins, Baltimore (1969)
25. Cho, Z.H.: *7.0 Tesla MRI Brain Atlas: In Vivo Atlas with Cryomacrotome Correlation*. Springer, Heidelberg (2009)
26. DeArmond, S.J., Fusco, M.M., Dewey, M.M.: *Structure of the Human Brain. A Photographic Atlas*, 3rd edn. Oxford University Press, New York (1989)
27. Duvernoy, H.M.: *The Human Brain. Surface, Three-Dimensional Sectional Anatomy with MRI, and Blood Supply*. Springer, New York (1999)
28. Duvernoy, H.M.: *The Human Hippocampus: An Atlas of Applied Anatomy*. Bergman, Munch (1988)
29. England, M., Wakeley, J.: *Color Atlas of the Brain and Spinal Cord*, 2nd edn. Mosby, St Louis (2005)
30. Fix, J.D.: *Atlas of the Human Brain and Spinal Cord*. Aspen, Rockville (1987)

31. Haines, D.E.: Neuroanatomy: An Atlas of Structures, Sections, and Systems, 7th edn. Lippincott Williams & Wilkins, Baltimore (2008)
32. Kraus, G.E., Bailey, G.J.: Microsurgical Anatomy of the Brain. A Stereo Atlas. Wiliams & Wilkins, Baltimore (1994)
33. Mai, J.K., Assheur, J., Paxinos, G.: Atlas of the Human Brain, 2nd edn. Academic, San Diego (2003)
34. Mai, J.K., Paxinos, G., Voss, T.: Atlas of the Human Brain, 3rd edn. Academic, Oxford (2008)
35. McMinn, R.M.H., Hutchings, R.T., Pegington, J., et al.: Color Atlas of Human Anatomy, 3rd edn. Mosby Year Book, St. Louis (1993)
36. Morel, A., Magnin, M., Jeanmonod, D.: Multiarchitectonic and stereotactic atlas of the human thalamus. *J. Comp. Neurol.* **387**, 588–630 (1997)
37. Naidich, T.P., Duvernoy, H.M., Delman, B.N., et al.: Duvernoy's Atlas of the Human Brain Stem and Cerebellum: High-Field MRI, Surface Anatomy, Internal Structure, Vascularization and 3D Sectional Anatomy. Springer, New York (2009)
38. Ono, M., Kubik, S., Abernathey, C.D.: Atlas of the Cerebral Sulci. Thieme, Stuttgart (1990)
39. Orrison Jr., W.W.: Atlas of Brain Function, 2nd edn. Thieme, New-York (2008)
40. Putz, R.: Sobotta Atlas of Human Anatomy: Head, Neck, Upper Limb, Thorax, Abdomen, Pelvis, Lower Limb, 14th edn. Churchill Livingstone, Oxford (2008)
41. Schaltenbrand, G., Bailey, W.: Introduction to Stereotaxis with an Atlas of the Human Brain. Thieme, Stuttgart (1959)
42. Schaltenbrand, G., Wahren, W.: Atlas for Stereotaxy of the Human Brain. Thieme, Stuttgart (1977)
43. Schitzlein, H.N., Murtagh, F.R.: Imaging Anatomy of the Head and Spine. A Photographic Color Atlas of MRI, CT, Gross, and Microscopic Anatomy in Axial, Coronal, and Sagittal Planes, 2nd edn. Urban & Schwarzenberg, Baltimore (1990)
44. Schuenke, M., Schulte, E., Schumacher, U., et al.: Head and Neuroanatomy. Thieme Atlas of Anatomy. Thieme, New York (2007)
45. Speigel, E.A., Wycis, H.T.: Stereoecephalotomy: Part I. Methods and Stereotactic Atlas of the Human Brain. Grune and Stratton, New York (1952)
46. Szikla, G., Bouvier, G., Hori, T.: Angiography of the Human Brain Cortex: Atlas of Vascular Patterns and Stereotactic Localization. Springer, Berlin (1977)
47. Talairach, J., David, M., Tournoux, P.: Atlas d'Anatomie Stereotaxique des Noyaux Gris Centraux. Masson, Paris (1957)
48. Talairach, J., Tournoux, P.: Co-Planar Stereotactic Atlas of the Human Brain. Thieme, Stuttgart (1988)
49. Talairach, J., Tournoux, P.: Referentially Oriented Cerebral MRI Anatomy: Atlas of Stereotaxic Anatomical Correlations for Gray and White Matter. Thieme, Stuttgart (1993)
50. Van Buren, J.M., Borke, R.C.: Variations and Connections of the Human Thalamus. Springer, Berlin (1972)
51. Woolsey, T.A., Hanaway, J., Mokhtar, H.G.: The Brain Atlas: A Visual Guide to the Human Central Nervous System, 2nd edn. Wiley, New Jersey (2003)

## ***Electronic Brain Atlases***

52. A.D.A.M.: A.D.A.M Animated Dissection of Anatomy for Medicine. User's Guide, A.D.A.M. (1996)
53. Bayer: Microvascular Atlas of the Head and Neck. CD-ROM for Macintosh and Windows (1996)
54. Berkovitz, B., Kirsch, C., Moxham, B., et al.: Interactive Head & Neck. CD-ROM PC and Mac compatible. Primal, London (2003)
55. Bertrand, G., Olivier, A., Thompson, C.J.: Computer display of stereotaxic brain maps and probe tracts. *Acta. Neurochir. Suppl.* **21**, 235–243 (1974)

56. Dev, P., Coppa, G.P., Tancred, E.: BrainStorm: designing in interactive neuroanatomy atlas. *Radiology* **185**, 413 (1992)
57. Evans, A.C., Collins, L., Milner, B.: An MRI-based stereotactic atlas from 250 young normal subjects. *Soc. Neurosci. Abstr.* **18**, 408 (1992)
58. Ganser, K.A., Dickhaus, H., Metzner, R., et al.: A deformable digital brain atlas system according to Talairach and Tournoux. *Med. Image Anal.* **8**(1), 3–22 (2004)
59. Greitz, T., Bohm, C., Holte, S., et al.: A computerized brain atlas: construction, anatomical content, and some applications. *J. Comput. Assist. Tomogr.* **15**(1), 26–38 (1991)
60. Hoehne, K.H.: VOXEL-MAN, Part 1: Brain and Skull, Version 2.0. Springer, Heidelberg (2001)
61. Kazarnovskaya, M.I., Borodkin, S.M., Shabalov, V.A.: 3-D computer model of subcortical structures of human brain. *Comput. Biol. Med.* **21**, 451–457 (1991)
62. Netter's Anatomy. 2008. [http://evolve.elsevier.com/staticPages/s\\_nettter\\_iphone.html](http://evolve.elsevier.com/staticPages/s_nettter_iphone.html)
63. Nowinski, W.L., Bryan, R.N., Raghavan, R.: The Electronic Clinical Brain Atlas. Multiplanar Navigation of the Human Brain. Thieme, New York (1997)
64. Nowinski, W.L., Thirunavuukarasu, A., Kennedy, D.N.: Brain Atlas for Functional Imaging. Clinical and Research Applications. Thieme, New York (2000)
65. Nowinski, W.L., Thirunavuukarasu, A., Bryan, R.N.: The Cerefy Atlas of Brain Anatomy. An Introduction to Reading Radiological Scans for Students, Teachers, and Researchers. Thieme, New York (2002)
66. Nowinski, W.L., Thirunavuukarasu, A.: The Cerefy Clinical Brain Atlas on CD-ROM. Thieme, New York (2004)
67. Nowinski, W.L., Thirunavuukarasu, A., Benabid, A.L.: The Cerefy Clinical Brain Atlas: Enhanced Edition with Surgical Planning and Intraoperative Support. Thieme, New York (2005)
68. Nowinski, W.L., Thirunavuukarasu, A., Volkau, I., et al.: The Cerefy Atlas of Cerebral Vasculature. Thieme, New York (2009)
69. Nowinski, W.L., Chua, B.C., Qian, G.Y., et al.: The Human Brain in 1492 Pieces. Structure, Vasculature, and Tracts. Thieme, New York (2011)
70. Nowinski, W.L., Thirunavuukarasu, A., Volkau, I., et al.: A three-dimensional interactive atlas of cerebral arterial variants. *Neuroinformatics* **7**(4), 255–264 (2009)
71. Sramka, M., Ruzicky, E., Novotny, M.: Computerized brain atlas in functional neurosurgery. *Stereotact. Funct. Neurosurg.* **69**, 93–98 (1997)
72. Sundsten, J.W., Brinkley, J.F., Eno, K., et al.: The Digital Anatomist. Interactive Brain Atlas. CD ROM for the Macintosh. University of Washington, Seattle (1994)
73. Yelnik, J., Bardinet, E., Dormont, D., et al.: A three-dimensional, histological and deformable atlas of the human basal ganglia. I. Atlas construction based on immunohistochemical and MRI data. *Neuroimage* **34**(2), 618–638 (2007)
74. Yoshida, M.: Three-dimensional maps by interpolation from the Schaltenbrand and Bailey atlas. In: Kelly, P.J., Kall, B.A. (eds.) Computers in Stereotactic Neurosurgery, pp. 143–152. Blackwell, Boston (1992)

## Others

75. Federative Committee on Anatomical Terminology (FCAT): Terminologia Anatomica. Thieme, Stuttgart (1999)
76. Nowinski, W.L., Volkau, I., Marchenko, Y., et al.: A 3D model of the human cerebrovasculature derived from 3 tesla 3 dimensional time-of-flight magnetic resonance angiography. *Neuroinformatics* **7**(1), 23–36 (2009)
77. Nowinski, W.L., Thirunavuukarasu, A., Volkau, I., et al.: A new presentation and exploration of human cerebral vasculature correlated with surface and sectional neuroanatomy. *Anat. Sci. Educ.* **2**(1), 24–33 (2009)

78. Nowinski, W.L.: The cerefy brain atlases: continuous enhancement of the electronic Talairach-Tournoux brain atlas. *Neuroinformatics* **3**(4), 293–300 (2005)
79. Nowinski, W.L.: Electronic brain atlases: features and applications. In: Caramella, D., Bartolozzi, C. (eds.) *3D Image Processing: Techniques and Clinical Applications*. Medical Radiology series, pp. 79–93. Springer, Berlin (2002)
80. Nowinski, W.L., Fang, A., Nguyen, B.T., et al.: Multiple brain atlas database and atlas-based neuroimaging system. *Comput. Aided Surg.* **2**(1), 42–66 (1997)
81. Marchenko, Y., Volkau, I., Nowinski, W.L.: Vascular editor: from images to 3D vascular models. *J. Digit. Imaging* **23**(4), 386–398 (2010)
82. Gelas, A., Valette, S., Prost, R., et al.: Variational implicit surface meshing. *Comput. Graph.* **33**, 312–320 (2009)
83. Volkau, I., Zheng, W., Aziz, A., et al.: Geometric modeling of the human normal cerebral arterial system. *IEEE Trans. Med. Imaging* **24**, 529–539 (2005)
84. Nowinski, W.L.: Anatomical and probabilistic functional atlases in stereotactic and functional neurosurgery. In: Lozano, A., Gildenberg, P., Tasker, R. (eds.) *Textbook of Stereotactic and Functional Neurosurgery*, 2nd edn, pp. 395–441. Springer, Berlin (2009)
85. Nowinski, W.L., Qian, G., Bhanu Prakash, K.N., et al.: A CAD system for acute ischemic stroke image processing. *Int. J. Comput. Assisted Radiol. Surg.* **2**(suppl 1), 220–222 (2007)
86. Nowinski, W.L., Qian, G., Bhanu Prakash, K.N., et al.: Analysis of ischemic stroke MR images by means of brain atlases of anatomy and blood supply territories. *Acad Radiol.* **13**(8), 1025–1034 (2006)
87. Nowinski, W.L., Belov, D.: The cerefy neuroradiology atlas: a Talairach-Tournoux atlas-based tool for analysis of neuroimages available over the internet. *Neuroimage* **20**(1), 50–57 (2003)
88. Nowinski, W.L., Thirunavuukarasuu, A.: A locus-driven mechanism for rapid and automated atlas-assisted analysis of functional images by using the Brain Atlas for Functional Imaging. *Neurosurg Focus* **15**(1), Article 3 (2003)
89. Nowinski, W.L., Benabid, A.L.: New directions in atlas-assisted stereotactic functional neurosurgery. In: Germano, I.M. (ed.) *Advanced Techniques in Image-Guided Brain and Spine Surgery*, pp. 162–174. Thieme, New York (2002)
90. Nowinski, W.L.: Computerized brain atlases for surgery of movement disorders. *Semin. Neurosurg.* **12**(2), 183–194 (2001)
91. Nowinski, W.L., Yang, G.L., Yeo, T.T.: Computer-aided stereotactic functional neurosurgery enhanced by the use of the multiple brain atlas database. *IEEE Trans. Med. Imaging* **19**(1), 62–69 (2000)
92. Nowinski, W.L., Chua, B.C., Volkau, I., et al.: Simulation and assessment of cerebrovascular damage in deep brain stimulation using a stereotactic atlas of vasculature and structure derived from multiple 3T and 7T scans. *J. Neurosurg.* **113**, 1234–1241 (2010)

# Chapter 3

## Introduction to Brain Imaging

Einat Liebenthal

### 3.1 Structural and Functional Brain Imaging: A Comparative Overview of Techniques

Anatomical landmarks are useful in describing the location of different functional brain regions, for example, the primary sensorimotor cortex in the pre- and post-central sulci, the primary auditory cortex on Heschl's gyrus, and the primary visual cortex in the calcarine sulcus [1]. However, early studies examining the effects of different brain lesions on function, and the advent of neuroimaging, have shown that there is tremendous intraindividual variability in both the structure and functional organization of the human brain. Like fingerprints, each brain has a unique configuration of gyri and sulci (crests and troughs, respectively, in the surface of the brain) [2, 3]. In addition, brain function may not be specifically localized with respect to sulcal neuroanatomy, prompting the conclusion that sulci are not generally valid landmarks of the microstructural organization of the cortex [4]. In patients with brain pathology, the use of anatomical landmarks can further be jeopardized due to edema or mass effects that obliterate the structure of gyri and sulci and can induce plasticity in functional organization. These findings highlight the important role of personalized structural and functional neuroimaging, especially for clinical applications such as presurgical brain mapping. In this chapter, the chief neuroimaging methods relevant to the diagnosis and management of patients with brain tumor or epilepsy are reviewed.

---

E. Liebenthal (✉)

Neuroscience, University of Manitoba, Winnipeg,  
Canada & Neurology, Medical College of Wisconsin, Milwaukee, USA  
e-mail: liebenth@cc.umanitoba.ca; einatl@mcw.edu

### ***3.1.1 Magnetic Resonance Imaging-Based Brain Imaging Techniques***

#### **3.1.1.1 Magnetic Resonance Imaging**

Magnetic resonance imaging (MRI) is an imaging technique that provides good contrast resolution between different soft tissues, making it particularly useful in the brain. The discoveries that led to the development of modern MRI were first reported in the 1970s [5, 6], and eventually won the inventors the Nobel prize in Physics or Medicine in 2003. Since its introduction as a diagnostic tool in the 1980s, MRI has become the main neuroimaging modality. The advent of higher field magnets has resulted in standard imaging at an exquisite spatial resolution around  $1 \text{ mm}^3$ , permitting visualization of fine anatomic details at clinically acceptable short acquisition times. MRI is vastly superior to other structural imaging methods such as X-ray, computer tomography (CT), and ultrasound, in terms of spatial resolution and the delineation of tumors [7]. In addition, contrary to X-ray and CT which involve ionizing radiation, MRI is based on noninvasive radio frequency excitation of biological molecules with magnetic properties.

#### **3.1.1.2 Functional Magnetic Resonance Imaging (fMRI)**

fMRI can map function in the entire living brain. fMRI is an indirect measure of neural activity that is based on the premise of a relationship between local changes in neural activity and cerebral blood dynamics. fMRI using the blood-oxygenation level-dependent (BOLD) contrast is a method to measure local changes in the concentration of paramagnetic deoxyhemoglobin that are associated with an increase in blood flow to active regions in the brain [8, 9]. First reports of fMRI in humans demonstrated that visual stimulation produces a detectable transient increase in the intensity of water proton magnetic resonance signal in primary visual cortex [10, 11]. Similar increases in fMRI signal were found in the motor cortex during finger movement [12]. The spatial resolution of fMRI is high, typically ranging 3–5 mm for most common applications. But the temporal resolution is low, with a mean rise time for signal change around 4 s, approximately two orders of magnitude slower than the underlying neural activity. fMRI has come to dominate the field of functional neuroimaging thanks to its low invasiveness, lack of radiation exposure, exquisite spatial resolution, and relatively wide availability.

fMRI has revolutionized the field of cognitive neuroscience. One of the unique strengths of this technique is its capability to image function in the entire brain non-invasively. Two decades of fMRI research in cognitive neuroscience have highlighted the distributed and dynamic nature of brain function, largely contradicting the classic view emerging from earlier lesions studies of a fixed and focal relationship between anatomy and brain function. Cognitive functions are represented in large-scale networks, with wide interindividual variability in the representation of

function across the different nodes of each network, and tremendous plasticity related to learning and memory or caused by pathological changes [13]. This modern understanding of the organization of cognitive brain functions emphasizes the value of fMRI mapping for identifying neural network systems in individual patients and also the limitation of this technique for predicting the necessity of any brain region for carrying out certain functions.

Factors related to the choice of fMRI activation paradigm (active or passive task, level of task performance, baseline condition, and the number of trials per task condition) can have a strong impact on the resulting functional maps and their interpretation, particularly for mapping cognitive functions such as language [14, 15]. As detailed further in the sections below, various procedures can be undertaken to optimize the design of fMRI activation paradigms for different clinical applications.

Many fMRI paradigms use a block design, in which a time series of images is acquired during periods of an experimental (ON) and a control (OFF) condition, in order to identify brain regions associated with processes engaged during the ON but not (or less) during the OFF period. fMRI paradigms using a block design tend to be simple to implement and provide high statistical power (with adequate sample sizes) and are therefore often preferred for clinical applications [16]. However, other more complicated designs using parametric, event-related, or conjunction approaches have been developed to improve the sensitivity of the method to subtle, individual or trial-wise changes, or to overcome problems related to the selection of an adequate baseline control condition [17, 18].

Another layer of difficulty inherent to fMRI is that the precise location and extent of observed brain activity depend on the statistical significance threshold used to create functional maps. Adaptive thresholding schemes, for example consisting of mapping the activation as a percentage of local excitation, have been suggested as a means to reduce the variability in the extent of activation between subjects [19]. This method was shown to yield highly reproducible and specific motor activation in a large cohort of subjects when the threshold was set at 40% of the most active voxels [20].

Given the significant variability in fMRI mapping associated with different activation paradigms and different procedures for data analysis, large scale and carefully designed studies are essential to systematically evaluate the reliability of each mapping paradigm and its predictive value for selected clinical applications.

### 3.1.1.3 Diffusion Tensor Imaging

Diffusion tensor imaging (DTI) is a newer method that can demonstrate the orientation and integrity of white matter fibers in vivo [21, 22]. The technique has generated much interest because it currently is the only approach available to noninvasively study the three-dimensional architecture of white matter tracts [23]. DTI is sensitive to the diffusion of water molecules in the direction of the field gradient. Diffusion is anisotropic in white matter tracts because the axonal membranes and myelin sheaths limit the motion of water molecules to the orientation parallel to the fiber. Thus, the

direction of maximum diffusivity has been shown to coincide with the white matter fiber tract orientation [24]. A minimum of six diffusion encoded measurements are required to accurately describe the diffusion tensor (mathematical 3D model of diffusion), but using more directions will improve the accuracy of the tensor measurement [25]. The direction of maximum diffusivity is often mapped by using red, green, and blue color to indicate diffusion in the left-right, anterior-posterior, and superior-inferior axes, respectively, with color brightness modulated by fractional anisotropy (indicating the degree of anisotropy) [26]. Fiber tractography is a post-processing derivation of the diffusion data whereby three-dimensional trajectories of white matter tracts are reconstructed based on the estimates of fiber orientation in each voxel. The visualization in three dimensions can assist in identifying specific fiber tracts. Various fiber tracking methods have been implemented, which compare local tensor field orientations measured by DTI from voxel to voxel, allowing non-invasive tracing of large fiber tracts in the human brain [23, 27, 28]. The tracking algorithm is initiated from seed regions that can be defined by the user, based on anatomical landmarks or functional maps.

### ***3.1.2 Electrophysiological Brain Imaging Techniques***

#### **3.1.2.1 Electroencephalography and Magnetoencephalography**

Electrophysiological techniques that can be used to probe electrical neural activity directly and noninvasively have been around for the better part of the last century. The discovery that small fluctuations in electrical potentials can be measured from the human scalp, a method termed scalp electroencephalography (EEG), was first reported by the German psychiatrist Berger in 1929. Magnetoencephalography (MEG), or the recording of magnetic fields produced by the electrical currents in the brain, was first achieved in the late 1960s [29, 30]. Both EEG and MEG have since evolved to include larger numbers of recording channels and improved amplification technology. From a practical standpoint, EEG devices are widely available, relatively low cost, and can also be portable and used for long-term recordings. On the other hand, multichannel MEG recording is more practical than multi channel EEG recording because EEG (but not MEG) requires establishing contact between each channel sensor and the scalp. Nevertheless, MEG scanners are still scant, generally limiting the use of this technology.

EEG and MEG both measure currents arising primarily from excitatory and inhibitory postsynaptic potentials along the dendritic tree of pyramidal neurons in the cerebral cortex [31]. Neurons in large areas of cortex, on the order of a few square centimeters, have to be synchronously active in order to generate a detectable electrical or magnetic field on the scalp. Both EEG and MEG have exquisite temporal resolution on the order of 1 ms, highly superior to the temporal resolution of fMRI. Despite the correspondence in the neural origin of the EEG and MEG signals, there are important differences between the techniques that result in different

sensitivity in certain brain areas. Electrical and magnetic fields have orientations perpendicular to one another, such that scalp EEG is sensitive to neural sources both tangential and radial to the scalp, whereas MEG is sensitive primarily to tangential sources. As a result, MEG selectively measures activity in the sulci of the brain, whereas scalp EEG measures activity both in the sulci and gyri. Magnetic fields are also less distorted by the resistive properties of the skull and scalp, and they decay faster as a function of distance from the source, than electrical fields. As a result, MEG has increased sensitivity and superior spatial resolution for superficial cortical activity, compared to EEG [32].

Modeling of EEG and MEG scalp activity to localize the neural source/s is fundamentally ill-posed because no unique solution exists to this inverse problem [33]. However, modeling of MEG activity is somewhat simplified by the fact that fewer sources are identified with this technique, and at higher spatial resolution. Generally, good agreement has been reported between EEG and MEG source localizations, although differences exist and can be attributed to the differences in orientation discussed above. Thus, the techniques are best considered complementary [34].

EEG and MEG responses associated with specific external or internal events, termed event-related potentials (ERPs), can be obtained by simple averaging of many epochs aligned according to the time of occurrence of the event of interest [35, 36]. ERP waveforms consist of a sequence of peaks which are characterized by their polarity, absolute and inter-peak latency, the type of stimuli and experimental conditions that elicit them, and their scalp topography. Latency measures are by far the most useful aspect of ERPs for clinical applications. Deviations in peak latency measures can indicate abnormal neural conduction, for example as a result of demyelination in a neurodegenerative disease such as multiple sclerosis [37]. ERPs are particularly useful in cases when MRI indices of multiple sclerosis are inconclusive [38]. Routine clinical evaluations can include the measurement of short- and middle-latency visual, somatosensory and auditory-evoked potentials for the differential diagnosis of sensory (peripheral) and central nervous system disorders. The measurement of ERPs is objective in that most clinically useful responses are obligatory and independent of the patient's compliance. ERPs can therefore be used to assess the neurological status in patients who are anesthetized or comatose.

### ***3.1.3 Multimodal Imaging***

#### **3.1.3.1 Simultaneous fMRI and EEG**

Simultaneous recording of brain activity with two neuroimaging modalities can provide information beyond that attainable with each technique alone. The development of simultaneous MRI/EEG was motivated by clinical interest in mapping sources of epileptic discharges onto MR images [39]. Simultaneous fMRI and EEG recording is particularly attractive because it holds the promise of maximizing

the fine spatial resolution of fMRI with the fine temporal resolution of EEG. The combination of these techniques may allow improved localization of neural generators identified with EEG, as well as enhanced temporal resolution of BOLD activation foci [40–43]. Simultaneous recordings are preferable to sequential recordings in that they allow perfect correspondence of experimental conditions (acoustic and visual environment) and cognitive factors (task performance, attention) between the recordings. This is critical for the study of cognitive functions relying on learning, memory, or attention. Simultaneous recordings can be technically challenging as they essentially involve running two experiments at the same time. Simultaneous fMRI/EEG involves extracting a small EEG signal from the increased background noise caused by the magnetic field [44–47]. The primary clinical application of simultaneous fMRI/EEG is for the localization of epileptic zones [48, 49].

### 3.2 Clinical Applications of Brain Imaging for Image-Guided Neurosurgery in Epilepsy and Brain Tumor Patients

The major objective of presurgical and intrasurgical brain mapping is to provide patient-specific structural and functional information that can facilitate maximal tumor or epileptic tissue surgical resection, while minimizing damage to surrounding gray and white matter structures supporting vital sensory and cognitive functions. Presurgical mapping of functional brain regions and their spatial relationship to a brain lesion can help predict possible deficits in sensory, motor, or cognitive functions due to surgery or due to continued lesion growth. Presurgical mapping can help guide the decision for course of intervention (extent of resection, alternative treatment) and the decision to conduct additional intrasurgical functional mapping. Presurgical mapping is also valuable for planning the surgical approach.

Mapping of functional areas is traditionally achieved by invasive methods such as presurgical intraarterial amobarbital (Wada) testing for the assessment of hemispheric language and memory dominance, presurgical or intrasurgical cortical stimulation mapping, and intrasurgical monitoring of sensory-evoked responses. These techniques require a separate surgical procedure or are performed intrasurgically, and therefore, tend to place additional stress on the patient and the clinical team. If presurgical functional mapping is not acquired, this may also result in less optimal surgical planning.

In contrast, MRI-based neuroimaging is always performed presurgically (and sometimes also intrasurgically) and the technique is completely noninvasive. Further contributing to the increasingly popular use of MRI for presurgical mapping are: the high sensitivity of MRI for visualization of brain lesions, the high spatial resolution afforded by fMRI and DTI for mapping of functional neuronal networks and white matter fibers, the relative safety of MRI, and the good access to MRI scanners in most medical centers. Compared to the alternative invasive functional mapping techniques for functional mapping, fMRI is more pleasant to the patient and less expensive. An example of MRI, fMRI, and DTI presurgical mapping in a patient with a left frontotemporal tumor is shown in Fig. 3.1.

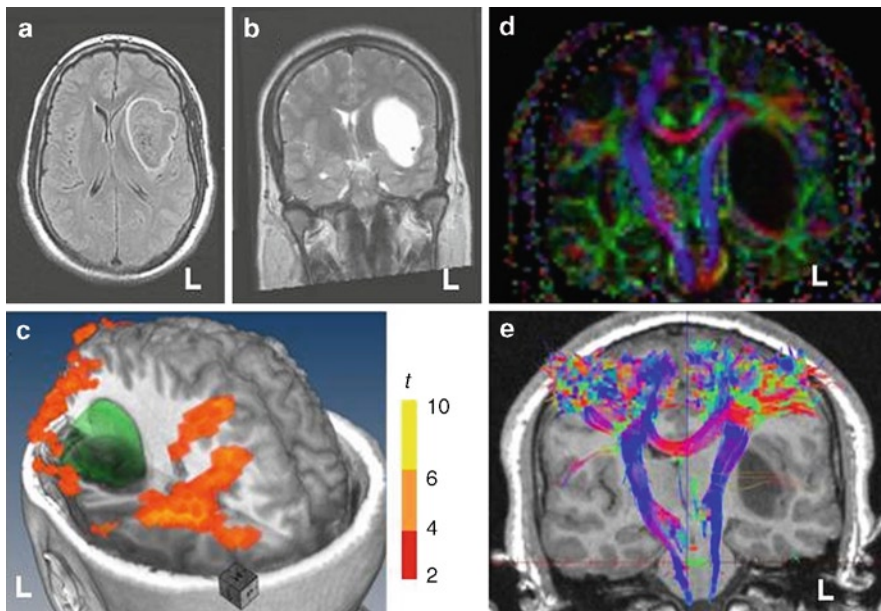


**Fig. 3.1** Presurgical fMRI and DTI in 29-year-old male with left frontotemporal low-grade glioma showing symptoms of seizures, mild word finding difficulty, and right arm and leg weakness. (a) FLAIR, and (b) T2-weighted structural MRI showing tumor outline. (c) Language map during semantic processing overlaid on 3D head model with segmented tumor (in green). (d) Fractional anisotropy, and (e) DTI tractography of corticospinal tracts. FMRI suggests anterior displacement of language areas in left frontal cortex. DTI shows inward displacement of the left corticospinal tract. FMRI and DTI data assisted in planning the surgical approach. L left

### 3.2.1 Structural MRI

MRI has revolutionized neurosurgery. The principal role of MRI for the diagnosis and management of brain tumor or epilepsy patients is to reveal the location and extent of cerebral tumors or lesions that might cause epilepsy. MRI has high sensitivity for the visualization of brain structural abnormalities. In brain tumor patients, resection of primary tumors can improve survival, functional capability, and the effect of adjuvant therapies, provided that postsurgical neurological deficits can be avoided [7, 50, 51].

In epilepsy patients, resection of an MR-visible lesion near the site of seizure onset, such as mesial temporal sclerosis (scarring of the hippocampus) or cortical dysplasia (cellular maturation abnormality), dramatically increases the chances of freedom from seizures [52]. The use of higher field MR scanners (3T), thinner image slices, and the implementation of advanced sequences such as fluid-attenuated inversion recovery (FLAIR) can improve the odds of detecting subtle focal cortical dysplasia [53]. MRI can also help visualize the location of intracranial electrodes (implanted for electrical source localization of seizure foci) with respect to

anatomical landmarks and lesions, provided that adequate safety measures are observed [54]. Alternatively, the location of the intracranial electrodes can be visualized on high-resolution CT, and those images can then be registered to MR images obtained prior to electrodes implantation.

However, in approximately 25% of epilepsy surgery candidates, structural MRI produces inconclusive evidence of brain lesions or evidence that is inconsistent with scalp EEG results. In some of those cases, positron emission tomography (PET) can be used to characterize cerebral metabolism and indicate the location of subtle abnormalities that can cause seizures. This information can further be used to guide the positioning of intracranial electrodes in order to identify the seizure foci [55, 56].

A relatively newer application of MRI is for intrasurgical imaging. The primary objective of intrasurgical imaging is for the detection *during* surgery of residual tumor or lesion tissue, thereby optimizing the resection and minimizing the need for corrective surgery [57]. Intrasurgical MRI can be implemented through use of a dedicated intrasurgical MR scanner or through adaptation of existing MRI scanner technology to the operating theater [58, 59]. Structural MR images are obtained in the operating room, usually after the planned resection is thought to be achieved, and sometimes also immediately after craniotomy to account for significant brain shifts. Intrasurgical MR imaging was shown to dramatically improve the estimate of residual tumor burden compared to a subjective evaluation of the operating neurosurgeon [60–62]. In a series of patients undergoing surgical resection to remove glial tumors or pituitary adenomas, intrasurgical MRI was found to significantly increase the rate of success in achieving the planned tumor removal, as confirmed by postsurgical imaging [63]. In addition, presurgical structural and functional images such as contrast-enhanced MRI, fMRI and DTI maps can be registered to the intrasurgical images, thereby making this information more readily available during the surgery [63].

However, a serious caveat of intrasurgical neuronavigation is that significant and difficult to predict brain shifts, up to 20 mm, can occur during the surgery, primarily in relation to craniotomy and tumor removal [64]. A variety of factors affect the brain shift, including the tissue characteristics, intrasurgical patient positioning, the size of the craniotomy, and the resected volume [65]. Presurgical information must therefore be compensated for such brain shift throughout the surgery for accurate registration to the intrasurgical space [66]. Estimation of intrasurgical brain shifts can be achieved with intrasurgical ultrasound [67] or MRI [65, 68]. However, accurate nonrigid registration of presurgical images to the intrasurgical space is computationally expensive and time-consuming, and therefore, challenging for real-time implementation [69, 70]. Recent advances achieved in this field [71] are discussed in detail in other chapters of this book.

### 3.2.2 *Presurgical fMRI Mapping*

fMRI using the endogenous BOLD contrast is increasingly used for presurgical mapping in epilepsy and brain tumor patients at many clinical centers. The fast

T2\*-weighted imaging capabilities necessary for fMRI are a standard feature on MRI clinical systems, and the implementation of audiovisual stimulation and response equipment needed for most fMRI activation paradigms is relatively low cost. Recent reports suggest that presurgical planning using fMRI can reduce surgical time, affect decisions regarding the targeted extent of resection [72, 73], and improve surgery outcome [74]. Compared to the gold standard cortical stimulation mapping [75, 76], fMRI is noninvasive and performed presurgically, without the time constraints and possible side effects on cognitive function associated with the surgical environment.

Nevertheless, clinical acceptance of fMRI for presurgical mapping is still impeded by several factors. Major obstacles include: (1) A lack of standardized acquisition paradigms and user-friendly analysis procedures for robust and reliable functional mapping in individual patients [77, 78]. (2) Spatial imprecision in presurgical maps due to surgically induced nonlinear brain shifts [79]. (3) A reduction of the fMRI response near tumors (particularly malignant glial tumors) despite presence of viable neuronal tissue (neurovascular uncoupling) [80, 81]. (4) A need for systematic evaluation in large multicenter studies specifically designed to establish the accuracy and predictive value of fMRI mapping for patient outcome [77].

The problem of lack of standardized acquisition paradigms and analysis procedures is that different paradigms and procedures can produce different brain activity patterns, and an area that is active in one scheme may not be active in another. In addition, whole-brain fMRI has the potential to reveal entire networks associated with different functions including those regions that are “merely” involved in a function but perhaps expendable [82]. Due to these characteristics, fMRI presurgical mapping carries two types of risks: (1) Surgically sparing fMRI active regions that are not essential for function, leading to suboptimal surgical resection. (2) Resecting critical functional areas that were not active in the selected scheme, resulting in postsurgical neurological deficit [83]. Given the serious implications of presurgical mapping, it is of utmost importance to identify paradigms and analysis procedures that reliably and robustly activate clinically relevant brain regions. A good starting point for selecting presurgical paradigms is from large-scale imaging studies conducted in healthy individuals and documented to produce replicable activation in target brain regions on an individual scale.

Perhaps even more problematic is the sparse experience and documentation of the predictive value of various fMRI paradigms and analysis procedures for patient postsurgical outcome. Given the complex representation of function in the brain, the large intraindividual variability in brain anatomy and function, and the potential for functional reorganization and plasticity in healthy brains and particularly as a result of disease, there is not a simple relationship between focal brain lesions and functional deficits. Therefore, the predictive value of fMRI presurgical mapping for patient outcome must be estimated based on experimental data and in the context of specific activation paradigms and analysis procedures. To date, however, systematic large-scale studies to determine the value of fMRI presurgical mapping of different activation paradigms in various patient populations are still rare.

Nevertheless, it is important to note that alternative mapping methods such as the gold standard cortical stimulation method suffer from similar ailments. Cortical stimulation is considered to identify regions that are functionally essential and their damage during surgery would therefore result in neurological deficit. However, this technique cannot account for possible postsurgical functional reorganization that could prevent permanent loss of function [78, 84]. Cortical stimulation can also in some cases indirectly interfere with brain areas connected with but removed from the stimulated site. Thus, there is a risk of false positive results with cortical stimulation, and similar to fMRI, the predictive power for patient outcome needs to be estimated based on systematic analysis of experimental data.

The main application of fMRI for neurosurgical planning is for the mapping of language and sensorimotor functions, because these functions are considered to be most vulnerable to neurosurgical procedures and most important for postsurgical quality of life. The specific challenges and advantages of fMRI presurgical mapping of language and sensorimotor systems relative to other clinical mapping techniques, in patients with brain tumors or epilepsy, are discussed in further detail in the next sections.

### 3.2.2.1 Functional Mapping of Sensory and Motor Systems

fMRI can provide detailed functional maps that are useful in guiding a surgical resection. fMRI has been used to localize the motor cortex presurgically and to guide subsequent intrasurgical stimulation studies, particularly in brain tumor patients in whom the anatomy has been distorted by developmental abnormality or mass lesions [85–90].

Concordance between cortical stimulation and fMRI mapping of somatosensory and motor functions has generally been reported to be very high, between 85 and 100% (with activations considered to match if they were found to be within 1 cm distance or less) [80, 90–96].

However, even in the case of motor cortex mapping, where robust activation of the primary motor cortex can be obtained with a simple hand motion task relative to rest, isolation of the primary hand motor cortex is complicated by the fact that additional nearby secondary motor and somatosensory areas are engaged. Identification of the primary hand motor area can be aided by anatomical landmarks, and in particular “the handknob” in the central sulcus [97], with the caveat that the mapping between function and anatomical landmarks is known to vary between individuals, and certainly in pathological conditions.

The mapping of focal primary sensory and motor regions is generally simpler than the mapping of cognitive functions that involve distributed networks identifiable through use of elaborate activation paradigms. The value of fMRI mapping of sensory and motor functions is also more evident than the value of mapping cognitive functions because there is a well-established relationship between focal lesions to sensorimotor regions and the pattern of deficits that can arise. In support of the relevance of fMRI motor mapping, several studies have

shown that the greater the distance between fMRI activation in motor cortex and the surgical resection margin, the lower the instance of postsurgical motor deficits [87, 94]. A distance of 1–2 cm from the fMRI activation margin has generally been proposed in these studies as “safe” for resection. As will be reiterated in the section about DTI, it is important to remember that distance of the resection margin from the corticospinal tracts is also bound to be an important determinant of the risk for postsurgical motor deficit [98].

fMRI can similarly be used to map primary auditory, somatosensory, and visual cortex. More precise mapping of cortical organization within each cortical region can be obtained. For example, in visual cortex, retinotopic maps of the visual field cortical representation can be used to predict the pattern of visual field loss from resection of particular cortical areas [99, 100].

### 3.2.2.2 Functional Mapping of Cognitive Systems

The mapping of cognitive functions, and in particular language, is more challenging than the mapping of sensory and motor functions. One of the main reasons is that cognitive functions involve widely distributed brain networks in which some regions may be essential to carry out a specific task or subtask, and other regions may play a redundant role or provide support for general cognitive processes. As a result, the relationship between the location of focal lesions and the occurrence of cognitive deficits is complex and not well understood. For example, in language, both speech production and language comprehension involve widely distributed brain networks that extend well beyond the regions of Broca and Wernicke that have traditionally been associated with these functions, respectively [101–105]. Accordingly, lesions to different left temporal and frontal brain areas can lead to deficits in seemingly similar language functions, and the prognosis for recovery from aphasia after seemingly similar focal lesions is difficult to predict [106, 107].

In light of the intricacies involved in fMRI language mapping, the choice of fMRI language paradigms is particularly decisive in determining the results of this procedure. fMRI paradigms with active tasks and careful monitoring of the patient’s task performance are generally preferable because inability or unwillingness of the patient to comply with task demands can result in uninterpretable mapping results. For mapping of cognitive functions, active control tasks rather than passive rest are recommended, because activation in the control condition can account for general executive, attentional, and motor processes that are unspecific to the tested cognitive function [15, 108]. This is critical for assessing language lateralization, because the activation pattern for language can appear to be bilateral in the absence of proper control for general sensory, executive, and attentional processes that are not left hemisphere dominant. In addition, activation during rest can be dominated by continuous processing of linguistically mediated thoughts, thereby effectively reducing the differential activation of language networks between the active and control conditions [109, 110].

Accordingly, it is not surprising that reported levels of fMRI language task sensitivity and specificity with regard to cortical stimulation mapping have been variable and strongly dependent on the particular task that is used for both cortical stimulation and fMRI [14]. High sensitivity (i.e., fMRI activates all or most sites identified by cortical stimulation) but low specificity (fMRI activates additional sites not identified by cortical stimulation) was reported for auditory language tasks and in particular word generation to auditory cue [111]. Importantly, higher sensitivity can generally be achieved with the conjunction of several fMRI language tasks, but specificity remains low [112–114]. Thus, combining several language tasks is a recommended strategy for improving the reliability of fMRI language mapping.

### 3.2.2.3 Measuring Language and Memory Hemispheric Lateralization

Perhaps the most reliable application of language fMRI mapping is for the assessment of language lateralization. The primary rationale for testing language lateralization is the basic assumption that carrying an operation on the language-dominant hemisphere increases the risk of postsurgical language decline. The current clinical gold standard for language lateralization is the Wada test that was developed 50 years ago to assess the hemispheric dominance of language, and thus the risk of language decline in patients undergoing brain surgery [115]. The Wada test is invasive, carries some risk, and is highly uncomfortable for the patient, involving intracarotid injection of a barbiturate to one hemisphere at a time. In this procedure, large parts of the anesthetized hemisphere are disabled for approximately 5 min, during which the other hemisphere is examined for language and other functional capacities. Several factors may confound the interpretation of the Wada test, including agitation or somnolence of the patient related to the anesthetization procedure, inadequate disabling of certain language brain regions (in particular in the temporoparietal cortex) in the anesthetized hemisphere, or uncontrolled crossover of the anesthetic to the examined hemisphere [116]. In comparison, fMRI is noninvasive, performed under conditions that facilitate closer-to-normal language processing, and can provide information at a subhemispheric spatial resolution. For these reasons, language fMRI has the potential of being more sensitive and more accurate than the Wada test. Concordance between fMRI and Wada language lateralization has generally been reported to be very high, in the range of 80–90% [117–119], although this evaluation depends on an assignment to dominance categories (left, right, bilateral) with arbitrarily defined boundaries [120]. An example of hemispheric lateralization in the language cortex, as assessed with fMRI in a patient with a right temporal tumor, is shown in Fig. 3.2.

Indeed, fMRI of language was demonstrated to predict language decline after left anterior temporal lobe resection to treat intractable epilepsy, as measured by postsurgical change in confrontation naming in the Boston Naming Test [121]. In that study, the lateralization of activation during semantic processing in a temporal lobe region of interest was the strongest predictor of outcome (stronger left lateralization in the

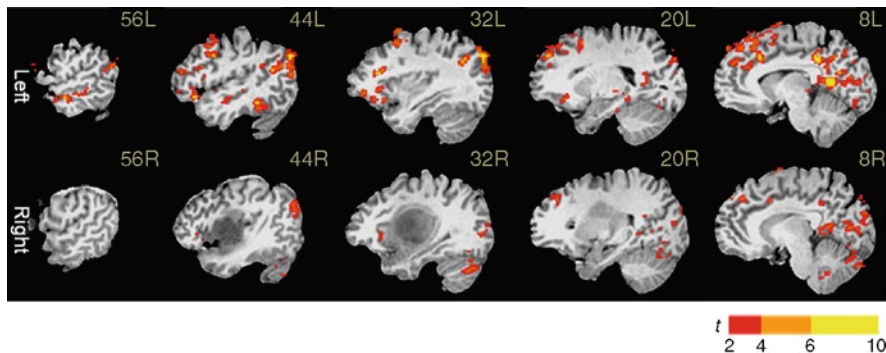


**Fig. 3.2** Presurgical language fMRI in 35-year-old male with high-grade glioma in the right medial temporal lobe. The patient is left handed and therefore at higher chance of atypical (right or bilateral) language dominance. The fMRI language map during semantic processing, overlaid on a series of sagittal slices in the left (*top*) and right (*bottom*) hemispheres, shows typical left hemispheric dominance in the middle temporal, inferior and middle frontal, angular, and fusiform gyri. Independent Wada testing results in this patient were also consistent with left hemisphere dominance for language. The fMRI and Wada presurgical information facilitated a more radical resection of the right temporal tumor

temporal lobe predicted poorer naming outcome). The temporal lateralization index showed sensitivity, specificity, and predictive values that were high and higher than those for the Wada test. It is important to bear in mind, however, that these results are limited to the specific language activation paradigm used in this study.

The Wada procedure can similarly be used to assess the hemispheric lateralization of memory functions and estimate the risk of postsurgical amnesia, and in particular, verbal memory decline in patients undergoing anterior temporal lobe resection. However, the validity and reliability of the Wada memory test have been questioned [122, 123], prompting much interest in developing fMRI indices in the medial temporal cortex to assess verbal memory lateralization. Findings regarding the predictive value of fMRI activation in the medial temporal lobe for verbal memory outcome after anterior temporal lobe surgery have been mixed [124–127]. A combination of factors may contribute to the ambiguity in these results. FMRI of the medial temporal cortex during memory encoding and retrieval is particularly challenging because of the small size of the hippocampal formation (relative to the typical voxel size used in fMRI) and the location of the hippocampal formation at the base of the brain, in an area near large air cavities prone to susceptibility artifacts and causing image distortions and MR signal loss [128, 129]. Another difficulty is that the hippocampus appears to be relatively active during rest, effectively reducing the differential signal observed in this region during active memory encoding tasks [110]. Recently, it has also been shown that verbal memory outcome can better be predicted by assessing the hemispheric dominance for language rather than for episodic memory [130], thereby further substantiating the value of language over memory paradigms for fMRI estimation of surgical risks.

These recent results in anterior temporal lobe epilepsy patients suggesting that using language fMRI lateralization indices (combined with other noninvasive measures such as handedness and age of epilepsy onset) can improve the predictive accuracy of postsurgical language and memory decline, and suggesting that Wada testing does not provide significant additional predictive power [121, 124], provide strong support for the value of noninvasive language fMRI as a valid alternative to the invasive Wada test [83].

### 3.2.2.4 Resting State fMRI

An interesting recent development in fMRI mapping is the study of functional connectivity during resting state [131, 132]. During resting state, the brain remains functionally and metabolically active and displays slow spontaneous fluctuations in the BOLD signal. These fluctuations of the BOLD signal show phase correlations, termed functional connectivity, in widely distributed functional networks including primary visual, auditory, somatomotor, attentional, and executive regions [133–135]. So far, the primary clinical application of this method has been to compare resting state functional connectivity in neurologically healthy volunteers and patients with various neurological and psychiatric diseases [131, 136]. However, functional connectivity is attractive for presurgical mapping because it does not require patient participation, and multiple functional networks can be identified from data acquired within approximately 10 min. Recent studies suggest that mapping of the motor cortex in brain tumor patients using resting state functional connectivity is a valid alternative to motor mapping using an active paradigm [137, 138]. In addition, at least some functional networks appear to be resilient to sleep [139] and perhaps anesthesia [140]. Functional connectivity could represent an alternative method for functional mapping in children and in patients who cannot comply with the demands of an active task, and in cases when mapping of certain regions not typically targeted by functional mapping paradigms is desired (for example the attention network). This method could also be eventually amenable to intrasurgical fMRI.

### 3.2.2.5 Functional Mapping in Patients with Malignant Brain Tumors

In patients with glial tumors, a significant difficulty with fMRI mapping is that the BOLD response can be reduced in the area surrounding the tumor despite presence of viable neuronal tissue, a phenomenon known as neurovascular uncoupling [141, 142]. Loss or reduction in cerebrovascular reactivity and tumor-induced changes in microvasculature have been suggested to contribute to the reduced BOLD response in the area adjacent to malignant tumors [80, 143]. Reduction in signal intensity in the tumor hemisphere relative to the healthy hemisphere was found to be significantly more pronounced in high-grade (IV) relative to lower-grade (II–III) gliomas, consistent with the notion that neurovascular uncoupling disproportionately affects

malignant tumors [144]. Neurovascular uncoupling is an inherent limitation of fMRI for presurgical mapping in tumor patients, because it can lead to erroneous interpretation of fMRI activation maps and lateralization patterns [74, 81]. In tumor patients (and particularly high-grade gliomas), it is therefore imperative to couple fMRI mapping with an assessment of cerebrovascular reactivity. Furthermore, maps of cerebrovascular reactivity can potentially provide useful information regarding the nature of the tumor and its boundaries [145].

Cerebrovascular reactivity can be studied with BOLD fMRI, by examining changes induced by a hypercapnia challenge such as CO<sub>2</sub> inhalation or breath-hold [146, 147]. Hypercapnia induces vasodilation and causes an increase in cerebral blood flow and oxygen concentration in normal blood vessels, resulting in an increase in the BOLD signal [148]. In tumors, increased cellularity or necrosis and low vascular density may cause reduced perfusion and hypoxia [149]. In tumors with neovasculature, in which there is abnormal microanatomy and cerebrovascular regulation, blood from a region of the tumor in which the vessels do not dilate can be redistributed to a responsive tumor region or to surrounding normal tissue, causing a focal worsening of tumor perfusion. Thus, in tumors with abnormal cerebrovascular microstructure or abnormal cerebrovascular regulation, low BOLD reactivity during hypercapnia is expected. Hypercapnia can be induced with a simple breath-hold challenge in human adults [147, 148, 150] and this paradigm is more practical and safer for brain tumor patients, compared to carbogen inhalation which can induce respiratory distress and elevated intracranial pressure [151, 152]. In neurologically healthy adults, BOLD signal increases of 1–5% largely confined to the gray matter were observed during breath-hold periods of 10–40 s, with larger increases observed during longer breath-hold periods [146, 150, 153].

In a small study of 6 patients with low-grade gliomas, BOLD increases comparable to those in healthy subjects were obtained in normal gray matter during 20 s breath-hold periods, while in the region of the tumor there was no change in the BOLD signal [154]. In one patient with high-grade glioma from the same study, breath-hold regulated decreases in BOLD signal were observed in the tumor and explained as steal effect or redistribution of blood flow to surrounding normal tissue [154]. Signal decreases in peritumoral areas were also observed in 4 patients with glioblastomas and one with astrocytoma, using high-resolution BOLD susceptibility-weighted imaging and carbogen breathing [145]. These results indicate that breath-hold fMRI is a promising method for studying neurovascular reactivity in patients with high-grade brain tumors. Combined with fMRI mapping, it could help differentiate between “true” absence of neural function in proximity of a tumor and neurovascular uncoupling.

### 3.2.3 Presurgical DTI Mapping

DTI is increasingly used for presurgical mapping in epilepsy and brain tumor patients because of its unique capability to describe noninvasively the spatial relationship

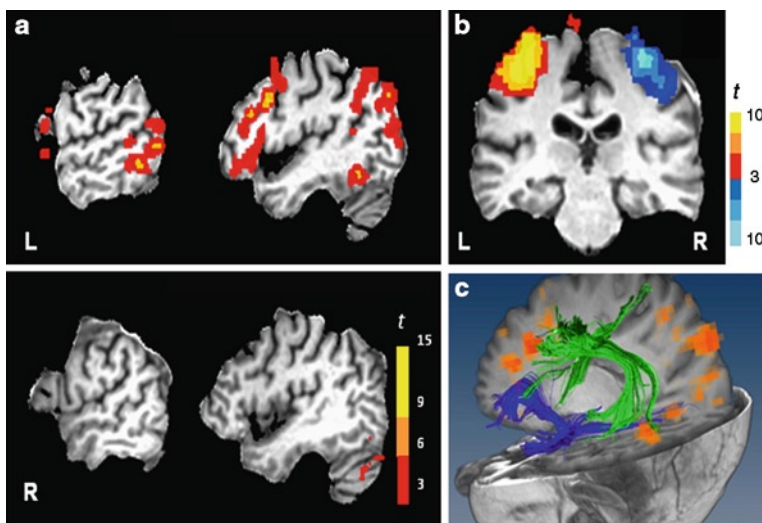


**Fig. 3.3** Presurgical fMRI and DTI maps in an epilepsy patient (female, 52 years, right-handed) with a left temporal seizure focus. (a) fMRI map during semantic processing shows strong left lateralized activity in language cortex (inferior and middle frontal, middle temporal, fusiform and angular gyri). (b) fMRI activation in somatomotor cortices during right hand (warm colors) and left hand (cold colors) finger tapping. (c) Left temporal language tracts, including the occipito-frontal, inferior longitudinal, and uncinate fasciculi (blue) and the superior longitudinal fasciculus (green). L left; R right

between brain tumors or lesions and white matter tracts [155–158]. Combined fMRI and DTI mapping can reveal both functional regions and their white matter connectivity and thus provide a more accurate estimate of the proximity of tumor borders to vital brain networks [155, 156, 158]. An example of fMRI and DTI pre-surgical mapping in an epilepsy patient with a left temporal seizure focus is shown in Fig. 3.3.

DTI can be useful in distinguishing between different effects of space occupying lesions such as displacement, disruption, or infiltration of the white matter tracts by the tumor [157, 159–162]. White matter fibers may remain intact but be displaced by a tumor, in which case their anisotropy would be maintained and their new location and orientation would be detectable on directional DTI maps. This pattern is most useful for presurgical planning because it confirms the existence of a peritumoral tract that can potentially be preserved during resection. Alternatively, edema or infiltration by the tumor may reduce the anisotropy of tracts, either still leaving enough directional organization to remain detectable on DTI maps or completely disrupting the directional organization. This latter pattern is more challenging and open for interpretation because the degree of integrity of the white matter tracts remains ambiguous.

DTI-based fiber tractography can be more challenging in cases of brain pathologies with space occupying lesions, because displaced fibers may not readily be traced with common methods for seed selection based on anatomical landmarks. In addition, tumor infiltration and edema may cause tissue deformation, resulting in reduced reliability of fiber tracking [163]. Recent work suggests that in brain tumor patients, seed region selection based on fMRI activation patterns rather than anatomical landmarks, combined with examination of principal diffusivity measures, can yield more sensitive tractography of corticospinal and superior longitudinal fasciculus tracts subserving motor and language systems [157, 159, 164, 165]. Fiber tracking in regions with edema can also potentially be improved by using sophisticated postprocessing algorithms for separating diffusion properties of neural tissue from surrounding free water [166].

The distance of the resection margin from the corticospinal tracts has been shown to be an important determinant of the risk for postsurgical motor deficit [98]. Similar to the fMRI studies, here too a distance of at least 1 cm from the corticospinal tract is considered “safe” for resection. Visual field deficits due to optic radiation injury are a common complication of temporal lobectomy in epilepsy surgery. The optic radiation can be visualized with DTI fiber tracking, and the distance of the Meyer loop of the optic radiation from the resection margin has been shown to be predictive of the risk of postsurgical visual field deficits [167, 168].

### **3.2.4 EEG and MEG Mapping**

EEG plays a central role in the diagnosis and management of patients with seizure disorders. EEG is highly accessible and available in all clinical centers, and the method incurs relatively low costs. Although EEG has relatively high specificity for the diagnosis of epilepsy, the sensitivity of the method is low [169]. Indeed, EEG is particularly useful if epileptic discharges are captured during the EEG recording session, as only this form of abnormal EEG activity is correlated highly enough with seizure disorders to be of clinical use [170]. EEG can help determine the seizure type (focal or generalized) and epilepsy syndrome, and thus guide the choice of antiepileptic medication and prognosis. In patients with medically refractory epilepsy (not responding to seizure medication) who are candidates for epilepsy surgery, long-term EEG monitoring may be recommended to characterize and quantify the frequency and type of seizures and to localize the sources of the epileptogenic activity.

Similar to EEG, the primary clinical application of MEG is for presurgical localization and characterization of epileptic sources, particularly in cases when MRI is inconclusive with regard to the seizure focus. The location, orientation, and spatial extent of epileptic discharges with respect to other spontaneous brain activity all contribute to the sensitivity of MEG and EEG, making it difficult to predict which method is best suited for each patient [171–174]. Most electrical discharges

can be detected by both EEG and MEG, for example, in most cases of temporal lobe epilepsy [174, 175]. However, MEG is more effective for the detection of epileptic activity arising from the superficial cortical convexity, such as in lateral neocortical epilepsy and cortical dysplasia [171, 174].

Scalp EEG can also be recorded simultaneously with fMRI (simultaneous EEG/fMRI) to map changes in cerebral BOLD signal associated with epileptic discharges [176–178]. The benefit of the simultaneous recordings arises from the fusion of high temporal EEG and high spatial fMRI data to inform the electrical source modeling. Indeed, electrical source modeling of the epileptic EEG activity can be used to resolve the BOLD changes related to the epilepsy onset from those related to the propagation of epileptic spikes [179, 180]. This technique can be particularly useful in cases when EEG and MRI data are not concordant [181].

EEG can also be used intrasurgically for the recording of event-related responses to monitor sensory functions. In particular, somatosensory-evoked potentials are used for continuous assessment of somatomotor functions in order to minimize the occurrence of postsurgical somatosensory and motor deficits.

Despite the important role of noninvasive EEG and MEG for the detection and localization of epileptic sources, these methods have lower detection rates of epileptic discharges compared to invasive electrophysiological methods, especially in the case of deep and focal spike sources such as in the hippocampus [182, 183]. Invasive electrophysiology is recommended in complicated cases such as when multiple epileptic sources are suspected, or when no underlying structural pathology has been identified. Depth electrodes inserted surgically (under MRI guidance) can be used for recording electrical signals from deep and focal brain areas. Subdural electrodes strips or grids (placed after craniotomy) are best suited for recording from wider cortical areas. Nevertheless, unlike scalp EEG or MEG, invasive electrophysiology carries some risks, including infection, hemorrhage, and cortical damage.

### 3.3 Summary and Conclusions

MR imaging is the primary tool for noninvasive localization of brain tumors and lesions that might cause epilepsy and for the mapping of functional brain areas and white matter fiber tracks with respect to structural abnormalities. The ultimate goal of presurgical brain mapping using MR imaging is to provide structural and functional information that can facilitate maximal tumor or epileptic tissue surgical resection, together with minimal damage to surrounding gray and white matter structures supporting vital sensory and cognitive functions.

fMRI can provide a comprehensive delineation (and perhaps overestimation) of somatomotor and language regions in proximity of a tumor or lesion at a spatial resolution of a few mm. DTI can show the connectivity pattern of somatomotor and language areas in proximity of the pathological tissue. Such structural and functional

MR images can assist in assessing the risks of a brain surgery and the benefit of conducting additional intrasurgical cortical stimulation to map functional organization. If functional regions and fiber tracks identified by fMRI and DTI are found to be distant from the pathological area, this can facilitate a decision for radical surgical resection. If fMRI activation associated with vital sensory, motor, or cognitive functions is demonstrated near the radiological pathological boundary, partial resection may be suggested, with cortical stimulation mapping to identify the exact resection margin intrasurgically. In this case, the presurgical MR information can also help to plan the extent of the craniotomy and the stimulation procedure, thereby potentially reducing surgical time [91, 113]. If the risk of resection for causing long-term severe functional deficit is considered too high, alternative approaches may in some cases be suggested.

Despite the tremendous potential of MR imaging for presurgical planning, several factors still limit a wider use of this technology. In particular, clinical implementation of fMRI is impeded by the lack of standardized acquisition paradigms and analysis procedures that are documented to produce highly reliable and robust activity in clinically relevant target brain region. To date, the most reliable clinical applications of fMRI appear to be for the mapping of sensory and motor functions and for the determination of language hemispheric dominance. However, systematic evaluation in large-scale studies specifically designed to establish the accuracy and predictive value for patient outcome of specific fMRI paradigms and specific fMRI and DTI analysis procedures is warranted.

Finally, electrophysiological functional brain mapping techniques such as EEG and MEG are complementary to fMRI in that they probe the neural activity directly at high temporal resolution. The primary clinical application of these techniques is for presurgical localization and characterization of epileptic sources, particularly in cases when MRI is inconclusive with regard to the seizure focus.

**Acknowledgments** The image data shown in Figs. 3.1–3.3 were collected at the National Research Council Institute for Biodiagnostics (NRC-IBD) from patients treated in the Neurosurgery Department of the Health Science Center (HSC) in Winnipeg. The author would like to thank Dr. Michael West, Head of the Neurosurgery Department at HSC, and Dr. Owen Williams from the same Department, for their involvement in referring patients and interpreting the image data shown in the figures in this chapter, and Dr. Uta Sboto-Frankenstein and Dr. Jordan Hovdebo from NRC-IBD for their assistance in collecting and analyzing the images.

## References

1. Naidich, T.P., Valavanis, A.G., Kubik, S.: Anatomic relationships along the low-middle convexity: part I—Normal specimens and magnetic resonance imaging. *Neurosurgery* **36**, 517–532 (1995)
2. Mazziotta, J.C., Toga, A.W., Evans, A., et al.: A probabilistic atlas of the human brain: theory and rationale for its development. The International Consortium for Brain Mapping (ICBM). *Neuroimage* **2**, 89–101 (1995)
3. Toga, A.W., Thompson, P.M., Mori, S., et al.: Towards multimodal atlases of the human brain. *Nat. Rev. Neurosci.* **7**, 952–966 (2006)

4. Zilles, K., Schleicher, A., Langemann, C., et al.: Quantitative analysis of sulci in the human cerebral cortex: development, regional heterogeneity, gender difference, asymmetry, intersubject variability and cortical architecture. *Hum. Brain Mapp.* **5**, 218–221 (1997)
5. Lauterbur, P.C.: Image formation by induced local interactions. Examples employing nuclear magnetic resonance. *Nature* **242**, 190–191 (1973)
6. Mansfield, P., Maudsley, A.A.: Medical imaging by NMR. *Br. J. Radiol.* **50**, 188–194 (1977)
7. Albert, F.K., Forsting, M., Sartor, K., et al.: Early postoperative magnetic resonance imaging after resection of malignant glioma: objective evaluation of residual tumor and its influence on regrowth and prognosis. *Neurosurgery* **34**, 45–60 (1994)
8. Ogawa, S., Lee, T.M., Kay, A.R., et al.: Brain magnetic resonance imaging with contrast dependent on blood oxygenation. *Proc. Natl. Acad. Sci. U.S.A.* **87**, 9868–9872 (1990)
9. Kwong, K.K., Belliveau, J.W., Chesler, D.A., et al.: Dynamic magnetic resonance imaging of human brain activity during primary sensory stimulation. *Proc. Natl. Acad. Sci. U.S.A.* **89**, 5675–5679 (1992)
10. Belliveau, J.W., Kennedy Jr., D.N., McKinstry, R.C., et al.: Functional mapping of the human visual cortex by magnetic resonance imaging. *Science* **254**, 716–719 (1991)
11. Ogawa, S., Tank, D.W., Menon, R., et al.: Intrinsic signal changes accompanying sensory stimulation: functional brain mapping with magnetic resonance imaging. *Proc. Natl. Acad. Sci. U.S.A.* **89**, 5951–5955 (1992)
12. Bandettini, P.A., Wong, E.C., Hinks, R.S., et al.: Time course EPI of human brain function during task activation. *Magn. Reson. Med.* **25**, 390–397 (1992)
13. Mesulam, M.M.: From sensation to cognition. *Brain* **121**(pt 6), 1013–1052 (1998)
14. Bookheimer, S.: Pre-surgical language mapping with functional magnetic resonance imaging. *Neuropsychol. Rev.* **17**, 145–155 (2007)
15. Binder, J.R., Swanson, S.J., Hammeke, T.A., et al.: A comparison of five fMRI protocols for mapping speech comprehension systems. *Epilepsia* **49**, 1980–1997 (2008)
16. Aguirre, G.K., D'Esposito, M.: Experimental design for brain fMRI. In: Moonen, C.T., Bandettini, P. (eds.) *Functional MRI*, pp. 369–380. Springer, Berlin (1999)
17. Price, C.J., Friston, K.J.: Cognitive conjunction: a new approach to brain activation experiments. *Neuroimage* **5**, 261–270 (1997)
18. Buckner, R.L., Braver, T.S.: Event-related functional MRI. In: Moonen, C.T., Bandettini, P. (eds.) *Functional MRI*, pp. 441–452. Springer, Berlin (1999)
19. Voyvodic, J.T.: Activation mapping as a percentage of local excitation: fMRI stability within scans, between scans and across field strengths. *Magn. Reson. Imaging* **24**, 1249–1261 (2006)
20. Voyvodic, J.T., Petrella, J.R., Friedman, A.H.: fMRI activation mapping as a percentage of local excitation: consistent presurgical motor maps without threshold adjustment. *J. Magn. Reson. Imaging* **29**, 751–759 (2009)
21. Basser, P.J., Pierpaoli, C.: Microstructural and physiological features of tissues elucidated by quantitative-diffusion-tensor MRI. *J. Magn. Reson. B* **111**, 209–219 (1996)
22. Pierpaoli, C., Jezzard, P., Basser, P.J., et al.: Diffusion tensor MR imaging of the human brain. *Radiology* **201**, 637–648 (1996)
23. Mori, S., van Zijl, P.C.: Fiber tracking: principles and strategies – a technical review. *NMR Biomed.* **15**, 468–480 (2002)
24. Moseley, M.E., Cohen, Y., Kucharczyk, J., et al.: Diffusion-weighted MR imaging of anisotropic water diffusion in cat central nervous system. *Radiology* **176**, 439–445 (1990)
25. Papadakis, N.G., Murrills, C.D., Hall, L.D., et al.: Minimal gradient encoding for robust estimation of diffusion anisotropy. *Magn. Reson. Imaging* **18**, 671–679 (2000)
26. Douek, P., Turner, R., Pekar, J., et al.: MR color mapping of myelin fiber orientation. *J. Comput. Assist. Tomogr.* **15**, 923–929 (1991)
27. Basser, P.J., Pajevic, S., Pierpaoli, C., et al.: In vivo fiber tractography using DT-MRI data. *Magn. Reson. Med.* **44**, 625–632 (2000)
28. Mori, S., Crain, B.J., Chacko, V.P., et al.: Three-dimensional tracking of axonal projections in the brain by magnetic resonance imaging. *Ann. Neurol.* **45**, 265–269 (1999)

29. Cohen, D.: Magnetoencephalography: detection of the brain's electrical activity with a superconducting magnetometer. *Science* **175**, 664–666 (1972)
30. Cohen, D.: Magnetoencephalography: evidence of magnetic fields produced by alpha-rhythm currents. *Science* **161**, 784–786 (1968)
31. Nunez, P.L.: *Electric Fields of the Brain: The Neurophysics of EEG*. Oxford University Press, New York (1981)
32. Hillebrand, A., Barnes, G.R.: A quantitative assessment of the sensitivity of whole-head MEG to activity in the adult human cortex. *Neuroimage* **16**, 638–650 (2002)
33. Stok, C.J., Meijis, J.W., Peters, M.J.: Inverse solutions based on MEG and EEG applied to volume conductor analysis. *Phys. Med. Biol.* **32**, 99–104 (1987)
34. Baillet, S., Garnero, L., Marin, G., et al.: Combined MEG and EEG source imaging by minimization of mutual information. *IEEE Trans. Biomed. Eng.* **46**, 522–534 (1999)
35. Galambos, R., Sheatz, G.C.: An electroencephalograph study of classical conditioning. *Am. J. Physiol.* **203**, 173–184 (1962)
36. Walter, W.G., Cooper, R., Aldridge, V.J., et al.: Contingent negative variation: an electric sign of sensorimotor association and expectancy in the human brain. *Nature* **203**, 380–384 (1964)
37. Halliday, A.M.: *Evoked Potentials in Clinical Testing*. Churchill Livingstone, Edinburgh (1993)
38. Aminoff, M.J., Eisen, A.A.: AAEM minimonograph 19: somatosensory evoked potentials. *Muscle Nerve* **21**, 277–290 (1998)
39. Ives, J.R., Warach, S., Schmitt, F., et al.: Monitoring the patient's EEG during echo planar MRI. *Electroencephalogr. Clin. Neurophysiol.* **87**, 417–420 (1993)
40. Laufs, H., Daunizeau, J., Carmichael, D.W., et al.: Recent advances in recording electrophysiological data simultaneously with magnetic resonance imaging. *Neuroimage* **40**, 515–528 (2008)
41. Liebenthal, E., Ellingson, M.L., Spanaki, M.V., et al.: Simultaneous ERP and fMRI of the auditory cortex in a passive oddball paradigm. *Neuroimage* **19**, 1395–1404 (2003)
42. Liebenthal, E., Desai, R., Ellingson, M.M., et al.: Specialization along the left superior temporal sulcus for auditory categorization. *Cereb. Cortex* **20**, 2958–2970 (2010)
43. Horovitz, S.G., Skudlarski, P., Gore, J.C.: Correlations and dissociations between BOLD signal and P300 amplitude in an auditory oddball task: a parametric approach to combining fMRI and ERP. *Magn. Reson. Imaging* **20**, 319–325 (2002)
44. Ellingson, M.L., Liebenthal, E., Spanaki, M.V., et al.: Ballistocardiogram artifact reduction in the simultaneous acquisition of auditory ERPs and fMRI. *Neuroimage* **22**, 1534–1542 (2004)
45. Schomer, D.L., Bonmassar, G., Lazeyras, F., et al.: EEG-Linked functional magnetic resonance imaging in epilepsy and cognitive neurophysiology. *J. Clin. Neurophysiol.* **17**, 43–58 (2000)
46. Lemieux, L., Allen, P.J., Franconi, F., et al.: Recording of EEG during fMRI experiments: patient safety. *Magn. Reson. Med.* **38**, 943–952 (1997)
47. Bonmassar, G., Purdon, P.L., Jaaskelainen, I.P., et al.: Motion and ballistocardiogram artifact removal for interleaved recording of EEG and EPs during MRI. *Neuroimage* **16**, 1127–1141 (2002)
48. Gotman, J., Kobayashi, E., Bagshaw, A.P., et al.: Combining EEG and fMRI: a multimodal tool for epilepsy research. *J. Magn. Reson. Imaging* **23**, 906–920 (2006)
49. Laufs, H., Duncan, J.S.: Electroencephalography/functional MRI in human epilepsy: what it currently can and cannot do. *Curr. Opin. Neurol.* **20**, 417–423 (2007)
50. Vlieger, E.J., Majoe, C.B., Leenstra, S., et al.: Functional magnetic resonance imaging for neurosurgical planning in neurooncology. *Eur. Radiol.* **14**, 1143–1153 (2004)
51. Keles, G.E., Lamborn, K.R., Berger, M.S.: Low-grade hemispheric gliomas in adults: a critical review of extent of resection as a factor influencing outcome. *J. Neurosurg.* **95**, 735–745 (2001)
52. Spencer, S., Huh, L.: Outcomes of epilepsy surgery in adults and children. *Lancet Neurol.* **7**, 525–537 (2008)

53. Duncan, J.S.: Imaging in the surgical treatment of epilepsy. *Nat. Rev. Neurol.* **6**, 537–550 (2010)
54. Carmichael, D.W., Thornton, J.S., Rodionov, R., et al.: Safety of localizing epilepsy monitoring intracranial electroencephalograph electrodes using MRI: radiofrequency-induced heating. *J. Magn. Reson. Imaging* **28**, 1233–1244 (2008)
55. Salamon, N., Kung, J., Shaw, S.J., et al.: FDG-PET/MRI coregistration improves detection of cortical dysplasia in patients with epilepsy. *Neurology* **71**, 1594–1601 (2008)
56. Lee, K.K., Salamon, N.: [18F] fluorodeoxyglucose-positron-emission tomography and MR imaging coregistration for presurgical evaluation of medically refractory epilepsy. *AJNR Am. J. Neuroradiol.* **30**, 1811–1816 (2009)
57. Bradley, W.G.: Achieving gross total resection of brain tumors: intraoperative MR imaging can make a big difference. *AJNR Am. J. Neuroradiol.* **23**, 348–349 (2002)
58. Albayrak, B., Samdani, A.F., Black, P.M.: Intra-operative magnetic resonance imaging in neurosurgery. *Acta Neurochir. (Wien)* **146**, 543–556 (2004)
59. Merkle, E.M., Lewin, J.S., Liebenthal, R., et al.: The interventional MR imaging suite: magnet designs and equipment requirements. *Magn. Reson. Imaging Clin. N. Am.* **13**, 401–413 (2005)
60. Nimsky, C., Ganslandt, O., Buchfelder, M., et al.: Glioma surgery evaluated by intraoperative low-field magnetic resonance imaging. *Acta Neurochir. Suppl.* **85**, 55–63 (2003)
61. Black, P.M., Alexander III, E., Martin, C., et al.: Craniotomy for tumor treatment in an intraoperative magnetic resonance imaging unit. *Neurosurgery* **45**, 423–431 (1999)
62. Schneider, J.P., Schulz, T., Schmidt, F., et al.: Gross-total surgery of supratentorial low-grade gliomas under intraoperative MR guidance. *AJNR Am. J. Neuroradiol.* **22**, 89–98 (2001)
63. Nimsky, C., Ganslandt, O., Buchfelder, M., et al.: Intraoperative visualization for resection of gliomas: the role of functional neuronavigation and intraoperative 1.5 T MRI. *Neurol. Res.* **28**, 482–487 (2006)
64. Hartkens, T., Hill, D.L., Castellano-Smith, A.D., et al.: Measurement and analysis of brain deformation during neurosurgery. *IEEE Trans. Med. Imaging* **22**, 82–92 (2003)
65. Nimsky, C., Ganslandt, O., Cerny, S., et al.: Quantification of, visualization of, and compensation for brain shift using intraoperative magnetic resonance imaging. *Neurosurgery* **47**, 1070–1079 (2000)
66. Nabavi, A., Black, P.M., Gering, D.T., et al.: Serial intraoperative magnetic resonance imaging of brain shift. *Neurosurgery* **48**, 787–797 (2001)
67. Keles, G.E., Lamborn, K.R., Berger, M.S.: Coregistration accuracy and detection of brain shift using intraoperative sononavigation during resection of hemispheric tumors. *Neurosurgery* **53**, 556–562 (2003)
68. Schwartz, R.B., Hsu, L., Wong, T.Z., et al.: Intraoperative MR imaging guidance for intracranial neurosurgery: experience with the first 200 cases. *Radiology* **211**, 477–488 (1999)
69. Archip, N., Clatz, O., Whalen, S., et al.: Non-rigid alignment of pre-operative MRI, fMRI, and DT-MRI with intra-operative MRI for enhanced visualization and navigation in image-guided neurosurgery. *Neuroimage* **35**, 609–624 (2007)
70. Warfield, S.K., Haker, S.J., Talos, I.F., et al.: Capturing intraoperative deformations: research experience at Brigham and Women's Hospital. *Med. Image Anal.* **9**, 145–162 (2005)
71. Wittek, A., Joldes, G., Couton, M., et al.: Patient-specific non-linear finite element modelling for predicting soft organ deformation in real-time; application to non-rigid neuroimage registration. *Prog. Biophys. Mol. Biol.* **103**, 292–303 (2010)
72. Petrella, J.R., Shah, L.M., Harris, K.M., et al.: Preoperative functional MR imaging localization of language and motor areas: effect on therapeutic decision making in patients with potentially resectable brain tumors. *Radiology* **240**, 793–802 (2006)
73. Van Westen, D., Skagerberg, G., Olsrud, J., et al.: Functional magnetic resonance imaging at 3T as a clinical tool in patients with intracranial tumors. *Acta Radiol.* **46**, 599–609 (2005)
74. Ulmer, J.L., Hacein-Bey, L., Mathews, V.P., et al.: Lesion-induced pseudo-dominance at functional magnetic resonance imaging: implications for preoperative assessments. *Neurosurgery* **55**, 569–579 (2004)

75. Duffau, H., Lopes, M., Arthuis, F., et al.: Contribution of intraoperative electrical stimulations in surgery of low grade gliomas: a comparative study between two series without (1985–96) and with (1996–2003) functional mapping in the same institution. *J. Neurol. Neurosurg. Psychiatry* **76**, 845–851 (2005)
76. Haglund, M.M., Berger, M.S., Shamseldin, M., et al.: Cortical localization of temporal lobe language sites in patients with gliomas. *Neurosurgery* **34**, 567–576 (1994)
77. Sunaert, S.: Presurgical planning for tumor resectioning. *J. Magn. Reson. Imaging* **23**, 887–905 (2006)
78. Rutten, G.J., Ramsey, N.F.: The role of functional magnetic resonance imaging in brain surgery. *Neurosurg. Focus* **28**, E4 (2010)
79. Upadhyay, U.M., Golby, A.J.: Role of pre- and intraoperative imaging and neuronavigation in neurosurgery. *Expert Rev. Med. Devices* **5**, 65–73 (2008)
80. Holodny, A.I., Schulder, M., Liu, W.C., et al.: The effect of brain tumors on BOLD functional MR imaging activation in the adjacent motor cortex: implications for image-guided neurosurgery. *AJNR Am. J. Neuroradiol.* **21**, 1415–1422 (2000)
81. Ulmer, J.L., Krouwer, H.G., Mueller, W.M., et al.: Pseudo-reorganization of language cortical function at fMRI imaging: a consequence of tumor-induced neurovascular uncoupling. *AJNR Am. J. Neuroradiol.* **24**, 213–217 (2003)
82. Desmond, J.E., Annabel Chen, S.H.: Ethical issues in the clinical application of fMRI: factors affecting the validity and interpretation of activations. *Brain Cogn.* **50**, 482–497 (2002)
83. Binder, J.R.: Functional MRI is a valid noninvasive alternative to Wada testing. *Epilepsy Behav.* **20**, 214–222 (2011)
84. Krainik, A., Duffau, H., Capelle, L., et al.: Role of the healthy hemisphere in recovery after resection of the supplementary motor area. *Neurology* **62**, 1323–1332 (2004)
85. Achten, E., Jackson, G.D., Cameron, J.A., et al.: Presurgical evaluation of the motor hand area with functional MR imaging in patients with tumors and dysplastic lesions. *Radiology* **210**, 529–538 (1999)
86. De Tiege, X., Connelly, A., Liegeois, F., et al.: Influence of motor functional magnetic resonance imaging on the surgical management of children and adolescents with symptomatic focal epilepsy. *Neurosurgery* **64**, 856–864 (2009)
87. Haberg, A., Kvistad, K.A., Unsgard, G., et al.: Preoperative blood oxygen level-dependent functional magnetic resonance imaging in patients with primary brain tumors: clinical application and outcome. *Neurosurgery* **54**, 902–914 (2004)
88. Mueller, W.M., Yetkin, F.Z., Hammeke, T.A., et al.: Functional magnetic resonance imaging mapping of the motor cortex in patients with cerebral tumors. *Neurosurgery* **39**, 515–520 (1996)
89. Pujol, J., Conesa, G., Deus, J., et al.: Clinical application of functional magnetic resonance imaging in presurgical identification of the central sulcus. *J. Neurosurg.* **88**, 863–869 (1998)
90. Lehericy, S., Duffau, H., Cornu, P., et al.: Correspondence between functional magnetic resonance imaging somatotopy and individual brain anatomy of the central region: comparison with intraoperative stimulation in patients with brain tumors. *J. Neurosurg.* **92**, 589–598 (2000)
91. Bartos, R., Jech, R., Vymazal, J., et al.: Validity of primary motor area localization with fMRI versus electric cortical stimulation: a comparative study. *Acta Neurochir. (Wien)* **151**, 1071–1080 (2009)
92. Hirsch, J., Ruge, M.I., Kim, K.H., et al.: An integrated functional magnetic resonance imaging procedure for preoperative mapping of cortical areas associated with tactile, motor, language, and visual functions. *Neurosurgery* **47**, 711–721 (2000)
93. Jack Jr., C.R., Thompson, R.M., Butts, R.K., et al.: Sensory motor cortex: correlation of pre-surgical mapping with functional MR imaging and invasive cortical mapping. *Radiology* **190**, 85–92 (1994)
94. Krishnan, R., Raabe, A., Hattingen, E., et al.: Functional magnetic resonance imaging-integrated neuronavigation: correlation between lesion-to-motor cortex distance and outcome. *Neurosurgery* **55**, 904–914 (2004)

95. Pujol, J., Conesa, G., Deus, J., et al.: Presurgical identification of the primary sensorimotor cortex by functional magnetic resonance imaging. *J. Neurosurg.* **84**, 7–13 (1996)
96. Yetkin, F.Z., Mueller, W.M., Morris, G.L., et al.: Functional MR activation correlated with intraoperative cortical mapping. *AJNR Am. J. Neuroradiol.* **18**, 1311–1315 (1997)
97. Yousry, T.A., Schmid, U.D., Alkhadi, H., et al.: Localization of the motor hand area to a knob on the precentral gyrus. A new landmark. *Brain* **120**, 141–157 (1997)
98. Mikuni, N., Okada, T., Enatsu, R., et al.: Clinical impact of integrated functional neuronavigation and subcortical electrical stimulation to preserve motor function during resection of brain tumors. *J. Neurosurg.* **106**, 593–598 (2007)
99. Sereno, M.I., Dale, A.M., Reppas, J.B., et al.: Borders of multiple visual areas in humans revealed by functional magnetic resonance imaging. *Science* **268**, 889–893 (1995)
100. DeYoe, E.A., Carman, G.J., Bandettini, P., et al.: Mapping striate and extrastriate visual areas in human cerebral cortex. *Proc. Natl. Acad. Sci. U.S.A.* **93**, 2382–2386 (1996)
101. Binder, J.R., Frost, J.A., Hammeke, T.A., et al.: Human brain language areas identified by functional magnetic resonance imaging. *J. Neurosci.* **17**, 353–362 (1997)
102. Binder, J.R., Desai, R.H., Graves, W.W., et al.: Where is the semantic system? A critical review and meta-analysis of 120 functional neuroimaging studies. *Cereb. Cortex* **19**, 2767–2796 (2009)
103. Damasio, H., Grabowski, T.J., Tranel, D., et al.: A neural basis for lexical retrieval. *Nature* **380**, 499–505 (1996)
104. Demonet, J.F., Thierry, G., Cardebat, D.: Renewal of the neurophysiology of language: functional neuroimaging. *Physiol. Rev.* **85**, 49–95 (2005)
105. Indefrey, P., Levelt, W.J.: The spatial and temporal signatures of word production components. *Cognition* **92**, 101–144 (2004)
106. Lazar, R.M., Antoniello, D.: Variability in recovery from aphasia. *Curr. Neurol. Neurosci. Rep.* **8**, 497–502 (2008)
107. Dronkers, N.F., Wilkins, D.P., Van Jr., V.R., et al.: Lesion analysis of the brain areas involved in language comprehension. *Cognition* **92**, 145–177 (2004)
108. Demonet, J.F., Chollet, F., Ramsay, S., et al.: The anatomy of phonological and semantic processing in normal subjects. *Brain* **115**(pt 6), 1753–1768 (1992)
109. McKiernan, K.A., D'Angelo, B.R., Kaufman, J.N., et al.: Interrupting the “stream of consciousness”: an fMRI investigation. *Neuroimage* **29**, 1185–1191 (2006)
110. Stark, C.E., Squire, L.R.: When zero is not zero: the problem of ambiguous baseline conditions in fMRI. *Proc. Natl. Acad. Sci. U.S.A.* **98**, 12760–12766 (2001)
111. Fitzgerald, D.B., Cosgrove, G.R., Ronner, S., et al.: Location of language in the cortex: a comparison between functional MR imaging and electrocortical stimulation. *AJNR Am. J. Neuroradiol.* **18**, 1529–1539 (1997)
112. Pouratian, N., Bookheimer, S.Y., Rex, D.E., et al.: Utility of preoperative functional magnetic resonance imaging for identifying language cortices in patients with vascular malformations. *J. Neurosurg.* **97**, 21–32 (2002)
113. Rutten, G.J., Ramsey, N.F., van Rijen, P.C., et al.: Development of a functional magnetic resonance imaging protocol for intraoperative localization of critical temporoparietal language areas. *Ann. Neurol.* **51**, 350–360 (2002)
114. Roux, F.E., Boulanouar, K., Lotterie, J.A., et al.: Language functional magnetic resonance imaging in preoperative assessment of language areas: correlation with direct cortical stimulation. *Neurosurgery* **52**, 1335–1345 (2003)
115. Wada, J., Rasmussen, T.: Intracarotid injection of sodium amytal for the lateralization of cerebral speech dominance. *J. Neurosurg.* **17**, 262–282 (1960)
116. Meador, K.J., Loring, D.W.: The Wada test: controversies, concerns, and insights. *Neurology* **52**, 1535–1536 (1999)
117. Binder, J.R., Swanson, S.J., Hammeke, T.A., et al.: Determination of language dominance using functional MRI: a comparison with the Wada test. *Neurology* **46**, 978–984 (1996)
118. Lehericy, S., Cohen, L., Bazin, B., et al.: Functional MR evaluation of temporal and frontal language dominance compared with the Wada test. *Neurology* **54**, 1625–1633 (2000)

119. Liegeois, F., Connelly, A., Salmond, C.H., et al.: A direct test for lateralization of language activation using fMRI: comparison with invasive assessments in children with epilepsy. *Neuroimage* **17**, 1861–1867 (2002)
120. Swanson, S.J., Sabsevitz, D.S., Hammeke, T.A., et al.: Functional magnetic resonance imaging of language in epilepsy. *Neuropsychol. Rev.* **17**, 491–504 (2007)
121. Sabsevitz, D.S., Swanson, S.J., Hammeke, T.A., et al.: Use of preoperative functional neuroimaging to predict language deficits from epilepsy surgery. *Neurology* **60**, 1788–1792 (2003)
122. Kubu, C.S., Girvin, J.P., McLachlan, R.S., et al.: Does the intracarotid amobarbital procedure predict global amnesia after temporal lobectomy? *Epilepsia* **41**, 1321–1329 (2000)
123. Simkins-Bullock, J.: Beyond speech lateralization: a review of the variability, reliability, and validity of the intracarotid amobarbital procedure and its nonlanguage uses in epilepsy surgery candidates. *Neuropsychol. Rev.* **10**, 41–74 (2000)
124. Binder, J.R., Sabsevitz, D.S., Swanson, S.J., et al.: Use of preoperative functional MRI to predict verbal memory decline after temporal lobe epilepsy surgery. *Epilepsia* **49**, 1377–1394 (2008)
125. Frings, L., Wagner, K., Halsband, U., et al.: Lateralization of hippocampal activation differs between left and right temporal lobe epilepsy patients and correlates with postsurgical verbal learning decrement. *Epilepsy Res.* **78**, 161–170 (2008)
126. Powell, H.W., Richardson, M.P., Symms, M.R., et al.: Preoperative fMRI predicts memory decline following anterior temporal lobe resection. *J. Neurol. Neurosurg. Psychiatry* **79**, 686–693 (2008)
127. Rabin, M.L., Narayan, V.M., Kimberg, D.Y., et al.: Functional MRI predicts post-surgical memory following temporal lobectomy. *Brain* **127**, 2286–2298 (2004)
128. Constable, R.T., Carpentier, A., Pugh, K., et al.: Investigation of the human hippocampal formation using a randomized event-related paradigm and Z-shimmed functional MRI. *Neuroimage* **12**, 55–62 (2000)
129. Fernandez-Seara, M.A., Wang, J., Wang, Z., et al.: Imaging mesial temporal lobe activation during scene encoding: comparison of fMRI using BOLD and arterial spin labeling. *Hum. Brain Mapp.* **28**, 1391–1400 (2007)
130. Binder, J.R., Swanson, S.J., Sabsevitz, D.S., et al.: A comparison of two fMRI methods for predicting verbal memory decline after left temporal lobectomy: language lateralization versus hippocampal activation asymmetry. *Epilepsia* **51**, 618–626 (2010)
131. Fox, M.D., Raichle, M.E.: Spontaneous fluctuations in brain activity observed with functional magnetic resonance imaging. *Nat. Rev. Neurosci.* **8**, 700–711 (2007)
132. Biswal, B.B., et al.: Toward discovery science of human brain function. *Proc. Natl. Acad. Sci. U.S.A.* **107**, 4734–4739 (2010)
133. Biswal, B., Yetkin, F.Z., Haughton, V.M., et al.: Functional connectivity in the motor cortex of resting human brain using echo-planar MRI. *Magn. Reson. Med.* **34**, 537–541 (1995)
134. Cordes, D., Haughton, V.M., Arfanakis, K., et al.: Mapping functionally related regions of brain with functional connectivity MR imaging. *AJNR Am. J. Neuroradiol.* **21**, 1636–1644 (2000)
135. Lowe, M.J., Lurito, J.T., Mathews, V.P., et al.: Quantitative comparison of functional contrast from BOLD-weighted spin-echo and gradient-echo echoplanar imaging at 1.5 Tesla and H<sub>2</sub><sup>15</sup>O PET in the whole brain. *J. Cereb. Blood Flow Metab.* **20**, 1331–1340 (2000)
136. Fox, M.D., Greicius, M.: Clinical applications of resting state functional connectivity. *Front. Syst. Neurosci.* **4**, 19 (2010)
137. Kokkonen, S.M., Nikkinen, J., Remes, J., et al.: Preoperative localization of the sensorimotor area using independent component analysis of resting-state fMRI. *Magn. Reson. Imaging* **27**, 733–740 (2009)
138. Liu, H., Buckner, R.L., Talukdar, T., et al.: Task-free presurgical mapping using functional magnetic resonance imaging intrinsic activity. *J. Neurosurg.* **111**, 746–754 (2009)
139. Larson-Prior, L.J., Zempel, J.M., Nolan, T.S., et al.: Cortical network functional connectivity in the descent to sleep. *Proc. Natl. Acad. Sci. U.S.A.* **106**, 4489–4494 (2009)

140. Vincent, J.L., Patel, G.H., Fox, M.D., et al.: Intrinsic functional architecture in the anaesthetized monkey brain. *Nature* **447**, 83–86 (2007)
141. Fujiwara, N., Sakatani, K., Katayama, Y., et al.: Evoked-cerebral blood oxygenation changes in false-negative activations in BOLD contrast functional MRI of patients with brain tumors. *Neuroimage* **21**, 1464–1471 (2004)
142. Schreiber, A., Hubbe, U., Ziyeh, S., et al.: The influence of gliomas and nonglial space-occupying lesions on blood-oxygen-level-dependent contrast enhancement. *AJNR Am. J. Neuroradiol.* **21**, 1055–1063 (2000)
143. Hou, B.L., Bradbury, M., Peck, K.K., et al.: Effect of brain tumor neovasculature defined by rCBV on BOLD fMRI activation volume in the primary motor cortex. *Neuroimage* **32**, 489–497 (2006)
144. Chen, C.M., Hou, B.L., Holodny, A.I.: Effect of age and tumor grade on BOLD functional MR imaging in preoperative assessment of patients with glioma. *Radiology* **248**, 971–978 (2008)
145. Rauscher, A., Sedlacik, J., Fitzek, C., et al.: High resolution susceptibility weighted MR-imaging of brain tumors during the application of a gaseous agent. *Rofo* **177**, 1065–1069 (2005)
146. Kastrup, A., Li, T.Q., Takahashi, A., et al.: Functional magnetic resonance imaging of regional cerebral blood oxygenation changes during breath holding. *Stroke* **29**, 2641–2645 (1998)
147. Rostrup, E., Larsson, H.B., Toft, P.B., et al.: Functional MRI of CO<sub>2</sub> induced increase in cerebral perfusion. *NMR Biomed.* **7**, 29–34 (1994)
148. Li, T.Q., Kastrup, A., Takahashi, A.M., et al.: Functional MRI of human brain during breath holding by BOLD and FAIR techniques. *Neuroimage* **9**, 243–249 (1999)
149. Robinson, S.P., Rijken, P.F., Howe, F.A., et al.: Tumor vascular architecture and function evaluated by non-invasive susceptibility MRI methods and immunohistochemistry. *J. Magn. Reson. Imaging* **17**, 445–454 (2003)
150. Stillman, A.E., Hu, X., Jerosch-Herold, M.: Functional MRI of brain during breath holding at 4 T. *Magn. Reson. Imaging* **13**, 893–897 (1995)
151. Taylor, N.J., Baddeley, H., Goodchild, K.A., et al.: BOLD MRI of human tumor oxygenation during carbogen breathing. *J. Magn. Reson. Imaging* **14**, 156–163 (2001)
152. Vigue, B., Ract, C., Zlotine, N., et al.: Relationship between intracranial pressure, mild hypothermia and temperature-corrected PaCO<sub>2</sub> in patients with traumatic brain injury. *Intensive Care Med.* **26**, 722–728 (2000)
153. Liu, H.L., Huang, J.C., Wu, C.T., et al.: Detectability of blood oxygenation level-dependent signal changes during short breath hold duration. *Magn. Reson. Imaging* **20**, 643–648 (2002)
154. Hsu, Y.Y., Chang, C.N., Jung, S.M., et al.: Blood oxygenation level-dependent MRI of cerebral gliomas during breath holding. *J. Magn. Reson. Imaging* **19**, 160–167 (2004)
155. Hendler, T., Pianka, P., Sigal, M., et al.: Delineating gray and white matter involvement in brain lesions: three-dimensional alignment of functional magnetic resonance and diffusion-tensor imaging. *J. Neurosurg.* **99**, 1018–1027 (2003)
156. Parmar, H., Sitoh, Y.Y., Yeo, T.T.: Combined magnetic resonance tractography and functional magnetic resonance imaging in evaluation of brain tumors involving the motor system. *J. Comput. Assist. Tomogr.* **28**, 551–556 (2004)
157. Schonberg, T., Pianka, P., Hendler, T., et al.: Characterization of displaced white matter by brain tumors using combined DTI and fMRI. *Neuroimage* **30**, 1100–1111 (2006)
158. Ulmer, J.L., Salvan, C.V., Mueller, W.M., et al.: The role of diffusion tensor imaging in establishing the proximity of tumor borders to functional brain systems: implications for preoperative risk assessments and postoperative outcomes. *Technol. Cancer Res. Treat.* **3**, 567–576 (2004)
159. Cruz Jr., L.C., Sorensen, A.G.: Diffusion tensor magnetic resonance imaging of brain tumors. *Magn. Reson. Imaging Clin. N. Am.* **14**, 183–202 (2006)

160. Wiesemann, U.C., Symms, M.R., Parker, G.J., et al.: Diffusion tensor imaging demonstrates deviation of fibres in normal appearing white matter adjacent to a brain tumour. *J. Neurol. Neurosurg. Psychiatry* **68**, 501–503 (2000)
161. Witwer, B.P., Moftakhar, R., Hasan, K.M., et al.: Diffusion-tensor imaging of white matter tracts in patients with cerebral neoplasm. *J. Neurosurg.* **97**, 568–575 (2002)
162. Jellison, B.J., Field, A.S., Medow, J., et al.: Diffusion tensor imaging of cerebral white matter: a pictorial review of physics, fiber tract anatomy, and tumor imaging patterns. *AJNR Am. J. Neuroradiol.* **25**, 356–369 (2004)
163. Guye, M., Parker, G.J., Symms, M., et al.: Combined functional MRI and tractography to demonstrate the connectivity of the human primary motor cortex in vivo. *Neuroimage* **19**, 1349–1360 (2003)
164. Assaf, Y., Pasternak, O.: Diffusion tensor imaging (DTI)-based white matter mapping in brain research: a review. *J. Mol. Neurosci.* **34**, 51–61 (2008)
165. Kleiser, R., Staempfli, P., Valavanis, A., et al.: Impact of fMRI-guided advanced DTI fiber tracking techniques on their clinical applications in patients with brain tumors. *Neuroradiology* **52**, 37–46 (2010)
166. Pasternak, O., Sochen, N., Gur, Y., et al.: Free water elimination and mapping from diffusion MRI. *Magn. Reson. Med.* **62**, 717–730 (2009)
167. Chen, X., Weigel, D., Ganslandt, O., et al.: Prediction of visual field deficits by diffusion tensor imaging in temporal lobe epilepsy surgery. *Neuroimage* **45**, 286–297 (2009)
168. Taoka, T., Sakamoto, M., Nakagawa, H., et al.: Diffusion tensor tractography of the Meyer loop in cases of temporal lobe resection for temporal lobe epilepsy: correlation between postsurgical visual field defect and anterior limit of Meyer loop on tractography. *AJNR Am. J. Neuroradiol.* **29**, 1329–1334 (2008)
169. Smith, S.J.: EEG in the diagnosis, classification, and management of patients with epilepsy. *J. Neurol. Neurosurg. Psychiatry* **76**(suppl 2), ii2–ii7 (2005)
170. Benbadis, S.R., Tatum, W.O.: Overinterpretation of EEGs and misdiagnosis of epilepsy. *J. Clin. Neurophysiol.* **20**, 42–44 (2003)
171. Knake, S., et al.: The value of multichannel MEG and EEG in the presurgical evaluation of 70 epilepsy patients. *Epilepsy Res.* **69**, 80–86 (2006)
172. Stufflebeam, S.M., Tanaka, N., Ahlfors, S.P.: Clinical applications of magnetoencephalography. *Hum. Brain Mapp.* **30**, 1813–1823 (2009)
173. Ramantani, G., Boor, R., Paetau, R., et al.: MEG versus EEG: influence of background activity on interictal spike detection. *J. Clin. Neurophysiol.* **23**, 498–508 (2006)
174. de Jongh, A., de Munck, J.C., Goncalves, S.I., et al.: Differences in MEG/EEG epileptic spike yields explained by regional differences in signal-to-noise ratios. *J. Clin. Neurophysiol.* **22**, 153–158 (2005)
175. Barkley, G.L., Baumgartner, C.: MEG and EEG in epilepsy. *J. Clin. Neurophysiol.* **20**, 163–178 (2003)
176. Gotman, J., Benar, C.G., Dubeau, F.: Combining EEG and fMRI in epilepsy: methodological challenges and clinical results. *J. Clin. Neurophysiol.* **21**, 229–240 (2004)
177. Grova, C., Daunizeau, J., Kobayashi, E., et al.: Concordance between distributed EEG source localization and simultaneous EEG-fMRI studies of epileptic spikes. *Neuroimage* **39**, 755–774 (2008)
178. Salek-Haddadi, A., Diehl, B., Hamandi, K., et al.: Hemodynamic correlates of epileptiform discharges: an EEG-fMRI study of 63 patients with focal epilepsy. *Brain Res.* **1088**, 148–166 (2006)
179. Groening, K., Brodbeck, V., Moeller, F., et al.: Combination of EEG-fMRI and EEG source analysis improves interpretation of spike-associated activation networks in paediatric pharmacoresistant focal epilepsies. *Neuroimage* **46**, 827–833 (2009)
180. Vulliemoz, S., Thornton, R., Rodionov, R., et al.: The spatio-temporal mapping of epileptic networks: combination of EEG-fMRI and EEG source imaging. *Neuroimage* **46**, 834–843 (2009)

181. Zijlmans, M., Huiskamp, G., Hersevoort, M., et al.: EEG-fMRI in the preoperative work-up for epilepsy surgery. *Brain* **130**, 2343–2353 (2007)
182. Agirre-Arrizubietta, Z., Huiskamp, G.J., Ferrier, C.H., et al.: Interictal magnetoencephalography and the irritative zone in the electrocorticogram. *Brain* **132**, 3060–3071 (2009)
183. Shigeto, H., Morioka, T., Hisada, K., et al.: Feasibility and limitations of magnetoencephalographic detection of epileptic discharges: simultaneous recording of magnetic fields and electrocorticography. *Neurol. Res.* **24**, 531–536 (2002)

# Chapter 4

## Brain Tissue Mechanical Properties

Lynne E. Bilston

### 4.1 Introduction

The human brain is soft highly metabolically active tissue, floating in cerebrospinal fluid (CSF) within the rigid cranium. This environment acts to isolate the brain from the majority of external mechanical loads experienced by the head during normal daily life. The brain does experience a range of mechanical loads directly, as a result of blood and CSF flow, and to some extent, body posture. The dynamic balance of pulsatile hydrodynamic forces in the skull is maintained by blood and CSF flow into and out of the skull throughout the cardiac cycle (the Monroe-Kelly hypothesis), since the internal volume of the skull is constant. Reflex responses maintain blood flow during changes in posture and activity, so as to stabilize the mechanical and biochemical environment of the brain.

Brain tissue consists of white and gray matter, and different regions of the brain are made up of different proportions of white and gray matter. White matter is largely composed of myelinated axons of nerve fibers, while the gray matter is dominated by unmyelinated axons and cell bodies.

Since the brain is so well insulated from mechanical perturbations under normal circumstances, one might ask why it is important to understand the mechanical properties of brain tissue. While mechanical factors are thought to play a role in a range of conditions, including brain development [1], brain mechanics have been most commonly studied in attempt to understand conditions where loads are applied either directly or indirectly to the brain. Much of the early work on brain mechanics was focused on understanding the biomechanics of traumatic brain injury, where high loading rate motion of, or impacts to, the skull results in internal damage to the

---

L.E. Bilston (✉)

Neuroscience Research Australia and University of New South Wales,  
Randwick, Sydney, NSW 2031, Australia  
e-mail: L.Bilston@neura.edu.au

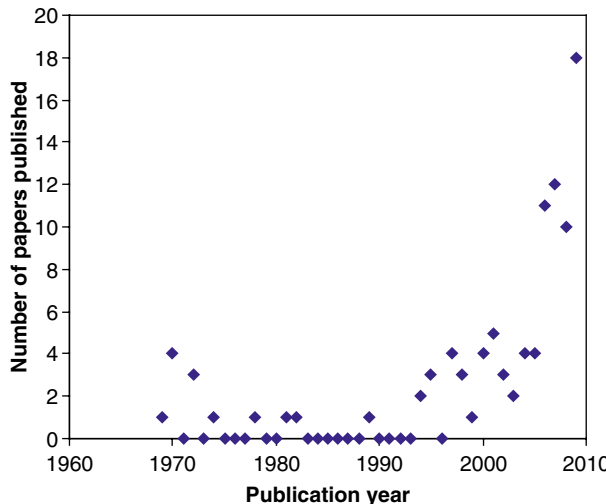


**Fig. 4.1** Number of peer-reviewed publications focused on brain tissue mechanical properties since the 1960s

brain. At the other end of the loading rate spectrum lie neurostructural conditions such as hydrocephalus, where very slow dilatation of the ventricles deep within the brain, often due to obstruction of a CSF outflow pathway, compresses the surrounding brain tissue. Either slow or fast loading can lead to neural injury and neurological and/or cognitive dysfunction. Brain tissue mechanical behavior has also been suggested to vary in some disease conditions [2–5], and non-invasive methods of measuring tissue properties *in vivo* could potentially be useful for discriminating between conditions that have similar symptoms and imaging appearance, but different treatment outcomes. An example of this is discriminating between normal pressure hydrocephalus, which responds well to surgical shunt placement, and cerebral atrophy due to other neurological disorders which does not [6, 7].

Another key driver for research aimed at understanding the fundamental biomechanical response of brain tissue is to provide high-quality experimental data to allow for development of mathematical and computational models of brain behavior. This includes development of accurate constitutive models of brain tissue behavior, relevant to the problem being studied, and also to allow finite element and other computational models to accurately simulate the brain response to complex loading conditions. Such simulations might include analysis of traumatic brain injury mechanisms and tissue injury thresholds, simulation of brain diseases that have a mechanical component (e.g. hydrocephalus), simulation of surgical procedures for surgical planning, or surgical training systems.

Brain tissue mechanics have become an increasing focus of research, as demonstrated by the number of peer-reviewed publications describing research aimed at measuring their properties (see Fig. 4.1 above).

In this chapter, the fundamental viscoelastic properties of brain tissue will be critically reviewed and limitations of the current state of knowledge and directions for future research will be identified.

## 4.2 Shear Properties of Brain Tissue

Interest in the shear response of brain tissue arose from early studies by Holbourn [8] who hypothesized that diffuse axonal damage seen in the brain parenchyma after traumatic brain injury occurred as a result of rotational shear within the brain. This was further substantiated in the 1980s by Thibault and Gennarelli's experimental work with non-human primates [9].

Methodological issues have played a major role in the apparently disparate shear properties reported for brain tissue in the literature, and only in the late 1990s did the rigor of rheology begin to be applied to measurement of shear properties of brain tissue. Much of the large disparity between previously reported data can be explained in the light of more rigorous approaches to control of sample preparation, test conditions, and the use of standard rheological test procedures. A key flaw of many early studies of shear properties in the literature was the (sometimes unstated) assumption of linear viscoelastic behavior, and therefore, flawed interpretation of large-amplitude oscillatory data. The appropriate approach is to first identify the linear viscoelastic limit for a tissue, conduct tests to characterize the linear viscoelastic response, and then conduct appropriate large-amplitude tests.

Shear response of a viscoelastic material is characterized in terms of the shear modulus, usually denoted by the symbol  $G$ . This quantity represents the unit stress response to a unit shear strain and is constant for a given frequency in linear viscoelastic materials. The relaxation shear modulus represents the temporal stress response to a unit shear strain and is typically denoted  $G(t)$ . The storage and loss moduli represent the elastic ( $G'$ ) and viscous ( $G''$ ) components of the linear viscoelastic shear modulus, respectively, and are a function of loading rate, often reported as frequency.

### 4.2.1 Linear Viscoelastic Properties

The traditional rheological approach to measuring viscoelastic properties of complex materials is to first establish the linear viscoelastic limit and characterize the material behavior at or below this limit. In the linear viscoelastic region, the stress generated is proportional to the strain applied, so that the shear modulus is constant.

#### 4.2.1.1 Oscillatory Loading

Oscillatory testing of tissues is most often carried out using parallel plate geometries, where one plate is fixed, while the other is moved sinusoidally parallel to the

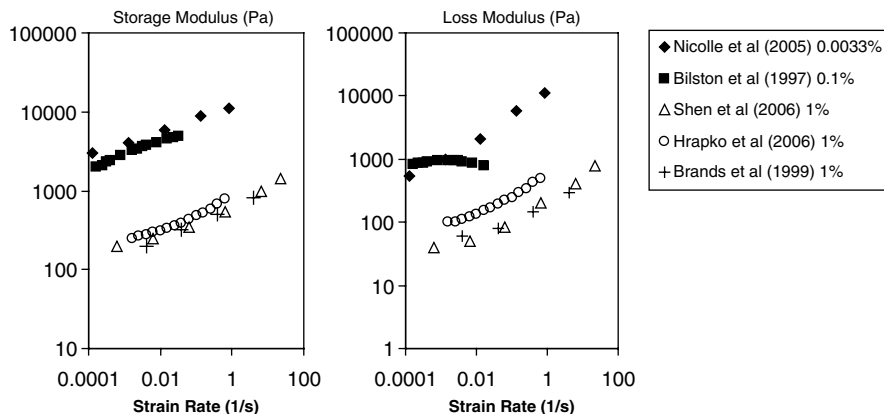


**Fig. 4.2** Linear viscoelastic shear moduli for brain tissue from ex vivo brain samples

fixed plate, while torque is recorded. Parallel plates are used because of the difficulty of cutting brain tissue samples to fit the cone-and-plate setup that is often used for viscoelastic fluids. The moving plate is typically either rotated about an axis perpendicular to the plates, as in traditional rotational rheometers, or moved linearly parallel to the fixed plate. Other methods have been used, including an eccentrically loaded sample in a rotational rheometry setup [10] and shear wave propagation methods such as magnetic resonance elastography (MRE) [11].

Oscillatory loading results are typically reported as the storage ( $G'$ ) and loss ( $G''$ ) moduli, which represent the elastic and viscous components of the dynamic shear modulus ( $G^* = G' + iG''$ ). The complex notation is used for the shear modulus to indicate that the stress associated with the viscous response is temporally out of phase with the elastic response and the input sinusoidal displacement (by  $\pi/2$ ).

Figure 4.2 above summarizes the data reported in the literature to be within the linear viscoelastic region [10, 12–15]. From this, it can be seen that brain tissue is a very soft solid, with a shear modulus of the order of a few kilopascals at physiological loading rates. The shear modulus increases in a power-law fashion with loading rate. This figure also shows reasonable consistency for both  $G'$  and  $G''$  measurements made at similar strains, but the studies which reported the linear viscoelastic regime to be at higher strains (e.g. 1%) report the brain to be softer than those who made measurements at lower strains. Since the brain exhibits shear thinning once the linear viscoelastic limit is exceeded, resulting in lower apparent shear moduli, it seems likely that the measurements made at larger strains are not, in fact, made within the linear viscoelastic regime, and this explains the discrepancy. The strain sweep data presented by Bilston et al. [12] indicate that between 0.1 and 1% strain the apparent storage modulus drops by approximately 40%, supporting this contention, and thus the data collected at 1% strain are likely not to be truly within the linear viscoelastic limit. The values reported by Bilston et al. [12] are also consistent with more recent in vivo elastography methods discussed below. The data of Shen et al. [15] were collected at long post-mortem times and are thus less likely to be reliable (see discussion below on methodological issues).

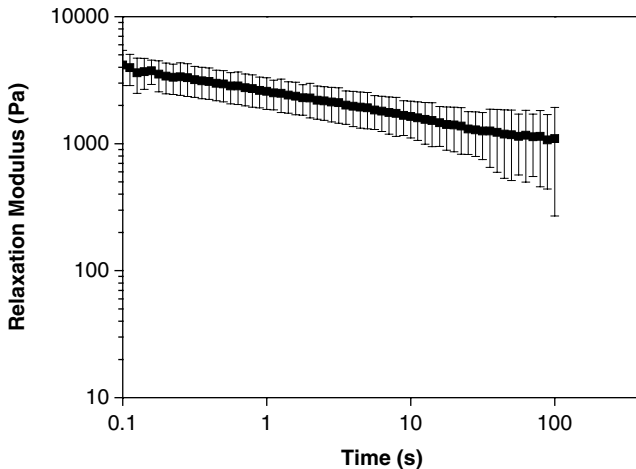


**Fig. 4.3** Linear viscoelastic relaxation modulus for brain tissue measured ex vivo (adapted from Bilston et al. [12])

Interestingly, the trend in strain-rate sensitivity is very similar for all test data, with a power-law increase of storage moduli with strain rate, where stress increases by an order of magnitude over approximately 5 decades of loading rate.

#### 4.2.1.2 Relaxation

The linear viscoelastic relaxation modulus for brain tissue has been measured less frequently than the oscillatory properties, at least partly because of the technical challenges in measuring these properties at very low strains. It is, however, quite important since the most commonly used non-linear models used to describe brain tissue rely on quasilinear viscoelastic theory (QLV, [16]), which has as a key requirement that the shape of the relaxation modulus be independent of strain. The only data set that is convincingly within the linear viscoelastic region is that of Bilston et al. [12], and the relaxation modulus is shown above in Fig. 4.3. Indeed, this data has been shown to be consistent with the small amplitude oscillatory data, since using it to predict the linear viscoelastic response gives results similar to the oscillatory data at 0.1% shown in Fig. 4.2 above (see Bilston et al. [12] for further details).

#### 4.2.1.3 Other Measurements

In recent years, researchers have attempted to use novel techniques to measure brain tissue properties, with a particular focus on those testing situations that are difficult to measure using traditional rheometry, such as very high loading rates and in vivo measurements.

One technique that has received significant recent attention is MRE, which relies on the relationship between the amplitude, wavelength, and velocity of propagating mechanical waves to extract linear viscoelastic properties of soft tissues. The MR scanner is used to image small amplitude vibration within the brain parenchyma, which is usually created by transmitting mechanical vibration (of frequency typically 15–100 Hz) to the skull. Mathematical analysis, involving localized inversion of the wave equation at each pixel in the image plane, allows estimation of the local wavelength. In the simplest implementation, this local wavelength is used to estimate the “elastic” shear modulus of the tissue, according to Muttupillai et al. [17]:

$$G = v^2 \lambda^2 \rho,$$

where  $v$  = frequency,  $\lambda$  = the local wavelength, and  $\rho$  = density.

More advanced implementations solve the full wave equation over the three-dimensional image domain. Some of these techniques use a correspondence principle approach, whereby the shear modulus is considered to be a complex quantity in the wave equation, allowing both the elastic and viscous components ( $G'$  and  $G''$  respectively) of the shear modulus to be extracted, if a sufficiently high signal-to-noise ratio is present in the image data. This relies on the attenuation of the propagating wave as it penetrates the brain parenchyma to estimate the viscous damping. The estimated shear moduli for healthy brain tissue that has been gathered using MRE, while not as widely varying as some of the early ex vivo brain data, are nevertheless somewhat variable, due in large part to the different analytical approaches taken to estimating the elastic and/or viscoelastic properties, and data quality (Fig. 4.4).

Vappou et al. [18] have published a direct comparison of rheometry data on ex vivo brain tissue with MRE measurements, but it is difficult to draw direct conclusions since their testing frequencies did not overlap for the two methods, their MRE shear moduli were estimated from a simple wavelength based formula rather than full inversion of the wave equation, and their rheometry testing was conducted at a shear strain of 0.5%, which the above discussion suggests may have been beyond the linear viscoelastic limit and thus have underestimated the shear modulus. Further rigorous validation of MRE is required before the absolute values estimated from this technique can be considered quantitatively reliable or results from different analytical techniques can be compared.

Despite these issues, MRE has great promise as a relatively non-invasive method of measuring in vivo human tissue properties. It may be useful for determining how brain mechanics might be affected by age and brain diseases, which is impossible using other more traditional techniques.

Ultrasound has also been used to estimate brain tissue properties, in the linear viscoelastic (small amplitude) range. Lippert et al. [19] used the “wave in a tube” technique, where a sample is placed in a tube and an ultrasonic (100 kHz–10 MHz) wave passed through the sample. By measuring this wave propagation, the wave speed in the tube is estimated and the linear viscoelastic shear modulus ( $G^*$ ) extracted. Lippert et al. [19] estimated the shear modulus for juvenile ovine brain tissue samples to be in the range of 140–400 MPa, where the larger values are

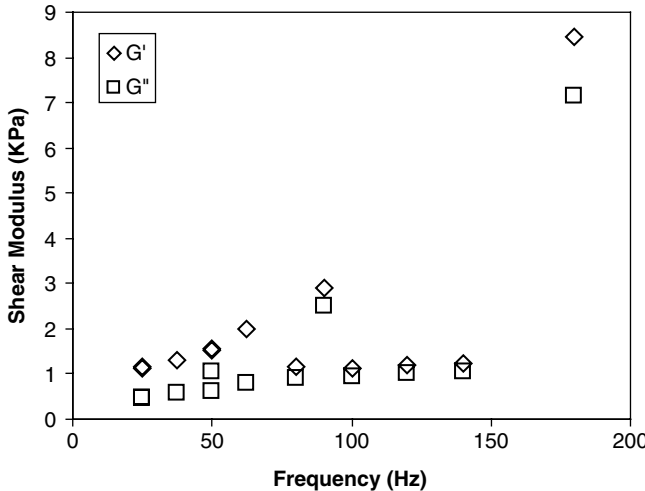


**Fig. 4.4** Brain shear modulus measurements made using MR elastography

associated with the higher frequencies. These values are orders of magnitude larger than values from lower frequencies, and somewhat higher than simple extrapolation of the power-law behavior measured at lower frequencies (e.g. the data shown above in Fig. 4.2) would predict. Atay et al. [20] measured mouse brain shear modulus using MR elastography at an intermediate frequency of 1 kHz, obtaining values of approximately 10–15 kPa, still well below the values obtained by high frequency ultrasound.

In summary, the linear viscoelastic properties of brain tissue, while a fundamental stepping stone for understanding the more complex non-linear properties, have been measured using reliable techniques in only a small number of studies and methodologically flawed data sets are common. There is still room for more robust characterisation of these properties under a wider range of loading conditions, including further cross-validation of data from one testing mode against another (e.g. oscillation vs. relaxation). The latter has rarely been done (e.g. see Bilston et al. [12]) and would create greater confidence in the quality and reliability of the data.

#### 4.2.2 Non-linear Viscoelastic Properties

Most soft biological tissues are thought to be non-linearly viscoelastic at moderate-to-large amplitudes of loading [16]. Non-linear viscoelastic materials require more complex mechanical testing protocols in order to characterize the behavior of the

material, in order to ascertain how the properties change with loading type, loading amplitude, and loading rate. Brain tissue has a very low linear viscoelastic limit, rendering it non-linearly viscoelastic at most strains of practical interest.

#### 4.2.2.1 Oscillatory Response

While there are several reports of oscillatory response of brain tissue in the literature [13, 21–23], most of these have interpreted data without proper analysis of the non-linear viscoelastic effects and are thus of questionable validity. The key problem is that in the non-linear viscoelastic regime, the shear modulus is a function of strain, and not independent of strain as it is within the linear viscoelastic regime. In the case of brain tissue, there is substantial shear thinning at strains beyond the linear viscoelastic regime, and the shear modulus estimated from larger amplitude test data can be significantly underestimated (as discussed above). Oscillatory tests at large amplitude require analysis of the full loading and unloading cycle, which is non-sinusoidal at large amplitudes, and thus the simple calculation of  $G'$  and  $G''$  from the phase difference between the peak torque and the peak shear strain is no longer valid. In addition, the decomposition of the complex modulus into the storage and loss modulus is typically based on the phase difference between the peak input shear strain and the peak torque generated. If the torque signal is non-sinusoidal, decomposition of the shear modulus based on this method will give erroneous values. Newer rheometers have the capacity to measure the full loading cycle, and thus more rheologically rigorous methodologies can, and should, be applied to study oscillatory loading of brain tissue, to better characterize not only the fully non-linear behavior, but also the transition regime between 0.1 and 1% strain just above the linear viscoelastic limit.

#### 4.2.2.2 Relaxation

Beyond the linear viscoelastic regime, the relaxation modulus for brain tissue decreases with applied shear strain (see data from the literature [12, 13, 15, 21, 24, 25] summarized in Fig. 4.5). This is consistent with the shear thinning seen in the oscillatory data noted above. Relaxation in brain tissue ex vivo appears to continue over the whole time period that has been measured to date, and while there are some minor differences in the shape of the relaxation curve at the early and later parts of the curves, there is moderate consistency of the approximate shape across much of the data. Note that the shape of the early part of the relaxation curve can be affected by the loading rate used for the initial “step,” which can never be instantaneous in practice [26]. At longer times, tests may be affected by post-mortem tissue changes, including degradation and/or dehydration. This is more marked at low strains where the torques are near the resolution of the test instrument and may explain some of the differences in shape in the relaxation curves at long times.

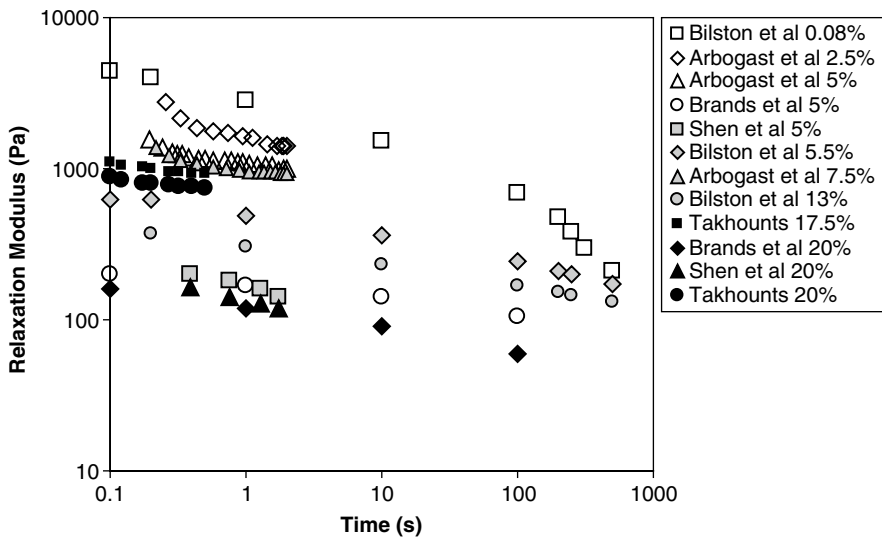


**Fig. 4.5** Relaxation modulus for brain tissue in shear

#### 4.2.2.3 Constant Loading Rate

Shear tests analogous to the traditional engineering tensile tests, aimed at constructing a stress-strain curve, have also been conducted by several researchers over a wide range of loading rates. These tests demonstrate the non-linear response of brain tissue, and almost all test series have shown a clear increase in apparent stiffness with increasing loading rate. Failure or tissue yield in shear appears to begin at approximately 100–200% strain at low-to-moderate loading rates, according to Bilston et al. [24]. This is significantly higher strain than brain can withstand in tension and compression (see below). Few constant shear rate tests in the literature have had inertia corrections applied to the data, and at high loading rates, the sample inertia may contribute to the recorded load. Data from the literature [10, 24, 27] are summarized in Fig. 4.6.

#### 4.2.2.4 Other Test Types

In rheological studies of polymers, it is standard practice to further characterize complex fluids and soft solids using combination and multi-step loading histories, such as multiple steps, including those in opposite directions. This has rarely been done in the study of brain tissue and would likely provide significant new information that would help in developing and establishing the validity of constitutive models for brain tissue.

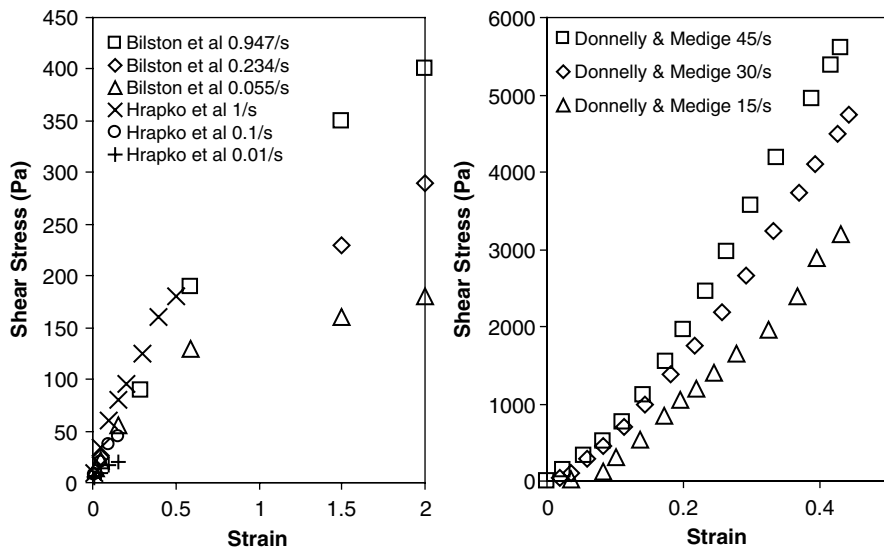


**Fig. 4.6** Constant shear rate test data for brain tissue at low-to-moderate loading rates (*left*) and high (*right*) loading rates

### 4.3 Compressive Properties of Brain Tissue

The earliest data for compressive properties of brain tissue are those of Estes and McElhaney [28], who compressed rhesus and human brain tissue to large strains over a broad range of loading rates. They found that brain tissue was notably strain-rate sensitive, with increasing stiffness at higher loading rates, and increasing stiffness with applied strain, resulting in a concave upward non-linear stress-strain curve (see Fig. 4.7 below). Miller and Chinzei [29] conducted compressive tests at lower strain rates and obtained similar qualitative results, although their data showed lower stresses for similar strains and strain rates. Cheng and Bilston [30] recently conducted compression tests of brain at very low strain rates, with similar stress-strain responses to those of Chinzei and Miller. Data from these tests are shown in Fig. 4.7 below. Tamura et al. [31] conducted moderate-to-high rate compression tests, and their data lie somewhat below that of Estes and McElhaney, suggesting the long post-mortem time used for Estes and McElhaney's work may have affected their results. Most recently, Pervin and Chen [32] conducted both quasistatic and high loading rate tests of brain tissue in compression, using a modified Hopkinson split bar technique, again confirming brain's strong strain-rate sensitivity. Their data, collected at 1,000–3,000/s from very fresh samples, lie well above those of Estes and McElhaney (an order of magnitude higher at 1,000/s, not shown below), which suggests that the strain-rate sensitivity does not disappear, even at very high loading rates. Neither studies considered inertial effects, which can be expected to be significant. Data are reported for peak strains up to 30–50% in compression, suggesting this is the onset of failure.

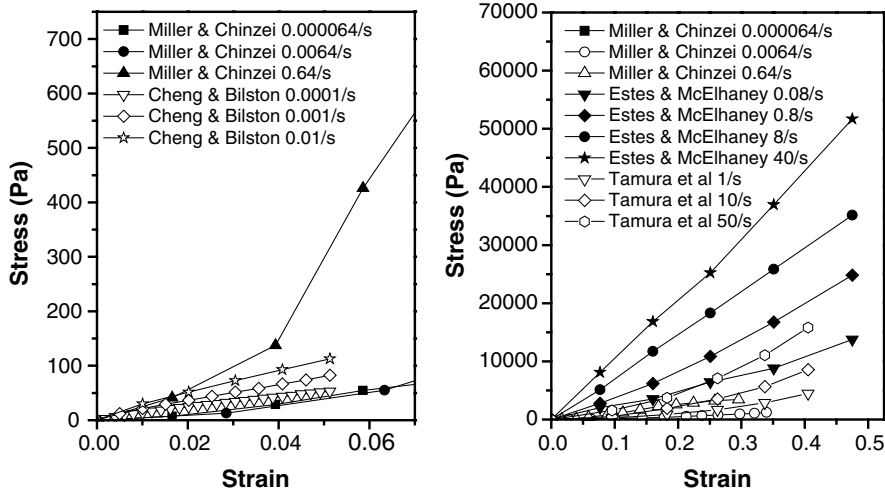


**Fig. 4.7** Compressive properties of brain tissue at low-to-moderate loading rates (*left*) and moderate-to-high loading rates (*right*)

Traditional rheological test protocols have rarely been applied to compression testing, and thus the linear viscoelastic properties of brain in compression have not been ascertained. Fallenstein et al. used sinusoidal indentation tests in the live macaque brain and showed that for very small indentations (25  $\mu\text{m}$ ) the force response was sinusoidal, suggesting linear response, but for larger indentations (300  $\mu\text{m}$ ) the responses were non-sinusoidal. The linear limit may lie between these two, but the local strain field is difficult to estimate, especially since the pia mater was intact underneath the probe, and thus these data do not give a clear value for the compressive linear viscoelastic strain limit, although it is likely to be quite low. Miller et al. [33] indented porcine brain *in vivo*, using a finite element model to extract parameters for a hyper-viscoelastic constitutive model.

Relaxation moduli in compression at large strains have been reported in a small number of studies [30, 31]. Cheng and Bilston [30] found that the relaxation response was relatively independent of loading rate, after the short period after the initial ramp (see Fig. 4.8 below). Tamura et al. [31] found a consistent reduced relaxation modulus over a range of large strains (20–70%).

Compressive properties have also been considered in the context of brain tissue being a fluid-saturated two-phase material. The main application of this type of modeling has been in the study of hydrocephalus. The simpler biphasic or poroelastic models, similar to those developed for modeling soils, assume a linear elastic tissue matrix saturated with an inviscid (or alternatively a Newtonian) fluid. This gives rise to flow through the interstitial spaces of the tissue according to Darcy's Law, coupled to linear elastic deformation.

Conducting the traditional soil consolidation tests on brain tissue samples has been said to be technically challenging [30] and thus unconfined compression data are often used to estimate the properties. Chinzei and Miller [34] showed that a simple

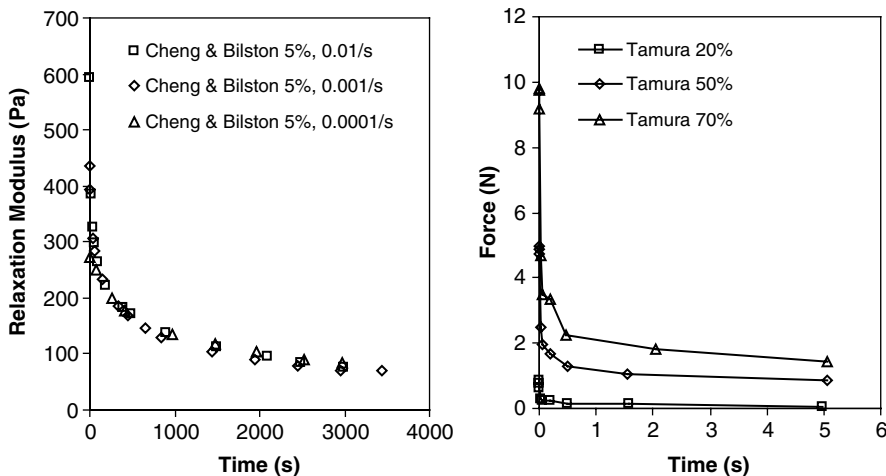


**Fig. 4.8** Compressive relaxation data for brain tissue

poroelastic model is not able to simulate the strain-rate sensitivity observed in brain tissue. That group have also published information on methodological issues with such multiphase models and for specific applications such as hydrocephalus [35, 36]. Cheng and Bilston [30] used a poroviscoelastic model for brain tissue to model their compressive data at low loading rates. There is a wide range of values approximately 3–4 orders of magnitude reported for the hydraulic conductivity of brain tissue in the literature ( $2 \times 10^{-10}$  to  $4 \times 10^{-7}$  m/s) [30, 37, 38], of which very few are based on definitive experimental work (e.g. Cheng and Bilston [30] who reported  $4.0 \times 10^{-7}$  m/s), and further research is needed to accurately characterize these parameters.

#### 4.4 Tensile Properties of Brain Tissue

Brain tissue properties in tension are less well characterized than those in other loading modes, with only a couple of studies reporting tensile properties. This is at least in part due to the difficulties of conducting these tests, particularly in gripping samples effectively. General observations of the behavior of brain tissue in tension are that it appears to soften with increasing strain, and exhibits a strain-rate sensitivity that is consistent with the response in other loading modes, that is, increasing apparent stiffness with increasing loading rate. Figure 4.9 below shows some of the data from the literature [39, 40]. Failure limits in tension are not well characterized, but appear to be in the range of 20–60% strain.

More recently, Schiavone et al. [41] have used an aspiration method to measure in vivo brain deformation with tensile loading at the surface intraoperatively on a human patient. They used a simplified finite element model to estimate hyperelastic parameters for that patient.

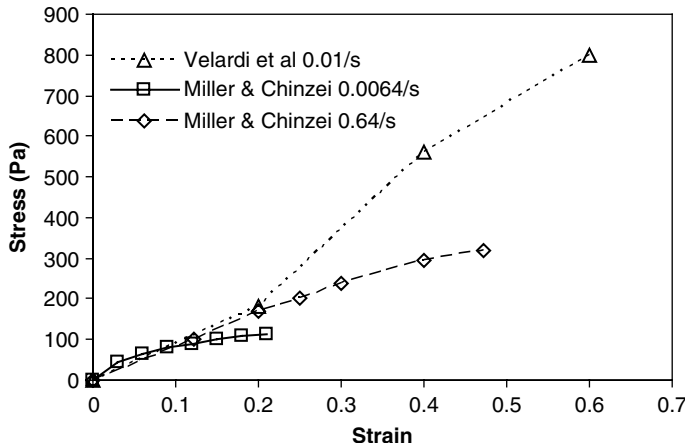


**Fig. 4.9** Tensile properties of brain tissue

## 4.5 Constitutive Models for Brain Tissue

As can be seen from the previous sections on brain tissue mechanical response, capturing the mechanical response of brain tissue in three dimensions over a broad range of loading types and loading rates is a very challenging task. The ideal constitutive equation would be able to model the shear, compressive, and tensile response of brain tissue, within the loading rate regime of interest for a particular study. There have been many studies that have developed constitutive equations for specific aspects of brain mechanical response, but few that have been widely used beyond the original description of test data. To date, there is no widely accepted constitutive model for brain tissue that is able to match the full spectrum of the strongly strain-rate sensitive, non-linearly viscoelastic behavior of brain tissue.

The most commonly used constitutive models used for computational calculations are based on quasilinear viscoelastic (QLV) theory (see Fung [16] for full discussion of this theory). These typically use a hyperelastic model to describe the non-linear elasticity, combined with a linear viscoelastic relaxation modulus to describe the time-dependent behavior.

Hyperelastic models were originally developed to describe the non-linear elastic behavior of rubbers. They use the concept of a strain energy potential function, from which the relationship between stress and strain tensors is derived. The strain energy function,  $W$ , is usually defined in terms of the invariants ( $I_1, I_2, I_3$ ) of the strain tensor,  $S$ , which is itself defined by the deformation gradient tensor,  $F$ . If a material is incompressible, the third strain invariant is unity, and the strain energy function is only a function of the first two invariants. The stress-strain relationship is then obtained from a partial derivative of the strain energy potential with respect to  $F$ . Depending on the choice of the strain energy potential, the particular stress and strain tensors used, and the invariants that the definition uses, this derivation can

become algebraically complex and the reader is referred to solid mechanics texts for further details. Common hyperelastic models include those that use strain energy functions that are polynomial functions of the invariants, such as the Mooney-Rivlin model and the Ogden model, which uses a strain energy function defined in terms of the principal stretch ratios occurring in a material. The Mooney-Rivlin model for an incompressible material defines the strain energy potential in terms of the material parameters,  $\mu_i$ , as:

$$W = \frac{\mu_1}{2}(I_1 - 3) + \frac{\mu_2}{2}(I_2 - 3). \quad (4.1)$$

The Ogden model defines the strain energy potential in terms of the material parameters,  $\mu_i$  and  $\alpha_i$ , and the principal stretch ratios,  $\lambda_i$ , as:

$$W = \sum_N \frac{2\mu_i}{\alpha_i^2} (\lambda_1^{\alpha_i} + \lambda_2^{\alpha_i} + \lambda_3^{\alpha_i} - 3). \quad (4.2)$$

The viscous or time-dependent behavior is often modeled as the sum of a series of Maxwell elements, so that the relaxation modulus is given by:

$$G(t) = \sum_N G_i e^{-t/\tau_i}. \quad (4.3)$$

One example of a model in this class is that of Miller and Chinzei [39], which is often used for neurosurgical modeling. This is based on the combination of an Ogden-like hyperelastic model and a Prony-series relaxation modulus, defined by (4.4) and (4.5):

$$W = \frac{2}{\alpha^2} \int_0^t [\mu(t-\tau) \frac{d}{d\tau} (\lambda_1^\alpha + \lambda_2^\alpha + \lambda_3^\alpha - 3)] d\tau \quad (4.4)$$

$$\mu = \mu_0 \left[ 1 - \sum_{k=1}^n g_k \left( 1 - e^{-(t/\tau_k)} \right) \right]. \quad (4.5)$$

Values for the material constants,  $\alpha$ , and the Prony-series coefficients suitable for modeling of surgical procedures are given in Miller and Chinzei [39]. The model has been based on tension and compression data from animals, and it has not yet been validated for human brain, or for shear loading.

Other models use rate-dependent viscosity, such as the Carreau model [24] or Ellis model [10]. The stress is then given by:

$$S(t) = \int_{-\infty}^t G(t-s) \frac{\partial T}{\partial s} ds, \quad (4.6)$$

where  $T$  is the elastic stress-strain function derived from the strain energy potential.

Use of this class of model assumes that the time-dependent behavior can be separated from the non-linear elastic behavior, an assumption that is not universally supported by experimental data [24]. Nevertheless, the errors introduced by deviation from such assumptions are probably less than the variation seen in the reported experimental data, as noted above.

Other researchers have developed, and implemented into finite element simulation software, more complex rheological models, including fully non-linear models in which strain-time separability is not assumed and that capture some of the yield behavior at large strains [15, 24].

The most appropriate constitutive model used to describe brain tissue will depend heavily on the topic of interest. Neurosurgical simulation not including cutting procedures has been shown to require a suitable large-deformation framework, but is not sensitive to the specific constitutive model used [42]. Modeling of hydrocephalus may be done with single-phase models if the fluid distribution in the brain is not of particular interest [43], but also with a suitable poroviscoelastic models with appropriate large-deformation formulation [30, 44]. Injury simulations are often done with simpler constitutive models due to the high computational demands of large 3D explicit simulations, despite their limitations. These include linear viscoelastic models [45, 46] as well as hyperelastic models, with or without the viscous component [47, 48].

## 4.6 Discussion

### 4.6.1 *Mechanical Characteristics of Brain Tissue*

Decades of research on brain tissue mechanics has established that brain tissue is a very soft, non-linearly viscoelastic solid material, with a very low linear viscoelastic strain limit, of the order of 0.1–0.3%. Brain tissue is strain-rate sensitive, with increasing stiffness with increasing strain rate. Failure occurs at moderate strains, of the order of 25–100%, depending on the loading type.

However, there is still much that is either not yet known about brain tissue mechanics or the subject of debate, due to inconsistent or contradictory data in the literature. Some of the reasons for these inconsistencies are discussed below.

Despite the well-defined structural anisotropy of white matter arising from the axonal fiber bundles, mechanical anisotropy has not been comprehensively established. Some studies suggest that there is moderate mechanical anisotropy in white matter under shear, with the axonal fiber direction up to twice as stiff as the perpendicular direction [21, 49] and in tension [40], while others have not found significant mechanical anisotropy in compression [32].

Regional variations in tissue properties across the brain have been suggested by some studies [21, 49, 50], although the differences are not large, and some of these studies suffer from methodological problems.

Like most very soft hydrated tissues, brain tissue is usually assumed to be incompressible, or nearly incompressible, due to its very high water content [29, 51]. There have been few studies that have directly examined this assumption, and its validity almost certainly depends on the mechanical process of interest. In very slow processes involving displacement of interstitial fluid within the brain parenchyma, such as hydrocephalus or mass lesions in the brain involving brain edema, this assumption may not be valid, as there is time for fluid to move within the brain tissue and regions could locally appear compressible due to fluid transfer. For processes at shorter time scales, there is no evidence that brain tissue is significantly compressible, at least at macroscopic length scales. Indeed, Franceschini et al. [37] report that the undrained (i.e. whole tissue) Poisson's ratio for brain tissue is 0.5, while the "drained" compressibility is 0.496, lending credence to the incompressibility assumption.

Age dependence of brain tissue properties has also been described in a small number of studies. Prange and Margulies [49] suggested neonatal brain tissue is stiffer than in adults, as did Gefen and Margulies [52]. Sack et al. [53] found that brain tissue shear modulus decreases with age from early adulthood to old age, using MR elastography *in vivo*. The latter study also observed a small difference between females and males, with female brain tissue being marginally stiffer. On the other hand, Thibault and Margulies [54] found that shear modulus of the brain was significantly greater for adult brain tissue than neonatal tissue. It is fair to say that this issue is not yet settled and methodologically robust studies are required.

Differences between measured properties of brain tissue *in vivo* and *ex vivo* have been debated for decades. Some studies show significant drops *in situ* immediately after death [23, 55, 56]. Weaver et al. attributed this change to drops in interstitial and cerebral perfusion pressure. Others show an increase in shear modulus beyond 6 h for samples tested *ex vivo* [57], while indentation tests have shown no effect on overall stiffness when comparing *in vivo* to *in situ*, but decreases in shear modulus *ex vivo* (within 6 h of death) compared to *in vivo* and *in situ* [58]. It seems likely on the basis of this data that there are drops in apparent tissue stiffness immediately after death and possibly increases at longer times post-mortem. Since the *ex vivo* studies in the literature have used a range of times after death up to days, this may be a significant factor in differences in reported data and such data should be viewed with caution.

Few studies have directly compared different species under the same testing protocols. The studies that have been done show that properties are similar, at least between human and porcine brains [54] and human and rhesus monkey [28].

#### 4.6.2 *Methodological Considerations*

As mentioned throughout the above sections, characterisation of brain tissue properties has been plagued by differences in results arising from differences in test methods. These differences fall into three main categories – sample preparation, post-mortem time, and testing conditions.

The issue of post-mortem time is discussed in the previous sections above, but it is likely that much of the data in the literature conducted at long times after death are of limited value due to significant changes in tissue properties post-mortem.

Sample preparation has received less attention, but it is also of importance. Delicate brain tissue is easily dehydrated and is also subject to osmotic swelling if bathed in fluids with inappropriate osmotic content [24]. Despite this, a range of bathing fluids have been used, including PBS [57], simple saline [27], and silicon oil [15] in addition to artificial CSF [24], which has a similar osmotic content to CSF. Ensuring that the sample has suitable dimensions to minimize the influence of edge effects, slip at gripping surfaces, or test platens, sample inertial effects at high loading rates is also essential. These issues are often not fully considered in published studies. Liu [59] showed that sample thickness affects measured shear moduli in a parallel plate configuration and similar results were observed by Garo et al. [57].

Sample preconditioning processes have not been studied in detail in brain tissue, although several studies have noted the effects of previous strain loading cycles on subsequent measured data. Gefen and Margulies discuss this in some detail [58]. A recent study in spinal cord tissue suggests that the amplitude of the preconditioning has a strong effect on the subsequently measured properties [60], and more recent unpublished data from our laboratory also suggest preconditioning strain rate can also alter subsequently measured properties.

It must be remembered here that the properties of prime interest are the *in vivo* properties of human brain tissue. It is only very recently that it has been possible to measure human brain properties *in vivo*, using MR elastography, and then only at very small deformations, corresponding to the linear viscoelastic regime. Response of brain tissue *in vivo* at larger deformations must be inferred from a combination of *ex vivo* tests and animal *in vivo* tests. This brings with it much uncertainty about how to extrapolate the available *ex vivo* data and animal *in vivo* results to the *in vivo* human brain.

## 4.7 Future Directions

It is clear from the discussion above that while we have made great strides in characterizing the mechanical properties of brain tissue, there is still much to be done. Consistent datasets for different loading regimes, such as shear, compression, and tension, are still not readily available. Data for complex loading histories, such as multiple step loading and step reversals which have been found to be useful in developing and testing accurate constitutive models for other complex non-linearly viscoelastic materials, are highly desirable. It is essential that such data be collected with full consideration of the methodological issues noted above.

Use of more rigorous rheological testing protocols in compression and testing may allow for more definitive determination of the true linear viscoelastic limit for brain tissue. The collection of data through the full loading and unloading cycle in oscillatory testing may also assist in all test modes.

The other key gap in the body of knowledge regarding brain tissue is integration of data from different loading types – particularly reconciling shear, compression, and tensile loading data. To date, this is not possible because data that have been collected in different testing modes come from different species, and have been subject to different loading regimes (strains, strain rates), been subject to different preparation methods, and been tested at different post-mortem times. There is a clear need for multi-modal data (shear, compression, tension, and combination loading) to be collected using robust rheological techniques so that reliable constitutive models can be developed and validated across all loading types.

Definitive conclusions about the effect of tissue perfusion pressure on the properties of brain tissue would be valuable in determining what corrections (if any) are required to adapt *ex vivo* data to predict *in vivo* brain response. Further *in vivo* measurements, of both linear viscoelastic (e.g. using MR elastography or similar methods) and large deformation measurements (e.g. by indentation, aspiration, or other methods), are needed.

Brain mechanics at high loading rates still requires more study, including separating out tissue inertial effects from inherent tissue viscoelasticity. At low loading rates, high-quality quantitative data on interstitial fluid flow in the brain, as is thought to be relevant for diseases such as hydrocephalus, are still lacking.

The use of easily interpretable constitutive models may also assist the field of brain tissue mechanics. While some mechanical properties have intrinsic definitions that are interpretable without reference to a constitutive model, such as the linear viscoelastic moduli, other parameters that are widely reported, often incorrectly, to describe tissue properties beyond this linear range are parameters within constitutive models, with their own inherent assumptions. Given the complexity and strong non-linearity of brain tissue mechanical response, it is unrealistic to expect that one constitutive model will fit all circumstances, and those who wish to describe brain tissue properties in a given context will need to select and use a model that can capture the features of brain tissue mechanics within the relevant loading regime. A model that works for quasistatic brain deformation during surgery will likely not be suitable for high velocity impact loading, for example.

## 4.8 Conclusions

While interest in brain tissue mechanics is enjoying a resurgence of late, and much data have been collected to characterize the response of brain tissue to mechanical loading, there is still much to be done to rigorously characterize this complex material. New developments in measuring techniques, however, have great potential for non-invasively measuring tissue properties *in vivo*, which may allow these properties to be used for diagnostic purposes, as well as shedding light on how this complex organ responds to loads, be they due to dynamic processes that lead to traumatic brain injury, or slow processes involved in neurological diseases such as brain tumors or hydrocephalus.

**Acknowledgements** Lynne Bilston is supported by an NHMRC Senior Research Fellowship. She would like to thank Dr Shaokoon Cheng for useful discussions and also for assistance with preparing figures for this chapter.

## References

1. Geng, G., Johnston, L.A., Yan, E., et al.: Biomechanisms for modelling cerebral cortical folding. *Med. Image Anal.* **13**, 920–930 (2009)
2. McHedlishvili, G., Itkis, M., Sikharulidze, N.: Mechanical properties of brain tissue related to oedema development in rabbits. *Acta Neurochir.* **96**, 137–140 (1989)
3. Pang, D., Altschuler, E.: Low-pressure hydrocephalic state and viscoelastic alterations in the brain. *Neurosurgery* **35**, 643–655 (1994). discussion 655–656
4. Kuroiwa, T., Yamada, I., Katsumata, N., et al.: Ex vivo measurement of brain tissue viscoelasticity in postischemic brain edema. *Acta Neurochir. Suppl.* **96**, 254–257 (2006)
5. Xu, L., Lin, Y., Han, J.C., et al.: Magnetic resonance elastography of brain tumors: preliminary results. *Acta Radiol.* **48**, 327–330 (2007)
6. Mase, M., Miyati, T., Kasai, H., et al.: Noninvasive estimation of intracranial compliance in idiopathic NPH using MRI. *Acta Neurochir. Suppl.* **102**, 115–118 (2008)
7. Tarnaris, A., Kitchen, N.D., Watkins, L.D.: Noninvasive biomarkers in normal pressure hydrocephalus: evidence for the role of neuroimaging. *J. Neurosurg.* **110**, 837–851 (2009)
8. Holbourn, A.: The mechanics of brain injury. *Br. Med. Bull.* **3**, 147–149 (1945)
9. Gennarelli, T.A., Thibault, L.E., Adams, J.H., et al.: Diffuse axonal injury and traumatic coma in the primate. *Ann. Neurol.* **12**, 564–574 (1982)
10. Hrapko, M., van Dommelen, J.A.W., Peters, G.W.M., et al.: The mechanical behaviour of brain tissue: large strain response and constitutive modelling. *Biorheology* **43**, 623–636 (2006)
11. Green, M.A., Bilston, L.E., Sinkus, R.: In vivo brain viscoelastic properties measured by magnetic resonance elastography. *NMR Biomed.* **21**, 755–764 (2008)
12. Bilston, L.E., Liu, Z., Phan-Thien, N.: Linear viscoelastic properties of bovine brain tissue in shear. *Biorheology* **34**, 377–385 (1997)
13. Brands, D.W.A., Bovendeerd, P.H.M., Peters, G.W.M., et al.: The large shear strain dynamic behaviour of in vitro porcine brain tissue and a silicone gel model material. *Proceedings of Stapp Car Crash Conference*: SAE, pp. 249–260 (2000)
14. Nicolle, S., Lounis, M., Willinger, R., et al.: Shear linear behavior of brain tissue over a large frequency range. *Biorheology* **42**, 209–223 (2005)
15. Shen, F., Tay, T.E., Li, J.Z., et al.: Modified Bilston nonlinear viscoelastic model for finite element head injury studies. *J. Biomech. Eng.* **128**, 797–801 (2006)
16. Fung, Y.C.: *Biomechanics: Mechanical Properties of Living Tissues*, 2nd edn. Springer, New York (1993)
17. Muthupillai, R., Lomas, D.J., Rossman, P.J., et al.: Magnetic resonance elastography by direct visualization of propagating acoustic strain waves. *Science* **269**, 1854–1857 (1995)
18. Vappou, J., Breton, E., Choquet, P., et al.: Magnetic resonance elastography compared with rotational rheometry for in vitro brain tissue viscoelasticity measurement. *Magn. Reson. Mater. Phys., Biol. Med.* **20**, 273–278 (2007)
19. Lippert, S.A., Rang, E.M., Grimm, M.J.: The high frequency properties of brain tissue. *Biorheology* **41**, 681–691 (2004)
20. Atay, S.M., Kroenke, C.D., Sabet, A., et al.: Measurement of the dynamic shear modulus of mouse brain tissue in vivo by magnetic resonance elastography. *J. Biomech. Eng.* **130**, 021013 (2008)
21. Arbogast, K.B., Meaney, D.F., Thibault, L.E.: Biomechanical characterization of the constitutive relationship for the brainstem. In: *Proceedings of Proceedings of the 39th Stapp Car Crash Conference*; Coronado, CA: SAE, pp. 153–159 (1995)

22. Darvish, K.K., Crandall, J.R.: Nonlinear viscoelastic effects in oscillatory shear deformation of brain tissue. *Med. Eng. Phys.* **23**, 633–645 (2001)
23. Fallenstein, G.T., Hulce, V.D., Melvin, J.W.: Dynamic mechanical properties of human brain tissue. *J. Biomech.* **2**, 217–226 (1969)
24. Bilston, L.E., Liu, Z., Phan-Thien, N.: Large strain behaviour of brain tissue in shear: some experimental data and differential constitutive model. *Biorheology* **38**, 335–345 (2001)
25. Takhounts, E., Crandall, J.R., Darvish, K.: On the importance of nonlinearity of brain tissue under large deformations. *Stapp Car Crash J.* **47**, 79–92 (2003)
26. Ferry, J.: *Viscoelastic Properties of Polymers*. Wiley, New York (1980)
27. Donnelly, B.R., Medige, J.: Shear properties of human brain tissue. *J. Biomech. Eng.* **119**, 423–432 (1997)
28. Estes, M.S., McElhaney, J.H.: Response of brain tissue to compressive loading. ASME Paper 70-BHF-13 (1970)
29. Miller, K., Chinzei, K.: Constitutive modelling of brain tissue: experiment and theory. *J. Biomech.* **30**, 1115–1121 (1997)
30. Cheng, S., Bilston, L.E.: Unconfined compression of white matter. *J. Biomech.* **40**, 117–124 (2007)
31. Tamura, A., Hayashi, S., Watanabe, I., et al.: Mechanical characterization of brain tissue in high-rate compression. *J. Biomech. Sci. Eng.* **2**, 115–126 (2007)
32. Pervin, F., Chen, W.W.: Dynamic mechanical response of bovine gray matter and white matter brain tissues under compression. *J. Biomech.* **42**, 731–735 (2009)
33. Miller, K., Chinzei, K., Orssengo, G., et al.: Mechanical properties of brain tissue in-vivo: experiment and computer simulation. *J. Biomech.* **33**, 1369–1376 (2000)
34. Chinzei, K., Miller, K.: Compression of swine brain tissue: experiment in vitro. *J. Mech. Eng. Lab.* **50**, 106–115 (1996)
35. Miller, K.: Modelling soft tissue using biphasic theory – a word of caution. *Comput. Meth. Biomed. Eng.* **1**, 261–263 (1998)
36. Taylor, Z., Miller, K.: Reassessment of brain elasticity for analysis of biomechanisms of hydrocephalus. *J. Biomech.* **37**, 1263–1269 (2004)
37. Franceschini, G., Bigoni, D., Reginig, P., et al.: Brain tissue deforms similarly to filled elastomers and follows consolidation theory. *J. Mech. Phys. Solids* **54**, 2592–2620 (2006)
38. Kaczmarek, M., Subramaniam, R., Neff, S.: The hydromechanics of hydrocephalus: steady-state solutions for cylindrical geometry. *Bull. Math. Biol.* **59**, 295–323 (1997)
39. Miller, K., Chinzei, K.: Mechanical properties of brain tissue in tension. *J. Biomech.* **35**, 483–490 (2002)
40. Velardi, F., Fraternali, F., Angelillo, M.: Anisotropic constitutive equations and experimental tensile behavior of brain tissue. *Biomech. Model. Mechanobiol.* **5**, 53–61 (2006)
41. Schiavone, P., Chassat, F., Boudou, T., et al.: In vivo measurement of human brain elasticity using a light aspiration device. *Med. Image Anal.* **13**, 673–678 (2009)
42. Wittek, A., Hawkins, T., Miller, K.: On the unimportance of constitutive models in computing brain deformation for image-guided surgery. *Biomech. Model. Mechanobiol.* **8**, 77–84 (2009)
43. Dutta-Roy, T., Wittek, A., Miller, K.: Biomechanical modelling of normal pressure hydrocephalus. *J. Biomech.* **41**, 2263–2271 (2008)
44. Cheng, S., Bilston, L.E.: Computational model of the cerebral ventricles in hydrocephalus. *J. Biomech. Eng.* **132**, 054501–054504 (2010)
45. Ruan, J.S., Khalil, T., King, A.I.: Dynamic response of the human head to impact by three-dimensional finite element analysis. *J. Biomech. Eng.* **116**, 44–50 (1994)
46. Zhang, L., Yang, K.H., King, A.I.: Comparison of brain responses between frontal and lateral impacts by finite element modeling. *J. Neurotrauma* **18**, 21–30 (2001)
47. Ho, J., Kleiven, S.: Can sulci protect the brain from traumatic injury? *J. Biomech.* **42**, 2074–2080 (2009)
48. Kleiven, S.: Influence of impact direction on the human head in prediction of subdural hematoma. *J. Neurotrauma* **20**, 365–379 (2003)

49. Prange, M.T., Margulies, S.S.: Regional, directional, and age-dependent properties of the brain undergoing large deformation. *J. Biomech. Eng.* **124**, 244–252 (2002)
50. Coats, B., Margulies, S.S.: Material properties of porcine parietal cortex. *J. Biomech.* **39**, 2521–2525 (2006)
51. Brands, D.W.A., Peters, G.W.M., Bovendeerd, P.H.M.: Design and numerical implementation of a 3-D non-linear viscoelastic constitutive model for brain tissue during impact. *J. Biomech.* **37**, 127–134 (2004)
52. Gefen, A., Gefen, N., Zhu, Q., et al.: Age-dependent changes in material properties of the brain and braincase of the rat. *J. Neurotrauma* **20**, 1163–1177 (2003)
53. Sack, I., Beierbach, B., Wuerfel, J., et al.: The impact of aging and gender on brain viscoelasticity. *Neuroimage* **46**, 652–657 (2009)
54. Thibault, K.L., Margulies, S.S.: Age-dependent material properties of the porcine cerebrum: effect on pediatric inertial head injury criteria. *J. Biomech.* **31**, 1119–1126 (1998)
55. Weaver, J.B., Perrinez, P.R., Bergeron, J.A., et al.: The effects of interstitial tissue pressure on the measured shear modulus in vivo. In: Manduca, A., Hu, X.P. (eds.) *Medical Imaging: Physiology, Function, and Structure from Medical Images, Proceedings of SPIE*, pp. 1A-1-11 (2007)
56. Metz, H., McElhaney, J., Ommaya, A.K.: A comparison of the elasticity of live, dead, and fixed brain tissue. *J. Biomech.* **3**, 453–458 (1970)
57. Garo, A., Hrapko, M., van Dommelen, J.A.W., et al.: Towards a reliable characterisation of the mechanical behaviour of brain tissue: the effects of post-mortem time and sample preparation. *Biorheology* **44**, 51–59 (2007)
58. Gefen, A., Margulies, S.S.: Are *in vivo* and *in situ* brain tissues mechanically similar? *J. Biomech.* **37**, 1339–1352 (2004)
59. Liu, Z.: *Rheological Properties of Biological Soft Tissues*. PhD Thesis. University of Sydney, Sydney (2001)
60. Cheng, S., Clarke, E.C., Bilston, L.E.: The effects of preconditioning strain on measured tissue properties. *J. Biomech.* **42**, 1360–1362 (2009)



# **Chapter 5**

## **Modeling of the Brain for Injury Simulation and Prevention**

**King H. Yang and Albert I. King**

### **5.1 Introduction**

According to the U.S. Centers for Disease Control and Prevention, traumatic brain injury (TBI) is a serious public health issue affecting 1.7 million people annually in the United States. Approximately 50,000 deaths were related to TBI each year [1] and at least 5.3 million Americans are living with TBI-related disabilities [2]. The most common causes of TBI include violent assaults, transportation-associated incidents, construction, and sports-related events [3]. As little can be done to reverse the initial brain damage caused by trauma, preventing TBI from happening and stabilizing a TBI victim to prevent further injury are two key areas of research. A better understanding of the causation and mechanisms of TBI can provide advancement in both areas.

Impact equipments (such as sleds, fluid percussion devices, or controlled cortical impact devices) are commonly used to generate sufficient force or acceleration to study injury mechanisms. During the test, globally measurable quantities (such as force and acceleration) and local variables (such as intracranial pressure) at a limited number of locations are measured. Based on these measurements, a number of injury mechanisms have been hypothesized [4]. As these mechanisms do not always correlate with clinical or pathological observations, considerable controversy still exists regarding the validity of these competing hypotheses.

Despite the fact that head injury mechanisms are not yet totally understood, some consumer protection and regulatory agencies (such as the Snell Foundation, Consumer Product Safety Commission, and National Operating Committee on Standards for Athletic Equipment) have prescribed minimal helmet performance criteria. These performance criteria are, in general, based on linear acceleration,

---

K.H. Yang (✉)  
Wayne State University, Detroit, MI 48201, USA  
e-mail: king.yang@wayne.edu

even though many researchers believe that rotational acceleration is the main culprit for TBI. Because helmets are designed to meet these standards, they function to reduce only the linear acceleration. Consequently, the inevitable question is why the helmet is effective in reducing head injury? Zhang et al. [5] conducted a series of mini-sled experiments to simulate American football-relevant impacts using the head and neck complex of a Hybrid III dummy. They found that the magnitude of angular acceleration was positively correlated with the magnitude of linear acceleration. Although not statistically significant, Rowson et al. [6] also reported a positive correlation between the magnitude of linear and angular accelerations in collegiate football collisions using specially arranged accelerometer array imbedded in helmets. Thus, even though football helmets are not explicitly designed to reduce rotational acceleration, diminishing linear acceleration also lessens angular acceleration.

Many researchers agree that injury mechanisms and thresholds based on externally measured linear or angular acceleration do not address the underlying biomechanical basis for injury. A number of studies have pointed out that brain deformation or strain is a principal cause of injury. Unfortunately, measuring strain, particularly *in vivo*, is almost impossible during an impact. At present, the best method to predict intracranial biomechanical responses is through numerical modeling. In particular, the finite element (FE) method is exclusively suitable to model structures of irregular geometry, multiple material compositions, and complex loading and boundary conditions and has been the preferred method to study head injury. Numerical models developed using FE method can provide tissue-level responses for correlation with the location and severity of injury outcomes. Considering the fact that globally based injury criteria have yet to bring about a further reduction in the incidence rate of TBI, it is perhaps necessary to seek criteria that are based on brain response, using FE computer models.

A number of human and animal FE brain models have been reported since the 1980s when computers became powerful enough to run these models. The general belief of these studies is that a fully validated human FE head model is needed to identify the injury mechanism, which in turn can be used as a surrogate to design countermeasures to mitigate head injury severity or eliminate head injury altogether. Because traffic-induced TBI accounted for a majority of the TBI cases, many of these numerical models were published in the Stapp Car Crash Conference Proceedings or Journals. Yang et al. [7] conducted a comprehensive review of these models on the occasion of the 50th anniversary of the Conference. It was concluded that even though significant insight into head injury biomechanics was attained through exercising these models, there was a glaring lack of brain material properties under loading rates relevant to impact-induced TBI. Additionally, experimental and real world data needed to properly validate these numerical models were in short supply. To date, the only cadaveric data available consist of two sets of intracranial pressure data reported by Nahum et al. [8] and Trosseille et al. [9] and a few sets of relative motion data between the brain and skull reported by Hardy et al. [10, 11]. Real world or live human data consisted of some 30 mild TBI cases reconstructed from National Football League games [12], 13 cases of reconstructed motorcycle

data [13, 14], and four sets of graded AIS scale head injury data derived from real world crashes [15]. Even if all these shortcomings are overcome, tissue-level injury thresholds are still needed to determine the risk of TBI based on FE model-predicted tissue response.

With an ever increasing number of head models being reported from around the world, we find that many of these models are largely repetitive of previous versions, are not validated at all, or utilize the same limited datasets for model validation. In short, they provide no additional insights into the solution of the head injury problem. The purpose of this chapter is to outline what we have learned in modeling and simulation of the brain for injury prevention and how the knowledge gained in the past several decades in studying head injury biomechanics has helped us reach the goals of mitigating brain injury. Throughout this chapter, the do's and don'ts of brain modeling are discussed to help modelers avoid repeating the mistakes of earlier developers.

## 5.2 Essentials of a Finite Element Head Model

The four key constituents of any FE model are the model geometry, material properties, boundary conditions, and loading conditions. Medical images are typically segmented to acquire various anatomical features within the brain. The segmented data can then be used to develop model geometry, or mesh. Detailed descriptions of brain imaging and segmentation can be found in Chap. 3 and will not be discussed here. Also, constitutive laws and material properties needed for the various materials within the brain will not be discussed as more information is provided in Chap. 4. In this chapter, emphasis will be placed on selecting the anatomical features of the brain for inclusion in an FE head model, boundary conditions, and loading conditions. Nevertheless, readers are advised of the fact that accurate material properties are key to model the brain accurately.

### 5.2.1 Selection of Anatomical Features

Before the turn of the century, when computational power was relatively limited, a problem-specific FE model was formulated to solve a specific problem. For example, if a FE model was created to find the displacement of a clamped plate with a concentrated load at its center, the mesh near the center was greatly refined while regions away from the center were modeled using larger elements. Two problems are associated with this approach. First, transitional elements are needed to gradually refine the mesh size towards the point of loading. In general, transitional elements are of lesser quality than regular elements and hence the solutions can be less accurate. As an example, triangular elements are commonly used as transitional elements to refine bilinear quadrilateral elements (Fig. 5.1). Since the strain

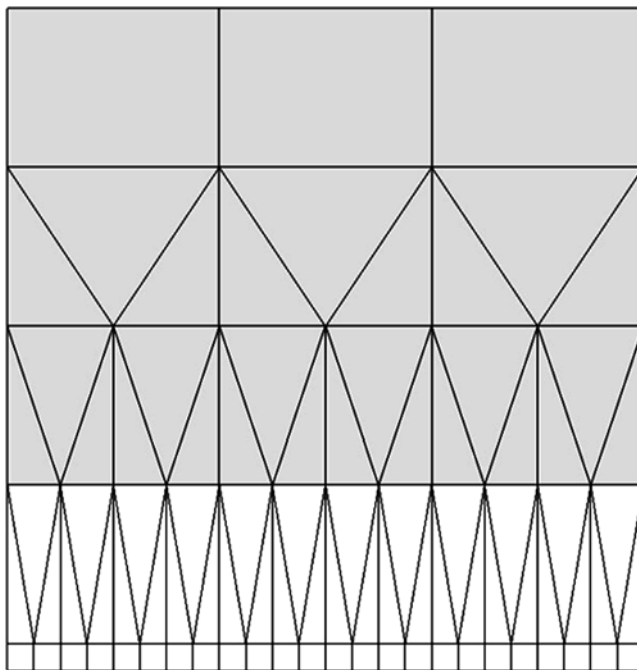


**Fig. 5.1** Application of triangular elements to increase the mesh density of 4-node bilinear elements

magnitude in a triangular element is constant, a lot of triangular elements are needed to study large strain variations near the loading position and hence not computationally efficient. Second, this type of problem-specific model cannot be used when different loading conditions are applied. Thus, a new model is needed for every new loading condition. As computing power became more widely available, most FE model developers made their models more versatile to handle all kinds of loading conditions, using a fine mesh for the entire model.

In terms of selecting the anatomical features, the skin and scalp layers need to be included in an FE head model, even though these structures are not needed when simulating a closed head injury in which skull deformation is of no concern. In these cases, it is a common practice to apply all three components of linear and angular accelerations to the center of gravity of the head model to determine intracranial tissue response [12, 16]. If simulation time is of concern, these layers can be assigned as rigid materials to reduce computational cost. On the other hand, a model with skin and scalp representation can be used directly if a real world direct impact scenario is to be considered. This same approach is also recommended for facial bones.

The bony skull plays a vital role in the protection of the brain from external loading. Mechanically, the rigidity of the skull (in terms of its modulus and thickness) determines the magnitude of the intracranial pressure due to direct impact or inertial loading. The adult human skull is made up of eight bones that are rigidly

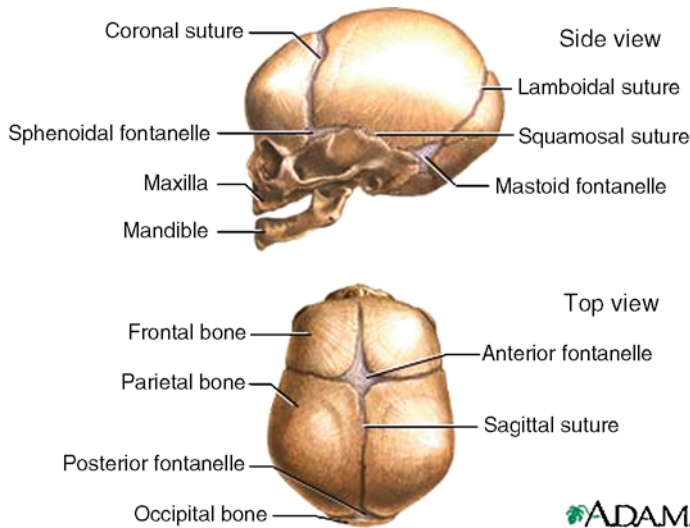


**Fig. 5.2** Fontanelles and sutures of the infant skull from <http://www.nlm.nih.gov/medlineplus/ency/imagepages/1127.htm>

connected by sutures. For this reason, there is no need to model them as separate bones. The skull is made up of three distinct layers, the outer table, diploe, and inner table. It has been reported that the skull thickness can vary from 4 to 9 mm [17]. However, there is no report on the thickness for each individual layer, extent of variation in the thickness for different bones, and age/gender dependency of the thickness. Without such data, FE head models developed thus far are based on a uniform thickness. Again, the skull bone may be treated as rigid material if close-head injury without any skull deformation is the only concern.

Cranial sutures in the adult allow only minimal movement between skull bones. In the infant, the skull bones can move relative to each other as they are separated by gaps called fontanelles (or soft spots), which are covered by a reasonably strong membrane with a smaller elastic modulus compared to skull bones (Fig. 5.2). Continued ossification and closure of the fontanelles occur at different times while complete closure of the sutures does not occur till the third decade of life [18]. For this reason, the infant skull cannot be modeled as a single bone as in the adult model.

Cranial meninges consist of the dura mater, arachnoid mater, and pia mater. Dural partitions include the falx cerebri, a sagittal partition which divides the brain into the left and right hemispheres, and the tentorium, which separates the cerebellum from the occipital lobes. It has been noted that a model without the falx cerebri and tentorium could not accurately predict brain motion within each compartment [19, 20]. For this reason, the falx and tentorium should be included in any future head model. Additionally, Haines et al. [21] reported multilayer structures between the skull and brain (Fig. 5.3). Because there is normally no space for fluid between the arachnoid and dura, the dural and arachnoid border cells and dura mater are considered as a

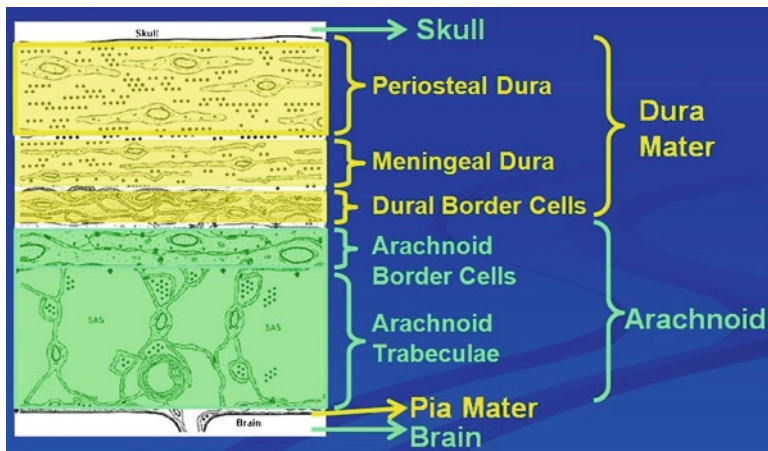


**Fig. 5.3** Anatomical layers between skull and brain reported by Haines et al. [21]

single entity in most models. The arachnoid trabeculae and cerebrospinal fluid (CSF) resemble a biphasic structure with CSF surrounding the solid arachnoid trabeculae. Due in part to the irregular distribution of trabeculae and a lack of computational power, most modelers define the subarachnoid space as a boundary condition between the skull and brain which will be discussed later. Using a 2D FE model, Cloots et al. [22] reported that gyri and sulci had no effect on the mean von Mises stress, but had a significant effect on its maximum value. However, current computational power is still inadequate to model cerebral convolutions in a 3D head model.

The cerebral ventricular system consists of four interconnected ventricles: the left and right lateral ventricles, third ventricle, and fourth ventricle. CSF occupies the ventricles and the subarachnoid space surrounding the brain and the spinal cord. Most models reported so far include the lateral ventricles, while a small number of finely meshed models also simulate the third and fourth ventricles. Since the ventricles are filled with CSF, fluid elements are generally used to represent this structure.

Neuronal tissue is anatomically divided into gray matter and white matter. Gray matter is made up mostly by cell bodies or neurons, while white matter is made up mostly by myelinated axonal tracts. Due to this morphological variation, mechanical properties of gray and white matter are expected to be different. Unfortunately, data reported in literature are not consistent in terms of which brain matter is stiffer than the other. Since white matter represents axonal tracts, some have contemplated the use of orthotropic properties to highlight its directional dependency. Again, there is a lack of mechanical property data on axonal directional dependency to justify the use of such a computationally expensive representation. Limited by computational power, it is also not practical to model individual cells and axons at this stage. As a result, most head models assume the brain to be a homogeneous and isotropic continuum.

Some models simulate the thalamus and hippocampus explicitly as separate organs mainly because of their important physiological functions. However, material properties used for these structures were based mainly on data taken from animal testing

acquired at low speed [23, 24]. We recommend that gray matter structures should include (but not limited to) the cortex, thalamus, and basal ganglia. The white matter in an FE head model should include the corpus callosum, corticospinal tract, and brainstem, including detailed geometry of the midbrain around the tentorium opening.

Parasagittal bridging veins have been included in many FE head models. Numerous articles have reported that acute subdural hematoma (ASDH) is due to rupture of these veins as a result of large relative motion between the brain and skull [25]. The reader is cautioned that the number of ASDH of arterial-origin equals, if not exceeds, that of ASDH of venous-origin [26]. Thus, calculating bridging vein stretch alone cannot fully predict the occurrence of ASDH. In any event, the direction, location, and length of the bridging vein all contribute to its strain and these data are not readily available. Additionally, readers should be aware that rate sensitivity of the bridging vein is still a controversial issue [27, 28].

Human brain tissue consists of a network of cerebral vasculature interspersed within a matrix of supporting cells. These vessels may or may not have a profound effect on overall *in vivo* material properties of the brain in contrast to brain properties measured *in vitro* where this tethering effect is not considered. Ho and Kleiven [29] developed a 3D head model in which major arteries and veins were represented by “beam” elements to study the effect of cerebral vasculature on brain response. The authors found minimal discrepancy between the models with and without explicit cerebral vasculature representations. Their result is different from that reported by Zhang et al. [30] using 2D FE models with and without major branches of cerebral arteries. Such differences can be attributed to the number vessels included in the head model, difference in mechanical properties between the brain parenchyma and cerebral vessels, and the method used to represent the blood vessels – “beam” elements or solid elements. Considering the fact that the diameter of the largest cerebral arteries is no more than 3 mm [31] while other vessels are 0.5 mm and less in diameter, inclusion of cerebral vasculature remains a major challenge for FE head model developers.

### 5.2.2 *FE Mesh Quality*

A FE model that employs a low quality mesh cannot yield the best results. This is particularly true for explicit FE modeling in which the one-point reduced integration scheme is the default integration method. The explicit scheme decreases computational cost, while at the same time improves solution accuracy by avoiding mesh locking. Factors that can affect the quality of a mesh include: Jacobian, warpage, aspect ratio, skew angle, and internal (edge) angle. Practically, all FE methods involve the shape functions [ $\mathbf{N}$ ], from which the strain-displacement matrix [ $\mathbf{B}$ ] and element stiffness matrix [ $\mathbf{k}$ ] are derived. These three matrices form the foundation for determining structural response under load. The standard or “parent” elements commonly adopted for 2D plane and 3D solid element formulations are the square and the cube, respectively.

Obviously, it is not practical to use only square- or cubic-shaped elements to represent a complex structure. Thus, isoparametric formulation, based on natural coordinate systems, is needed to allow for elements with more general shapes. Intuitively, one is led to believe that a mesh with all elements shaped very closely to their corresponding parent elements will yield the best solution and indeed this is the case.

The Jacobian matrix is a function which maps one Euclidean space to another. The determinant of the Jacobian matrix (often simply called the Jacobian) reports the maximum variation of an element from the idealized element based on the same shape functions. Definition for the aspect ratio, warpage, and skew angle varies slightly depending on the type of elements used. For example, aspect ratio is defined as the length to width ratio in a triangular or quadrilateral element, as the ratio of height to square root of opposing face area in a tetrahedral element, or the ratio of the maximum to minimum distance between opposing faces for a hexahedral element. Warpage tests the extent of deviation out of the plane formed by the other three nodes on the same face of a quadrilateral, wedge, or hexahedral element. The skew angle is generally calculated using an edge bisector method. Although there are no specific guidelines available, our in-house practice is to have a minimum Jacobian of 0.7, all internal angles between 45 and 135°, a maximum aspect ratio of 3, and a maximum skew angle of 30°. Additionally, the mesh quality goal for warpage angle, taper, and element length to thickness ratio shall be less than 20, 0.5, and 3, respectively, for 2D elements and the warpage angle and tetra collapse shall be less than 5 and 0.5, respectively, for 3D elements. Figure 5.4 shows some 2D and 3D elements with qualities right at these recommended limits. Readers are also referred to a set of test problems reported by MacNeal and Harder [32] to learn more about large errors induced by ill-shaped elements compared to elements with standard shapes.

As the structure of interest becomes more complex, meshing it with isoparametric 2D quadrilateral elements or 3D brick elements can be quite challenging. On the other hand, the use of 2D triangular elements and 3D tetrahedral elements is an easy task because there are numerous software packages available to automatically generate meshes based on triangular and tetrahedral elements. In general, formulations of triangular and tetrahedral elements are based on degenerations of 4-node plane or 8-node brick elements, respectively. For example, a 4-node tetrahedral element (N1-N2-N3-N4), when mixed with other hexahedral elements, is treated as a degenerate 8-node solid element with node number N1-N2-N3-N4-N4-N4-N4-N4 in LS-DYNA code (LS-DYNA user manual). One problem associated with degenerated elements is related to an uneven mass distribution. For example, node 4 of a degenerate tetrahedron has five times the mass of nodes 1, 2, and 3. Similarly, a 6-node pentahedral element is degenerated from 8-node brick with node number N1-N2-N3-N4-N5-N5-N6-N6 (Fig. 5.5). Different software packages employ different degeneration schemes. For example, some may assign node 4 of a triangular element, with nodes 1, 2, and 3, to be located at the same coordinates as node 3, while others may assign node 3 to be located between nodes 2 and 4 on one side of a triangle formed by nodes 1, 2, and 4. These degenerated elements are very different in shape compared to standard elements and have been shown to require a lot of elements to



**Fig. 5.4** Quadrilateral elements with mesh quality exceed the minimal in-house recommended values of a Jacobian of 0.7 (*left*), internal angle of 55, 10° exceed the recommended 45° (*center*), and a warpage of 1.65 (*right*)

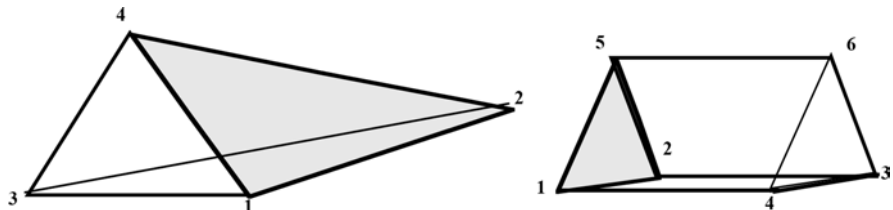


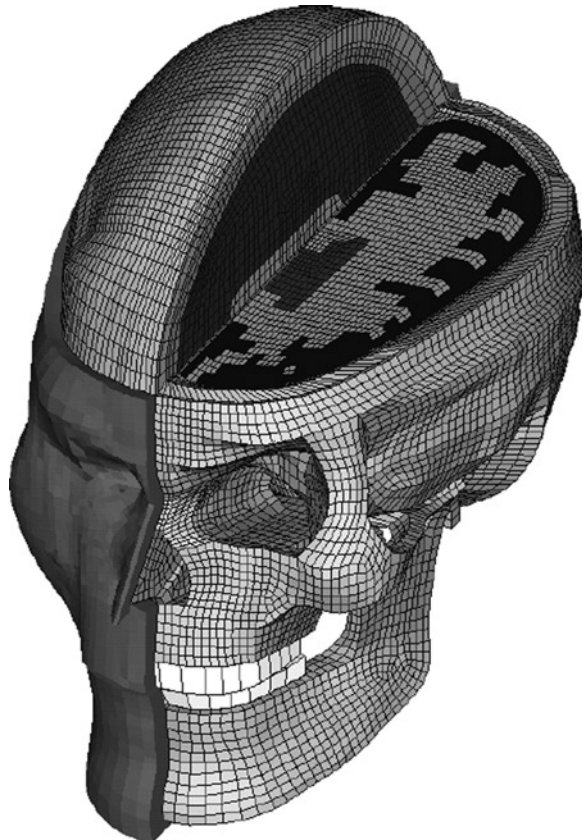
**Fig. 5.5** When mixed with 8-node hexahedral elements, 4-node tetrahedral elements and 6-node pentahedral elements in LS-DYNA are treated as degeneration of 8-node hexahedral elements

achieve the same accuracy as what a small number of standard elements can do. If the element density does not increase when degenerated elements are used, the solution may not be as accurate. For our in-house FE models, we recommend that less than 10% of all elements be in the form of triangular or tetrahedral elements.

### 5.2.3 Numerical Convergence and Hourglass Energy

Mesh convergence refers to how small the element size should be in a FE model to ensure that simulation results are unaffected by changing the size of the mesh. The convergence issue is frequently overlooked for three reasons. First, a FE model with high mesh density may not be solvable when computing resources are limited. This issue is no longer a critical one as newer computers are capable of handling a large quantity of random access memory. Second, developing FE models with a different mesh density requires significant effort. Unless each refinement represents a division of one 3D element into eight elements (that is, dividing each edge of an element into two), substantial work is involved when refining a mesh. While this issue persists to the present, it is less critical now because there are software packages which allow users to parameterize the mesh so that little effort is needed to adjust the mesh density. Still, refinement of the mesh using such automatic meshing software usually has limitations if the parameterized surface is poorly formulated and there is no guarantee that the refined mesh will be of high quality. Third, many research groups have in their databases numerous models available and hence have a tendency to take an old model that was previously published for use in a new loading condition without testing for convergence to ensure that the mesh density is sufficient to solve the new problem.

**Fig. 5.6** The Wayne State University head injury model



To check for convergence, strains or stresses in several regions of interest are computed and plotted as a function of mesh density. If simulation results from two FE models with different mesh densities are within a few percentage points of each other, then mesh convergence has been achieved. Otherwise, continued refinement of the mesh should be carried out and the FE simulation repeated. Typically, differences in strains or stresses in two consecutive refinements will decrease as the mesh is refined. Eventually, the difference will be sufficiently small so that convergence is deemed achieved. In some cases, such as impact of soft tissue by a very small diameter pendulum, convergence is very difficult to achieve due to the large deformation confined to a small region. In this case, a report must be generated to indicate how far away the mesh is from full convergence. Although some advanced FE solution methods are, in theory, not affected by mesh size, testing for convergence is a recommended practice in our laboratory in the event that the software does not live up to its expectation. Figure 5.6 shows the Wayne State University head injury model, consisting of more than 314,000 uniformly meshed high-quality elements. The solution was found to be convergent when the model was used to simulate direct and indirect impacts with combined accelerations of up to 200 g and 12,000 rad/s<sup>2</sup>.

In explicit FE analysis of soft tissue subjected to dynamic loading, large hourglass energy is frequently needed to prevent the mesh from going into various hourglass modes. This is of great concern. Formation of hourglass modes is primarily due to rank deficiency. Consider a 4-node bilinear 2D element, the element stiffness matrix  $[k]$  has a size of  $8 \times 8$  but only a rank of 5, which can be calculated by taking away three rigid body motions (two translations and one rotation) from the eight degrees-of-freedom available for a 2D bilinear element. A one-point reduced integration scheme would decrease the rank from 5 to 3, which means two hourglass modes could occur. Explanations of hourglass modes and the energy needed to control these modes are tedious and the reader is referred to relevant papers on the subject, such as Hughes [33]. Many software packages allow changing the hourglass energy coefficient to adjust the hourglass energy. It has been recommended that the hourglass energy should not exceed 10% of the total energy in order to assure accuracy of simulation results.

### 5.2.4 ***Boundary Conditions***

Representing the pia-arachnoid complex (PAC), within which the CSF flows, remains an unresolved issue in brain modeling. Techniques used in the past include a direct connection with no slip, direct coupling at the junction, sliding interface with different coefficients of friction, or tie-break with a preset threshold. A major reason for these selections is probably due to the fact that some researchers were either unaware of or decided to ignore the existence of trabeculae in the subarachnoid space. Also, the complex and random nature of the distribution of trabeculae in the PAC makes it impossible to model them explicitly. While the exact method to model the PAC and the CSF within it has not been agreed upon, it has been noted that representing this layer by a gap cannot be used to generate tension in the contrecoup site, thus making it unsuitable to model the contrecoup phenomenon reported by clinicians.

Experimental data reported by Jin et al. [34, 35] on bovine PAC showed that the trabeculae in the CSF layer offers finite shear resistance, thus it would be a mistake to model this layer as an incompressible fluid. A set of constitutive equations has been developed for bovine PAC [36]. Effort should be devoted to determine in-plane, traction, and shear loading responses in human pia-arachnoid samples using methods similar to those reported by Jin et al. [34, 35]. Once a set of constitutive equations is developed to represent the PAC and CSF, this combined structure can be properly modeled. There is no evidence to suggest the need to model the CSF surrounding the spinal cord. Unless there is new information to suggest otherwise, the sliding of the cord relative to the surrounding dura can be represented by a sliding interface.

### 5.2.5 ***Types of Injury To Be Simulated***

A good understanding of the injury mechanism is one of the most important components when studying injury prevention. Without knowing the proper injury mechanism

and the associated injury threshold, it is not possible to use a FE head model to predict the type, location, and severity of TBI. Because a FE head model can only be used to calculate the corresponding responses at the instant of impact, secondary head injury (defined as the pathological, physiological, and biochemical changes to the brain tissue after the primary injury) is beyond the capability of current FE head models and will not be discussed in this chapter.

The mechanism of open and close-head injury is quite different. Because skull and facial bone fractures do not always correlate with brain injury, such fractures are not simulated in most FE head models. Nevertheless, readers should be aware that a fractured skull could affect subsequent intracranial response and a skull fracture is more complicated than a long bone fracture. Gurdjian and Webster [37] in their stress-coating and strain gauge study showed that there was a momentary in-bending at the site of impact and out-bending at the adjacent regions with linear fractures occurring in the out-bended area. Additionally, an instantaneous increase in intracranial pressure upon impact may contribute to the incident rate of skull fracture or to the fracture length.

Only four types of brain injury (cerebral contusion, diffuse axonal injury (DAI), acute subdural hematoma (ASDH), and subarachnoid hematoma (SAH)) are discussed in this chapter. Figures 5.7 shows two magnetic resonant images of a cerebral contusion case. Cerebral contusion is a bruising of the brain surface where hemorrhagic necrosis and acute brain swelling occur. Contusions usually involve the surface of the brain, especially the crowns of gyri, and are more frequent in the orbital surfaces of the frontal lobes and the tips of the temporal lobes irrespective of the site of impact [38, 39]. Most researchers believe that this focal injury is associated with intracranial pressure generated as a result of high linear acceleration. Positive pressure, typically associated with the so-called coup injury mechanism, is assumed to be the result of the moving skull towards the stationary brain, producing a compressive wave in the brain at the time of impact or direct compression of the brain due to in-bending of the skull. Negative pressure, which has been associated with the so-called contrecoup injury mechanism, is hypothesized to be the result of tension generated by skull moving away from the brain that is lagging behind skull. If pressure is the underlining mechanism of this coup-contrecoup phenomenon, FE model-predicted pressure levels can be used to estimate the risk of contusion injury. Alternately, the negative pressure could be due to a tensile wave that was formed by the reflection of the original compression wave off the skull. Cavitation (collapse of a vapor bubble) occurs if negative pressure is lower than the vapor pressure of water. In this case, negative pressures below atmospheric pressure may be a good indicator for contusion injury. This cavitation-induced injury mechanism has not been proven experimentally and readers should bear in mind that this may not be a true mechanism.

DAI is a well-known consequence of blunt head injury and is characterized by immediate onset of coma at the time of injury or cognitive dysfunction. Pathologically, DAI comprises diffuse changes in the white matter tracts, including focal perturbation of axolemma, cytoskeletal misalignment, disruption of axoplasmic transport (manifested as axonal swelling), formation of retraction balls, and axonal

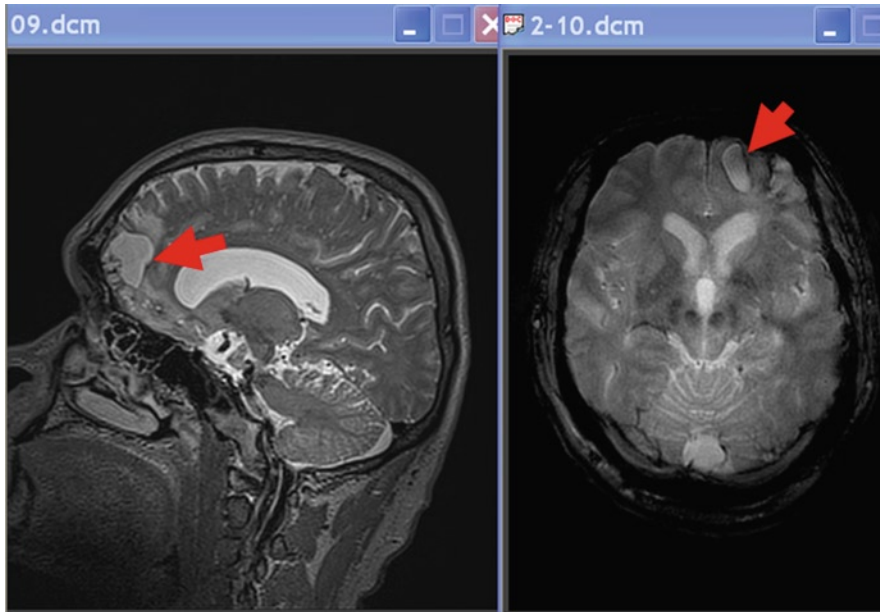
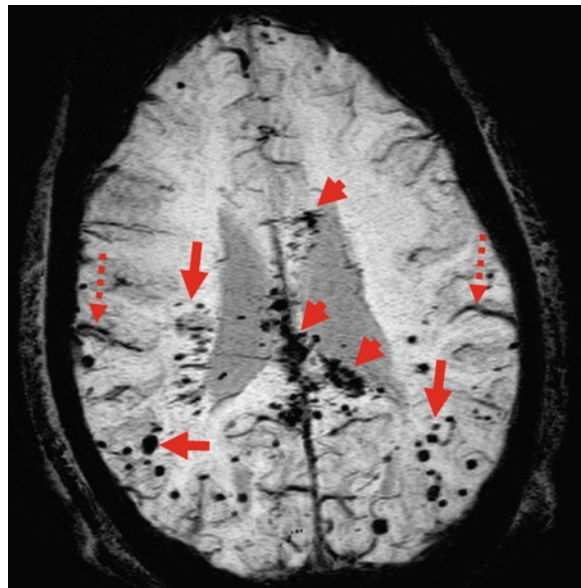


**Fig. 5.7** T2 images of a patient suffering focal contusion (*left image*: sagittal view; *right image*: axial view). As shown in the above images indicated by *arrows*, a focal contusion happened on the surface area of right frontal lobe. In radiology, *right side* of an image represents left side of the brain; and vice versa (courtesy of Dr. Zhifeng Kou)

disconnection. A typical case of DAI is shown in Fig. 5.8. As most FE head models are too coarse to include explicit representation of these anatomical features, overall model-predicted response at the tissue level is used to correlate with the risk of DAI. Although extremely high angular acceleration was needed, Gennarelli et al. [40, 41], were able to induce DAI in an experimental animal model. Since brain material has a very low shear modulus and a very high bulk modulus, high shear strains or stresses can be easily generated during rotational loading. Consequently, the magnitude of shear strain or maximum principal strain predicted by a FE head model is commonly used to indicate the risk of DAI. The cumulative strain damage measure (CSDM), proposed by Bandak and Eppinger [42] and Takhounts et al. [43], hypothesized that DAI is associated with the cumulative volume of all brain tissue elements which experienced a strain higher than a prescribed threshold. From a biomechanical point of view, this measure seems to be very reasonable but experiments specifically designed to verify this hypothesis are needed to ensure its validity.

ASDH describes an abnormal blood collection between the dura and arachnoid maters. ASDHs are one of the most frequently seen forms of high severity acute head injuries. There is evidence that ASDH is usually formed within the first several minutes and certainly by the end of the first hour after a severe impact. Many researchers believe that the cause of ASDH is the rupture of parasagittal bridging veins. Hence, relative motions between the brain and skull are a good predictor to

**Fig. 5.8** Susceptibility-weighted imaging of a severe brain injury case. The patient is a classical DAI case with numerous hemorrhagic lesions at the genu, body and splenium of corpus callosum (see arrowheads), and gray and white matter junction area (see arrows). The patient also suffers subarachoid hemorrhage (SAH), which travels into the brain sulcus area on both sides of the brain (see dashed arrows) (courtesy of Dr. Zhifeng Kou)



estimate the risk of ASDH. While this hypothesis may have clinical correlation in a number of cases, Maxeiner and Wolff [26] showed that there was an equal probability of ASDH caused by bridging vein rupture and by cortical artery rupture. Moreover, Shenkin [44] reviewed 39 consecutive cases of ASDH and found that there was a high incidence rate of cortical artery rupture (61.5%). Additionally, relative motions between the brain and skull measured by Hardy et al. [10] indicated that relative motions in the peripheral region of the cortex were less than those measured in the central region of the brain. For these reasons, we cannot confirm the precise injury mechanisms of ASDH until new experiments are carried out.

SAH or hemorrhage is the result of ruptured corticomeningeal vessels or bridging veins upon blunt impact. As the hemorrhage occurs in the CSF space, intracranial pressure is not likely to rise significantly and this injury type does not present a significant challenge in clinical practice. Additionally, it is computationally too expensive to explicitly model these corticomeningeal vessels. Hence, this type of brain injury has been mostly ignored by most FE models. Similarly, epidural hematoma (EPH) is seen in less than 5% of TBI cases and has a low mortality rate. Although there is no space between skull and dura, there is a natural epidural space around the spinal cord for the hemorrhage to move into. Consequently, simulating the risk of EPH is not a great concern to many researchers.

### 5.3 Validation of Simulation Results

As mentioned in Sect. 5.1, only limited datasets are available to validate FE models. These datasets can be grouped into two categories: laboratory experiments and reconstructed real world data. Practically, any FE head model that has been validated

includes the use of intracranial pressure data from the oft-cited Test 37 reported by Nahum et al. [8] probably due to the fact that this was the only time history data presented in the paper. Note that the same publication [8] also included peak data in tabular form, reporting on a number of experiments in which intracranial pressures were measured. For example, there were padded and rigid impacts, using three different impactor masses (2.7, 5.23, 5.59 kg) and six different velocities (4.36, 6.3, 8.69, 8.75, 9.94, 12.95 m/s). Some of the intracranial pressure data did not make sense from a mechanical point of view and were apparently outliers. Obviously, there were inherent problems associated with these experiments. Gurdjian et al. [45] once wrote: “Due to the error introduced resulting from deformation of the scalp, muscles, skull, and striker itself, it appeared more accurate to measure the acceleration of the skull.” As a result, the most commonly used head injury criteria are all based on acceleration without considering the intracranial responses. Explanations for the unreasonable measurements reported by Nahum et al. [8] may include data acquisition system errors, variations in the cadaveric anthropometry, and the unspecified locations of pressure transducer placements. Similar problems can also be found in newer laboratory generated experimental data reported by other authors. For examples, Hardy et al. [10] reported large standard deviations observed in the motions of the brain with respect to skull using the same cadaveric head under very similar loading conditions. Lastly, using real world accident reconstruction data for model validation presents even more problems because the only known variable is the injury outcome.

To correct this deficiency, experiments specifically designed to generate data for model validation are needed. One such dataset has been generated to validate human neck models subjected to rear-end impact [46]. In this series of experiments, high-resolution CT scans were conducted on each cadaver to document the cervical spine geometry and to generate subject-specific neck models, while cervical spine kinematics were obtained by a high-speed bi-planar X-ray system for model validation. Obviously, experiments of this kind will be very expensive and require pooling of financial resources from all stake holders to achieve the goal.

## 5.4 Revamp FE Modeling of Human Head

We hypothesize that successful development of human head models for preventing blunt impact-induced TBI depends to a great extent on animal experiments. There are several reasons for this assumption. First, freshly dead human heads (and brains) are very hard to obtain and studying the TBI injury mechanism and threshold requires a large number of cadavers because of the inherent variability of cadaver data. Second, for those cadavers available for impact testing, it is very difficult to prepare them to imitate *in vivo* conditions. Third, cadaver experiments will not reveal any brain injury. Animal studies, on the other hand, enable the measurement of biomechanical parameters, investigation of behavioral changes, and evaluation of histological changes to identify the type and severity of brain injury due to impact. More importantly, laboratory-raised animals are genetically the same and easier to secure for testing once the experimental protocol passes the stringent protocol review process.

It has been nearly 20 years since animals larger than rodents were used to determine TBI injury mechanisms and thresholds due to blunt impact. While valuable data were gathered from animals in the old days, biomechanical parameters measured were limited to mostly external impact parameters (such as the pendulum mass and speed) and global responses (such as linear and angular accelerations). Unfortunately, computer modeling technologies were not sophisticated enough to model these experiments at that time and hence anthropometry and other data needed for validation of numerical models were not obtained. Nevertheless, full utilization of these data should be attempted so that no additional animals need to be sacrificed unless it is absolutely necessary. It is our understanding that the U.S. Department of Transportation is organizing an effort to revive some primate data from its archives across the globe. Successful retrieval of these primate data in conjunction with numerical modeling of these animal impacts will promote a better understanding of the relationship between injury outcome and model-predicted intracranial responses.

As previously described, earlier experiments were not conducted for the purpose of obtaining data for model validation. Thus, it is fully expected that new animal experimental data are necessary. The following list outlines some key information needed if financial resources are put in place for doing such experiments:

1. Clear identification of animal head anthropometry and experimental conditions. For example, stiffness of the foam used to soften a blow in pendulum testing or used as a cushion in weight drop Marmarou type of testing should be measured.
2. Sufficient biomechanical parameters should be measured during impact and used for model validation. When possible, intracranial tissue kinematics should be measured using bi-planar X-ray techniques such as those reported by Hardy et al. [11]. Efforts should be devoted to accurate modeling of the pia-arachnoid junction because the complex anatomy at this region greatly affects the model-predicted responses.
3. Thorough histological investigations of TBI are needed. Because the counting of brain lesions under the microscope can be an extremely labor-intensive process, even with the aid of a computer, researchers typically only study a handful of sections at a couple of selected regions of interest. Studies have shown that brain injury can occur in regions remote from the impact site [47], but these data are not routinely acquired and reported upon. An entire 3D injury map is needed for correlation with FE model-predicted tissue-level responses.
4. Careful correlation between injury outcome and FE model-predicted biomechanical responses is needed to identify region-specific injury thresholds. Intuitively, one can imagine that a 10% stretch in gray matter may not be injurious, while the same magnitude of stretch in white matter may be devastating. Hence, it is fully expected that injury threshold should be different for different regions of the brain.
5. A suitable scaling methodology should be developed so that injury threshold derived from animals can be scaled to protect the human. A minimum of two animal experimental models (a small and a large one) need to be conducted to develop a scaling method based on parameters such as age, gender, size, material

properties, etc. Preferably, a third animal model should be tested to validate the accuracy of the scaling law and to develop a scaling method to estimate the tissue-level injury threshold in humans. Note that this method does not account for species differences in tolerance and may not provide a direct correlation between size and tolerance.

Once these animal experiments are completed, there are still numerous hurdles to overcome in developing fully validated animal brain models. For examples, while material properties available on animal brain tissues are more abundant compared to human tissues, more studies are still needed to develop proper constitutive laws and more accurate material properties at strain rates relevant to the impact condition. Even in a systematic series of investigations, the data are expected to have a fairly large standard deviation due to biological variations. Presently, FE brain models are based on a deterministic approach by inserting a set of material properties into the model which is then subjected to a set of loading conditions to calculate intracranial responses. Because variations exist in material properties and loading conditions, a probabilistic approach should be applied to determine the spectrum of response variables. In other words, there will be a range of model-predicted intracranial responses reflecting the dissimilarities among the population and the relative risk of injury.

It can be expected that accurate FE human head models can only be developed with success after completing the modeling of animal brains through which one can identify material laws and associated constants, define with accuracy the loading conditions, and ascertain regional tissue-level injury thresholds through 3D injury mapping. The human head models developed based on this principle can then be used as the surrogate to design better countermeasures to prevent or mitigate brain injury. As the human brain is better protected against blunt impact, the incident rate of TBI should decrease. Nevertheless, complete elimination of TBI may not be immediately achievable. Thus, newer and higher quality real world data need to be gathered continuously to improve the simulation models so that their capability in accurately predicting the risk of brain injury under a variety of blunt impact conditions is augmented.

## 5.5 Conclusions

A large number of FE human and animal brain models for blunt impact simulation have been published. We do not know what motivated the development of so many brain injury models, but one of the reasons must be related to the desire of model developers to show that their model is better than existing ones. This reason alone should not be the primary basis for model development. To varying extents, these models have been validated against a very limited number experimental datasets in which insufficient details were available to accurately define the model geometry, loading conditions, and impact responses. For this reason, continued development of new human brain models is not likely to improve the quality of these models or provide additional insights. However, the possibility of having another “run-of-the-mill”

human brain model published in the literature is highly likely because the resources needed to develop a computer model is nothing more than a high-end computer and a commercially available software package. It is sad to see that some journal reviewers are not requiring all models to demonstrate proper convergence and validation. More importantly, we will continue to see FE model-derived injury thresholds without the acknowledgement that these thresholds are model-dependent and not necessarily universally valid or even reliable.

To alter the direction of model development, we need high-quality experimental data, especially animal experiments, designed to acquire biomechanical and injury data for model validation. With a majority of government (NIH) funding being directed towards translational research and treatment, very little resources are still available to prevent TBI from happening, even though prevention is the best treatment for TBI. Automotive and sports equipment manufacturers have a keen interest in preventing TBI. However, these companies are not willing to support animal research because bad press can hurt their business. Until this culture is changed, one may continue to see more TBI victims in the years to come. It is hoped that this chapter can change some minds to redirect more effort and funding to developing better FE human head models to reduce the number of future TBI victims.

## References

1. Langlois, J.A., Rutland-Brown, W., Thomas, K.E.: Traumatic brain injury in the United States: Emergency Department Visits, Hospitalizations, and Deaths. Atlanta, GA: Dept. of Health and Human Services (US), Centers for Disease Control and Prevention, National Center for Injury Prevention and Control (2004)
2. Thurman, D.J., Alverson, C., Dunn, K.A., et al.: Traumatic brain injury in the United States: a public health perspective. *J. Head Trauma Rehabil.* **14**(6), 602–615 (1999)
3. Kushner, D.: Mild traumatic brain injury: toward understanding manifestations and treatment. *Arch. Intern. Med.* **158**, 1617–1624 (1998)
4. King, A.I., Yang, K.H., Zhang, L., et al.: Is head injury caused by linear or angular acceleration? Proceedings of the IRCOBI Conference, Lisbon, Portugal, 24–27 September 2003
5. Zhang, L., Dwarampudi, R., Yang, K.H., et al.: Effectiveness of the football helmet assessed by finite element modeling and impact testing. Proceedings of the 2003 IRCOBI Conference, Lisbon, Portugal, pp. 27–38, 24–27 September 2003
6. Rowson, S., Brolinson, G., Goforth, M., et al.: Linear and angular head acceleration measurements in collegiate football. *J. Biomech. Eng.* **131**(6), 061016 (2009)
7. Yang, K.H., Hu, J., White, N.A., et al.: Development of numerical models for injury biomechanics research: a review of 50 years of publications in the Stapp Car Crash Conference. *Stapp Car Crash J.* **50**, 429–490 (2006)
8. Nahum, A.M., Smith, R., Ward, C.C.: Intracranial pressure dynamics during head impact. Proceedings of the 21st Stapp Car Crash Conference, SAE Paper No. 770922 (1977)
9. Trosseille, X., Tarriere, C., Lavaste, F., et al.: Development of a FEM of the human head according to a specific test protocol. Proceedings of the 30th Stapp Car Crash Conference, SAE 922527, pp. 235–253 (1992)
10. Hardy, W.N., Foster, C.D., Mason, M.J., et al.: Investigation of head injury mechanisms using neutral density technology and high-speed biplanar x-ray. *Stapp Car Crash J.* **45**, 337–368 (2001)

11. Hardy, W.N., Mason, M.J., Foster, C.D., et al.: A study of the response of the human cadaver head to impact. *Stapp Car Crash J.* **51**, 17–80 (2007)
12. Viano, D.C., Casson, I.R., Pellman, E.J., et al.: Concussion in professional football: brain responses by finite element analysis – part 9. *J. Neurosurg.* **57**, 891–916 (2005)
13. Marjoux, D., Baumgartner, D., Deck, C., et al.: Head injury prediction capability of the HIC, HIP, SIMon and ULP criteria. *Accid. Anal. Prev.* **40**(3), 1135–1148 (2008)
14. Kleiven, S.: Predictors for traumatic brain injuries evaluated through accident reconstructions. *Stapp Car Crash J.* **51**, 81–114 (2007)
15. Franklyn, M., Fildes, B., Zhang, L., et al.: Analysis of finite element models for head injury investigation: reconstruction of four real-world impacts. *Stapp Car Crash J.* **49**, 1–32 (2005)
16. Zhang, L., Yang, K.H., King, A.I.: A proposed new injury tolerance for mild traumatic brain injury. *J. Biomech. Eng.* **126**, 226–236 (2004)
17. Ruan, J., Prasad, P.: The effects of skull thickness variations on human head dynamic impact responses. *Stapp Car Crash J.* **45**, 395–414 (2001)
18. Kabbani, H., Raghubeer, T.S.: Craniostylosis. *Am. Fam. Physician* **69**(12), 2863–2870 (2004)
19. Ward, C., Thompson, R.B.: The development of a detailed finite element brain model, 19th Stapp Car Crash Conference, San Diego, CA, USA, SAE 751163 (1975)
20. Li, J., Zhang, J., Yoganandan, N., et al.: Regional brain strains and role of falx in lateral impact-induced head rotational acceleration. *Biomed. Sci. Instrum.* **43**, 24–29 (2007)
21. Haines, D.E., Harkey, H.L., Al-Mefty, O.: The “subdural” space: a new look at an outdated concept. *Neurosurgery* **32**(1), 111–120 (1993)
22. Cloots, R.J., Gervaise, H.M., van Dommelen, J.A., et al.: Biomechanics of traumatic brain injury: influences of the morphologic heterogeneities of the cerebral cortex. *Ann. Biomed. Eng.* **36**(7), 1203–1215 (2008)
23. Elkin, B.S., Azeloglu, E.U., Costa, K.D., et al.: Mechanical heterogeneity of the rat hippocampus measured by atomic force microscope indentation. *J. Neurotrauma* **24**(5), 812–822 (2007)
24. van Dommelen, J.A., van der Sande, T.P., Hrapko, M., et al.: Mechanical properties of brain tissue by indentation: interregional variation. *J. Mech. Behav. Biomed. Mater.* **3**(2), 158–166 (2010)
25. Gennarelli, T.A., Thibault, L.E.: Biomechanics of acute subdural hematoma. *J. Trauma* **22**(8), 680–686 (1982)
26. Maxeiner, H., Wolff, M.: Pure subdural hematomas: a postmortem analysis of their form and bleeding points. *Neurosurgery* **50**, 503–509 (2002)
27. Lee, M.C., Haut, R.C.: Insensitivity of tensile failure properties of human bridging veins to strain rate: implications in biomechanics of subdural hematoma. *J. Biomech.* **22**(6–7), 537–542 (1989)
28. Löwenhielm, P.: Dynamic properties of the parasagittal bridging veins. *Z. Rechtsmed.* **74**, 55–62 (1974)
29. Ho, J., Kleiven, S.: Dynamic response of the brain with vasculature: a three-dimensional computational study. *J. Biomech.* **40**(13), 3006–3012 (2007)
30. Zhang, L., Bae, J., Hardy, W.N., et al.: Computational study of the contribution of the vasculature on the dynamic response of the brain. *Stapp Car Crash J.* **46**, 145–164 (2002)
31. Serrador, J.M., Picot, P.A., Rutt, B.K., et al.: MRI measures of middle cerebral artery diameter in conscious humans during simulated orthostasis. *Stroke* **31**(7), 1672–1678 (2000)
32. MacNeal, R.H., Harder, R.L.: A proposed standard set of problems to test finite element accuracy. *Finite Elem. Anal. Des.* **1**, 3–20 (1985)
33. Hughes, T.J.R.: The Finite Element Method – Linear Static and Dynamic Finite Element Analysis, Chapter 4. Prentice-Hall, New Jersey (1987). ISBN 0-13-317025-X
34. Jin, X., Lee, J.B., Leung, L.Y., et al.: Biomechanical response of the bovine pia-arachnoid complex to tensile loading at varying strain-rates. *Stapp Car Crash J.* **50**, 637–649 (2006)
35. Jin, X., Ma, C., Zhang, L., et al.: Biomechanical response of the bovine pia-arachnoid complex to normal traction loading at varying strain rates. *Stapp Car Crash J.* **51**, 115–126 (2007)
36. Jin, X.: Biomechanical response and constitutive modeling of bovine pia-arachnoid complex. Ph.D. thesis, Wayne State University (2009)

37. Gurdjian, E.S., Webster, J.E.: Head Injuries, pp. 62–76. Little Brown, Boston (1958)
38. Gurdjian, E.S., Lissner, H.R., Hodgson, V.R., et al.: Mechanisms of head injury. *Clin. Neurosurg.* **12**, 112–128 (1966)
39. Ommaya, A.K., Grubb, R.L., Naumann, R.A.: Coup and contrecoup injury: observations on the mechanics of visible brain injuries in the rhesus monkey. *J. Neurosurg.* **35**, 503–516 (1971)
40. Gennarelli, T.A., Adams, J.H., Graham, D.I.: Acceleration induced head injury in the monkey. I. The model, its mechanical and physiological correlates. *Acta Neuropathol. Suppl.* **7**, 23–25 (1981)
41. Gennarelli, T.A., Thibault, L.E., Adams, J.H., Graham, D.I., Thompson, C.J., Marcincin, R.P.: Diffuse axonal injury and traumatic coma in the primate. *Ann Neurol.* **12**(6), 564–574 (1982)
42. Bandak, F.A., Eppinger, R.H.: A three-dimensional finite element analysis of the human brain under combined rotational and translational accelerations. Proceedings of the 38th Stapp Car Crash Conference, Ft. Lauderdale, FL. SAE, Warrendale (1994)
43. Takhounts, E.G., Eppinger, R.H., Campbell, J.Q., et al.: On the development of the SIMON finite element head model. *Stapp Car Crash J.* **47**, 107–133 (2003)
44. Shenkin, H.A.: Acute subdural hematoma. Review of 39 consecutive cases with high incidence of cortical artery rupture. *J. Neurosurg.* **57**, 254–257 (1982)
45. Gurdjian, E.S., Lissner, H.R., Latimer, F.R., et al.: Quantitative determination of acceleration and intracranial pressure in experimental head injury: preliminary report. *Neurology* **3**(6), 417–423 (1953)
46. White, N.A., Begeman, P.C., Hardy, W.N., et al.: Investigation of upper body and cervical spine kinematics of post mortem human subjects (PMHS) during low-speed, rear-end impacts. SAE 2009 World Congress and Expo 2009-01-0387 (2009)
47. Igarashi, T., Potts, M.B., Noble-Haeusslein, L.J.: Injury severity determines Purkinje cell loss and microglial activation in the cerebellum after cortical contusion injury. *Exp. Neurol.* **203**(1), 258–268 (2007)

# **Chapter 6**

## **Biomechanical Modeling of the Brain for Computer-Assisted Neurosurgery**

**K. Miller, A. Wittek, and G. Joldes**

### **6.1 Introduction**

During neurosurgery, the brain significantly deforms. Despite the enormous complexity of the brain (see Chap. 2) many aspects of its response can be reasonably described in purely mechanical terms, such as displacements, strains and stresses. They can therefore be analyzed using established methods of continuum mechanics. In this chapter, we discuss approaches to biomechanical modeling of the brain from the perspective of two distinct applications: neurosurgical simulation and neuroimage registration in image-guided surgery. These two challenging applications are described below.<sup>1</sup>

#### **6.1.1 *Neurosurgical Simulation for Operation Planning, Surgeon Training and Skill Assessment***

The goal of surgical simulation research is to model and simulate deformable materials for applications requiring real-time interaction. Medical applications for this include simulation-based training, skills assessment and operation planning.

Surgical simulation systems are required to provide visual and haptic feedback to a surgeon or trainee. Various haptic interfaces for medical simulation are especially

---

<sup>1</sup> Parts of this chapter were previously published in Miller et al. [1] and Wittek et al. [2].

K. Miller (✉)  
Intelligent Systems for Medicine Laboratory, School of Mechanical  
and Chemical Engineering, The University of Western Australia,  
35 Stirling Highway, Crawley/Perth, WA 6009, Australia  
e-mail: kmiller@mech.uwa.edu.au

useful for training surgeons for minimally invasive procedures (laparoscopy/interventional radiology) and remote surgery using tele-operators. These systems must compute the deformation field within a soft organ and the interaction force between a surgical tool and the tissue to present visual and haptic feedback to the surgeon. Haptic feedback must be provided at frequencies of at least 500 Hz [3]. From a solid-mechanical perspective, the problem involves large deformations, non-linear material properties and non-linear boundary conditions. Moreover, it requires extremely efficient solution algorithms to satisfy stringent requirements on the frequency of haptic feedback. Surgical simulation is a very challenging problem of solid mechanics.

When a simulator is intended to be used for surgeon training, a generic model developed from average organ geometry and material properties can be used in computations. However, when the intended application is for operation planning, the computational model must be patient-specific. This requirement adds to the difficulty of the problem – the question of how to rapidly generate patient-specific computational models still awaits a satisfactory answer.

### ***6.1.2 Image Registration in Image-Guided Neurosurgery***

One common element of most new therapeutic technologies, such as gene therapy, stimulators, focused radiation, lesion generation, nanotechnological devices, drug polymers, robotic surgery and robotic prosthetics, is that they have extremely localized areas of therapeutic effect. As a result, they have to be applied precisely in relation to the patient's current (i.e. intra-operative) anatomy, directly over the specific location of anatomic or functional abnormality [4]. Nakaji and Speltzer [5] list the “accurate localization of the target” as the first principle in modern neuro-surgical approaches.

As only pre-operative anatomy of the patient is known precisely from medical images (usually magnetic resonance images – MRI), it is now recognized that the ability to predict soft organ deformation (and therefore intra-operative anatomy) during the operation is the main problem in performing reliable surgery on soft organs. In the context of brain surgery, it is very important to be able to predict the effect of procedures on the position of pathologies and critical healthy areas in the brain. If displacements within the brain can be computed during the operation, then they can be used to warp pre-operative high-quality MR images so that they represent the current, intra-operative configuration of the brain, see Fig. 6.1.

The neuroimage registration problem involves large deformations, non-linear material properties and non-linear boundary conditions as well as the difficult issue of generating patient-specific computational models. However, it is easier than the previously discussed surgical simulation problem in two important ways. Firstly, we are interested in accurate computations of the displacement field only. Accuracy of stress computations is not required. Secondly, the computations must be conducted intra-operatively, which practically means that the results should be available to an

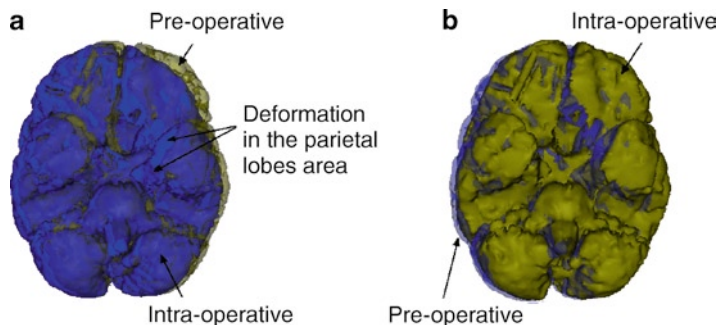


**Fig. 6.1** Comparison of a brain surface determined from images acquired pre-operatively with the one determined intra-operatively from images acquired after craniotomy. Inferior (i.e. “bottom”) view. (a) Pre-operative surface is semi-transparent; (b) Intra-operative surface is semi-transparent. Deformation of the brain surface due to craniotomy is clearly visible. Intra-operative displacements of over 20 mm have been reported in medical literature [90]. Surfaces were determined from the images provided by Department of Surgery, Brigham and Women’s Hospital (Harvard Medical School, Boston, MA, USA)

operating surgeon in less than 40 s [6–9]. This still forms a stringent requirement for computational efficiency of methods used, but is much more easily satisfied than the 500 Hz haptic feedback frequency requirement for neurosurgical simulation.

Following the Introduction (Sect. 6.1), in Sect. 6.2, we describe difficulties in modeling geometry, boundary conditions, loading and material properties of the brain. In Sect. 6.3, we consider example application in the area of computational radiology. Numerical algorithms devised to efficiently solve brain deformation behavior models are described in Chap. 9. We conclude this chapter with some reflections about the state of the field.

## 6.2 Biomechanics of the Brain-Modelling Issues

When considering approaches to modeling the brain, one should clearly realize whether the intended application is *generic* or *patient-specific*. If the biomechanical model is constructed for a generic application, e.g. a neurosurgical simulator for surgeon training, the typical, in some sense “average”, geometry and mechanical properties of an organ and tissues should be modeled. If, however, a patient-specific model is required, for example for operation planning, then clearly a “generic” model is of little utility and patient-specific data must be incorporated in the model. The reader is warned here that the question of how to generate patient-specific biomechanical models quickly and reliably remains unresolved (see Chap. 9 for current attempts to address this issue using meshless methods). Another aspect worth considering is that for computational biomechanics to be accepted and beneficial in clinical practice, biomechanical computations must be seamlessly

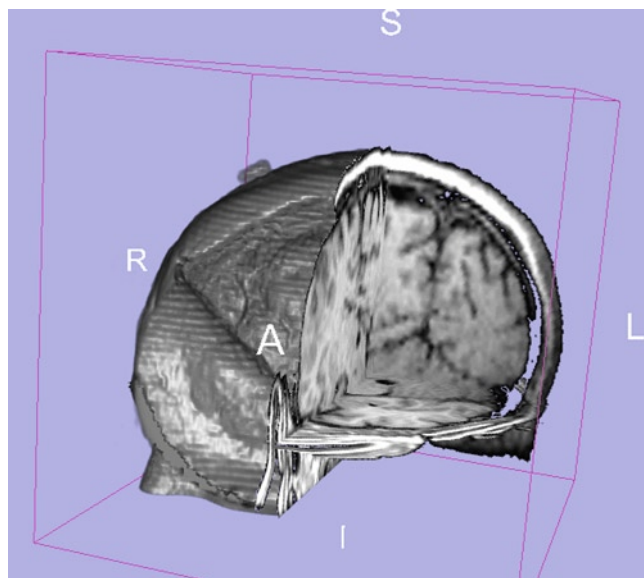


**Fig. 6.2** 3D magnetic resonance image (MRI) presented as a tri-planar cross-section. Slices with clearly visible tumors are shown in Sect. 6.3, Fig. 6.8. Public domain software Slicer ([www.slicer.org](http://www.slicer.org)), developed by our collaborators from Surgical Planning Laboratory, Harvard Medical School, was used to generate the image

incorporated in the clinical work flow. This can only be achieved if these computations are conducted in real or at least close to real-time (how to achieve this is discussed in Chap. 9).

In the remainder of this section, we will discuss the main modeling issues: geometry, boundary conditions, loading and tissue mechanical properties.

### 6.2.1 Geometry

Detailed geometric information is needed to define the domain in which the deformation field needs to be computed. Such information is provided by electronic brain atlases described in detail in Chap. 2. In applications that do not require patient-specific data (such as neurosurgical simulators for education and training), the geometric information provided by these atlases is sufficient. However, other applications such as neurosurgical simulators for operation planning and image registration systems do require patient-specific data. This patient-specific data can be obtained from radiological images (for examples see Fig. 6.2 and Chap. 3); however, the quality is significantly inferior to the data available from anatomical atlases (see Chap. 2).

The accuracy of neurosurgery is not better than 1 mm [4]. Voxel size in high-quality pre-operative MR images is usually of similar magnitude. Therefore, we can conclude

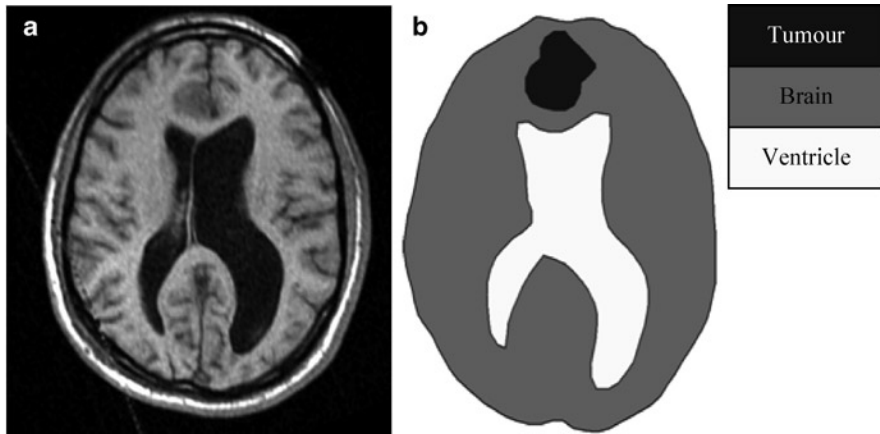


**Fig. 6.3** (a) 2D slice of 3D brain MR volume; (b) Segmented image. Such “hard” segmentation is necessary for finite element mesh development

that patient-specific models of the brain geometry can be constructed with approximately 1 mm accuracy, and that higher accuracy is probably not required. The question arises, however, of which brain structures should be explicitly included in the model and which omitted? As described in Chap. 2, anatomists recognize well over a 1,000 structures within the brain. Very little (if anything) is known about relative mechanical properties of these structures. Therefore, even the most sophisticated models used by the scientific community only include brain parenchyma, ventricles, tumor (if present) and skull. A necessary step in constructing patient-specific models of brain geometry is medical image *segmentation*. Segmentation is a process that essentially explains what is what on the image, see Fig. 6.3.

Unfortunately, despite years of effort by the medical image analysis community, a generally accepted automatic brain MRI segmentation method is not yet available. In practice, very laborious semi-automatic or manual methods are employed [2, 10]. It is clear that if one attempted to include many brain structures in the patient-specific biomechanical model, then one would need to identify them in the medical image and segment them. This is a daunting task that at the time of writing does not appear to be practical.

On the other hand, when a generic application that does not require patient-specific data is considered, the 3D geometry of essentially all structures that might possibly be of interest can be imported from electronic brain atlases. For example, a hippocampus is often of interest, and its geometry and location can be clearly seen in Fig. 2.6 of Chap. 2.

To develop a numerical model of the brain biomechanics, it is necessary to create a computational grid, which in most practical cases is a finite element mesh (or a cloud of points required by a meshless method, see also Chaps. 5 and 9). Because of the stringent computation time requirements, the mesh must be constructed using low order elements that are computationally inexpensive. The linear under-integrated hexahedron is the preferred choice.

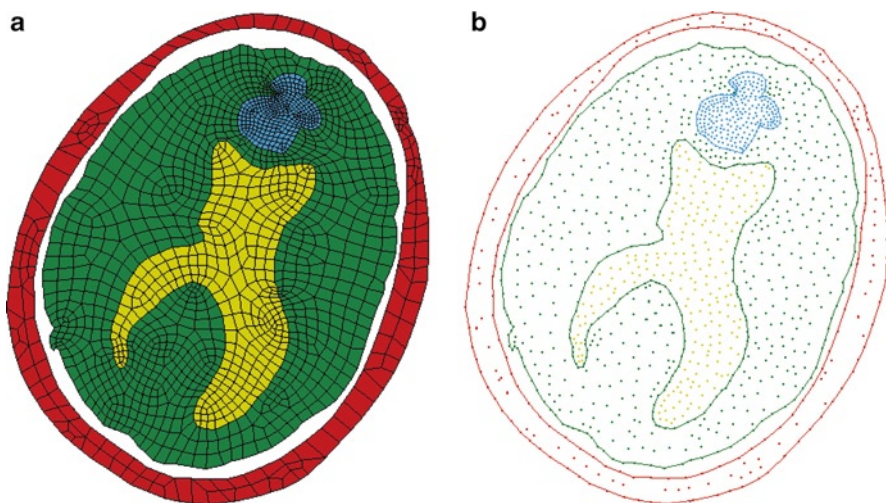


**Fig. 6.4** A 2D slice of the brain discretized by (a) quadrilateral finite elements; and (b) nodes of the modified Element-Free Galerkin method. Development of a good-quality finite element mesh is time-consuming. Generation of the meshless grid is almost instantaneous

Many algorithms are now available for fast and accurate automatic mesh generation using tetrahedral elements, but not for automatic hexahedral mesh generation [11–13]. Template-based meshing algorithms can be used for discretizing different organs using hexahedrons [14–16], but these types of algorithms only work for healthy organs. In the case of severe pathologies (such as a brain tumor or severely enlarged ventricles), such algorithms cannot be used as the shape, size and position of the pathology are unpredictable. This is one reason why many authors proposed the use of tetrahedral meshes for their models [6, 8, 17, 18]. In order to automate the simulation process, mixed meshes having both hexahedral and linear tetrahedral elements are the most convenient. Examples of such meshes are shown in Fig. 6.9 in the next section.

An alternative to using the finite element method is to use one of the available meshless methods. The problem of generating the computational grid disappears as one needs only to drop a cloud of points into the volume defined by a 3D medical image [19–25], see Fig. 6.4. Details of Meshless Total Lagrangian algorithm for computing soft tissue deformations are given in Chap. 9.

### 6.2.2 *Boundary Conditions*

The formulation of appropriate boundary conditions for computation of brain deformation during surgery constitutes a significant problem because of the complexity of the brain–skull interface (see Fig. 5.3 in Chap. 5 on modeling the brain for injury prevention where this problem is also highlighted).

A number of researchers fix the brain surface to the skull [26, 27]. We do not recommend this approach. One alternative is to use a gap between the brain and the skull that allows for motion of the brain within the cranial cavity [9, 28–32]. Another alternative is to use a frictionless sliding (with separation) contact model [33, 34], which can be incorporated into finite element computations very efficiently, see Chap. 9. The reader should be warned, however, that biomechanical knowledge about the properties of the brain–skull interface is very limited [35] and the brain–skull interface models used in the literature are “best guesses” and their relation to reality is unclear.

The skull should be included in the model either explicitly or in the form of an appropriate boundary condition for the brain. As the skull is orders of magnitude stiffer than the brain tissue, its rigidity can be assumed. The spine–spinal cord interactions and constraining effects of the spinal cord on the brain’s rigid body motion can be simulated by constraining the spinal end of the model.

### 6.2.3 *Loading*

We advocate loading the models through imposed displacements on the model surface, [2, 9, 30, 36] see Fig. 6.5. In the case of neurosurgical simulation, this loading will be imposed by known motion of a surgical tool. In the case of intra-operative image, registration the current (intra-operative) position of the exposed part of the brain surface can be measured using various techniques [37]. This information can then be used to define model loading.

As suggested in papers [36, 38–40] for problems where loading is prescribed as forced motion of boundaries, the unknown deformation field within the domain depends very weakly on the mechanical properties of the continuum. As this feature is of great importance in biomechanical modeling, where there are always uncertainties in patient-specific properties of tissues, it warrants more detailed discussion.

Let us look at this from the perspective of non-rigid image registration in intra-operative image-guided procedures where high-resolution pre-operative scans are warped onto lower quality intra-operative ones [7, 41]. We are particularly interested in registering high-resolution pre-operative MRIs with lower quality intra-operative imaging modalities, such as multi-planar MRIs and intra-operative ultrasound.

This problem, when viewed from the perspective of a mechanical or civil engineer, can be considered as follows: the brain, whose detailed pre-operative image is available, after craniotomy, due to a number of physical and physiological reasons, deforms (so-called brain shift). We are interested in the intra-operative (i.e. current) position of the brain, of which partial information is provided by low-resolution intra-operative images. In mathematical terms, this problem can be described by equations of solid mechanics.

Consider motion of a deforming body in a stationary co-ordinate system, Fig. 6.6.

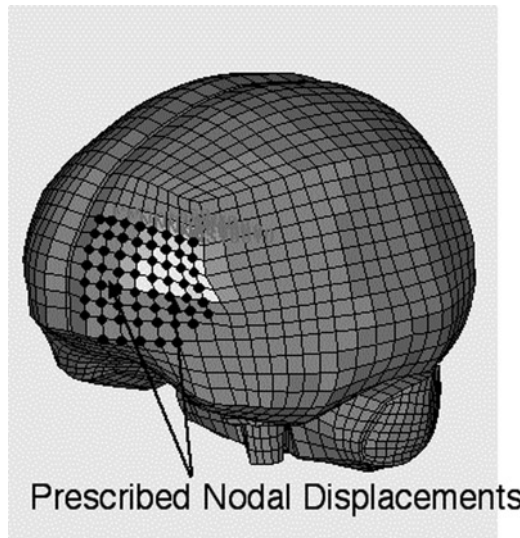


**Fig. 6.5** Model loading through prescribed nodal displacements at the exposed brain surface

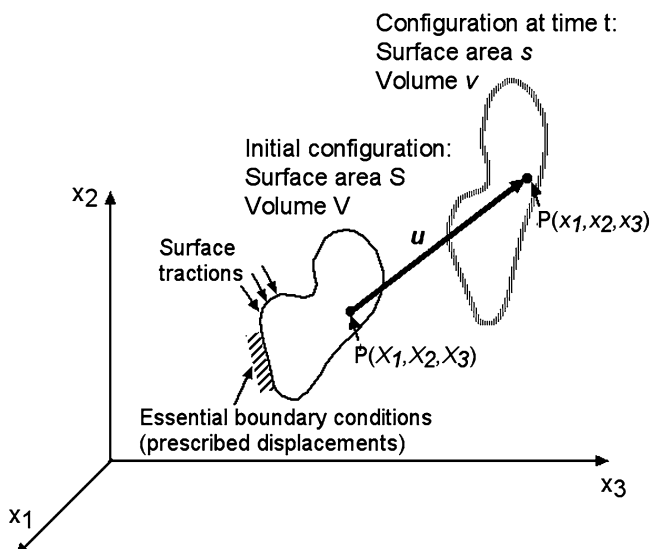


**Fig. 6.6** Motion of a body in a stationary co-ordinate system. Initial configuration, described by upper case coordinates, can be considered as a high-quality pre-operative image. Current, deformed configuration (described by lower-case coordinates) is unknown; however, partial information is available from a lower resolution intra-operative image

In the analysis, we follow all particles in their motion, from the original to the final configuration of the body, which means that the Lagrangian (or material) formulation of the problem is adopted. Motion of the system sketched in Fig. 6.6 can be described by equations of motion often written in so-called weak formulation:

$$\int_V \tau_{ij} \delta \epsilon_{ij} dV = \int_V f_i^B \delta u_i dV + \int_S f_i^S \delta u_i dS, \quad (6.1)$$

where  $\epsilon$  is the Almansi strain,  $\int_V \tau_{ij} \delta \epsilon_{ij} dV$  is the internal virtual work,  $\int_V f_i^B \delta u_i dV$  is the virtual work of external body forces (this includes inertial effects), and  $\int_S f_i^S \delta u_i dS$  is the virtual work of external surface forces. As the brain undergoes finite deformation, current volume  $V$  and surface  $S$ , over which the integration is to be conducted, are unknown: they are part of the solution rather than input data. Therefore, appropriate solution procedures which allow finite deformation must be used, see Chap. 9. Integral equation (9.1) must be supplemented by formulae describing the mechanical properties of materials, i.e. appropriate constitutive models. However, an important advantage of the weak formulation is that the essential (displacement) boundary conditions are automatically satisfied [42].

Boundary conditions may prescribe kinematic variables such as displacements and velocities (essential boundary conditions) or tractions (natural boundary conditions, these also include point forces). It should be noted that “boundary conditions” do not have to be applied at the physical boundary of the deforming object.

Depending on the amount of information about the intra-operative position of the brain available from intra-operative imaging modalities, brain registration can be described in mathematical terms as follows:

**Case I:** Entire boundary of the brain can be extracted from the intra-operative image.  
Mathematical description:

- Known: initial position of the domain (i.e. the brain), as determined from pre-operative MRI
- Known: current position of the entire boundary of the domain (the brain)
- Unknown: displacement field within the domain (the brain), in particular current position of the tumor and critical, from the perspective of a surgical approach, healthy tissues

No information of surface tractions is required for the solution of this problem. Problems of this type are called in theoretical elasticity “pure displacement problems” [43].

**Case II:** Limited information about the boundary (e.g. only the position of the brain surface exposed during craniotomy) and perhaps about current position of clearly identifiable anatomical landmarks, e.g. as described in [44]. No external forces applied to the boundary. Mathematical description:

- Known: initial position of the domain (i.e. the brain), as determined from pre-operative MRI

- Known: current position of some parts of the boundary of the domain (the brain); zero pressure and traction forces everywhere else on the boundary
- Unknown: displacement field within the domain (the brain), in particular current position of the tumor and critical healthy tissues

Problems of this type are very special cases of so-called “displacement – traction problems” that have not, to the best of our knowledge, been considered as a separate class and no special methods of solution for these problems exist. In Miller [45], it was suggested to call such problems “displacement – zero traction problems”.

The solution in displacements for both pure displacement problems and displacement-zero traction problems is only very weakly sensitive to mechanical properties of the deforming continuum. To see why let us first consider an (oversimplified) linear-elastic case. Then the following simple dimensional reasoning applies: The loading is provided by the enforced motion of boundaries measured in meters [m]; the result of computations are displacements measured in [m]; therefore the result cannot depend on the stress parameter measured in [ $\text{Pa} = \text{N/m}^2$ ]. We should note here that the result can depend on (dimensionless) Poisson’s ratio and on (dimensionless) ratios of stress parameters if the model contains different materials with different stiffness. In the general non-linear case, the displacement results will still remain insensitive to the stress parameter appearing in the non-linear material law, but may depend on the particular form of that law. This dependency can, however, be expected to be rather weak. The explicit demonstration of this was given in [38, 40] where the shapes of compressed and extended cylinders were shown to be essentially independent of the material law used for the cylinder’s material, see Fig. 6.7.

In the case of the full-scale brain deformation computation, our experience confirms the expected insensitivity of computed displacement fields to chosen tissue constitutive models [30]. This result is important because it demonstrates the utility of computational biomechanics even in the most common situation when the patient-specific mechanical properties of tissues remain unknown.

#### **6.2.4 Models of Mechanical Properties of Brain Tissue**

The first question to address is whether a single-phase continuum model for the tissue should be used or if bi-phasic and even more complicated multi-phase models are preferable. Many researchers conclude that the brain is obviously a hydrated tissue and therefore use bi-phasic models based on consolidation theory, see e.g. [46] and references cited therein. We are of the opinion that bi-phasic, consolidation theory-based models are inconsistent with brain tissue behavior observed in simple experiments. For example, no leakage of CSF was observed in brain tissue samples loaded by CSF pressure difference [47]. Another argument against using bi-phasic models is that during numerous unconfined compression experiments [48], we never

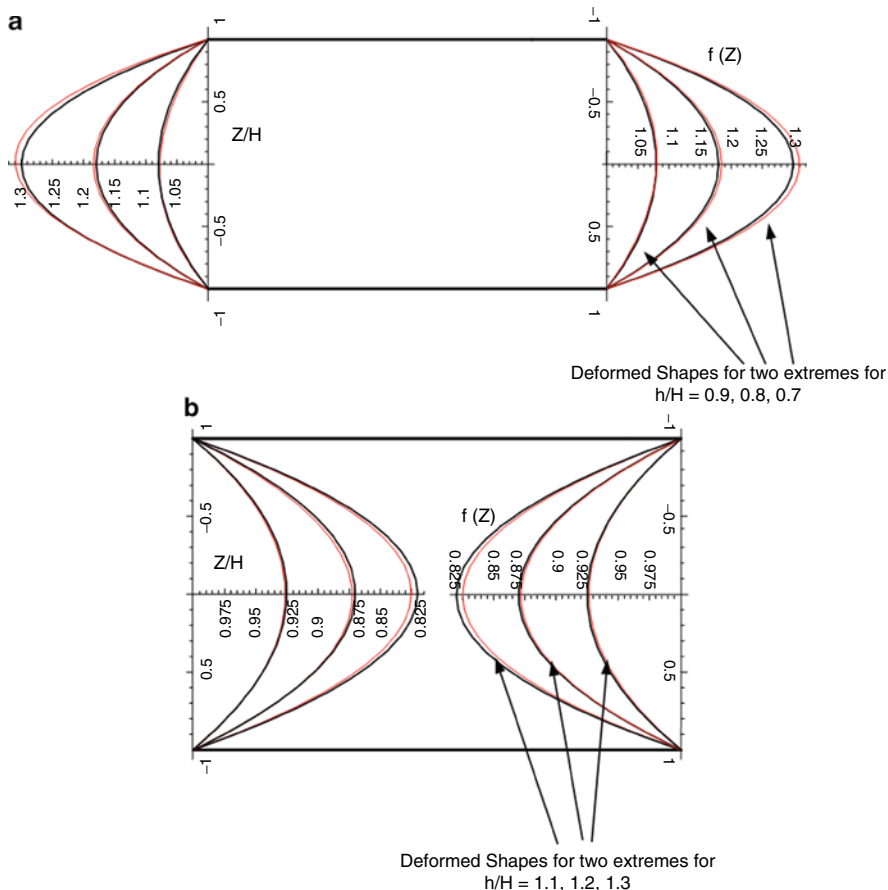


**Fig. 6.7** Shapes of cylinders modeled as Extreme-Mooney and Neo-Hookean materials. **(a)** compression by 10, 20 and 30%. **(b)** extension by 10, 20 and 30%.  $Z/H$  denotes a dimensionless coordinate along the height of the cylinder.  $f(Z)$  stands for the shape of the side of the deformed cylinder. Shape of a cylinder made from a “real” material is expected to fall between the two extremes

observed fluid leaking from the side of the samples. Such leakage is predicted by a bi-phasic theory. Therefore, in the remainder of this chapter, we will discuss only single-phase modeling approaches.

Experimental results show that the mechanical response of brain tissue to external loading is very complex. The stress-strain relationship is clearly non-linear with no portion in the plots suitable for estimating a meaningful Young’s modulus. It is also obvious that the stiffness of the brain in compression is much higher than in extension. The non-linear relationship between stress and strain-rate is also apparent. Detailed exposition of the current knowledge about mechanical properties of brain tissue is given in Chap. 4. Here we only discuss modeling issues directly pertinent to modeling neurosurgery.

The great majority of brain models assume brain tissue *incompressibility* and *isotropy* (see also Chaps. 4 and 5). The assumption of incompressibility is not contentious. Whether it is reasonable to assume brain tissue to be isotropic (i.e. mechanical properties to be the same in all directions) is less clear, especially in view of the obviously directional character of white matter fibers. Brain tissues do not normally bear mechanical loads and do not exhibit directional structure, provided that a large enough length scale is considered. Therefore, they may be assumed to be initially isotropic, see e.g. [49–57]. When modeling brain deformations during surgery, we need to keep in mind that the accuracy of displacement computations rarely needs to be better than about 1 mm – the claimed accuracy of neurosurgery. Therefore, “average isotropic” properties at the length scales relevant to surgical procedures are most probably sufficient. These properties are relatively well accounted for by an Ogden-type hyperviscoelastic model [54] described in Chap. 4, equations (4.4) and (4.5).

Average properties, such as those described above, are not sufficient for patient-specific computations of stresses and reaction forces because of the very large variability inherent to biological materials. This variability is clearly demonstrated in the biomechanics literature, see e.g. [54, 58–60]. Unfortunately, despite recent progress in elastography using ultrasound [61] and magnetic resonance [62–64], reliable methods of measuring patient-specific properties of the brain are not yet available.

Nevertheless, as shown in the previous section on modeling loading, a lot can be achieved even without a patient-specific model of brain tissue mechanical properties if the model is loaded by the enforced motion of a boundary and the problem is formulated as a pure displacement or displacement-zero traction problem. As the computed results are then almost insensitive to the assumed mechanical properties of the tissue, we advocate using the simplest model that is compatible with finite deformation solution procedures: a Neo-Hookean model:

$${}^0S = \mu J^{-2/3} \left( I_3 - \frac{1}{3} I'_0 C^{-1} \right) + k (J - 1) J'_0 C^{-1}, \quad (6.2)$$

where  ${}^0S$  is the second Piola-Kirchhoff stress,  $I$  is the first invariant of the deviatoric Right Cauchy Green deformation tensor  $C$  (the first strain invariant),  $J$  is the determinant of the deformation gradient (representing the volume change),  $I_3$  is the  $3 \times 3$  identity matrix,  $\mu$  is the shear modulus, and  $k$  is the bulk modulus of the material.

The accuracy of this approach is demonstrated in the next section.

### 6.2.5 Model Validation

For mathematical modeling and computer simulation to be of any practical use – to be *reliable* [65] – the results derived from the models must be known to lie within

the prescribed margins of accuracy. As we have seen in Chap. 5, ascertaining that this is the case when modeling high-speed impacts and brain injury is a very difficult task. Modelers of the brain for neurosurgery are, however, in a better position – they have at their disposal intra-operative imaging modalities (see Chap. 3) providing images that can be used for a relatively straightforward validation of the results of computer simulations of brain deformations.

Biomechanical models of the brain contain a lot of simplifying assumptions to make them mathematically and computationally tractable. To be of practical use, solutions to these models must be obtained in real or close-to-real time. Therefore, often non-standard, specially designed solution algorithms and software implementations are used (see Chap. 9). It is very important, and unfortunately overlooked by many researchers, that the biomechanical model and solution method be validated separately! For, if we evaluated a “software system” consisting of implemented non-standard solution algorithms to a complicated biomechanical model and found discrepancies when compared with experiments, we would have no indication whether these discrepancies are due to inappropriate modeling assumptions or faulty numerical procedure (or both).

We recommend that the new real-time solution algorithms be verified against well-established solution procedures implemented in commercial software. The assumptions of the biomechanical model need to be evaluated against available experimental data. The biomechanical model should then be validated by comparing the solutions computed using established numerical procedures and the experiment. If these hurdles are cleared and it can be also demonstrated that replacing established numerical procedures with the specialized ones developed for real-time applications does not affect the computed results, then one may treat the “software system” with some confidence.

How accurate should the results of the computational biomechanics model of the brain be? Accuracy of manual neurosurgery is not better than 1 mm. The voxel size of currently the best available experimental tool for model validation – the intra-operative MRI – is of the same order. Therefore, the computed intra-operative displacements do not need to be more accurate than about 1 mm. We may note here that, paradoxically, this accuracy requirement is much less stringent than what we are used to in traditional engineering disciplines. How about stresses? In image-guided surgery applications, we are not interested in stress distributions, only in the displacement field. This is one of the reasons simple constitutive models of the brain tissue can be used. However, for surgical simulation applications, we need to compute reaction forces on surgical tools that will be displayed to the user through a haptic interface. At present, there is no consensus regarding how accurate this haptic feedback should be to facilitate the user’s realistic experience. Given the present state of biomechanical knowledge, the best that can be achieved is qualitative agreement between real and computed interaction forces (see e.g. [55]). This is despite examples of excellent agreement between computations and phantom experiments [66] as well as controlled *in vitro* experiments [67].

## 6.3 Application Example: Computer Simulation of the Brain Shift

A particularly exciting application of non-rigid image registration is in intra-operative image-guided procedures, where pre-operative scans are warped onto sparse intra-operative ones [7, 41]. We are especially interested in registering high-resolution pre-operative MRIs with lower quality intra-operative imaging modalities, such as multi-planar MRIs and intra-operative ultrasound. To achieve accurate matching of these modalities, precise and fast algorithms to compute tissue deformations are fundamental.

Here we present the analysis of five cases of craniotomy-induced brain shift representing different situations that may occur during neurosurgery [2].

### 6.3.1 *Generation of Computational Grids: From Medical Images to Finite Element Meshes*

Three-dimensional patient-specific brain meshes were constructed from the segmented pre-operative MRIs (Fig. 6.8) obtained from the anonymized retrospective database of Computational Radiology Laboratory (Children’s Hospital, Boston, MA). The parenchyma, ventricles and tumor were distinguished in the segmentation process, Fig. 6.8.

Because of the stringent computation time requirements, the meshes had to be constructed using low order elements that are not computationally expensive. The under-integrated hexahedron with linear shape functions is the preferred choice due to its superior convergence and accuracy characteristics. To partly automate the meshing, we used mixed meshes consisting of both hexahedral and tetrahedral elements with linear shape functions (Fig. 6.9, Table 6.1). The meshes were built using IA-FEMesh (a freely available software toolkit for hexahedral mesh generation developed at the University of Iowa) [68] and HyperMesh™ (a high-performance commercial finite element mesh generator by Altair, Ltd. of Troy, MI, USA). Following the literature [69, 70], hexahedral elements with Jacobian of below 0.2 were regarded as unacceptably poor quality and replaced with the tetrahedral elements. Because of irregular geometry of ventricles and tumor, vast majority of tetrahedral elements were located in the ventricles and tumor as well as in the adjacent parenchyma areas. It took between 1 and 2 working days for a graduate student (assisted by an experienced finite element analyst) to generate the brain mesh for each of the craniotomy cases analyzed in this study.

As the parenchyma was modeled as an incompressible continuum, average nodal pressure (ANP) formulation by [71] was applied to prevent volumetric locking (i.e. artificial stiffening due to incompressibility) in the tetrahedral elements. We refer to these elements as non-locking ones.

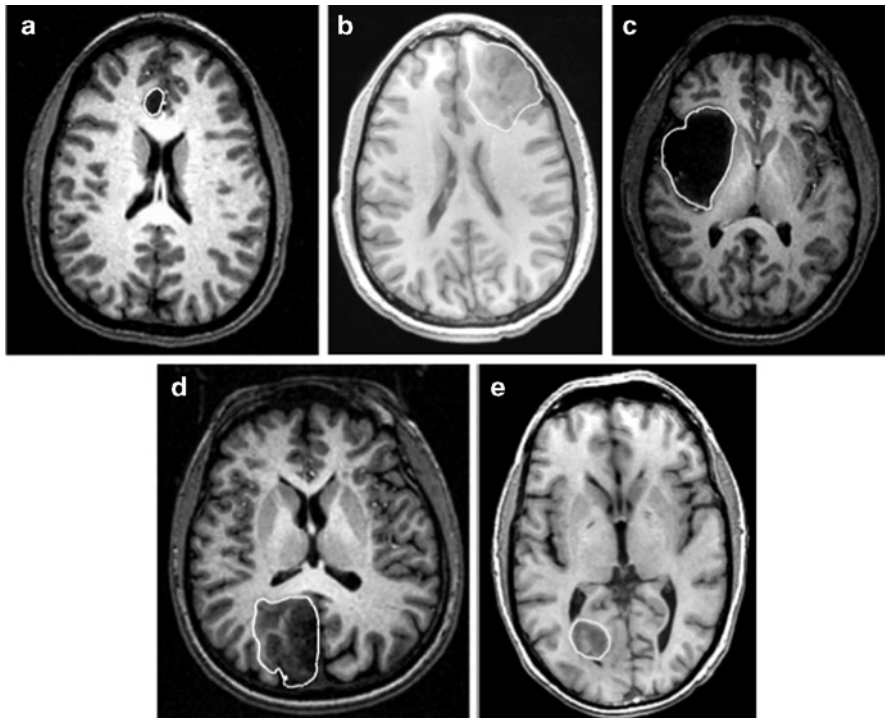


**Fig. 6.8** Pre-operative T1 MRI showing tumor location in five craniotomy cases analyzed in this study. White lines indicate the tumor segmentations

To eliminate instabilities (known as zero-energy modes or hourgassing) that arise from single-point integration, the stiffness-based hourglass control method by [72] was used for under-integrated hexahedral elements.

The non-locking tetrahedron and the hourglass control method are described in detail in Chap. 9.

### 6.3.2 Loading, Boundary Conditions and Brain Tissue Constitutive Model

There are always uncertainties regarding the patient-specific properties of the living tissues. To reduce the effects of such uncertainties, we loaded the models by prescribing displacements on the exposed (due to craniotomy) part of the brain surface (Fig. 6.5). As discussed in Sect. 6.2.3, for this type of loading the unknown deformation field within the brain depends very weakly on the mechanical properties of the brain tissues. The displacements for loading the models were determined from distances between the pre-operative and intra-operative cortical

**Fig. 6.9** Patient-specific brain meshes. **(a)** Case 1; **(b)** Case 2; **(c)** Case 3; **(d)** Case 4; **(e)** Case 5. Because of the complex geometry of ventricles and tumor, tetrahedral elements were mainly used for discretization of the ventricles and tumor as well as the adjacent parenchyma areas

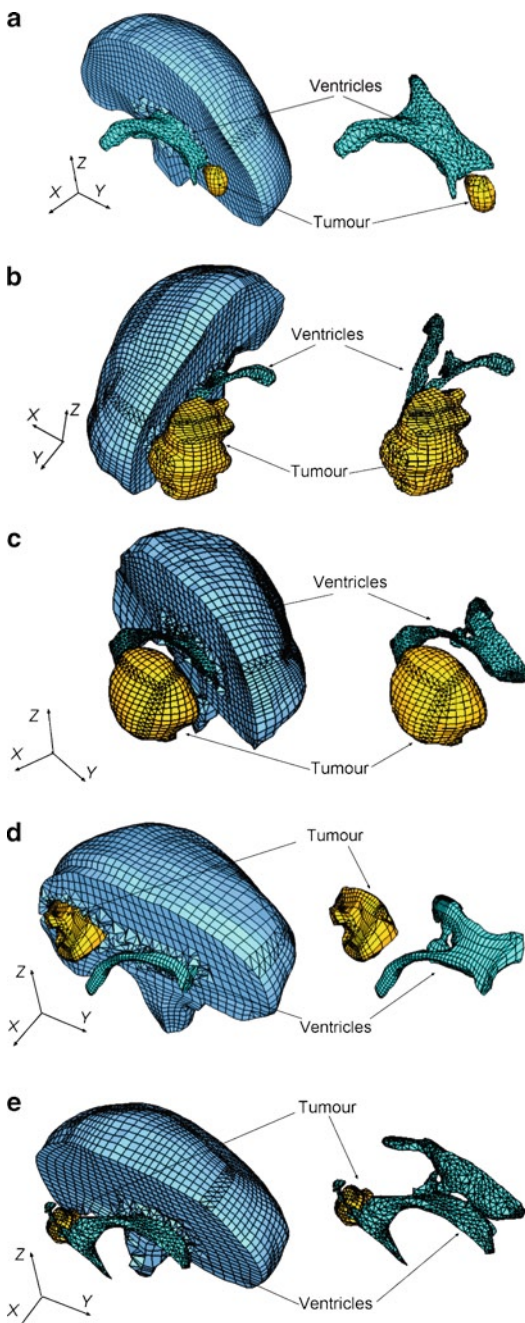


**Table 6.1** Summary of the patient-specific brain meshes used in this study. Every node in the mesh has three degrees of freedom

	Case 1	Case 2	Case 3	Case 4	Case 5
Number of hexahedral elements	14,447	10,258	10,127	9,032	8,944
Number of tetrahedral elements	13,563	20,316	23,275	23,688	21,160
Number of nodes	18,806	15,433	15,804	14,732	14,069

surfaces segmented in the MRIs. The correspondences between the pre-operative and intra-operative surfaces were determined by applying the vector-spline regularization algorithm to the surface curvature maps [73, 74].

To define the boundary conditions for the remaining nodes on the brain model surface, a contact interface was defined between the rigid skull model and areas of the brain surface where the nodal displacements were not prescribed. This formulation prevents the brain surface from penetrating the skull while allowing for frictionless sliding and separation between the brain and skull, see Chap. 9 for details. Although modeling of the brain-skull interactions through a sliding contact with separation may be viewed as an oversimplification since the anatomical structures forming the interface between the brain and skull are not directly represented, such modeling has been widely used in the literature when computing the brain deformations during brain shift [9, 29, 75].

Despite continuous efforts (see Chap. 4), commonly accepted non-invasive methods for determining patient-specific constitutive properties of the brain and other soft organs' tissues have not been developed yet. Constitutive models of the brain tissue applied for computing the brain deformation for non-rigid registration vary from simple linear-elastic model [76] to Ogden-type hyperviscoelasticity [9] and bi-phasic models relying on consolidation theory [77]. However, as explained in more detail in Sect. 6.2.3, the strength of the modeling approach used in this study is that the calculated brain deformations depend very weakly on the constitutive model and mechanical properties of the brain tissues. Therefore, following [33], we used the simplest hyperelastic model, the Neo-Hookean [78].

Based on the experimental data by Miller et al. [55] and Miller and Chinzei [54]), the Young's modulus of 3,000 Pa was assigned for the brain parenchyma tissue. For the tumor, we used the Young's modulus two times larger than for the parenchyma. This is consistent with the experimental data of [63]. As the brain and other very soft tissues are most often assumed to be incompressible, the Poisson's ratio of 0.49 was used for the parenchyma and tumor. Following [9], the ventricles were assigned the properties of a very soft compressible elastic solid with Young's modulus of 10 Pa and Poisson's ratio of 0.1 to account for possibility of leakage of the cerebrospinal fluid from the ventricles during surgery.

### 6.3.3 Results and Validation

In image-guided surgery, accuracy of tissue motion prediction is typically assessed by evaluating the accuracy of alignment between the registered position of the pre-operative image predicted by the non-rigid registration and the actual patient position established by an intra-operative image or navigation system. Universally accepted “gold standards” for such evaluation have not been developed yet [79]. Objective metrics for the alignment of the image can be provided by automated methods using image similarity metrics, e.g. Mutual Information [80, 81] and Normalized Cross-Correlation [82]. From the perspective of validation of biomechanical models for computing the deformation field within the brain, one of the key deficiencies of such metrics is that they quantify the alignment error in terms that do not have straightforward geometrical interpretation in terms of Euclidean distance. Therefore, validation of predictions obtained using biomechanical models has often been done using landmarks manually selected (by neuroradiology experts) in the MRIs [6, 29]. Although interpretation of the results of landmarks-based validation is very straightforward, the method provides accuracy estimation only at the landmark locations. Furthermore, determining these locations is typically very time-consuming and its accuracy relies on the experience of an expert [83].

Another option is to use the 95-percentile Hausdorff distance between sets; in our case non-rigidly registered pre-operative surfaces of the tumor and ventricles and surfaces of the tumor and ventricles obtained from the intra-operative image segmentation. We have followed this procedure in [2]. However, the resulting Hausdorff distances are highly sensitive to the segmentation accuracy. We feel that the qualitative results in the visual form of overlayed images are more reliable and convincing.

A detailed comparison between the contours of ventricles in the intra-operative images and the ones predicted by the finite element brain models is presented in Figs. 6.10 and 6.11. The comparison indicates good overall agreement between the predicted and actual intra-operative contours with the differences not exceeding the voxel size of the image ( $0.86 \times 0.86 \times 2.5 \text{ mm}^3$ ). However, some local misalignment between these contours is clearly visible. Examples of such misalignment include the third ventricle area in Case 2 (Figs. 6.9 and 6.11b) and the posterior horn of the left lateral ventricle in the area adjacent to the tumor in Case 5 (Fig. 6.11).

Five cases of craniotomy-induced brain shift analyzed here are characterized by tumors located in different parts of the brain. Comparison of the pre-operative, intra-operative and registered images indicates that detailed information about anatomical structures required for building accurate biomechanical models may be difficult to obtain for tumors that affect geometry of such structures. For instance, in Case 5, the posterior horn of the left lateral ventricle was compressed by the tumor. Consequently, a large part of the horn could not be seen in the pre-operative images (Fig. 6.11). This, in turn, limited the accuracy when simulating the posterior horn of the left lateral ventricle in the biomechanical model for predicting the brain deformations in Case 5, which led to local misregistration (Fig. 6.11).

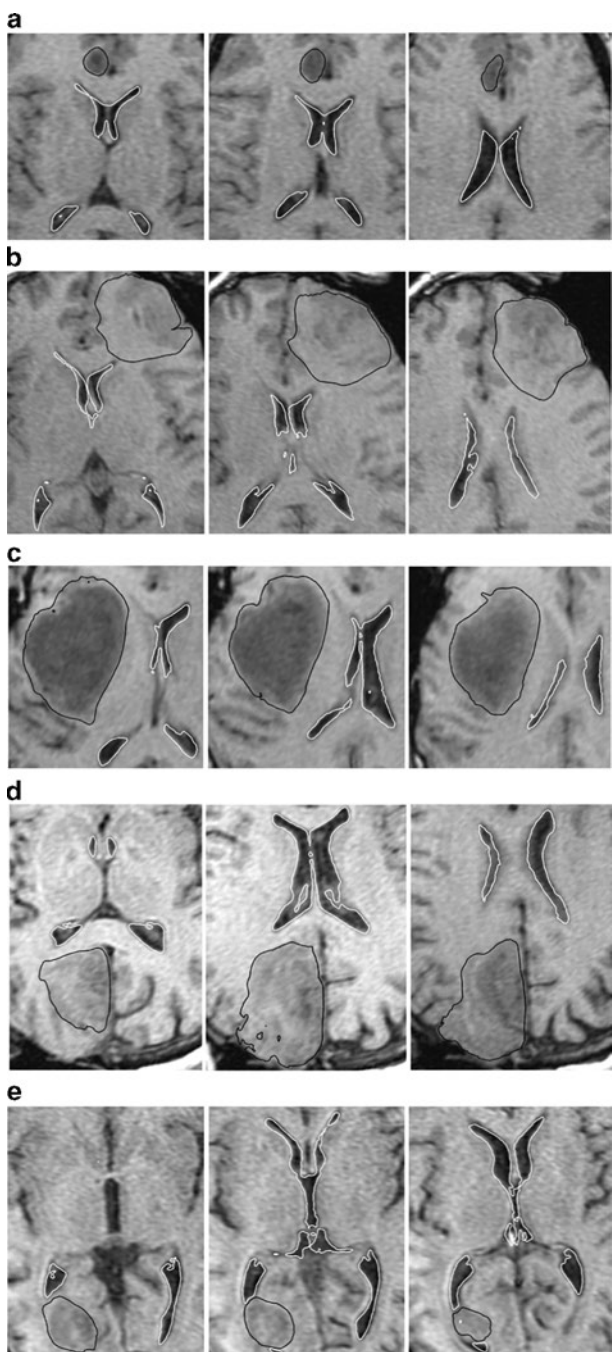


**Fig. 6.10** The registered (i.e. deformed using the calculated deformation field) pre-operative contours of ventricles (white lines) and tumor (black lines) imposed on the intra-operative MRI. Three transverse image sections are presented for each case, selected so that the tumor and ventricles are clearly visible. The images were cropped and enlarged. **(a)** Case 1; **(b)** Case 2; **(c)** Case 3; **(d)** Case 4; and **(e)** Case 5. For Case 2 (*row B – left-hand-side figure*), note the differences between registered contours and intra-operative image in the third ventricle area

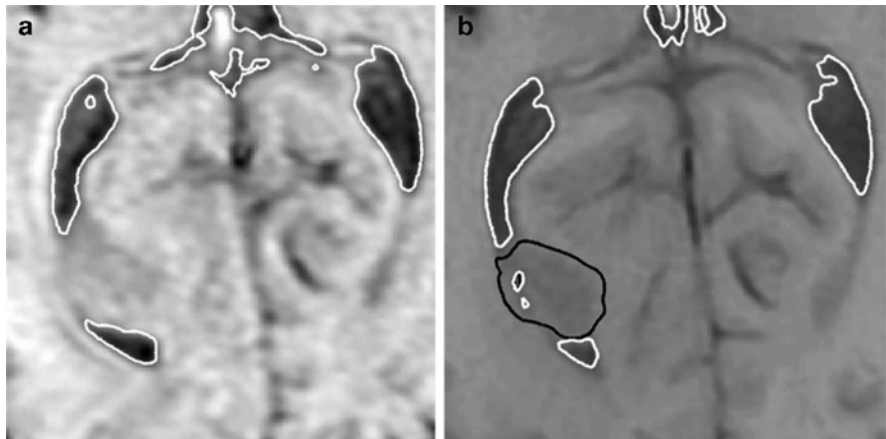


**Fig. 6.11** Close-up at Case 5: **(a)** The segmented intra-operative image; **(b)** The segmented pre-operative image. Segmentation of the ventricles is indicated by *white lines* and segmentation of the tumor by *black lines*. Note the appreciable differences in shape and size of the posterior horn of left lateral ventricle between the intra-operative and pre-operative images in the area adjacent to the tumor. The horn is appreciably larger in the intra-operative than pre-operative image, which indicates that it was compressed by the tumor

### 6.3.4 Discussion

In this example, we used finite element meshes consisting of hexahedral and tetrahedral elements combined with the specialized non-linear (i.e. including both geometric and material non-linearities) finite element algorithms (see Chap. 9) to predict the deformation field within the brain due to craniotomy-induced brain shift. Despite abandoning unrealistic linearization (i.e. assumptions about infinitesimally small brain deformations during craniotomy and linear stress–strain relationship of the brain tissues) typically applied in biomechanical models to satisfy real-time constraints of neurosurgery, we were able to predict deformation field within the brain in less than 40 s using a standard personal computer (with a single 3 GHz dual-core processor) and less than 4 s using a graphics processing unit (NVIDIA Tesla C870) for finite element meshes of the order of 18,000 nodes and 30,000 elements (~50,000 degrees of freedom).

Despite the fact that we used only very limited intra-operative information (deformation on the brain surface exposed during the craniotomy) when prescribing loading for the models and did not have patient-specific data about the tissues' mechanical properties, our application of the specialized non-linear finite element algorithms made it possible to obtain a very good agreement between the observed positions in the intra-operative MRIs and predicted positions and deformations of the anatomical structures within the brain (Figs. 6.10 and 6.11). Nevertheless, before non-linear biomechanical models using state-of-the-art finite element algorithms, such as those applied in this example, can become a part of clinical systems for image-guided neurosurgery, reliability and accuracy of such models must be confirmed against a much larger data sample.

## 6.4 Conclusions

Computational mechanics has become a central enabling discipline that has led to greater understanding and advances in modern science and technology [84]. It is now in a position to make a similar impact in medicine. We have discussed modeling approaches to two applications of clinical relevance: surgical simulation and neuroimage registration. These problems can be reasonably characterized with the use of purely mechanical terms such as displacements, internal forces, etc. Therefore, they can be analyzed using the methods of continuum mechanics. Moreover, similar methods may find applications in modeling the development of structural diseases of the brain [28, 85–87].

As the brain undergoes large displacements (~10–20 mm in the case of a brain shift) and its mechanical response to external loading is strongly non-linear, we advocate the use of general, non-linear finite element procedures for the numerical solution of the proposed models.

The brain's complicated mechanical behavior – non-linear stress–strain, stress–strain rate relationships and much lower stiffness in extension than in compression – require very careful selection of the constitutive model for a given application. The selection of the constitutive model for surgical simulation problems depends on the characteristic strain rate of the process to be modeled and to a certain extent on computational efficiency considerations. Fortunately, as shown in Sect. 6.2.3 and [30], the precise knowledge of patient-specific mechanical properties of brain tissue is not required for intra-operative image registration.

A number of challenges must be met before Computer-Integrated Surgery systems based on computational biomechanical models can become as widely used as Computer-Integrated Manufacturing systems are now. As we deal with individual patients, methods to produce patient-specific computational grids quickly and reliably must be improved. Substantial progress in automatic meshing methods is required, or alternatively meshless methods may provide a solution. Computational efficiency is an important issue, as intra-operative applications, requiring reliable results within approximately 40 s, are most appealing. Progress can be made in non-linear algorithms by identifying parts that can be pre-computed, and parts that do not have to be calculated at every time step. One such possibility is to use the Total Lagrangian Formulation of the finite element method [65, 88, 89], where all field variables are related to the original (known) configuration of the system and therefore most spatial derivatives can be calculated before the simulation commences during the pre-processing stage. Implementation of algorithms in parallel on networks of processors and harnessing the computational power of graphics processing units provide a challenge for coming years.

**Acknowledgements** The financial support of the Australian Research Council (Grants No. DP0343112, DP0664534 and LX0560460), National Health and Medical Research Council Grant No. 1006031 and NIH (Grant No. 1-RO3-CA126466-01A1) is gratefully acknowledged. We thank our collaborators Dr Ron Kikinis and Dr Simon Warfield from Harvard Medical School and Dr Kiyoyuki Chinzei and Dr Toshikatsu Washio from Surgical Assist Technology Group of AIST, Japan, for help in various aspects of our work.

The medical images used in the present study (provided by Dr Simon Warfield) were obtained in the investigation supported by a research grant from the Whitaker Foundation and by NIH grants R21 MH67054, R01 LM007861, P41 RR13218 and P01 CA67165.

We thank Toyota Central R&D Labs. (Nagakute, Aichi, Japan) for providing the THUMS brain model.

## References

1. Miller, K., Wittek, A., Joldes, G., et al.: Modelling brain deformations for computer-integrated neurosurgery. *Int. J. Numer. Methods Biomed. Eng.* **26**, 117–138 (2010)
2. Wittek, A., Joldes, G., Couton, M., et al.: Patient-specific non-linear finite element modelling for predicting soft organ deformation in real-time; application to non-rigid neuroimage registration. *Prog. Biophys. Mol. Biol.* **103**, 292–303 (2010)
3. Dimaio, S.P., Salcudean, S.E.: Interactive simulation of needle insertion models. *IEEE Trans. Biomed. Eng.* **52**, 1167–1179 (2005)
4. Bucholz, R., MacNeil, W., McDermont, L.: The operating room of the future. *Clin. Neurosurg.* **51**, 228–237 (2004)
5. Nakaji, P., Speltzer, R.F.: The marriage of technique, technology, and judgement. *Innov. Surg. Approach* **51**, 177–185 (2004)
6. Ferrant, M., Nabavi, A., Macq, B., et al.: Serial registration of intraoperative MR images of the brain. *Med. Image Anal.* **6**, 337–359 (2002)
7. Warfield, S.K., Haker, S.J., Talos, F., et al.: Capturing intraoperative deformations: research experience at Brigham and Women's Hospital. *Med. Image Anal.* **9**, 145–162 (2005)
8. Warfield, S.K., Talos, F., Tei, A., et al.: Real-time registration of volumetric brain MRI by biomechanical simulation of deformation during image guided surgery. *Comput. Vis. Sci.* **5**, 3–11 (2002)
9. Wittek, A., Miller, K., Kikinis, R., et al.: Patient-specific model of brain deformation: application to medical image registration. *J. Biomech.* **40**, 919–929 (2007)
10. Joldes, G., Wittek, A., Couton, M., et al.: Real-time prediction of brain shift using nonlinear finite element algorithms. In: *Medical Image Computing and Computer-Assisted Intervention – MICCAI 2009*. Springer, Berlin (2009a)
11. Owen, S.J.: A survey of unstructured mesh generation technology. In: LAB, S. N., ed. *7th International Meshing Roundtable*, Dearborn, Michigan, USA, pp. 239–267, October 1998
12. Owen, S.J.: Hex-dominant mesh generation using 3D constrained triangulation. *Comput. Aided Des.* **33**, 211–220 (2001)
13. Viceconti, M., Taddei, F.: Automatic generation of finite element meshes from computed tomography data. *Crit. Rev. Biomed. Eng.* **31**, 27–72 (2003)
14. Castellano-Smith, A.D., Hartkens, T., Schnabel, J., et al.: Constructing patient specific models for correcting intraoperative brain deformation. In: *4th International Conference on Medical Image Computing and Computer Assisted Intervention MICCAI*, Lecture Notes in Computer Science 2208, Utrecht, The Netherlands, pp. 1091–1098 (2001)
15. Couteau, B., Payan, Y., Lavallée, S.: The Mesh-Matching algorithm: an automatic 3D Mesh generator for finite element structures. *J. Biomech.* **33**, 1005–1009 (2000)
16. Luboz, V., Chabanas, M., Swider, P., et al.: Orbital and maxillofacial computer aided surgery: patient-specific finite element models to predict surgical outcomes. *Comput. Meth. Biomed. Eng.* **8**, 259–265 (2005)
17. Clatz, O., Delingette, H., Bardinet, E., et al.: Patient specific biomechanical model of the brain: application to Parkinson's disease procedure. In: Ayache, N., Delingette, H. (eds.) *International Symposium on Surgery Simulation and Soft Tissue Modeling (IS4TM'03)*, pp. 321–331. Springer, Juan-les-Pins, France (2003)

18. Ferrant, M., Macq, B., Nabavi, A., et al.: Deformable modeling for characterizing biomedical shape changes. In: Borgefors, I.N.G., Sanniti di Baja, G. (eds.) *Discrete Geometry for Computer Imagery: 9th International Conference*, Uppsala, Sweden, pp. 235–248. Springer, London (2000)
19. Belytschko, T., Lu, Y.Y., Gu, L.: Element-free Galerkin methods. *Int. J. Numer. Methods Eng.* **37**, 229–256 (1994)
20. Horton, A., Wittek, A., Joldes, G., et al.: A meshless Total Lagrangian explicit dynamics algorithm for surgical simulation. *Int. J. Numer. Methods Biomed. Eng.* **26**, 117–138 (2010)
21. Horton, A., Wittek, A., Miller, K.: Computer simulation of brain shift using an element free galerkin method. In: Middleton, J., Jones, M. (eds.) *7th International Symposium on Computer Methods in Biomechanics and Biomedical Engineering CMBEE 2006*, Antibes, France (2006a)
22. Horton, A., Wittek, A., Miller, K.: Towards meshless methods for surgical simulation. In: *Computational Biomechanics for Medicine Workshop, Medical Image Computing and Computer-Assisted Intervention MICCAI 2006*, Copenhagen, Denmark, pp. 34–42 (2006b)
23. Horton, A., Wittek, A., Miller, K.: Subject-specific biomechanical simulation of brain indentation using a meshless method. In: Ayache, N., Ourselin, S., Maeder, A., eds. *International Conference on Medical Image Computing and Computer-Assisted Intervention MICCAI 2007*, Brisbane, Australia, pp. 541–548. Springer, Berlin, 29 October to 2 November (2007)
24. Li, S., Liu, W.K.: *Meshfree Particle Methods*. Springer, Berlin (2004)
25. Liu, G.R.: *Mesh Free Methods: Moving Beyond the Finite Element Method*. CRC, Boca Raton (2003)
26. Hagemann, A., Rohr, K., Stiehl, H.S., et al.: Biomechanical modeling of the human head for physically based, nonrigid image registration. *IEEE Trans. Med. Imaging* **18**, 875–884 (1999)
27. Miga, M.I., Paulsen, K.D., Hoopes, P.J., et al.: In vivo quantification of a homogenous brain deformation model for updating preoperative images during surgery. *IEEE Trans. Biomed. Eng.* **47**, 266–273 (2000)
28. Dutta-Roy, T., Wittek, A., Miller, K.: Biomechanical modelling of normal pressure hydrocephalus. *J. Biomech.* **41**, 2263–2271 (2008)
29. Hu, J., Jin, X., Lee, J.B., et al.: Intraoperative brain shift prediction using a 3D inhomogeneous patient-specific finite element model. *J. Neurosurg.* **106**, 164–169 (2007)
30. Wittek, A., Hawkins, T., Miller, K.: On the unimportance of constitutive models in computing brain deformation for image-guided surgery. *Biomech. Model. Mechanobiol.* **8**, 77–84 (2009)
31. Wittek, A., Kikinis, R., Warfield, S.K., et al.: Brain shift computation using a fully nonlinear biomechanical model. In: *8th International Conference on Medical Image Computing and Computer Assisted Surgery MICCAI 2005*, Palm Springs, California, USA (2005)
32. Wittek, A., Omori, K.: Parametric study of effects of brain-skull boundary conditions and brain material properties on responses of simplified finite element brain model under angular acceleration in sagittal plane. *JSME Int. J.* **46**, 1388–1398 (2003)
33. Joldes, G., Wittek, A., Miller, K.: Suite of finite element algorithms for accurate computation of soft tissue deformation for surgical simulation. *Med. Image Anal.* **13**, 912–919 (2009)
34. Joldes, G.R., Wittek, A., Miller, K., et al.: Realistic and efficient brain-skull interaction model for brain shift computation. In: Karol Miller, P.M.F.N. (ed.) *Computational Biomechanics for Medicine III Workshop, MICCAI 2008*, New-York, pp. 95–105 (2008)
35. Jin, X.: Biomechanical response and constitutive modeling of bovine pia-arachnoid complex. PhD thesis, Wayne State University (2009)
36. Miller, K., Wittek, A.: Neuroimage registration as displacement – zero traction problem of solid mechanics. In: Miller, K., Poulikakos, D. (eds.) *Computational Biomechanics for Medicine MICCAI-associated Workshop*, Copenhagen, pp. 1–14 (2006)
37. Miga, M.I., Sinha, T.K., Cash, D.M., et al.: Cortical surface registration for image-guided neurosurgery using laser-range scanning. *IEEE Trans. Med. Imaging* **22**, 973–985 (2003)

38. Miller, K.: How to test very soft biological tissues in extension. *J. Biomech.* **34**, 651–657 (2001)
39. Miller, K.: Biomechanics without mechanics: calculating soft tissue deformation without differential equations of equilibrium. In: Middleton, J., Shrive, N., Jones, M. (eds.) 5th Symposium on Computer Methods in Biomechanics and Biomedical Engineering CMBBE2004 Madrid, Spain. First Numerics (2005b)
40. Miller, K.: Method for testing very soft biological tissues in compression. *J. Biomech.* **38**, 153–158 (2005)
41. Ferrant, M., Nabavi, A., Macq, B., et al.: Registration of 3-D intraoperative MR images of the brain using a finite-element biomechanical model. *IEEE Trans. Med. Imaging* **20**, 1384–1397 (2001)
42. Fung, Y.C.: *A First Course in Continuum Mechanics*. Prentice-Hall, London (1969)
43. Ciarlet, P.G.: *Mathematical Elasticity*. North Holland, The Netherlands (1988)
44. Nowinski, W.L.: Modified Talairach landmarks. *Acta Neurochir.* **143**, 1045–1057 (2001)
45. Miller, K.: Biomechanics without mechanics: calculating soft tissue deformation without differential equations of equilibrium. In: Middleton, J., Shrive, N., Jones, M. (eds.) 5th Symposium on Computer Methods in Biomechanics and Biomedical Engineering, Madrid, Spain. First Numerics (2005a)
46. Dompuri, P., Thompson, R.C., Dawant, B.M., et al.: An atlas-based method to compensate for brain shift: preliminary results. *Med. Image Anal.* **11**, 128–145 (2007)
47. Dutta Roy, T.: Does normal pressure hydrocephalus have mechanistic causes? PhD Thesis, The University of Western Australia (2010)
48. Miller, K., Chinzei, K.: Constitutive modelling of brain tissue: experiment and theory. *J. Biomech.* **30**, 1115–1121 (1997)
49. Bilston, L., Liu, Z., Phan-Tiem, N.: Large strain behaviour of brain tissue in shear: some experimental data and differential constitutive model. *Biorheology* **38**, 335–345 (2001)
50. Farshad, M., Barbezat, M., Flüeler, P., et al.: Material characterization of the pig kidney in relation with the biomechanical analysis of renal trauma. *J. Biomech.* **32**, 417–425 (1999)
51. Mendis, K.K., Stalnaker, R.L., Advani, S.H.: A constitutive relationship for large deformation finite element modeling of brain tissue. *J. Biomech. Eng.* **117**, 279–285 (1995)
52. Miller, K.: Constitutive model of brain tissue suitable for finite element analysis of surgical procedures. *J. Biomech.* **32**, 531–537 (1999)
53. Miller, K.: Constitutive modelling of abdominal organs. *J. Biomech.* **33**, 367–373 (2000)
54. Miller, K., Chinzei, K.: Mechanical properties of brain tissue in tension. *J. Biomech.* **35**, 483–490 (2002)
55. Miller, K., Chinzei, K., Orssengo, G., et al.: Mechanical properties of brain tissue in-vivo: experiment and computer simulation. *J. Biomech.* **33**, 1369–1376 (2000)
56. Nasseri, S., Bilston, L.E., Phan-Thien, N.: Viscoelastic properties of pig kidney in shear, experimental results and modelling. *Rheol. Acta* **41**, 180–192 (2002)
57. Walsh, E.K., Schettini, A.: Calculation of brain elastic parameters in vivo. *Am. J. Physiol.* **247**, R637–R700 (1984)
58. Bilston, L.E., Liu, Z., Phan-Tien, N.: Linear viscoelastic properties of bovine brain tissue in shear. *Biorheology* **34**, 377–385 (1997)
59. Miller, K.: *Biomechanics of Brain for Computer Integrated Surgery*. Publishing House of Warsaw University of Technology, Warsaw (2002)
60. Prange, M.T., Margulies, S.S.: Regional, directional, and age-dependent properties of the brain undergoing large deformation. *J. Biomech. Eng.* **124**, 244–252 (2002)
61. Salcudean, S., Turgay, E., Rohling, R.: Identifying the mechanical properties of tissue by ultrasound strain imaging. *Ultrasound Med. Biol.* **32**, 221–235 (2006)
62. McCracken, P.J., Manduca, A., Felmlee, J., et al.: Mechanical transient-based magnetic resonance elastography. *Magn. Reson. Med.* **53**, 628–639 (2005)
63. Sinkus, R., Tanter, M., Xydeas, T., et al.: Viscoelastic shear properties of in vivo breast lesions measured by MR elastography. *Magn. Reson. Imaging* **23**, 159–165 (2005)
64. Green, M.A., Bilston, L.E., Sinkus, R.: In vivo brain viscoelastic properties measured by magnetic resonance elastography. *NMR Biomed.* **21**(7), 755–764 (2008)

65. Bathe, K.-J.: *Finite Element Procedures*. Prentice-Hall, New Jersey (1996)
66. Ma, J., Wittek, A., Singh, S., et al.: Evaluation of accuracy of non-linear finite element computations for surgical simulation: study using brain phantom. *Comput. Methods Biomed. Eng.* **13**, 783–794 (2010)
67. Wittek, A., Dutta-Roy, T., Taylor, Z., et al.: Subject-specific non-linear biomechanical model of needle insertion into brain. *Comput. Methods Biomed. Eng. J.* **11**, 135–146 (2008)
68. Grosland, N.M., Shivanna, K.H., Magnotta, V.A., et al.: IA-FEMesh: an open-source, interactive, multiblock approach to anatomic finite element model development. *Comput. Meth. Programs Biomed.* **94**, 96–107 (2009)
69. Ito, Y., Shih, A.M., Soni, B.K.: Octree-based reasonable-quality hexahedral mesh generation using a new set of refinement templates. *Int. J. Numer. Methods Eng.* **77**, 1809–1833 (2009)
70. Shepherd, J.F., Zhang, Y., Tuttle, C.J., et al.: Quality improvement and boolean-like cutting operations in hexahedral meshes. In: 10th Conference of the International Society of Grid Generation, Crete, Greece (2007)
71. Joldes, G.R., Wittek, A., Miller, K.: Non-locking tetrahedral finite element for surgical simulation. *Commun. Numer. Methods Eng.* **25**, 827–836 (2008)
72. Joldes, G.R., Wittek, A., Miller, K.: An efficient hourglass control implementation for the uniform strain hexahedron using the Total Lagrangian formulation. *Commun. Numer. Methods Eng.* **24**, 1315–1323 (2008)
73. Arganda-Carreras, I., Sorzano, S.C.O., Marabini, R., et al.: Consistent and elastic registration of histological sections using vector-spline regularization. International Conference on Computer Vision Approaches to Medical Image Analysis. LNCS. Springer, Setubal, Portugal (2006)
74. Joldes, G.R., Wittek, A., Miller, K.: Real-time nonlinear finite element computations on GPU – application to neurosurgical simulation. *Comput. Methods Appl. Mech. Eng.* **199**, 3305–3314 (2010)
75. Skrinjar, O., Nabavi, A., Duncan, J.: Model-driven brain shift compensation. *Med. Image Anal.* **6**, 361–373 (2002)
76. Warfield, S.K., Ferrant, M., Gallez, X., et al.: Real-time biomechanical simulation of volumetric brain deformation for image guided neurosurgery. In: SC 2000: High Performance Networking and Compting Conference, Dallas, USA, pp. 1–16 (2000)
77. Miga, M.I., Roberts, D.W., Kennedy, F.E., et al.: Modeling of retraction and resection for intraoperative updating of images. *Neurosurgery* **49**, 75–85 (2001)
78. Yeoh, O.H.: Some forms of strain-energy function for rubber. *Rubber Chem. Technol.* **66**, 754–771 (1993)
79. Chakravarty, M.M., Sadikot, A.F., Germann, J., et al.: Towards a validation of atlas warping techniques. *Med. Image Anal.* **12**, 713–726 (2008)
80. Viola, P., Wells III, W.M.: Alignment by maximization of mutual information. *Int. J. Comput. Vision* **24**, 137–154 (1997)
81. Wells III, W.M., Viola, P., Atsumi, H., et al.: Multi-modal volume registration by maximization of mutual information. *Med. Image Anal.* **1**, 35–51 (1996)
82. Rexilius, J., Warfield, S., Guttmann, C., et al.: A novel nonrigid registration algorithm and applications. Medical Image Computing and Computer-Assisted Intervention – MICCAI 2001, Toronto, Canada (2001)
83. Miga, M.I., Paulsen, K.D., Lemery, J.M., et al.: Model-updated image guidance: initial clinical experiences with gravity-induced brain deformation. *IEEE Trans. Med. Imaging* **18**, 866–874 (1999)
84. Oden, J.T., Belytschko, T., Babuska, I., et al.: Research directions in computational mechanics. *Comput. Meth. Appl. Mech. Eng.* **192**, 913–922 (2003)
85. Berger, J., Horton, A., Joldes, G., et al.: Coupling finite element and mesh-free methods for modelling brain defromations in response to tumour growth. In: Miller, K., Nielsen, P.M.F. (eds.) Computational Biomechanics for Medicine III MICCAI-Associated Workshop, 2008. MICCAI, New York (2008)

86. Miller, K., Taylor, Z., Nowinski, W.L.: Towards computing brain deformations for diagnosis, prognosis and neurosurgical simulation. *J. Mech. Med. Biol.* **5**, 105–121 (2005)
87. Taylor, Z., Miller, K.: Reassessment of brain elasticity for analysis of biomechanisms of hydrocephalus. *J. Biomech.* **37**, 1263–1269 (2004)
88. Miller, K., Joldes, G., Lance, D., et al.: Total Lagrangian explicit dynamics finite element algorithm for computing soft tissue deformation. *Commun. Numer. Methods Eng.* **23**, 121–134 (2007)
89. Zienkiewicz, O.C., Taylor, R.L.: *The Finite Element Method*. McGraw-Hill, London (2000)
90. Roberts, D.W., Hartov, A., Kennedy, F.E., et al.: Intraoperative brain shift and deformation: a quantitative analysis of cortical displacement in 28 cases. *Neurosurgery* **43**, 749–758 (1998)

## Chapter 7

# Dynamics of Cerebrospinal Fluid: From Theoretical Models to Clinical Applications

Marek Czosnyka, Zofia Czosnyka, Olivier Baledent, Ruwan Weerakkody, Magdalena Kasprówicz, Piotr Smielewski, and John D. Pickard

## 7.1 Introduction

Modeling of cerebrospinal fluid (CSF) circulation usually differs from models of brain tissue deformation. Hydrodynamics of CSF and its links with cerebral blood flow (CBF) are here of interest, as opposed to displacement of anatomical structures or distribution of stress-strain in the brain tissue in deformation modeling. In clinical practice, dynamics of the pressure may be easily monitored (although invasively, with directly placed pressure transducers) and dynamics of CSF flow and CBF can be imaged with phase-coded MRI (PCMRI; noninvasively). These two methods have an established clinical application in diagnosis and management of diseases associated with CSF circulatory dysfunctions, like hydrocephalus of various types, idiopathic intracranial hypertension, syringomyelia, etc.

This chapter describes the methodology of modeling of CSF dynamics and attempts to illustrate some most common clinical applications to give a reader a taste of links between physics and a practice of clinical neurosciences.

Before embarking on the particulars, it is worth considering the question: why quantitatively assess CSF dynamics? Quantitative assessment in general provides robust evidence to support clinical intuition as well as imparting a measure of the degree of dysfunction, particularly useful where clinical parameters are subtle and ambiguous [1]. For normal pressure hydrocephalus (NPH), where this is particularly true, theoretical consensus regarding the use of physiological parameters in conjunction with clinical information and imaging has been reached. It has been published in the latest guidelines for the management of NPH [2].

---

M. Czosnyka (✉)

Neurosurgical Unit, Department of Clinical Neurosciences,  
University of Cambridge, Cambridge, UK  
e-mail: mc141@medsch.cam.ac.uk

More specifically, the ability to obtain variables that describe CSF dynamics allows us to more categorically address some key questions in the clinical decision-making process:

1. Scope for improvement with CSF shunting: shunts work by providing an alternative (normal resistance) pathway for CSF outflow. If resistance to CSF outflow ( $R_{CSF}$ ) is in the normal range, a shunt will theoretically not be of benefit [3].
2. To determine which is the best shunt system to use.
3. In suspected shunt failure, providing a baseline for postshunt comparison.

Shunt failure occurs at a rate of approximately 20–30% in the first year, and 3–5% per annum subsequently [4]. Deterioration is often gradual and subtle rather than sudden and dramatic, and in such cases, it can be difficult to justify revision without quantitative evidence and comparative analysis [5–7]. Similarly, in patients presenting with persistent symptoms postshunting, CSF dynamics assessment is a useful means of excluding revision, if relative normalization of CSF dynamics has been demonstrated [8].

The current range of clinical application for CSF dynamics testing includes hydrocephalus, idiopathic intracranial hypertension [9], craniostenosis, and traumatic brain injury (TBI) – the latter useful in differentiating posttraumatic hydrocephalus from atrophy [10] and assessing CSF pathways following decompressive craniectomy [11].

## 7.2 Physiology and Pathophysiology

CSF dynamics comprises the interaction between five components: CSF production, flow, absorption, pulsations, and dynamics of CBF. CSF production occurs by active secretion at a relatively constant rate, but is dependent upon brain metabolic rate and reducing with age [12]. The role of free, unobstructed flow of CSF is threefold: (1) it provides a shock absorptive function for the brain and spinal cord, important in trauma; (2) allows even distribution of pressure throughout the intracranial vault, canceling out pressure gradients and preventing brain shift or herniation; and (3) allows washing out brain metabolites.

The second point explains why a very high ICP ( $\approx 40$  mmHg) can be tolerated relatively asymptotically in communicating hydrocephalus (for example, during CSF infusion tests; *vide infra*). In contrast, when CSF pathways are obstructed, for example by diffuse cerebral edema in TBI, marked clinical deterioration is seen at ICP exceeding only 20 mmHg.

Absorption occurs in a pressure-dependent fashion via the arachnoid granulations at the superior sagittal sinus, first mathematically described by Davson [13]. Alternative outflow of CSF may occur by periventricular leakage into the brain parenchyma, as suggested in NPH patients [14, 15]. CSF circulates not only in a constant way with a rate equivalent to CSF production, but also in pulsations. CSF pulsatile flow is observed in the cerebral aqueduct (approximately 40  $\mu$ L in stroke volume) and in the cervical region of subarachnoid space (SAS) (approximately

500  $\mu\text{L}$  stroke volume) [16]. For a half of the cardiac cycle, CSF flows down into the spinal SAS, and for the other half, upward from it. The role of pulsatile CSF flow and pressure pulsations is still unclear, but becomes more often studied in hydrocephalus and other diseases manifesting with abnormal CSF dynamics [17–19].

### 7.3 Model of CSF Circulation

The mathematical model of CSF pressure–volume compensation, introduced by Marmarou [20] and modified in later studies [21, 22], provides a theoretical basis for the differential diagnosis in hydrocephalus. Since then, components of this model have been identified in many clinical scenarios [23–29] and it is in use in clinical diagnostic procedures [2, 10, 30].

Under normal conditions, production of CSF is balanced by its storage and reabsorption to sagittal sinus:

$$\text{Production of CSF} = \text{Storing of CSF} + \text{Reabsorption of CSF} \quad (7.1)$$

Production of CSF is almost constant. Reabsorption is proportional to the gradient between CSF pressure ( $p$ ) and pressure in sagittal sinuses ( $p_{ss}$ ):

$$\text{Reabsorption} = \frac{p - p_{ss}}{R}, \quad (7.2)$$

$p_{ss}$  is considered to be a constant parameter, determined by central venous pressure. However, it is not certain that interaction between changes in CSF pressure and  $p_{ss}$  does not exist in all circumstances: in patients with idiopathic intracranial hypertension,  $p_{ss}$  is frequently elevated due to stenosis of lateral sinuses. Similar situation can be seen in venous sinus thrombosis.

The coefficient  $R$  (symbol  $R_{\text{CSF}}$  is also used) is termed as the resistance to CSF reabsorption or outflow (units: [ $\text{mmHg}/(\text{mL/min})$ ]).

Storage of CSF is proportional to the cerebrospinal compliance  $C$  (units: [ $\text{mL}/\text{mmHg}$ ]):

$$\text{Storage} = C \cdot \frac{dp}{dt}. \quad (7.3)$$

The compliance of the cerebrospinal space is inversely proportional to the gradient of CSF pressure  $p$  and the reference pressure  $p_o$  (7.4) [21]:

$$C = \frac{1}{E \cdot (p - p_o)}. \quad (7.4)$$

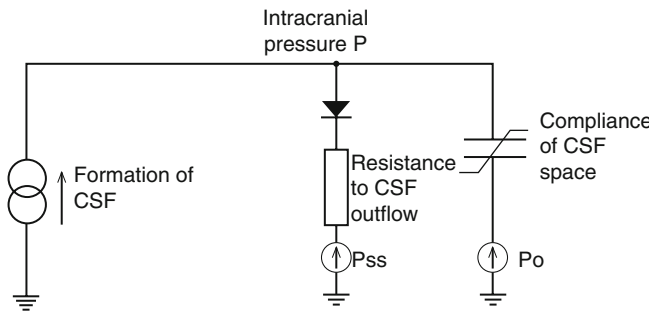


**Fig. 7.1** Electrical model of CSF circulation. Current source represents production of CSF, resistor, and diode – unilateral absorption to sagittal sinus (voltage source  $p_{ss}$  represents sagittal sinus pressure). Capacitor – nonlinear compliance of CSF space

Some authors suggest that the relationship (7.4) is valid only above a certain pressure level called the “optimal pressure” [22]; however this is still a point of some dispute. The coefficient  $E$  is termed the cerebral elasticity (or elastance coefficient) (units: [ $\text{mL}^{-1}$ ]). Elevated elasticity ( $>0.18 \text{ mL}^{-1}$ ) signifies a poor pressure–volume compensatory reserve [31]. This coefficient has been recently confirmed to be useful in predicting response to third ventriculostomy [29]. Coefficient  $E$  is associated with the resistance to CSF outflow [31].

The reference pressure  $p_o$  is a parameter of uncertain significance. Some authors suggest that it is the pressure in the venous compartment and may be equal to  $p_{ss}$ . Others assume that this variable can be neglected [30].

The relationship (7.4) expresses a fundamental law of the cerebrospinal dynamic compensation: When the CSF pressure increases, the compliance of the brain decreases.

Combination of (7.1) with (7.2) and (7.4) gives a final equation (7.5):

$$\frac{1}{E \cdot (p - p_o)} \cdot \frac{dp}{dt} + \frac{p - p_b}{R} = I(t), \quad (7.5)$$

where  $I(t)$  is the rate of external volume addition and  $p_b$  is a baseline pressure.

The model described by this equation may be presented in the form of its electric equivalent [20] (Fig. 7.1).

Equation (7.5) can be solved for various types of external volume additions  $I(t)$ . The most common in clinical practice is:

- (a) A constant infusion of CSF ( $I(t)=0$  for  $t<0$  and  $I(t)=I_{inf}$  for  $t>0$ ) – see Fig. 7.2:

$$P(t) = \frac{\left[ I_{inf} + \frac{p_b - p_o}{R} \right] \cdot [p_b - p_o]}{\frac{p_b - p_o}{R} + I_{inf} \cdot \left[ e^{-E[((p_b - p_o)/R) + I_{inf}] \cdot t} \right]} + p_o. \quad (7.6)$$

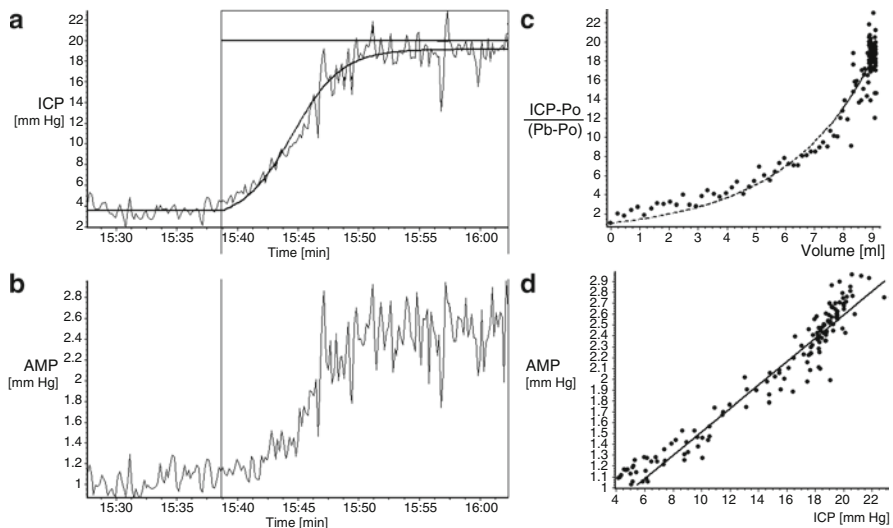


**Fig. 7.2** Methods of identification of the model of CSF circulation during constant rate infusion study. (a) Recording of real CSF pressure (ICP) vs. time increasing during infusion with interpolated modeling curve (7.6). Infusion of constant rate of 1.5 (mL/min) starts from vertical line. (b) Recording of pulse amplitude (AMP) during infusion. It is customary presented as different variable, in addition to mean ICP. Rise in AMP is usually well correlated with rise in ICP. (c) Pressure–volume curve. On x axis, effective volume increase is plotted (i.e., infusion and production minus reabsorption of CSF). On y axis – increase in pressure measured as a gradient of current pressure minus reference pressure  $p_o$ , relative to baseline pressure  $p_b$ . (d) Linear relationship between pulse amplitude and mean ICP. Intercept of the line with x axis (ICP) theoretically indicates the reference pressure  $p_o$ .

The analytical curve (7.6) can be matched to the real recording of the pressure during the test, which results in an estimation of the unknown parameters:  $R$ ,  $E$ , and  $p_o$  – see Fig. 7.2a.

(b) A bolus injection of CSF (volume  $\Delta V$ ):

$$P(t) = \frac{(p_b - p_o) \cdot e^{E \left[ \frac{\Delta V + \frac{p_b - p_o}{R} \cdot t}{R} \right]}}{1 + e^{E \Delta V} \cdot \left[ e^{\frac{E \cdot \frac{p_b - p_o}{R} \cdot t}{R}} - 1 \right]} + p_o \quad (7.7)$$

The bolus injection can be used for calculation of the so-called pressure–volume index (PVI), defined as the volume added externally to produce a tenfold increase in the pressure [20]:

$$\text{PVI} \stackrel{\text{def}}{=} \frac{\Delta V}{\log_{10} \left( \frac{p_p - p_o}{p_b - p_o} \right)}, \quad \text{PVI} \cong \frac{1}{0.434 \cdot E}, \quad (7.8a, b)$$

$P_p$  in a formula (7.8a) is a peak-pressure recorded just after addition of the volume  $\Delta V$ . PVI is theoretically proportional to the inverse of the brain elastance coefficient  $E$ .

The pressure–volume compensatory reserve is insufficient when PVI<13 mL. A value of PVI above 26 mL signifies an “over-compliant” brain. These norms are valid for the PVI calculated as inverse of E (according to (7.8b)) using slow infusion. If the bolus test is used, norms for PVI are higher (the threshold equivalent to 13 mL is around 25 mL [20]).

The formula (7.7) for time  $t=0$  describes the shape of the relationship between the effective volume increase  $\Delta V$  and the CSF pressure, called the pressure–volume curve – Fig. 7.2c:

$$p = (p_b - p_o) \cdot e^{E\Delta V} + p_o. \quad (7.9)$$

It is interesting that pressure–volume curve plotted during increase in ICP has different shape than plotted using the subsequent decrease [32].

Finally, the (7.7) can be helpful in the theoretical evaluation of the relationship between the pulse wave amplitude of ICP and the mean CSF pressure. If we presume that the rise in the blood volume after a heart contraction is equivalent to a rapid bolus addition of CSF fluid at the baseline pressure  $p_b$ , the pulse amplitude (AMP) can be expressed as:

$$\text{AMP} = p_p - p_b = (p_b - p_o) \cdot (e^{E\Delta V} - 1). \quad (7.10)$$

In almost all the cases, when CSF pressure is being increased by an external volume addition, the pulse amplitude rises [21, 33] – see Fig. 7.2b, d. The gradient of the regression line between AMP and  $p$  is proportional to the elasticity. The intercept, theoretically, marks the reference pressure  $p_o$ .

In all pressure–volume testing techniques, parameters of model (7.5) are estimated using various algorithms and various volume-adding techniques. However, the presented model has a limited scope: it cannot interpret dynamic interactions between the rising CSF pressure, expanding ventricles, and cerebral blood volume. More sophisticated models have been formulated, but none of them has yet become established in clinical practice.

## 7.4 Infusion Test

The computerized infusion test [34, 35] is a modification of the traditional constant rate infusion as described by Katzman and Hussey [28]. The method requires fluid infusion to be made into any accessible CSF compartment. Lumbar infusion, even if it has understandable limitations, is less invasive than intraventricular.

The alternative is an infusion into a subcutaneously positioned reservoir, connected to an intraventricular catheter or shunt-antechamber. In such cases, two hypodermic needles (gauge 25) are used: one for the pressure measurement and the second for the infusion.

During the infusion, the computer calculates and graphically presents mean pressure and pulse amplitude over time (Fig. 7.2a, b). The resistance to CSF outflow can be calculated using simple arithmetic as the difference between the value of the plateau

pressure during infusion and the baseline pressure, divided by the infusion rate. However, the precise measurement of the final plateau pressure is not possible when strong vasogenic waves arise or an excessive elevation of the pressure above the safe limit of 40 mmHg is recorded. Computerized analysis produces results even in difficult cases when the infusion is terminated prematurely. The pressure–volume curve is additionally investigated (Fig. 7.2c). It represents relative rise in CSF pressure as a function of effective change of CSF volume (i.e., volume infused and produced minus volume absorbed). The algorithm utilizes time-series analysis for volume–pressure curve retrieval, the least-mean-square model fitting, and an examination of the relationship between the pulse amplitude and the mean CSF pressure (Fig. 7.2d).

## 7.5 Overnight ICP Monitoring

Monitoring of ICP over a longer period can be performed safely using intraparenchymal probes [36, 37]; less frequently, this is performed by lumbar puncture or a needle inserted in a preimplanted reservoir. Continuous, real-time analysis of the data, using a pressure monitor connected to a computerized system, is very helpful. We have found that the most reliable results require overnight monitoring [37]; however, when this is impossible, a minimum half an hour monitoring is necessary. In contrast, it is well established that a single manometric lumbar CSF pressure measurement may be misleading [38].

## 7.6 Compensatory Parameters Derived from the Infusion Test and ICP Monitoring

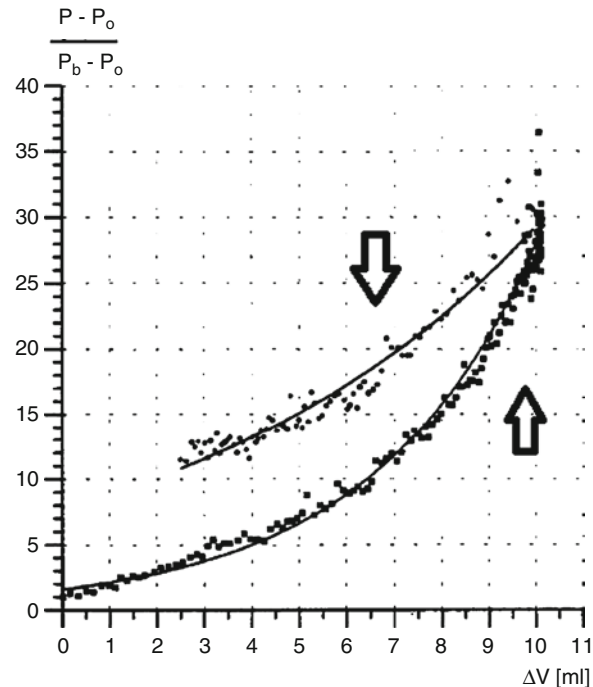
### 7.6.1 $R_{CSF}$ & $P_b$

Infusion study (constant rate [39], or any other variation of controlled but variable rate [25, 27, 40]) allows variables describing the state of CSF compensatory reserve to be estimated. Traditionally, the two most important parameters are resistance to CSF outflow ( $R_{CSF}$ ) and baseline CSF pressure ( $p_b$ ). Elevated  $R_{CSF}$  (>13 mmHg/(mL/min) [24, 41] or >18 mmHg/(mL/min) [23]) signifies disturbed CSF circulation. Elevated baseline pressure ( $p_b$  > 18 mmHg) may signify an uncompensated cerebrospinal volume-expanding process.

### 7.6.2 Elastance Coefficient (or Elasticity)

The exact clinical significance and interpretation of the elastance coefficient ( $E$ ) is not yet fully documented, though theoretically it describes brain stiffness. Tans and Poortvliet [31] showed that  $E$  weakly correlated with the resistance to CSF outflow, though no further studies exploring this concept have followed. Tisell [29]

**Fig. 7.3** “Hysteresis” of pressure–volume curve. After the test (decreasing ICP – down arrow), branch of the curve is shifted upward in comparison to the curve plotted from the ascending part of the test (upright arrow)



demonstrated that  $E$  correlated positively with the result of third ventriculostomy: those with a stiffer brain (higher  $E$ ) have a better chance to improve after surgery. In addition to absolute values of elastance coefficient, the pressure–volume curve itself can be derived from any given infusion study, as demonstrated by Frieden [26].

### 7.6.3 Pressure–Volume Curve and Its Hysteresis

The pressure–volume curve described by (7.9) can be empirically retrieved from infusion test (see Fig. 7.2c). However, slope of the curve in most of cases is different during ascending and descending phase of the test (Fig. 7.3).

Width of hysteresis was significantly associated with a higher cerebral elastance coefficient and clinical presentation [32].

### 7.6.4 ICP Waveform Components

Furthermore, ICP recording made overnight [37] or at baseline before the infusion test allows the observation of various cyclical or random dynamic changes in ICP of

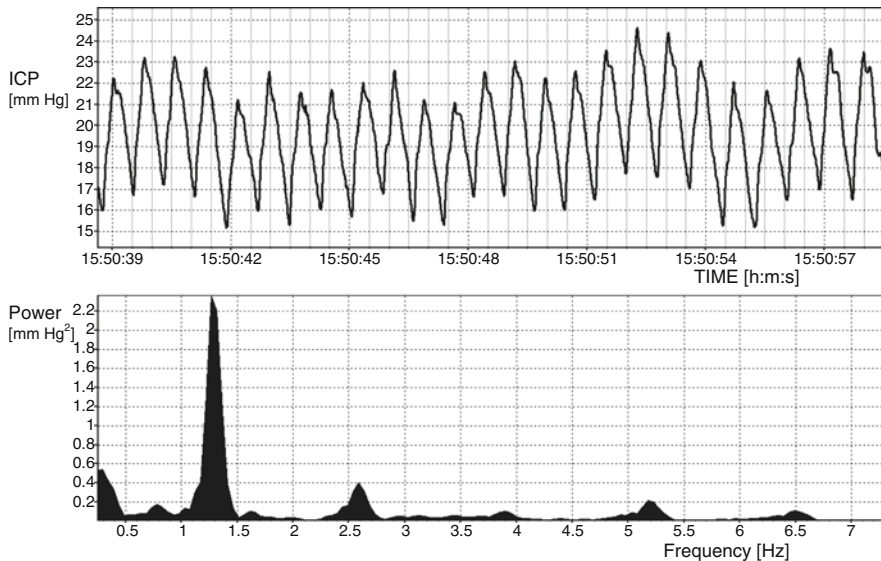


**Fig. 7.4** Example of pulse wave of ICP. Time plot and spectral analysis showing fundamental amplitude (frequency equivalent to a heart rate) and higher harmonics

vasogenic origin (i.e., forced by change in cerebral blood volume). These include: pulse, respiratory, or slow vasogenic waves.

With respect to pulse waves (caused by changes in cerebral blood volume related to the heart beat), the ICP waveform can be processed through a Fourier transform to determine the pulse amplitude of ICP (AMP) as the magnitude of the first harmonic component related to the heart rate [35] (Fig. 7.4). This method is an alternative to time-domain analysis [33] and, in our experience, both methods are generally equivalent. They produce different numerical values which are perfectly linearly associated. During the infusion study, AMP increases with mean ICP and the rate of increase of amplitude per rise in ICP is called the AMP/P slope [21, 22].

Lunberg “B waves” [42] – slow waves of ICP with periods of 20 s to 2 min – are almost universally present in ICP recordings, probably even in healthy volunteers. According to historical standards [14, 24, 43], when they were present for more than 80% of the time of overnight ICP monitoring, shunting was recommended. Using spectral analysis, a variable has been proposed, being an equivalent of the amplitude (i.e., the amplitude of sine wave bearing the same energy) of the slow waves. B waves are associated with fluctuations of CBF and arterial blood pressure [44] as well as brain tissue oxygenation (detected with near infrared spectroscopy) (Fig. 7.5).

Respiratory waves, associated with changes in venous blood volume and changes in sagittal sinus pressure as a result of ventilation, are probably less useful in assessment of CSF dynamics.

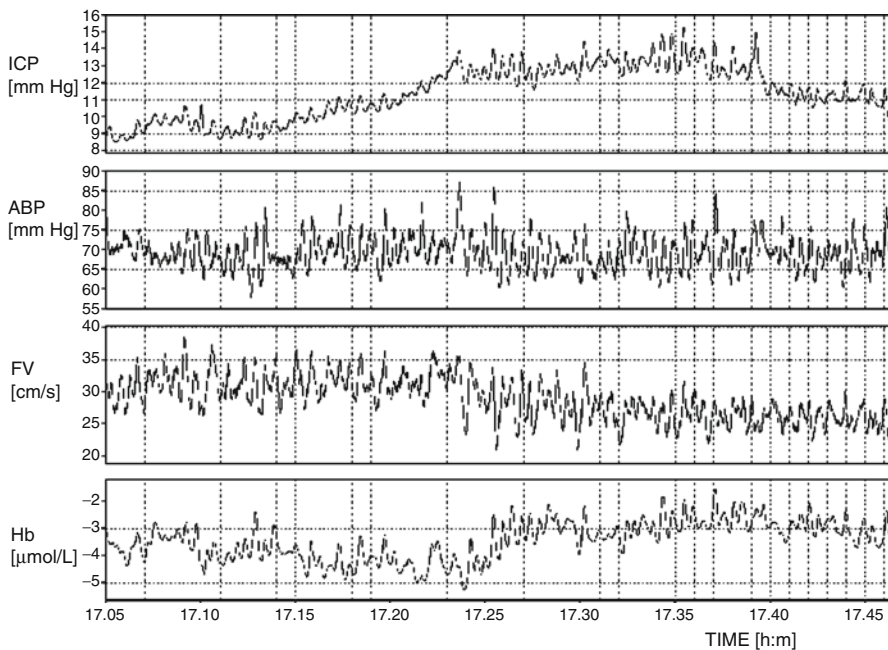


**Fig. 7.5** B waves seen in ICP, arterial pressure (ABP), blood flow velocity in MCA (FV, detected noninvasively using transcranial Doppler ultrasonography), and concentration of deoxygenated hemoglobin (detected with near infrared spectroscopy). Recording was performed during infusion study in patients with initial diagnosis of NPH. Infusion of 1.5 mL/min rate started around 17:12 and overall pressure increased was from 9 to 13 mmHg, revealing low resistance to CSF outflow

### 7.6.5 Derived Parameters, RAP Index

Conventionally, pressure–volume compensatory reserve is assessed using intracranial volume addition [20, 30, 45]. Changes in ICP in response to a known volume change allow such parameters as PVI to be derived from bolus volume addition or  $E$  (which characterizes the shape of the pressure–volume curve over its exponential region) to be derived from constant rate infusion. However, under certain assumptions, external volume addition is not necessary as it is possible to assess pressure–volume compensation by taking into account the change in pressure with every heart beat, where a certain volume of arterial blood is added to the cerebrospinal space in a pulsatile manner. Although the added volume is not known, the pressure response is recorded continuously in the form of the “pulse waveform” of the ICP recording. The RAP index (correlation coefficient [ $R$ ] between the pulse amplitude [ $A$ ] and the mean intracranial pressure [ $P$ ]) is derived by linear correlation between 30 consecutive, time-averaged data points of pulse amplitude of ICP (AMP) and mean ICP acquired within a 10 s-wide time-window. RAP describes the degree of correlation between AMP and mean ICP over short periods of time (5 min). Theoretically, the RAP

coefficient indicates the relationship between ICP and changes in intracerebral volume – the “pressure–volume” curve.  $E$  and PVI describe how fast pressure rises per unit of volume addition in an exponential region of the curve. RAP coefficient close to 0 indicates a lack of coupling between the changes in AMP and the mean ICP. This denotes a good pressure–volume compensatory reserve at low ICP, i.e., the “working point” is still below exponential region of the curve. When the pressure–volume curve starts to increase exponentially, AMP covaries directly with ICP and consequently RAP rises to +1. This indicates a low compensatory reserve [36, 46].

## 7.7 Pulsatile Flow of CSF: Phase Contrast MRI Perspective

Previous sections described theory and clinical applications of the methods, which may be implemented using CSF volume–pressure tests or continuous monitoring of ICP. However, CSF flows in pulsatile manner. These pulsations can be detected using phase contrast MRI [47–51].

## 7.8 Pulsatile CSF Flow-Basic Models

Pulsatile movement of CSF is a consequence of pulsatile inflow and outflow of cerebral blood. Therefore, the introductory modeling considerations start from dynamics of CBF.

Value of ICP directly results from the circulation of cerebral blood, CSF, compliance of the crano-spinal system, and conditions for venous blood outflow [20, 52]. Mean CBF is around 700 mL/min in adult, but arterial inflow is not constant during the cardiac cycle (systolic peak flow is around 1,000 mL/min and diastolic around 550 mL/min) [48]. Compared to arterial flow, cerebral venous outflow is delayed with lower peak flow amplitude (around 800 mL/min) and a time profile of flow shape less pulsatile [48]. The difference in time profile between arterial and venous flows results in a net change in intracranial blood volume during a cardiac cycle. The blood volume expansion during one cycle is of order of few milliliters [49].

CSF moves into the spinal canal during systole and returns to the cranial compartment during diastole [48, 49, 53–55] (Fig. 7.6).

The volume (“stroke volume”) of intracranial CSF displaced during one cardiac cycle is around 450  $\mu\text{L}$  [48, 51]. Ventricular CSF contributes only in a small part (around 10%) of cerebrospinal volume exchange [48, 51, 56].

During systolic phase of blood inflow, the brain mainly expands outward into the intracranial subarachnoid space (SAS). These CSF oscillations during a cardiac cycle are possible because of the compliance of the lumbar space which may expand within spinal channel against venous plexi.

The CSF and cerebral blood volume interaction also depend on the ability of liquids to move from one compartment of the crano-spinal system to another.

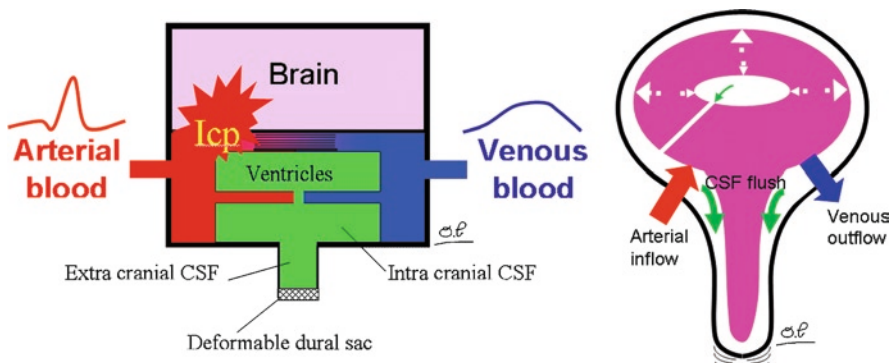


**Fig. 7.6** Intracranial fluids relationships. *Left:* general scheme showing equilibrium between volumes: arterial (red) and venous (blue) blood, brain tissue (pink), and CSF (green). *Right:* anatomical equivalent. Intracranial arterio-venous blood volume increases during systole and mainly expands the brain outward (white large arrows) flushing extraventricular CSF through the spinal canal. White thinner arrows symbolize small brain displacement caused by expansion of the ventricular CSF compartments

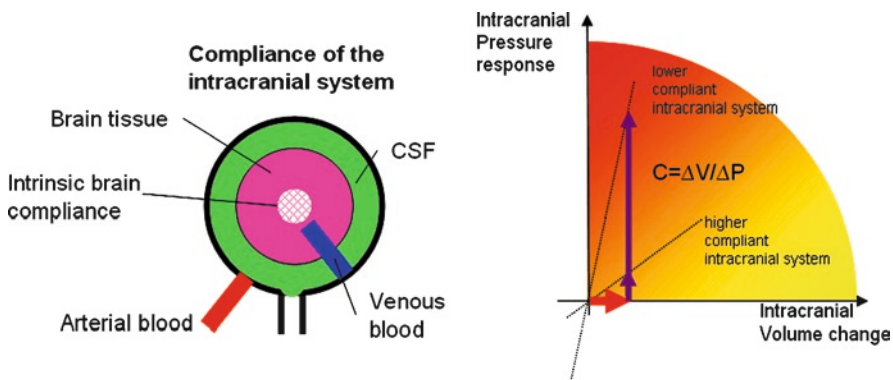


**Fig. 7.7** Intracranial compliance compartments (*left*) and compliance definition (*right*)

Compliance of the cranio-spinal system is a fundamental mechanism limiting large ICP rise after systolic arterial brain expansion (Fig. 7.7). In the rigid cranial box, without displacement of other volumes, pulsatile blood inflow would be impossible.

The compliance of cranio-spinal system is mainly moderated by a venous blood outflow and the “intrinsic brain” compliance (spinal displacements), the CSF moving in the spinal canal.

Compliance of the cranio-spinal system is therefore a function of the abilities of fluids to move from the cranial compartment to the extracranial part (Fig. 7.8). In this way, the CSF and blood viscosities, flow resistances of blood vessels and CSF SAS, intracranial pressure, thoracic pressure, lumbar pressure, and cardiac aspiration, can impact the cranio-spinal compliance.

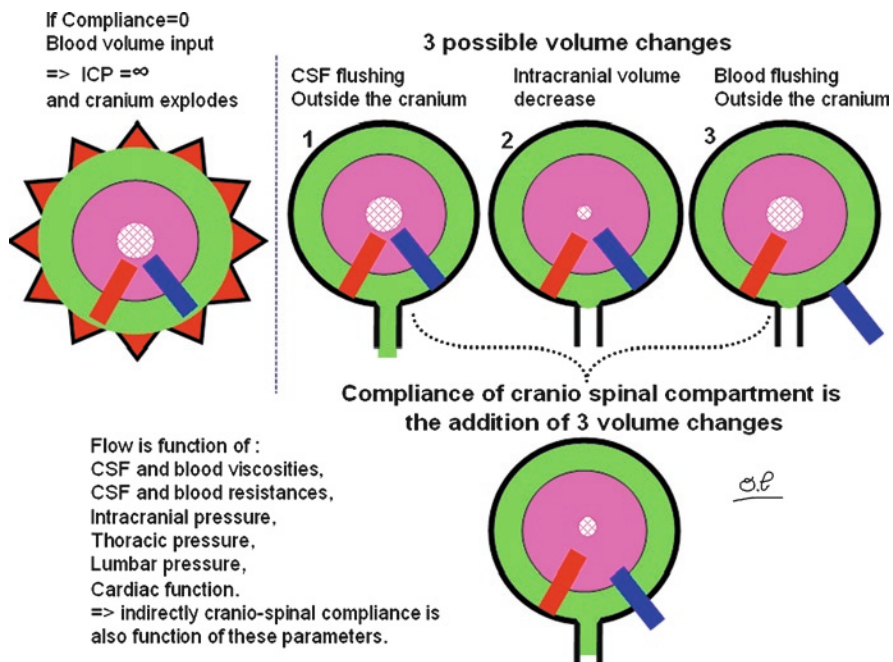


**Fig. 7.8** Intracranial compliance response to arterial blood flow input. Intracranial arterial input blood volume during systole implies (1) CSF flushing into the spinal canal, (2) intracranial volume displacement (in the eyes and ears cavities, in the spinal canal), and (3) venous blood outflow. These volumes displacements correspond to the net compliance of the intracranial space

Part of knowledge of interactions between intracranial flows during the cardiac cycle has been gathered thanks to the use of phase contrast magnetic resonance imaging [57].

## 7.9 Methodology of Phase Contrast MRI

Phase contrast MRI, which depicts motions and flows through the cardiac cycle, can be used to evaluate the presence, direction, and temporal flow dynamics, both qualitatively and quantitatively [53, 54, 57–59]. This ability to characterize direction, pulsatility, and distribution of fluid flows in physiological conditions offers a powerful tool to study physiological cerebral dynamic interactions and provide complementary view to understand pathological processes such as hydrocephalus [47, 56, 60–64].

Phase contrast MRI exploits the fact that spins moving through magnetic field gradients acquire a phase different from static spins. Then, flow-sensitive images, where pixel intensities represent the phase parameters allowing velocity calculation [65], can be produced. This technique can be associated with cardiac triggering or gating in order to decompose the cardiac cycle into several time intervals. Series of temporal images are then generated [59].

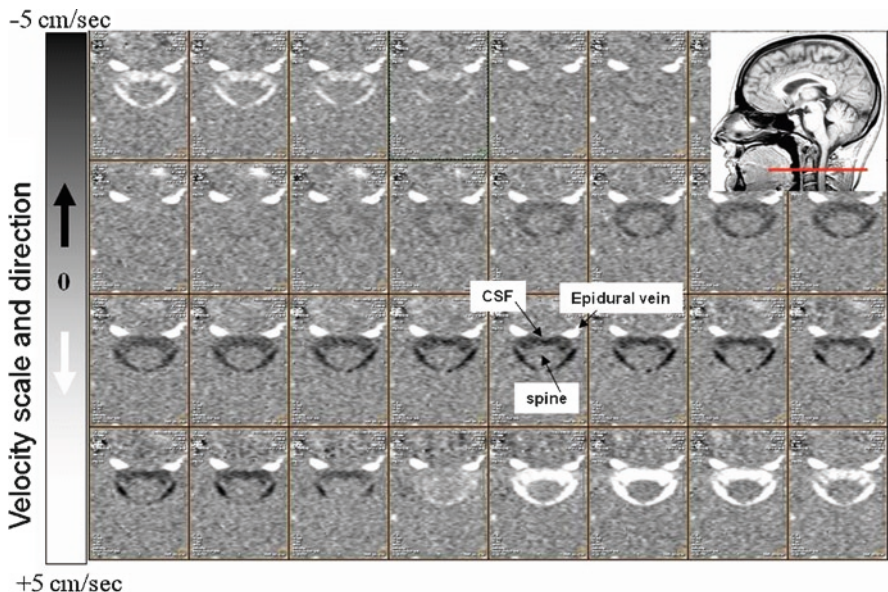


**Fig. 7.9** PC-MRI images of the CSF around the spine during one cardiac cycle. It is a visualization of 32 images of cervical CSF flow around the spine during cardiac cycle. *White pixels* depict downward CSF flow flushing into the spinal canal and *black pixels* correspond to upward motion of CSF filling the cranium

Because CSF flows' velocities (around 5 cm/s) are largely different from blood flows' velocities (60 cm/s), PC-MRI sensitivity must be adapted using a velocity encoding ( $V_{enc}$ ) set to a value near the maximum velocity of the studied flow.

In the MR image example depicted in Fig. 7.9, hyperintense regions correspond to voxels where flow velocity, positively directed cranio-caudally perpendicular to the slice plane, approaches the  $V_{enc}$  absolute value. Conversely, hypointense areas represent the voxels in which the flow is directed from caudal to cranial. Immobile tissues, corresponding to no flow regions, will be represented with gray pixels. This color convention can be reversed according to the MRI manufacturer.

For quantitative characterization and to increase the accuracy of velocity measurements [65], the acquisition plane must be selected perpendicular to the flow direction, positioned in the anatomic part corresponding to a supposed laminar flow. Such an acquisition, providing 32 images per cardiac cycle, can be accomplished, with an acceptable quality, using 3 T MR, in nearly 2 min.

Phase contrast MRI is able to quantify flows of moving liquids – see Fig. 7.9.

From those PC MRI data, it is possible to calculate cerebral CSF flows using an image processing software including an optimized CSF and blood flows segmentation algorithm – see Fig. 7.10. The same technique can be applied to carotid/vertebral arteries and jugular veins blood flows.

Knowledge of all individual flow curves permits reconstruction of cerebral blood inflow (sum of arterial flows in left and right internal carotids and vertebral arteries) and

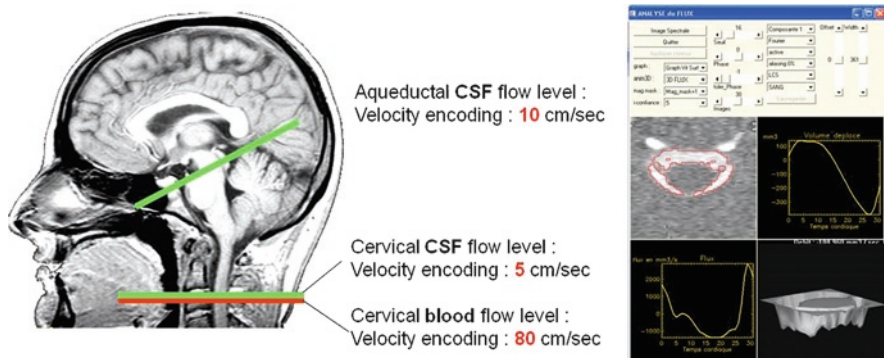


**Fig. 7.10** PC-MRI acquisition planes and example of cervical CSF segmentation

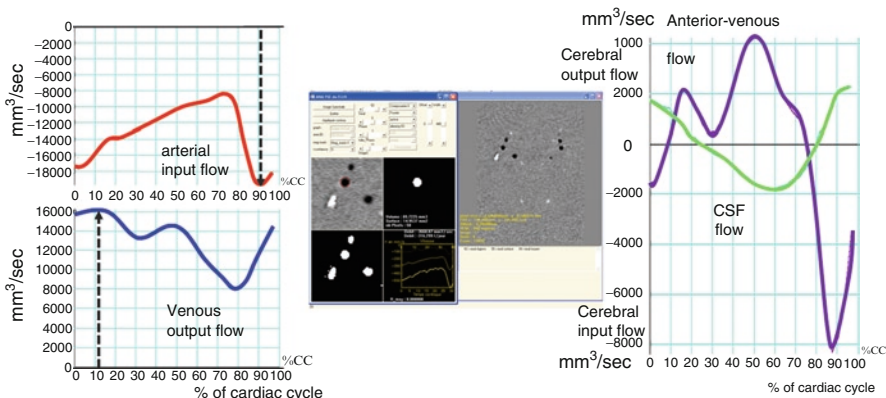


**Fig. 7.11** Arterial, venous, and CSF intracranial flows calculated from PC-MRI acquisition

cerebral venous flow (sum of venous flows in left and right internal jugular and epidural veins) and then, by summing the “positive” venous flow with the “negative” arterial flow, to obtain the arterio-venous flow curves (Fig. 7.11). This curve describes the global instantaneous displacement of cerebral blood during a cardiac cycle [48, 66].

The cerebral vascular flow curve presents a negative systolic peak flow (arterial flow > venous flow) and two diastolic positive bumps (venous flow > arterial flow). This curve is reversed compared to the CSF oscillation curve in the cervical spaces.

In the same manner, the net CSF and vascular flow curves can be computed to obtain the total cerebral brain fluid flow oscillation during the cardiac cycle [48, 66] (Fig. 7.12).

After time integration of the global cerebral flow curve, the intracranial volume change (IVC) during a cardiac cycle can be calculated (Fig. 7.13). When intracranial volume increases quickly and largely during systole, the decrease in intracranial volume takes place in two steps corresponding to the two bumps of Fig. 7.12 [66].

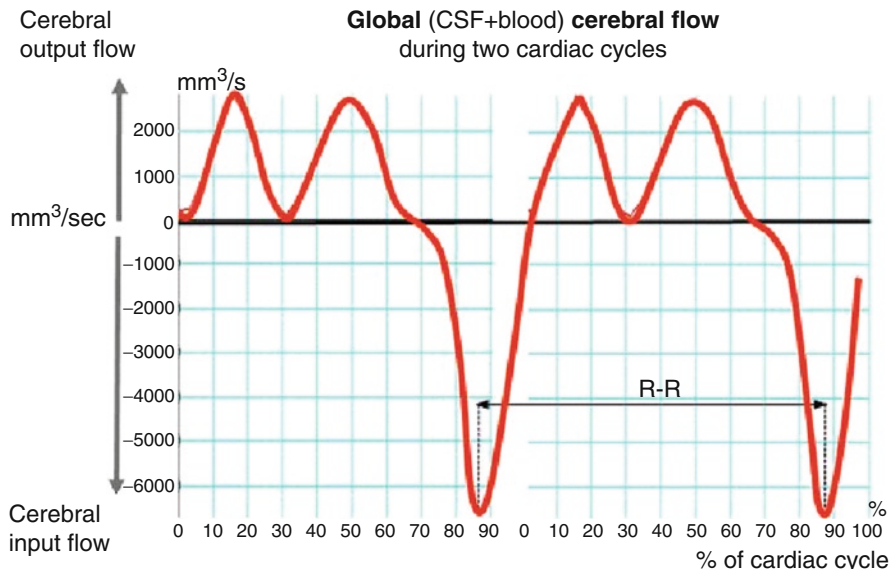


**Fig. 7.12** Global cerebral flows during two cardiac cycles calculated from PC-MRI acquisition

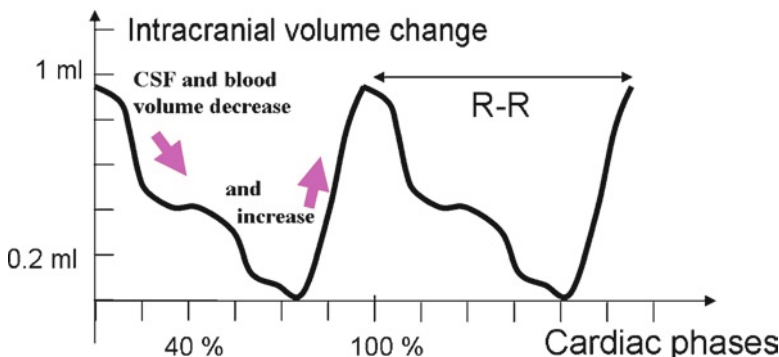


**Fig. 7.13** Intracranial volume change during cardiac cycle calculated from PC-MRI data

As a function of the cranio-lumbar compliance, IVC generates pressure variations. In order to model ICP, IVC can be transformed by Marmarou's equation (see Fig. 7.14; [20]). Figure 7.14 shows the result of the simulation during a cardiac cycle using a resting pressure  $p_o$  and brain elastance index  $k$  (equivalent to elasticity  $E$ ), respectively, set to 10 mmHg and  $0.11 \text{ mL}^{-1}$ .

Four phases of ICP cycle can be defined to explain the intracranial dynamics (P1–P4; see Fig. 7.14). During the first period (denoted P1), a sudden pressure rise, induced by the arterial systolic inflow inside the cranial cavity, occurred. Then, during the second period P2, the CSF and the venous flows are set in motion to reduce intracranial pressure until a pressure balance between intracranial and extracranial

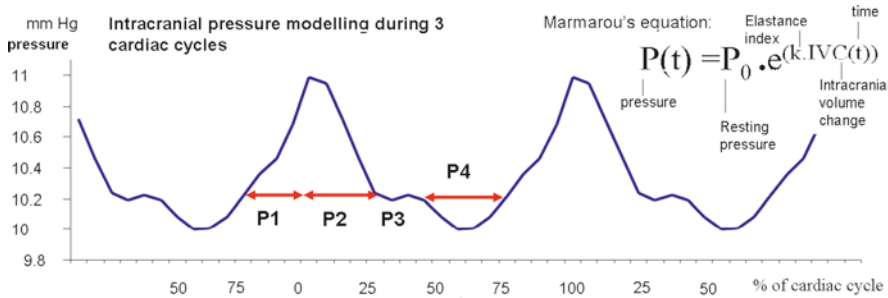


**Fig. 7.14** Modeling of ICP from CSF and blood flows calculated from PC-MRI data

spaces is reached. This balance defines the brain equilibrium pressure, i.e., P3. During equilibrium pressure phase, arterial flow equals venous flow and cervical CSF flow is null.

At the beginning of P4, ICP decrease continues. We hypothesized that this could be explained by the venous negative pressure caused by opening of the tricuspid valve and filling of the right ventricle. At the end of P4, this low pressure is finally compensated by CSF filling from cervical spaces to intracranial spaces. This would show that the influence of intracranial venous flow on brain pressure regulation is not only inherent to passive mechanisms [67] but is also shaped by heart aspiration.

Assessment of all cerebral flows allows the study of the interactions between arterial, venous, and CSF flows in the brain which control ICP. Alperin had proposed a method to directly measure ICP by PCMRI and image processing [67] and mathematical models of cerebral hydrodynamics are used to study CSF and blood relationships in the brain [68, 69].

## 7.10 Clinical Applications

The Review of clinical applications is based on 2,620 clinical infusion studies and 250 overnight ICP monitoring performed at Addenbrooke's Hospital, Cambridge UK in more than 1,400 patients suffering from hydrocephalus of various etiologies (idiopathic NPH 47%, postsubarachnoid hemorrhage NPH 12%, other communicating hydrocephalus 19%, noncommunicating hydrocephalus 22%). The mean age of the patients was 65 (range 24–94) and the male to female ratio was around 2:1. All of the patients were referred to the CSF clinic by their treating neurosurgeon, geriatrician, or neurologist, based on the presence of ventricular dilatation on brain scan (CT or MRI) and symptoms within Hakim's triad and other clinical presentations like headaches, etc. This group of patients, in addition to the clinical and imaging assessment, was investigated with a constant rate infusion study (via the lumbar approach 20%, a preimplanted Ommaya reservoir 38%, shunt prechamber 40%, or open EVD, 2%).

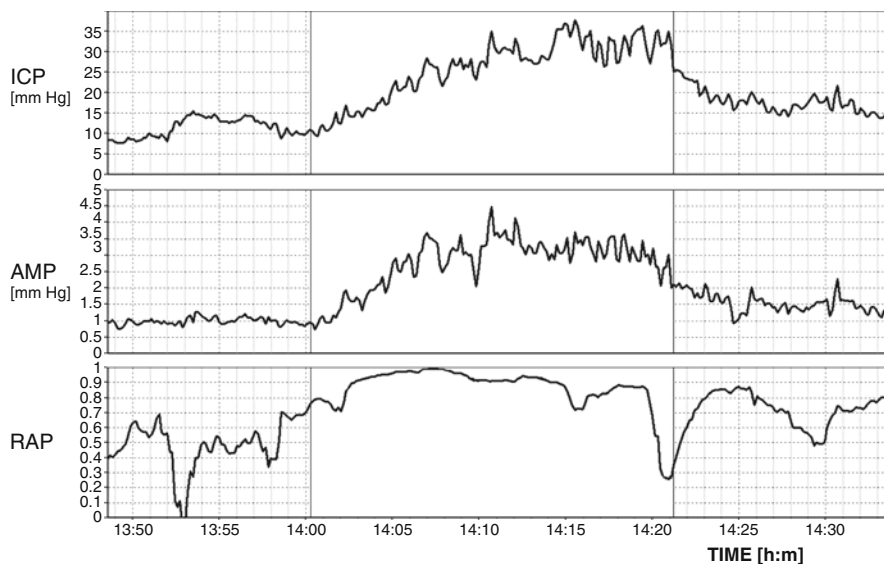


**Fig. 7.15** Example of infusion study in patient suffering from NPH: normal baseline pressure (9 mmHg), normal baseline pulse amplitude, and good compensatory reserve (RAP index at baseline below 0.6). During infusion with a rate of 1.5 mL/min (*unchecked area*), pressure increased to 35 mmHg (resistance to CSF outflow was 17.8 [mmHg/(mL/min)]), pulse amplitude increased proportionally to mean ICP, RAP coefficient increased to +1 (indicating decrease in compensatory reserve during infusion), and slow vasogenic waves appeared in ICP and AMP recordings

PC-MRI material was derived from the database at Department of Image Processing, Amiens University Hospital, France, containing more than 500 volunteers and patients suffering from hydrocephalus, syringomyelia, and other CSF circulatory defects.

Although illustrative material is derived from two centers, similar results are reported from many other hospitals worldwide, known as a centers of excellence in studies on hydrocephalus and CSF disorders [4, 10, 23–25, 27, 30, 37, 49, 62, 68, 69].

### 7.10.1 Differentiation Between Brain Atrophy and Normal Pressure Hydrocephalus

CSF dynamics in NPH is characterized by a normal baseline pressure (ICP < 18 mmHg). The resistance to CSF outflow is increased (>13 [mmHg/(mL/min)]). B waves recorded during infusion are regular. Pulse amplitude is well correlated with mean ICP. Compensatory reserve at baseline is usually good (RAP index below 0.6) and usually elastance coefficient slightly increased ( $E>0.2\text{ mL}^{-1}$ ) (see Fig. 7.15).

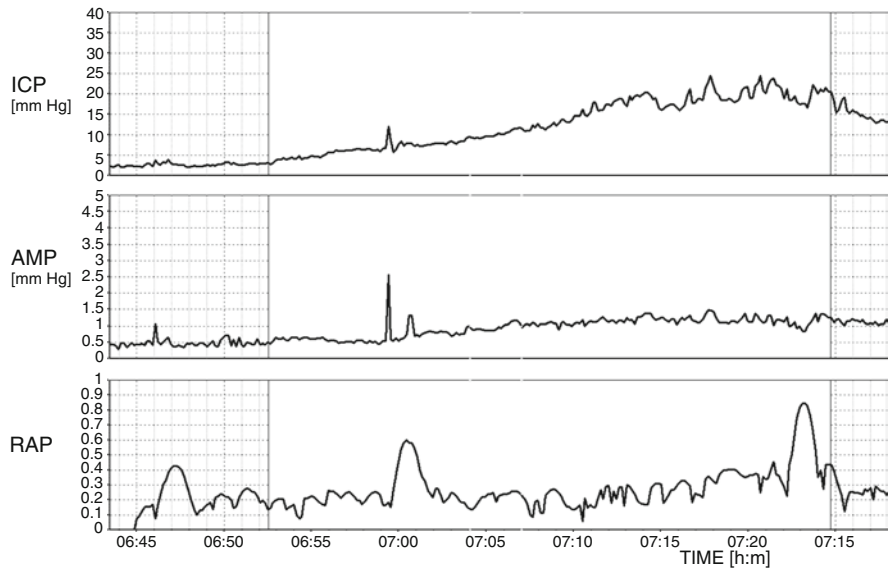


**Fig. 7.16** Example of infusion study in patient with predominant atrophy. Baseline pressure was low (3 mmHg) and increased only slightly to 18 mmHg during infusion of a rate of 1.5 mL/min, giving normal value of resistance to CSF outflow (10 mmHg/(mL/min)). Compensatory reserve was good, even during infusion (RAP did not increase), pulse amplitude increased very modestly in response to rising ICP, and there was very little slow waves in recording

Patients suffering predominantly from brain atrophy have normal CSF circulation. Typically, opening pressure, resistance to CSF outflow and pulse amplitude are low ( $ICP < 12 \text{ mmHg}$ ,  $R_{CSF} < 12 \text{ mmHg}/(\text{mL/min})$ , amplitude  $< 2 \text{ mmHg}$ ). The compensatory reserve at baseline is good ( $RAP < 0.5$ ), reflecting low elasticity of the atrophic brain ( $E < 0.2 \text{ mL}^{-1}$ ). Vasogenic waves are rather limited during recording. The mean ICP increases smoothly during the infusion and decreases in a similar fashion following infusion, comparable to the inflation and deflation of a balloon – Fig. 7.16.

### 7.10.2 Noncommunicating and Acute Communicating Hydrocephalus

Lumbar infusion is not recommended in noncommunicating hydrocephalus because of the risk of brain herniation in the event of uncontrolled CSF leak. However, this type of hydrocephalus may not always be easy to detect by the brain scan. In those few instances of noncommunicating hydrocephalus where lumbar infusion is

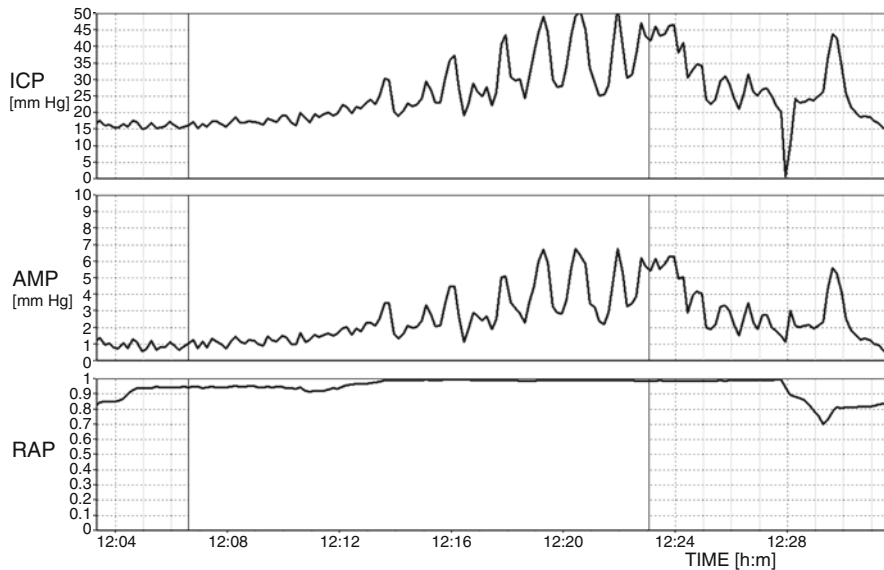


**Fig. 7.17** Acute hydrocephalus. Opening pressure was slightly elevated (17 mmHg), resistance to CSF outflow was 26 mmHg/(mL/min), and RAP close to +1 all the time indicated permanently depleted compensatory reserve. Very strong vasogenic waves were recorded during the test (of maximum magnitude around 25 mmHg)

performed, the resistance to CSF outflow is normal because the lumbar infusion is not able to detect the proximal narrowing in CSF circulatory pathways. Paradoxically elasticity is relatively low ( $E < 0.20 \text{ mL}^{-1}$ ). In acute hydrocephalus  $R_{\text{csf}}$  is elevated, the resting pressure and pulse amplitude are also elevated (ICP  $> 15 \text{ mmHg}$ , pulse amplitude  $> 4 \text{ mmHg}$ ) and compensatory reserve is poor (RAP  $> 0.6$  at baseline).

Obstructive hydrocephalus can be safely assessed using ventricular infusion (via a reservoir). This demonstrates high intracranial resting pressure and high resistance to CSF outflow (ICP  $> 15 \text{ mmHg}$ ,  $R_{\text{CSF}} > 13 \text{ mmHg}/(\text{mL/min})$ ). The elasticity is high ( $> 0.20 \text{ mL}^{-1}$ ), RAP is elevated above 0.6, and the pulse amplitude is high ( $> 4 \text{ mmHg}$ ) indicating poor compensatory reserve – see Fig. 7.17.

Acute communicating hydrocephalus (as in post-SAH) presents with a similar pattern of parameters, with frequent deep vasogenic waves (including plateau waves [42]) (Fig. 7.18).

### 7.10.3 Testing of CSF Dynamics in Shunted Patients

The methods for evaluation of CSF dynamics in shunted patients can be supportive for assessment of shunt function [4, 70, 71]. When a shunt drains properly, the resting

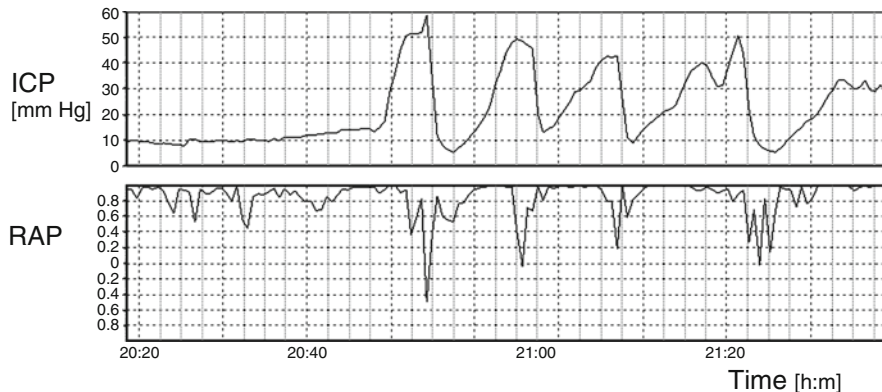


**Fig. 7.18** Example of recording of ICP in patient after SAH, with moderate ventricular dilatation, in whom baseline pressure was normal (10 mmHg). Computer recording revealed a regular pattern of plateau waves up to 60 mmHg. This patient previously had a series of manometric lumbar CSF measurements yielding mixed results: some measurements indicating normal pressure, while others showed elevated ICP

pressure remains at or below the shunt's operating pressure. Infusion testing or overnight ICP monitoring repeated after shunting should always be considered for comparison with the tests performed before surgery. Abnormal cerebrospinal compensatory parameters, such as high resting pressure, increased resistance to CSF outflow, low compensatory reserve, increased activity of slow waves, or high amplitude of pulse waveform, should return to normal after successful shunting [7, 8]. In valves with a low hydrodynamic resistance and a well-defined opening pressure, a sharp plateau of the pressure trend is seen at about 1–5 mmHg above the level of the shunt's operating pressure [72]. The magnitude of this plateau should not exceed a value as defined by the equation:

$$\text{Critical pressure} = \text{Shunt operating pressure} + (R_{\text{shunt}} \times \text{Infusion rate}) + 5 \text{ mmHg},$$

where  $R_{\text{shunt}}$  is the hydrodynamic resistance of the opened shunt and 5 mmHg is a “safety margin” and a credit for possible nonzero abdominal pressure (in patients with possible increased abdominal pressure, this value should be increased to 10–15 mmHg). Both shunt operating pressures and  $R_{\text{shunt}}$  can be measured in the laboratory, but once evaluated, these parameters provide an invaluable guidelines for shunt testing *in vivo* [71] (Fig. 7.19).

These methods of assessing CSF dynamics in shunted patients can be based on different techniques. The simplest and least invasive way is an infusion study through a previously implanted subcutaneous CSF reservoir. Lumbar puncture in communicating hydrocephalus or measurement of the pressure inside the chamber of the shunt are also possible. Pressure measurement and infusion into shunt chamber is only

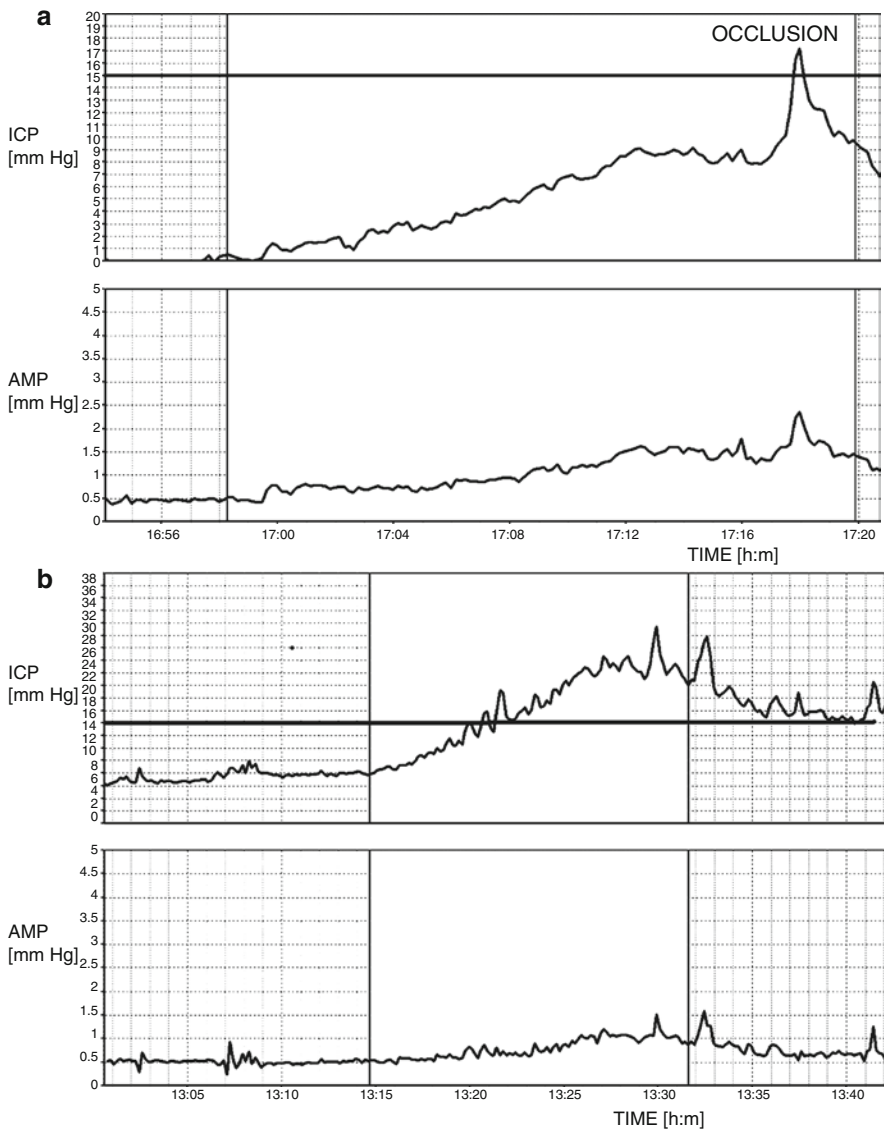


**Fig. 7.19** Examples of infusion studies performed in shunted patients through shunt prechamber with working (a) and blocked (b) shunt. (a) Patient with a Strata Valve set for 1.5 in situ. Pulse amplitude was low but clearly recordable, confirming patency of ventricular drain. Opening pressure was low, and during infusion pressure increased to the value below “critical threshold” for this valve (thick vertical line). During infusion, transcutaneous occlusion (external compression of siphon-control device) was performed. Such a compression stops the drainage through the valve. Pressure started to rise immediately, confirming that shunt system was patent. (b) Patient with Hakim-Programmable Valve set at 100 mmH<sub>2</sub>O. Pressure increased well above “critical threshold” (horizontal line). Spontaneous vasogenic waves were recorded during the test. Pulse waveform was present in recording. There was distal obstruction of shunt system confirmed during the revision of the shunt

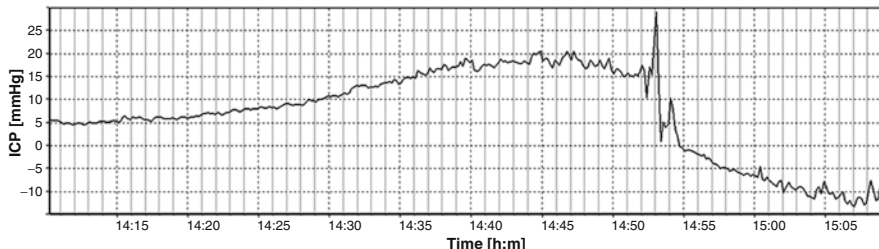


**Fig. 7.20** Overdrainage test. Showing excessive decrease in ICP during sitting up at the time point indicated after 14:53 (below  $-14$  mmHg). During sitting up, pulse amplitude may not change

possible with shunts having a CSF sampling reservoir proximal to the valve; therefore, the method is not useful for the testing of majority of burr-hole valves.

With pressure measurement via the shunt chamber, the presence of a CSF pressure pulse wave and a pressure increase in response to coughing should indicate pressure transmission between the needle and the CSF space, confirming the patency of the ventricular catheter.

When a shunted patient presents with low-pressure headache, small or slit ventricles, subdural collections, or chronic subdural hematomas, CSF overdrainage can be suspected. Overdrainage related to body posture may be assessed using a tilting test. When the baseline pressure measured in the horizontal body position is low (usually negative), overdrainage is possible. A change of posture to sitting usually produces a further decrease in pressure. If the pressure decreases to a value lower than  $-10$  mmHg (95% confidence limit for ICP in upright position in nonshunted patients is approximately  $-8$  mmHg), overdrainage is likely (Fig. 7.20).

The majority of contemporary valves usually have a low hydrodynamic resistance [70], a feature which may cause overdrainage resulting from the periodic oscillations of cerebrovascular volume. The expanding vascular bed would act like the membrane of a water pump with a distal low-resistance valve [73]. Early morning headache should not be always assumed to be a “high pressure”: they may instead be a consequence of low pressure caused by nocturnal overdrainage.

In shunted patients with slit ventricles, baseline pressure recorded from the shunt prechamber would not comprise a pulse waveform as the ventricle walls would be collapsed around the catheter and therefore no pressure transmission would take place. Often, however, the pulse wave appears after infusion starts, as the pressure builds up and opens up the ventricles (Fig. 7.21).

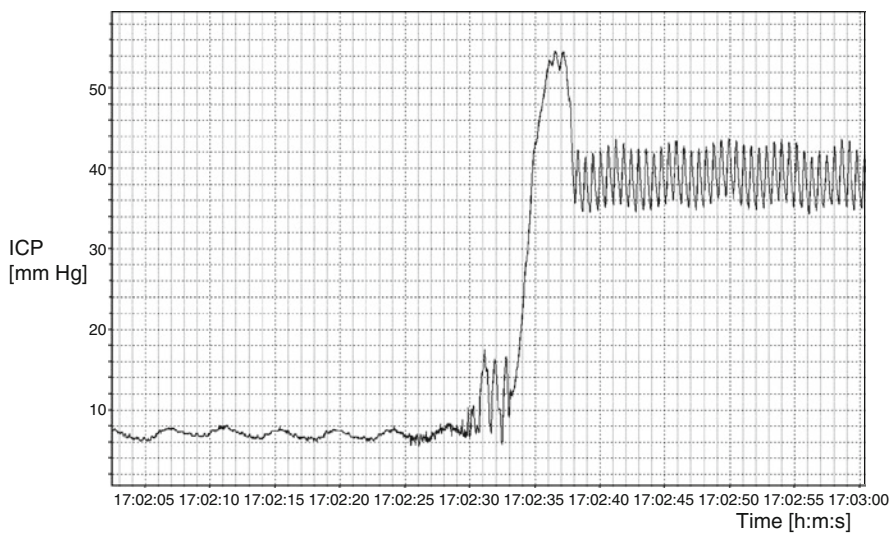


**Fig. 7.21** In patients with slit ventricles, the pulse wave of ICP is rarely visible in recording. During infusion into shunt prechamber, all fluid is drained; distally recorded pressure is equivalent to shunt operating pressure plus pressure gradient along distal tube plus abdominal pressure. Respiratory wave can be visible – it is commonly transmitted from abdominal space. In patients with membrane siphon, preventing device occlusion can be performed during infusion (17:02). Pressure increases quickly to very high values (in this case above 50 mmHg), collapsed ventricles open within relatively short time, and pressure stabilizes at lower level with a pulse wave clearly visible. The “stabilization pressure” is elevated, as in slit ventricles syndrome, and intraparenchymal ICP is usually high. Ventricles may stay open over longer time, but more frequently they collapse again after the end of infusion

#### 7.10.4 Phase-Coded MRI in Clinical Practice

PC MRI is used in clinical practice to study hydrocephalus and other CSF circulatory disorders. In case of obstructive hydrocephalus, PC MRI is a rapid and accurate tool to confirm aqueductal stenosis, detecting no flow in the aqueduct [50]. In the case of noncommunicating hydrocephalus depicted in Fig. 7.22, treatment by endoscopic third ventriculostomy (ETV) was an alternative to ventricular shunting for the treatment of hydrocephalus. The PC-MRI technique is now largely widespread to measure CSF flow in the third ventricle aperture to check the viability of ETV.

For many authors, in case of communicating hydrocephalus, increased ventricular CSF oscillations are predictive of a favorable outcome of shunting [56, 60, 62–64]. A recent study found a relationship between poor clinical outcome and low ventricular CSF pulsation [74]. It has been suggested [60] that increase in aqueductal CSF pulsatile flow was not associated with increased CSF flow at the cervical level (Fig. 7.23). Therefore, if communicating hydrocephalus cervical flow was stable

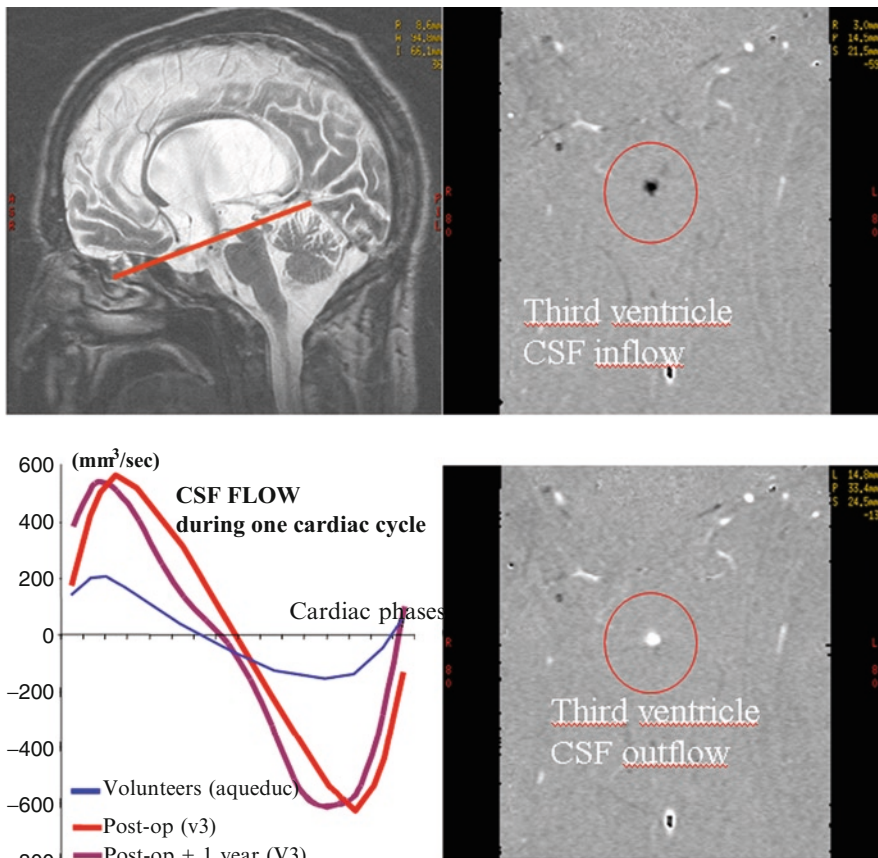


**Fig. 7.22** Example of noncommunicating hydrocephalus studied using PC-MRI examination. The patient had aqueductal stenosis, detected by PC-MRI and treated by ETV. PC-MRI was performed 3 months after surgery to confirm the aperture of the third ventricle. In comparison with volunteer curve flow (in blue), we can see that CSF flow in the third ventricle aperture has the same temporal evolution, whereas its amplitude is increased. This difference can be due to the third ventricle aperture flow resistance which is smaller than in normal aqueduct. One year later, PC-MRI in the same patient showed a similar CSF flow curve at the third ventricle aperture

while ventricular flow was dramatically increased, intracranial SAS flow must have been dramatically decreased. These results confirm that, in healthy volunteers, the intracranial mobile compliance predominantly depends on the intracranial subarachnoid pulsation. Communicating hydrocephalus seems to be an adaptation process of the vascular brain expansion when intracranial SAS CSF pulsation is altered.

PC-MRI, now available to neurosurgeons, is complementary to morphological MR and provides quantitative information on cerebral hydrodynamics (Fig. 7.24). This information is mainly used to confirm alteration of CSF flow in the cerebral

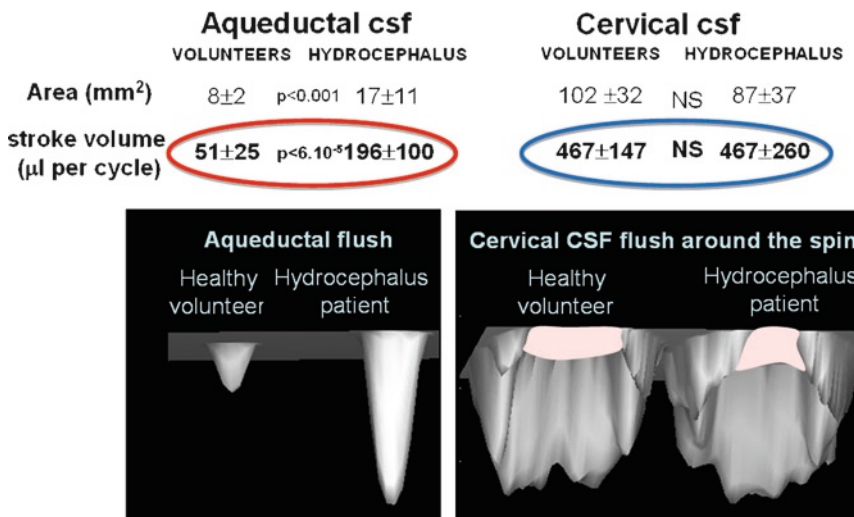
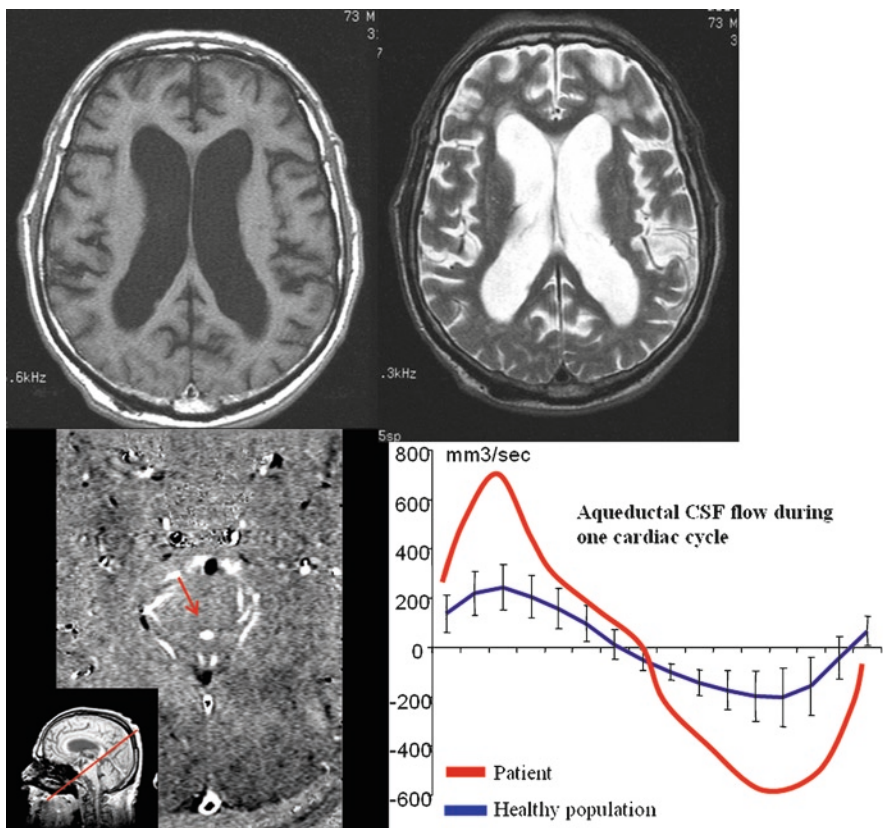


**Fig. 7.23** CSF flows in communicating hydrocephalus population studied using PCMRI



and spinal compartments. PC-MRI is also a functional tool to better understand the pathophysiology of hydrocephalus and it should lead in the medium term to an assessment of intracranial pressure.

## 7.11 Conclusion

Understanding of dual aspects of CS dynamics emerging of time profiles of pressures (studied using ICP monitoring, infusion tests, etc.) and flows (visualized and analyzed using PCMRI) is paramount in contemporary diagnostic of hydrocephalus and other CSF disorders. Fluid circulation and pressure–volume compensation can be studied using invasive pressure measurement or noninvasive PCMRI techniques, allowing description of patients' status using modeling parameters: resistance to CSF outflow, elasticity, or CSF stroke volume in various craniocerebral compartments (Table 7.1). Future clinical works should be focused on integration of pressure-measurement techniques and PCMRI.

**Table 7.1** Typical values for parameters of CSF dynamics in nonshunted patients

	Atrophy	NPH	Acute hydrocephalus
$p_b$ [mmHg]	<10	<15	>15
$R_{CSF}$ [mmHg/ (mL/min)]	<10	>13	>18
AMP [mmHg]	<2	>2	>4
$E$ [ $mL^{-1}$ ]	<0.1	<0.2	>0.2
Vasogenic waves	No vasogenic waves	B waves present and increased during infusion	Increased B waves and plateau waves
RAP	<0.6 all time	<0.6 at baseline >0.6 during test	>0.6 all time

$p_b$  baseline value of intracranial pressure;  $R_{CSF}$  resistance to CSF outflow; AMP pulse amplitude of intracranial pressure;  $E$  elasticity or elastance coefficient; RAP index of brain compliance

 **Fig. 7.24** CSF flows in communicating hydrocephalus patient studied by PC-MRI. This 73-year-old man, with a history of hypertension, was referred for assessment of disorders of higher functions associated with gait disorders (ataxia) and sphincter disorders. Morphological MR demonstrated: a dilation of the ventricular system, a deep cortical sulci, and nonspecific abnormalities of the periventricular white matter. The clinical and morphological assessment was unable to formally demonstrate the active nature of the ventricular dilation and the indication for ventricular shunting. The oscillatory flow volume measured in the cerebral aqueduct was very high, but normal CSF fluctuations were observed in the cervical subarachnoid spaces. The blood flow was small (334 mL/min) and the peak jugular vein outflow velocity was observed early after the arterial systolic peak. Ventriculoperitoneal shunting induced a marked clinical improvement with resolution of the gait disorders and sphincter disorders. Radiological follow-up demonstrated a reduction of ventricular volume. In this clinical case, demonstration of a markedly hyperdynamic ventricular system supported the indication for ventricular shunting in this patient, as for many authors, increased ventricular activity is predictive of a favorable outcome of shunting

**Acknowledgment** Financial support: European Community INTERREG grant (Amiens, Cambridge).

## References

1. Stein, S.C., Burnett, M.G., Sonnad, S.S.: Shunts in normal pressure hydrocephalus: do we place too many or too few? *J. Neurosurg.* **105**, 815–822 (2006)
2. Marmarou, A., Black, P., Bergsneider, M., et al.: International NPH Consultant Group. Guidelines for management of idiopathic normal pressure hydrocephalus: progress to date. *Acta Neurochir. Suppl.* **95**, 237–240 (2005)
3. Pickard, J.D., Spiegelhalter, D., Czosnyka, M.: Health economics and the search for shunt-responsive symptomatic hydrocephalus in the elderly. *J. Neurosurg.* **105**, 811–814 (2006)
4. Drake, J.M., Saint-Rose, C.H. (eds.): Shunt complications. In: *The Shunt Book*, pp. 23–92. Blackwell Science, Oxford (1995)
5. Czosnyka, M., Maksymowicz, W., Batorski, L., et al.: Comparison between classic differential and automatic shunt functioning on the basis of infusion tests. *Acta Neurochir.* **106**, 1–8 (1990)
6. Maksymowicz, W., Czosnyka, M., Koszewski, W., et al.: Post shunting improvement in hydrocephalic patients described by cerebrospinal compensatory parameters. In: Avezaat, C.J.J., van Eijndhoven, J.H.M., Maas, A.I.R., Tans, J.T.J. (eds.) *Intracranial Pressure VIII*, pp. 829–832. Springer, Berlin (1994)
7. Maksymowicz, W., Czosnyka, M., Koszewski, W., et al.: The role of cerebrospinal system compensatory parameters in estimation of functioning of implanted shunt system in patients with communicating hydrocephalus. *Acta Neurochir.* **101**, 112–116 (1989)
8. Petrella, G., Czosnyka, M., Keong, N., et al.: How does CSF dynamics change after shunting? *Acta Neurol. Scand.* **118**(3), 182–188 (2008)
9. Sorenson, P.S., Gjerris, F., Schmidt, J.: Resistance to CSF outflow in benign intracranial hypertension (pseudotumor cerebri). In: Gjerris, F., Borgesen, S.E., Sorensen, P.S. (eds.) *Outflow of Cerebrospinal Fluid*, pp. 343–55. Munskgaard, Copenhagen (1989)
10. Tans, J.T., Boon, A.J.: Study Group. How to select patients with normal pressure hydrocephalus for shunting. *Acta Neurochir. Suppl.* **81**, 3–5 (2002)
11. Czosnyka, M., Copeman, J., Czosnyka, Z., et al.: Post-traumatic hydrocephalus: influence of craniectomy on the CSF circulation. *J. Neurol. Neurosurg. Psychiatry* **68**, 246–247 (2000)
12. May, C., Kaye, J.A., Atack, J.R., et al.: Cerebrospinal fluid production is reduced in healthy aging. *Neurology* **40**, 500–503 (1990)
13. Davson, H., Welch, K., Segal, M.B.: *The Physiology and Pathophysiology of Cerebrospinal Fluid*. Churchill Livingstone, New York (1987)
14. Gjerris, F., Borgesen, S.E.: Pathophysiology of CSF circulation. In: Crockard, A., Hayward, A., Hoff, J.T. (eds.) *Neurosurgery. The scientific basis of clinical practice*, pp. 146–174. Blackwell Scientific, Oxford (1992)
15. Momjian, S., Owler, B.K., Czosnyka, Z., et al.: Pattern of white matter regional cerebral blood flow and autoregulation in normal pressure hydrocephalus. *Brain* **127**(pt 5), 965–972 (2004)
16. Stoquart-ElSankari, S., Lehmann, P., Villette, A., et al.: A phase-contrast MRI study of physiological cerebral venous flow. *J. Cereb. Blood. Flow Metab.* **29**, 1208–1215 (2009)
17. Bradley Jr., W.G., Whittemore, A.R., Kortman, K.E., et al.: Marked cerebrospinal fluid void: indicator of successful shunt in patients with suspected normal-pressure hydrocephalus. *Radiology* **178**(2), 459–466 (1991)
18. Egnor, M., Zheng, L., Rosiello, A., et al.: A model of pulsations in communicating hydrocephalus. *Pediatr. Neurosurg.* **36**(6), 281–303 (2002)
19. Eide, P.K.: Intracranial pressure parameters in idiopathic normal pressure hydrocephalus patients treated with ventriculo-peritoneal shunts. *Acta Neurochir.* **148**(1), 21–29 (2006)

20. Marmarou, A., Shulman, K., Rosende, R.M.: A non-linear analysis of CSF system and intracranial pressure dynamics. *J. Neurosurg.* **48**, 332–344 (1978)
21. Avezaat, C.J.J., Eijndhoven, J.H.M.: Cerebrospinal fluid pulse pressure and craniospinal dynamics. A theoretical, clinical and experimental study (thesis). Jongbloedrr A, The Hague (1984)
22. Sliwka, S.: A clinical system for the evaluation of selected dynamic properties of the intracranial system. PhD Thesis, Polish Academy of Sciences, Warsaw (in Polish) (1980)
23. Boon, A.J., Tans, J.T., Delwel, E.J., et al.: Dutch normal-pressure hydrocephalus study: prediction of outcome after shunting by resistance to outflow of cerebrospinal fluid. *J. Neurosurg.* **87**(5), 687–693 (1997)
24. Borgesen, S.E., Gjerris, F.: The predictive value of conductance to outflow of CSF in normal pressure hydrocephalus. *Brain* **105**, 65–86 (1982)
25. Ekstedt, J.: CSF hydrodynamic studies in man. Method of constant pressure CSF infusion. *J. Neurol. Neurosurg. Psychiatry* **40**, 105–119 (1977)
26. Frieden, H., Ekstedt, J.: Instrumentation for cerebrospinal fluid hydrodynamic studies in man. *Med. Biol. Eng. Comput.* **20**, 167–180 (1982)
27. Jurkiewicz, J., Czernicki, Z., Berdyga, J., et al.: Three-phase infusion test. *Neurol. Neurochir. Pol.* **28**, 363–369 (1994)
28. Katzman, R., Hussey, F.: A simple constant infusion manometric test for measurement of CSF absorption. *Neurology* **20**, 534–544 (1970)
29. Tisell, M., Edsbagge, M., Stephensen, H., et al.: Elastance correlates with outcome after endoscopic third ventriculostomy in adults with hydrocephalus caused by primary aqueductal stenosis. *Neurosurgery* **50**, 70–76 (2002)
30. Marmarou, A., Foda, M.A., Bandoh, K., et al.: Posttraumatic ventriculomegaly: hydrocephalus or atrophy? A new approach for diagnosis using CSF dynamics. *J. Neurosurg.* **85**(6), 1026–1035 (1996)
31. Tans, J.T., Poortvliet, D.C.: Relationship between compliance and resistance to outflow of CSF in adult hydrocephalus. *J. Neurosurg.* **71**(1), 59–62 (1989)
32. Kasprowicz, M., Czosnyka, M., Czosnyka, Z., et al.: Hysteresis of the cerebrospinal pressure-volume curve in hydrocephalus. *Acta Neurochir. Suppl.* **86**, 529–532 (2003)
33. Eide, P.K.: A new method for processing of continuous intracranial pressure signals. *Med. Eng. Phys.* **28**(6), 579–587 (2006)
34. Borgesen, S.E., Albeck, M.J., Gjerris, F., et al.: Computerized infusion test compared to steady pressure constant infusion test in measurement of resistance to CSF outflow. *Acta Neurochir.* **119**, 12–16 (1992)
35. Czosnyka, M., Batorski, L., Laniewski, P., et al.: A computer system for the identification of the cerebrospinal compensatory model. *Acta Neurochir.* **105**, 112–116 (1990)
36. Czosnyka, M., Czosnyka, Z., Momjian, S., et al.: Cerebrospinal fluid dynamics. *Physiol. Meas.* **25**, R51–R76 (2004)
37. Schuhmann, M.U., Sood, S., McAllister, J.P., et al.: Value of overnight monitoring of intracranial pressure in hydrocephalic children. *Pediatr. Neurosurg.* **44**(4), 269–279 (2008)
38. Owler, B.K., Fong, K.C., Czosnyka, Z.: Importance of ICP monitoring in the investigation of CSF circulation disorders. *Br. J. Neurosurg.* **15**(5), 439–440 (2001)
39. Czosnyka, M., Whitehouse, H., Smielewski, P., et al.: Testing of cerebrospinal compensatory reserve in shunted and non-shunted patients: a guide to interpretation based on an observational study. *J. Neurol. Neurosurg. Psychiatry* **60**, 549–558 (1996)
40. Sklar, F.H., Beyer, C.W., Ramanathan, M., et al.: Servo-controlled lumbar infusions: a clinical tool for determination of CSF dynamics as a function of pressure. *Neurosurgery* **3**, 170–178 (1978)
41. Borgesen, S.E., Gjerris, F., Sorensen, S.C.: The resistance to cerebrospinal fluid absorption in humans: a method of evaluation by lumbo-ventricular perfusion, with particular reference to normal pressure hydrocephalus. *Acta Neurol. Scand.* **57**, 88–96 (1978)
42. Lundberg, N.: Continuous recording and control of ventricular fluid pressure in neurosurgical practice. *Acta Psychiatr. Scand. Suppl.* **36**(149), 1–193 (1960)

43. Pickard, J.D., Teasdale, G., Matheson, M., et al.: Intraventricular pressure waves – the best predictive test for shunting in normal pressure hydrocephalus. In: Shulman, K., Marmarou, A., Miller, J.D., Becker, D.P., Hochwald, D.M., Brock, M. (eds.) *Intracranial Pressure IV*, pp. 498–500. Springer, Berlin (1980)
44. Drost, D.W., Krauss, J.K.: Intracranial pressure B-waves precede corresponding arterial blood pressure oscillations in patients with suspected normal pressure hydrocephalus. *Neurol. Res.* **21**(7), 627–630 (1999)
45. Piper, I.R., Miller, J.D., Whittle, I.R., et al.: Automated time-averaged analysis of craniospinal compliance (short pulse response). *Acta Neurochir. Suppl.* **51**, 387–390 (1990)
46. Kim, D.J., Czosnyka, Z., Keong, N., et al.: Index of cerebrospinal compensatory reserve in hydrocephalus. *Neurosurgery* **64**(3), 494–501 (2009)
47. Baledent, O., Gondry-Jouet, C., Stoquart-Elsankari, S., et al.: Value of phase contrast magnetic resonance imaging for investigation of cerebral hydrodynamics. *J. Neuroradiol.* **33**(5), 292–303 (2006)
48. Baledent, O., Henry-Feugeas, M.C., Idy-Peretti, I.: Cerebrospinal fluid dynamics and relation with blood flow: a magnetic resonance study with semiautomated cerebrospinal fluid segmentation. *Invest Radiol* **36**(7), 368–377 (2001)
49. Bhadelia, R.A., Bogdan, A.R., Kaplan, R.F., et al.: Cerebrospinal fluid pulsation amplitude and its quantitative relationship to cerebral blood flow pulsations: a phase-contrast MR flow imaging study. *Neuroradiology* **39**(4), 258–264 (1997)
50. Stoquart-El Sankari, S., Lehmann, P., Gondry-Jouet, C., et al.: Phase-contrast MR imaging support for the diagnosis of aqueductal stenosis. *AJNR Am. J. Neuroradiol.* **30**(1), 209–214 (2009)
51. Stoquart-ElSankari, S., Baledent, O., Gondry-Jouet, C., et al.: Aging effects on cerebral blood and cerebrospinal fluid flows. *J. Cereb. Blood Flow Metab.* **27**(9), 1563–1572 (2007)
52. Marmarou, A., Schulman, K., LaMorgese, J.: Compartmental analysis of compliance and outflow resistance of cerebrospinal fluid system. *J. Neurosurg.* **43**, 523–534 (1975)
53. Enzmann, D.R., Pelc, N.J.: Cerebrospinal fluid flow measured by phase-contrast cine MR. *AJNR Am. J. Neuroradiol.* **14**(6):1301–1307; discussion 1309–1310 (1993)
54. Greitz, D., Wirestam, R., Franck, A., et al.: Pulsatile brain movement and associated hydrodynamics studied by magnetic resonance phase imaging. The Monro-Kellie doctrine revisited. *Neuroradiology* **34**(5), 370–380 (1992)
55. Henry-Feugeas, M.C., Idy-Peretti, I., Baledent, O., et al.: Origin of subarachnoid cerebrospinal fluid pulsations: a phase-contrast MR analysis. *Magn. Reson. Imaging* **18**(4), 387–395 (2000)
56. Wagshul, M.E., Chen, J.J., Egnor, M.R., et al.: Amplitude and phase of cerebrospinal fluid pulsations: experimental studies and review of the literature. *J. Neurosurg.* **104**(5), 810–819 (2006)
57. Feinberg, D.A., Crooks, L.E., Sheldon, P., et al.: Magnetic resonance imaging the velocity vector components of fluid flow. *Magn. Reson. Med.* **2**(6), 555–566 (1985)
58. Henry-Feugeas, M.C., Idy-Peretti, I., Blanchet, B., et al.: Temporal and spatial assessment of normal cerebrospinal fluid dynamics with MR imaging. *Magn. Reson. Imaging* **11**(8), 1107–1118 (1993)
59. Nayler, G.L., Firmin, D.N., Longmore, D.B.: Blood flow imaging by cine magnetic resonance. *J. Comput. Assist. Tomogr.* **10**(5), 715–722 (1986)
60. Baledent, O., Gondry-Jouet, C., Meyer, M.E., et al.: Relationship between cerebrospinal fluid and blood dynamics in healthy volunteers and patients with communicating hydrocephalus. *Invest Radiol* **39**(1), 45–55 (2004)
61. Bateman, G.A.: Vascular compliance in normal pressure hydrocephalus. *AJNR Am. J. Neuroradiol.* **21**(9), 1574–1585 (2000)
62. Bradley, W., Scalzo, D., Queralt, J., et al.: Normal-pressure hydrocephalus: evaluation with cerebrospinal fluid flow measurements at MR imaging. *Radiology* **198**(2), 523–529 (1996)
63. Luetmer P.H., Huston, J., Friedman, J.A., et al.: Measurement of cerebrospinal fluid flow at the cerebral aqueduct by use of phase-contrast magnetic resonance imaging: technique validation and utility in diagnosing idiopathic normal pressure hydrocephalus. *Neurosurgery* **50**(3):534–543; discussion 543–534 (2002)

64. Mase, M., Yamada, K., Banno, T., et al.: Quantitative analysis of CSF flow dynamics using MRI in normal pressure hydrocephalus. *Acta Neurochir. Suppl.* **71**, 350–353 (1998)
65. Buonocore, M.H., Bogren, H.: Factors influencing the accuracy and precision of velocity-encoded phase imaging. *Magn. Reson. Med.* **26**(1), 141–154 (1992)
66. Baledent, O., Fin, L., Khuoy, L., et al.: Brain hydrodynamics study by phase-contrast magnetic resonance imaging and transcranial color doppler. *J. Magn. Reson. Imaging* **24**(5), 995–1004 (2006)
67. Enzmann, D.R., Ross, M.R., Marks, M.P., Pelc, N.J.: Blood flow in major cerebral arteries measured by phase-contrast cine MR. *AJNR Am. J. Neuroradiol.* **15**(1), 123–129 (1994)
68. Egnor, M., Rosiello, A., Zheng, L.: A model of intracranial pulsations. *Pediatr. Neurosurg.* **35**(6), 284–298 (2001)
69. Penn, R.D., Linninger, A.: The physics of hydrocephalus. *Pediatr. Neurosurg.* **45**(3), 161–174 (2009)
70. Aschoff, A., Kremer, P., Benesch, C., et al.: Overdrainage and shunt technology. *Childs Nerv. Syst.* **11**, 193–202 (1995)
71. Czosnyka, Z.H., Czosnyka, M., Pickard, J.D.: Shunt testing in-vivo: a method based on the data from the UK shunt evaluation laboratory. *Acta Neurochir. Suppl.* **81**, 27–30 (2002)
72. Taylor, R., Czosnyka, Z., Czosnyka, M., et al.: A laboratory model of testing shunt performance after implantation. *Br. J. Neurosurg.* **16**, 30–35 (2002)
73. Czosnyka, Z., Czosnyka, M., Richards, H.K., et al.: Posture-related overdrainage: comparison of the performance of 10 hydrocephalus shunts in vitro. *Neurosurgery* **42**(2), 327–333 (1998)
74. Scollato, A., Gallina, P., Gautam, B., et al.: Changes in aqueductal CSF stroke volume in shunted patients with idiopathic normal-pressure hydrocephalus. *AJNR Am. J. Neuroradiol.* **30**(8), 1580–1586 (2009)



# **Chapter 8**

## **Computational Fluid Dynamics for the Assessment of Cerebrospinal Fluid Flow and Its Coupling with Cerebral Blood Flow**

**Vartan Kurtcuoglu**

### **8.1 Introduction**

The dynamics of cerebrospinal fluid flow are directly linked to those of the cardiovascular system. The heart not only drives blood flow, but is also at the origin of CSF pulsation through the expansion and contraction of cerebral blood vessels. As was detailed in the preceding chapter, CSF dynamics can be altered by diseases and conditions such as hydrocephalus and, in turn, CSF dynamics can be analyzed to aid in the diagnosis of these. Bulk models describing intracranial fluid dynamics and punctual flow measurements using MRI have thus become important tools for this purpose.

The strength of bulk models is that they are computationally inexpensive. Simulations performed with such models and processing of the results generally do not require high-performance computing (HPC) resources and can be carried out very quickly on common personal computers. This is currently a prerequisite for application in clinical settings, where typically no access to HPC infrastructure is available. In terms of applicability, the hunger for computer power is the main differentiator between bulk models and computational fluid dynamics (CFD) models of intracranial dynamics. Unlike the bulk approach, however, CFD models can provide spatially resolved information on flow, pressure and mass transport, which opens the door to subject-specific calculations of intracranial dynamics based on medical imaging data. This chapter elucidates current approaches to CFD modeling of cerebrospinal fluid flow and its interaction with blood flow.

The development of CFD was driven by the lack of analytical solutions for the Navier–Stokes (NS) equations that describe momentum conservation in Newtonian

---

V. Kurtcuoglu (✉)

Laboratory of Thermodynamics in Emerging Technologies, Department of Mechanical and Process Engineering, ETH Zurich, Sonneggstrasse 3, ML J 27.2 8092 Zurich, Switzerland  
e-mail: vartan.kurtcuoglu@ethz.ch

fluids. Together with the continuity equation, i.e. the expression of mass conservation and energy conservation, the NS equations can be used to characterize continuum flows. For incompressible flows without external body forces, Equations (8.1) and (8.2) show the NS and continuity equations, respectively:

$$\rho \left( \frac{\partial u}{\partial t} + u \cdot \nabla u \right) = -\nabla p + \mu \nabla^2 u \quad (8.1)$$

$$\nabla \cdot u = 0. \quad (8.2)$$

Here,  $\rho$  is density,  $u$  is the velocity vector,  $t$  is time,  $p$  is pressure and  $\mu$  is dynamic viscosity.

CFD simulations in the CSF system started in 1996 with the work of Jacobsen et al. [1]. This is quite late compared to CFD work on blood flow that began in the early 1970s and can be attributed to both the fact that the cardiovascular system is better known to the non-medical public (which includes the engineers, mathematicians and physicists who develop CFD methods and search for applications of these) and to the anatomically more complex structure of the CSF space that cannot be easily reduced to 2D representations. The widespread availability of magnetic resonance imaging systems in medical research institutions at the turn of the century was a prerequisite for the transition from generic to subject-specific, anatomically accurate computational models, and thereby paved the way for CFD simulations of flow in the CSF space.

The procedural steps in the CFD modeling of cerebrospinal fluid flow are similar to those encountered in more generic problems of incompressible, isothermal internal flows: In a first step, the simulation domain has to be defined, which consists of at least one fluid domain and, if the deformation of surrounding tissue is to be modeled, one or more solid domains. In the second step, these domains have to be discretized, i.e. a spatial discretization scheme needs to be chosen and a computational grid has to be generated. Next, the behavior of the fluids and solids at their respective domain boundaries needs to be prescribed, i.e. corresponding pressures, velocities or their derivatives in those areas must be determined a priori and set accordingly. In the fourth step, the physical properties of the fluids and solids (rheology, material properties) have to be set. Finally, the NS and continuity equations have to be solved based on appropriate initial conditions. If the problem is transient, a suitable temporal discretization scheme is required for this. The following section discusses these steps for the case of subject-specific CSF flow simulations based on MRI data.

## 8.2 Procedural Steps in CFD Modeling of CSF Dynamics

### 8.2.1 Obtaining the Model Domain

Magnetic resonance imaging is the most widely used method for obtaining representations of the CSF spaces as well as of arterial blood vessels in the head. However, the effective obtainable resolution is limited by comparably slow acquisition times

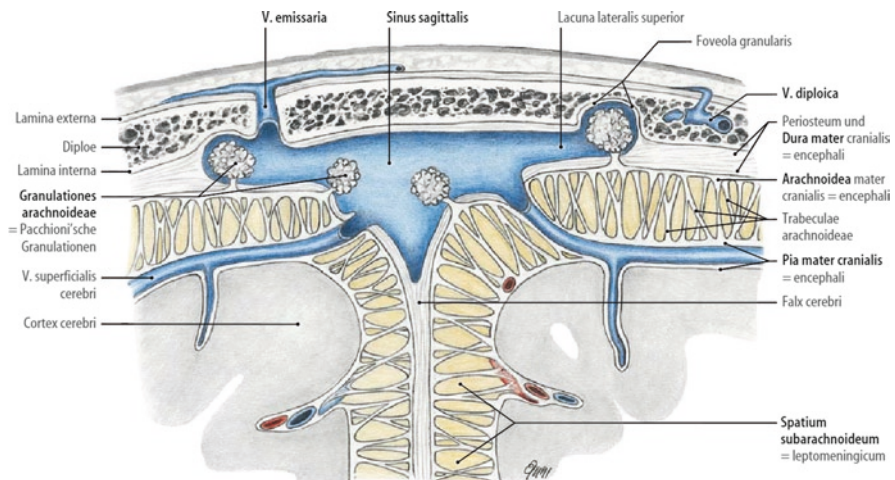


**Fig. 8.1** Schematic of the subarachnoid space (spatium subarachnoideum) in the vicinity of the superior sagittal sinus. Trabeculae connect the arachoid and pia membranes (arachnoidea mater cranialis, pia mater cranialis). From Tillmann [57]

combined with the fact that the brain moves inadvertently due to cardiac pulsation and breathing. Consequently, the largest part of the cerebral vasculature cannot be acquired in sufficient detail for modeling with CFD. If the coupling between blood and cerebrospinal fluid flow is to be taken into account explicitly by calculating the transient displacements of the arterial walls and their transmission to the CSF space, then smaller vessels have to be simulated via lower order models. The representation of the smaller vessels can then be coupled to full 3D CFD models of larger vessels, such as the internal carotid arteries, vertebral arteries, basilar artery and the circle of Willis (see Figs. 2.17 and 2.21 in Chap. 2). Similar limitations with respect to the effective resolution of MRI also affect the CSF space directly: Structures such as small diameter sections of the foramina of Monroe, Luschka and Magendie, the posterior horns of the lateral ventricles, the aqueduct of Sylvius and the recesses of the third and fourth ventricle (see Fig. 2.7, Chap. 2) will be substantially affected by partial volume effects [2]. Nevertheless, the overall feature size of these structures is large enough that lower order modeling is not required. In contrast, the subarachnoid space (SAS) features a micro-scale substructure that is well below the resolution limit of clinical MRI systems even in the absence of brain motion: Fine filaments (trabeculae) with diameters in the double digit micron range bridge the SAS between the pia and arachnoid membranes (Fig. 8.1). Despite their small size, the trabeculae may increase the pressure drop along the SAS significantly [3, 4]. Consequently, their effect on CSF flow and associated mass transport should be taken into account, e.g. by approximating the trabecular network as a porous medium with specified permeability [3]. Unfortunately, there is no experimental data on the permeability of the SAS. Thus, SAS porosity has to be obtained first, wherefrom permeability values can be derived. The best description of the trabecular structure for the purpose of deriving porosity

can be found in analyses of electron microscopy acquisitions [5–7]. Once porosity is determined, permeability can be estimated through CFD or analytical exploration in an idealized SAS representation, most likely the simplest of which is an array of straight circular cylinders connecting two parallel plates that represent the pia and arachnoid layer [8]. For this case, the relationship between porosity and permeability is given by

$$\frac{k_l}{r^2} = \frac{\varepsilon^2(\pi + 2.157(1-\varepsilon))}{48(1-\varepsilon)^2} \quad \text{and} \quad \frac{k_t}{r^2} = \frac{\pi\varepsilon(1-\sqrt{1-\varepsilon})^2}{24(1-\varepsilon)^{3/2}}, \quad (8.3)$$

where  $k_l$  is longitudinal permeability (i.e. permeability in direction parallel to the cylinders representing the trabeculae),  $k_t$  is transverse permeability,  $r$  is the radius of the cylinders and  $\varepsilon$  is the porosity of the SAS. The flow resistance caused by the porous micro-structure of the SAS can then be accounted for by the addition of a pressure gradient to the right hand side of the NS equations, e.g. for a coordinate system aligned with the direction of the trabeculae:

$$\rho \left( \frac{\partial u}{\partial t} + u \cdot \nabla u \right) = -\nabla p + \mu \nabla^2 u - \mu \begin{pmatrix} u_1 / k_l \\ u_2 / k_t \\ u_3 / k_t \end{pmatrix}. \quad (8.4)$$

Equation (8.4) is valid if inertial losses due to the porous micro-structure are small compared to its viscous drag, i.e. if the Reynolds number with trabecular diameter as characteristic length is smaller than 0.5 [9]. This is presumably the case in the SAS [3], but more accurate information on trabecular geometry and configuration is needed to validate this finding. When blood vessels in the SAS are considered as well, inertial losses will become important. However, these vessels cannot be treated as part of the homogeneous trabecular micro-structure, but could be introduced within the framework of a multi-scale porous model. While this has not been attempted in the CSF space, there are examples of comparable models in other application areas [10].

After MR images of the central nervous system are acquired, the anatomical structures that are to be included in the CFD model need to be extracted, i.e. image segmentation has to be performed. Various algorithms exist for the automatic segmentation of larger vessels [11]. Some manual post-processing for the removal of artefacts is often required before the next steps in the CFD analysis chain can be performed. For the CSF space, much lower quality results can be expected from automatic segmentation. While some algorithms exist that deliver automatic results for visualization and crude calculation purposes, these do not reach the quality required for accurate CFD simulations even after manual clean-up. Consequently, semi-automatic segmentation of the CSF domain is necessary. This is arduous, time consuming and poses severe limitations on the applicability of CFD for clinical CSF flow simulations.

The output of the segmentation step is a volumetric representation of the anatomical structures of interest. For CFD modeling, a distinction needs to be made between the internal fluid region and its boundaries. This is generally achieved by

surface triangulation [12]. The triangulation step is straightforward and can be carried out by various open source and commercial programs. As an alternative to segmentation and triangulation, splines [13] can be used to delineate the contour of the structure of interest in each MRI slide, followed by a surface reconstruction step that smoothly joins the splines to an approximation of the respective boundary. Surface reconstruction can also be performed after triangulation, which combines the benefits of voxel-based segmentation (preservation of original shape details) with those of spline description (scalability, small file size, best template for computational grid generation). The disadvantage is that surface reconstruction of complex triangulated surfaces requires substantial manual work.

It is common in classical CFD applications to reduce the size of the fluid domain by making use of symmetries, or by reducing a 3D structure to a 2D representation. The latter can be used, for example, to investigate the performance of airplane wings, where instead of calculating the flow around the entire 3D profile, only the flow around an axial cross-section (airfoil) would be considered. While tip effects and interactions with the airplane fuselage cannot be studied in this way, the approach is nonetheless permissible, since there is only limited flow perpendicular to the axial section. It is more difficult to find viable reductions of dimension for use within the CSF space. One might consider conducting a 2D CFD study on the third ventricle limited to its mid-sagittal plane. However, the inlets to this ventricle, the foramina of Monro, are located outside the mid-sagittal plane and their center lines are angled towards it, causing considerable CSF flow through this plane. Similarly, representing the cranial SAS by a 2D projection to its mid-sagittal plane is not permissible: The foramina of Luschka – two of the pathways connecting the ventricular space with the SAS – are not located in the mid-sagittal plane. The situation is better in the spinal SAS, where subsections with limited curvature and thus little flow perpendicular to the longitudinal axis exist (discounting substructures such as nerves and trabeculae). Flow in the perivascular space (extension of the SAS along blood vessels [14]) can most likely be simplified to 2D as well, although very little is known about fluid flow therein.

### 8.2.2 *Spatial Discretization*

CFD requires the discretization of the governing equations in space and, if transient flows are to be studied, also in time. For spatial discretization, the domain under investigation has to be divided into small sub-volumes, i.e. a computational grid has to be generated. The structure of this grid will depend on the expected characteristics of the flow and on the discretization methods to be applied. For the study of CSF dynamics, the finite-volume discretization scheme is used most often, followed by the finite-element method, although other approaches are principally just as suitable. When anatomically accurate modeling of the CSF flow is carried out, either unstructured grids or an immersed boundary method [15] need to be used, as structured grids that follow the domain contours are very difficult to generate due to the geometric complexity of the CSF spaces. State-of-the-art grid generation software

allows for mostly automatic unstructured meshing, usually with tetrahedral elements. Hexahedral elements that are commonly used in structured grids offer higher solution accuracy at the same overall number of elements, but they often necessitate buffer elements (pyramids, prisms and tetrahedra) in areas of high grid density gradients, increasing the complexity of grid generation. Prismatic buffer elements are also used in conjunction with otherwise tetrahedral grids in boundary layer areas, where high velocity gradients need to be resolved. Less common but emerging are polyhedral grids that can be generated with the same level of automation as tetrahedral grids, while offering more accurate solutions [16].

It is evident that by solving the discretized versions of the NS and continuity equations, only an approximate solution of the original set of governing equations is obtained. The quality of the approximation is, among other factors, dependent on the quality of the computational grid. Since the original solution is not known and, thus, the relative error of the discretized solution cannot be specified, solutions obtained with different grids have to be compared. Such grid independence studies will give an estimate of the relative error introduced by the spatial discretization. Ultimately, a balance between the accuracy of the results and cost in terms of grid generation and computational time has to be found.

### **8.2.3 Obtaining Boundary Conditions**

Boundary conditions (BC) need to be specified at the domain margins for closure of the governing equations. CFD models of CSF flow are generally set up with BC based on MRI data. Unfortunately, it is not possible to obtain absolute pressures via MRI. This leads to the unsatisfactory situation that only velocity, flow rate or similar BC can be prescribed in a subject-specific manner, while pressure or impedance BC that are required to ensure mass conservation in non-compliant domains are generic or based on generalized lower order models.

The ideal locations for acquisition of flow BC in the CSF space are the aqueduct of Sylvius and the cervical spinal canal. The geometry of these areas is well defined and velocities therein are mostly limited to the axial direction, allowing for the placement of a single perpendicular measurement plane. Furthermore, there are closed-form solutions of flow in idealized representations of the aqueduct (e.g. straight elliptic pipe [17]) and the spinal canal (straight elliptic annulus [18]), allowing for the filtering of higher frequency noise components in the acquired flow data. This can be done by first integrating the flow profile in space for each measured point in time which yields a volumetric or mass flow curve that contains less random noise. In order to recuperate the spatial distribution of the flow, this flow rate is applied to the respective idealized geometry with available closed-form solution of the governing equations [19]. Finally, conformal mapping is performed to map the solution back to the actual domain [20].

Pulsatile CSF flow is driven by the expansion and contraction of blood vessels in and around the central nervous system, as well as by diaphragm motion in the

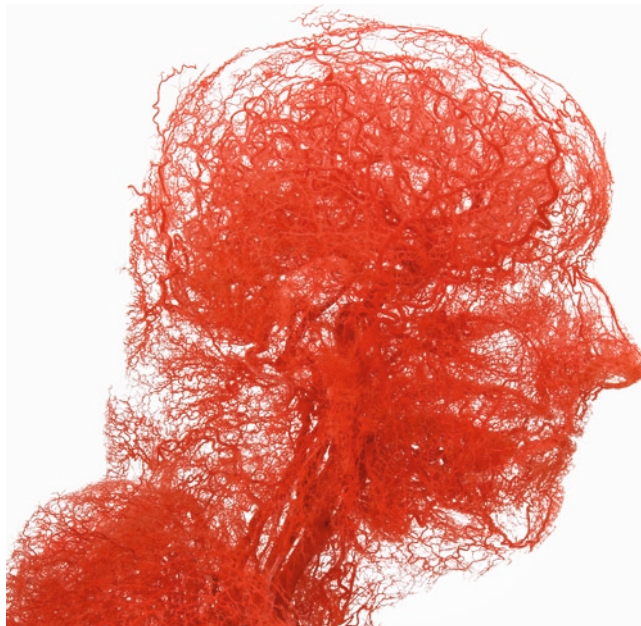


**Fig. 8.2** Corrosion cast of the head and neck vasculature of a human cadaver. Image courtesy of Axel Lang (corrosion casting) and Heinz Sonderegger (photography). Copyright Institute of Anatomy, University of Zurich, Switzerland

abdominal space due to breathing. This means that the boundaries of the CSF compartments have to be flexible entities that can transfer momentum by deformation. Most existing CFD models assume nevertheless rigid CSF domain boundaries, as this simplifies model setup and calculations tremendously. There are two general approaches by which the motion of the CSF boundaries can be taken into account: Either the entire chain of displacements from blood vessels or the diaphragm to tissue and CSF domain boundaries is modeled, or the displacement of the boundaries is measured directly. The former approach poses great challenges, the most serious of which is the lack of material data to realistically model the interaction between blood vessels or the diaphragm and the surrounding tissue. In addition, the complexity of the vascular network in the brain (see Fig. 8.2) as well as limits in the effective resolution of MRI require simplifications of the vascular model (see Sect. 8.2.1), introducing errors that are difficult to quantify.

Measuring the motion of the CSF space boundaries directly is not straightforward, but it is feasible: Displacement-encoded MR imaging can detect brain displacements down to 0.01 mm [21] (Fig. 8.3), which is sufficient to derive ventricle wall motion, but not necessarily the motion of the pia mater. The MRI acquisitions result in a discrete displacement map within which the CSF boundaries do not necessarily coincide with the measured locations. Hence, a spatial interpolation has to be performed first to cover the boundaries. Since the temporal frequency spectrum

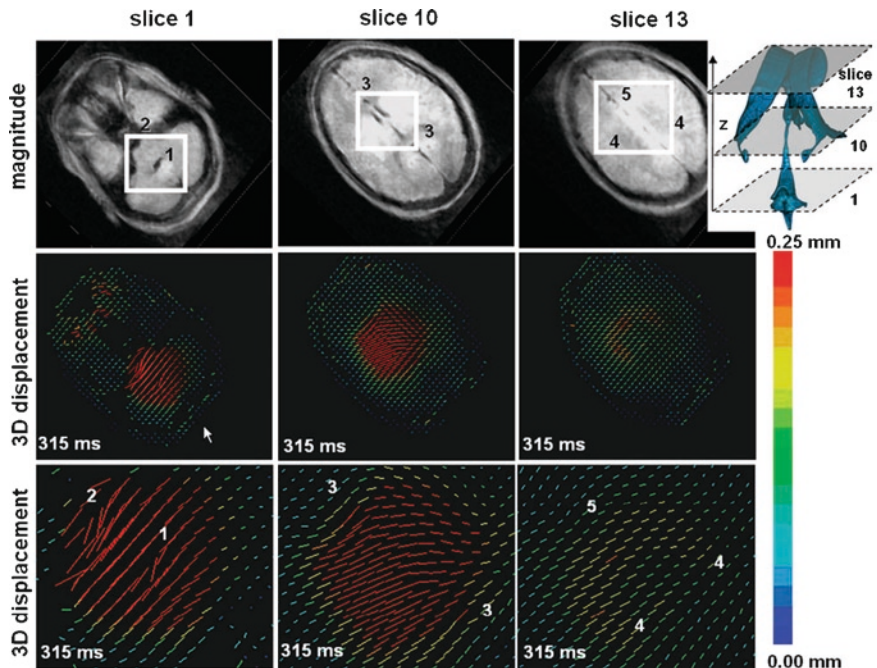


**Fig. 8.3** Selected slices of a 3D brain motion data set covering the volume of the ventricular system [21]. The locations of the slices are indicated in the *upper right corner* with respect to the ventricular system of the brain. The *colors* and the *length* (scaled by a factor of 100) of the bars represent the motion amplitude of the brain, and the *bar orientation* indicates the displacement direction

of blood flow into the brain through the carotid and vertebral arteries does not extend beyond 10 Hz under normal resting conditions (Fig. 8.4), a brain motion acquisition interval of 0.05 s within a cardiac cycle is sufficient to meet the Nyquist–Shannon sampling criterion [22, 23]. However, the temporal discretization of the governing equations requires much smaller time steps, which necessitates a temporal interpolation of the acquired brain motion data. This can be done, for example, by Fourier decomposition of the acquired discrete signal and re-sampling of the reconstructed continuous signal [19].

Both ventricle wall motion and transient displacement of the pia mater transfer momentum to the CSF and thus contribute to its pulsation. Even a small displacement of the pia mater will result in substantial volume flow due to its large surface area. Thus, pia motion cannot be neglected. Since, as mentioned, MR imaging cannot capture the displacement of the pia mater, a simplified BC has to be introduced. One option is to prescribe uniform perpendicular flow across the pia, such that the corresponding flow rate is equal to the difference between in- and outflow at the aqueduct of Sylvius and the spinal canal [4]. This simplified BC is relatively easy to implement, but will lead to errors in the reported flow velocities close to the pia surface.

The pulsatile motion of CSF is superimposed onto its steady flow caused by production in the choroid plexus and absorption in the arachnoid granulations,

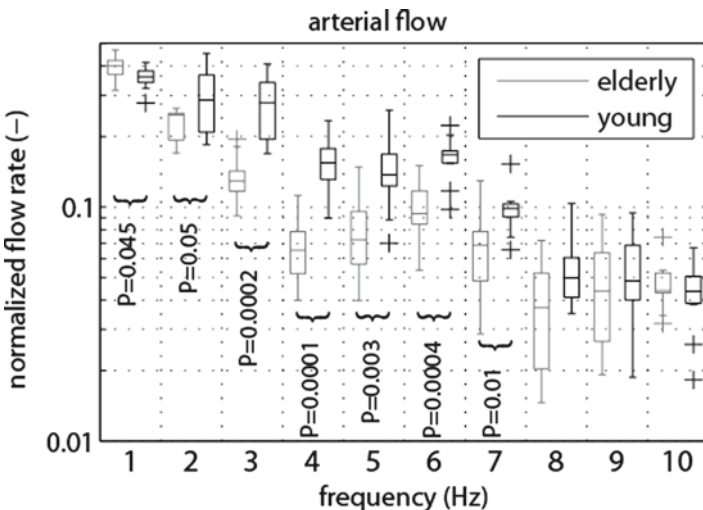


**Fig. 8.4** Frequency spectrum of combined carotid and vertebral arterial blood flow in 11 elderly (gray, left, mean age  $70 \pm 5$  years) and 11 young (black, right, mean age  $24 \pm 3$  years) healthy subjects illustrated using boxplots [58]. The upper and lower edges of each box represent the 25th and 75th percentiles, respectively. The center line represents the median and the whiskers extend to the most extreme data points not considered outliers, which are plotted individually (+). Curly brackets indicate significant differences (non-parametric Mann–Whitney test). Distinction between signal and noise is not possible at frequencies beyond 7 Hz

extra-cranial lymphatic pathways and possibly through cerebral capillaries [24]. The choroid plexus has a filamentous structure that cannot be acquired by MRI in its full detail. For CFD modeling, its simplified macroscopic shape can be segmented from MR images and CSF flow rates corresponding to the production value can be imposed on the idealized boundaries. Alternatively, the choroid plexus geometry can be neglected altogether and inflow imposed at a part of the respective ventricle wall. Combined CSF production rates in the choroid plexus of the third and lateral ventricles can, principally, be obtained by integrating the MRI-acquired CSF flow profile in the aqueduct of Sylvius over a cardiac cycle. While this method is used throughout the literature, there is not conclusive data on the accuracy of this approach. Obtaining CSF production rates in the fourth ventricle via MRI is more difficult and would require measurement of flow through the small foramina of Luschka and Magendie. This is not possible with a sufficient level of accuracy on current clinical MRI scanners. In order to still take CSF production in the fourth ventricle into account, a ratio between the production rates in this and the remaining cerebral ventricles can be assumed.

Under physiological conditions, the average CSF absorption rate is equal to the respective production rate. CSF absorption locations are distributed throughout the cranial and spinal cavity, and there is no consensus on the relative importance of the various pathways, let alone on the actual drainage rates through each [25]. The classically accepted locations of CSF re-absorption are the arachnoid granulations (AG) that drain into the superior sagittal, transverse and sigmoid sinuses. It is possible

to locate large AG through MRI, but most of the smaller granulations cannot be detected. Cadaver data on their distribution are available [26], and areas of the arachnoid mater boundary can be assigned AG functionality in CFD simulations. Concretely, the AG can be assumed to act as one-way differential pressure valves with associated hydraulic conductivity of approximately  $92.5 \text{ } \mu\text{L min}^{-1} \text{ mmHg}^{-1} \text{ cm}^{-2}$  [27].

Other drainage routes, namely drainage through lymphatic pathways, are clearly more difficult to model because there is no data available on local outflow rates and because, unlike the AG, no straightforward boundary condition can be implemented. This is not to say that those drainage pathways are unimportant: All drainage routes link the intracranial space and its dynamics with either the cardiovascular system or the lymphatic pathways. Increased pressure in either of these may reduce the re-absorption rate of CSF, thereby contributing to elevated intracranial pressure or hydrocephalus [28].

#### 8.2.4 Calculating the Flow

Once the computational grid and the boundary conditions are in place, initial values of flow velocity and pressure have to be defined throughout the computational domain. Unless results of similar previous calculations exist from which initial conditions can be extra- or interpolated, zero pressure and velocity are usually assumed. Since the corresponding fluid dynamic state does not match to the actual flow field, transient calculations will have to be performed over a few cardiac (and, if considered, respiratory) cycles until no significant difference in the state between two subsequent cycles can be observed. Depending on the CFD solver used, a zero initial condition may render the calculations unstable. In that case, the magnitudes or amplitudes of the applied boundary conditions can be scaled down initially and increased to their actual values over several cycles.

Steady-state calculations of arterial blood flow are quite common. While they do not capture all the details of the flow, their use can be justified if estimates of average wall shear stress distribution or other similar parameters linked to long-term processes such as atherosclerosis are to be studied [29]. In contrast to arterial blood flow, CSF flow has a much stronger pulsatile component compared to its net flow, which makes it more difficult to advocate steady-state simulations of cerebrospinal fluid dynamics. For transient CFD simulations, the proper temporal discretization step size has to be chosen, which will depend on the expected flow frequencies (see Sect. 8.2.3), the discretization scheme, the spatial resolution of the computational grid and the CFD solver. Commonly used time step sizes in the CSF space are on the order of 1 ms. As with the grid independence study (Sect. 8.2.2), time step independence of the acquired solution has to be ensured.

CSF is a Newtonian fluid with a viscosity of approximately  $0.8 \text{ mPa s}$  at  $37^\circ\text{C}$  that is fairly stable with respect to protein content, blood cell count and glucose concentration [30, 31]. In its entire domain, CSF flow is laminar and does not require any turbulence modeling. There are various CFD software frameworks and stand-alone solvers suitable for CSF flow calculations, and the decision in favor of the one or the

other will depend, to a large extent, on the background and preferences of the user. Despite the incompressibility of the cerebrospinal fluid, transient flow calculations in anatomically accurate, deforming representations of the CSF space demand substantial computer power. Consequently, CFD codes that support parallel processing on deforming grids with high scaling efficiency and without the need for manual partitioning should be preferred. Scaling efficiency generally decreases with increasing number of parallel processors used. The current trend in the development of computer hardware towards larger numbers of cores per CPU, but only slowly increasing clock speeds, is contributing to the rise of lattice Boltzmann (LB) CFD methods, where the discrete Boltzmann equation is solved instead of the Navier–Stokes equations [32]. LB codes scale better with increasing number of processors than classical NS solvers, and they are easier to implement on GPUs, which promise to deliver significant speed-ups compared to calculations on CPUs alone. High-end workstations running lattice Boltzmann codes on GPUs may be the most promising route for bringing CFD simulations of cerebrospinal fluid flow into the clinical environment.

## 8.3 Existing CFD Models

There are currently no CFD models that capture the CSF space in its entirety. Instead, the existing models focus on individual compartments or small groups of these. This section gives an overview of CFD models of the ventricular, subarachnoid and perivascular spaces.

### 8.3.1 *Ventricular Space*

The first CFD work on flow in the CSF space was the investigation of Jacobson and co-workers in 1996, where they investigated steady and oscillatory fluid dynamics through a representation of the aqueduct of Sylvius with stiff walls and reported (singularly considering net flow) that the aqueduct provides less than 5% of the total resistance to CSF flow within the CSF pathways [1]. The same authors followed up with an investigation of aqueduct stenosis in 1999. They approximated the geometry of the aqueduct of Sylvius based on published anatomic data and reported that a stenosis may increase the pressure drop across the aqueduct by two orders of magnitude compared to the physiological case [33]. Again, the aqueduct wall was considered to be stiff. Several years later, Fin and Grebe modeled the aqueduct wall as a deformable membrane and compared therewith obtained results to data attained with rigid walls [34]. The domain geometry was obtained via MRI and the CSF flow was solved using finite element and immersed boundaries methods. Under steady flow conditions, they obtained a 37% lower pressure drop in the case with deformable walls compared to rigid walls. This remarkable difference raises the question whether such a large influence of boundary conditions on the results does not diminish the value of CFD, as the actual aqueduct wall stiffness is not known. One may ask why the time and effort needed for CFD modeling should be invested

as opposed to the use of simple bulk models: Bulk models will be sufficient if bulk values such as the pressure drop across a simple structure are sought. If, however, one is interested in the effect of local geometric features on flow, CFD models will provide added value. To be clear, this still requires that the boundary conditions, which to a large extent determine the accuracy of the model, are as close as possible to the actual values that they represent.

After the CFD studies of the aqueduct of Sylvius, other researchers directed their efforts at the remainder of the ventricular space, using varying levels of detail in both the representation of the anatomy as well as in the acquisition of the boundary conditions. In 2005, my co-workers and I published results of simulations on a simplified representation of the entire ventricular space, within which CSF flow was driven by the expansion and contraction of the third ventricle walls [35]. While it is not known how exactly vascular deformation is translated to CSF motion, it is clear that this does not occur exclusively through the third ventricle as formerly suggested by Du Boulay [36]. The amplitude of the wall expansion was chosen such that a Reynolds number of ten was obtained in the aqueduct, as this corresponded to flow velocities reported in the literature. However, current MRI studies indicate that velocities should be up to a factor of five higher, which we also showed in a later study on CSF flow in an anatomically accurate representation of the third ventricle and the aqueduct of Sylvius [19]. In that study, the domain geometry was reconstructed based on MRI data. The ventricle wall motion in feet-head direction as well as the flow profile in the aqueduct of Sylvius was obtained as boundary conditions again via magnetic resonance imaging. The main finding was that the third ventricle displayed comparably complex flow with two mobile recirculation zones of different sizes generated by a jet emanating from the aqueduct of Sylvius. While a relatively high maximum Reynolds number of 340 was observed in the aqueduct, there were no indications of transitional or turbulent flow. In a follow-up paper, we investigated mass transport in the same domain [37]. We found that while in the center of the third ventricle transport is entirely convection-driven, the regions of the anterior and posterior recess show markedly lower Péclet numbers, indicating that mass transport through diffusion cannot be neglected there a priori. We further hypothesized that the characteristic shape of the third ventricle may facilitate endocrine communication between hypothalamus and pituitary gland through the CSF, which had been shown to occur in sheep [38]. In 2010, Cheng et al. investigated, also with an MRI-derived CFD model of the third ventricle and aqueduct of Sylvius, how the position of the interthalamic adhesion affects CSF flow [39]. They imposed flow at the foramina of Monro based on published values, set constant pressure at the distal end of the aqueduct and assumed rigid ventricle walls. The authors investigated four different positions of the interthalamic adhesion and found that the pressure in the third ventricle is higher when the adhesion is located close to the aqueduct. They went on to hypothesize that such morphologies with the adhesion in proximity of the aqueduct may have increased susceptibility to hydrocephalus if obstructions occur along the CSF flow pathway. As we did in our 2005 study [35], Cheng and co-workers relied on MRI flow data that underestimated velocities. It is likely that the stated main findings of their work would not change if higher velocities were considered. However, the detailed flow

fields and locations of recirculation zones would be different. In 2008, Howden and co-workers presented the first anatomically accurate 3D CFD model of the entire ventricular space [40]. Instead of using constant pressure boundary conditions at the domain outlets (the foramina of Luschka and Magendie), the authors applied transient pressure. This pressure curve was estimated using a geometrically simplified 3D model of the combined cranial and spinal CSF spaces that featured a pulsatile velocity inlet at the choroid plexus and constant pressure at the AG. While such a staggered approach is, in principle, preferable to using constant pressure, it is difficult to carry out in practice: The pulsation of the choroid plexus is not the sole origin of CSF oscillation, and the relative importance of the choroid plexus, ventricles and SAS as potential contributors to pulsatile flow is not known. The flow velocities at the boundaries reported by the simplified model were too low by a factor of two at minimum, and consequently, the validity of the entire flow and pressure field of the accurate model that depended on these boundary conditions was jeopardized. In 2011, Sweetman et al. proposed a model of the entire CSF space as an expansion of their previous 2D and 3D work on the cranial compartments [41–43]. The authors took a distinctly different approach than Howden et al., in that they prioritized the scope of the model over detail of the individual modules. While they included the SAS, they neglected its porous structure, which we had shown earlier to provide significant resistance to CSF flow [4]. To induce CSF pulsation, Sweetman et al. imposed a volume change in brain tissue that is transmitted to the fluid domain through deformable superior wall sections of the lateral ventricles. The temporal profile of the tissue volume change corresponded to measured basilar artery volumetric blood flow rate. The model displayed good agreement with spatially integrated MRI flow measurements at several locations. Given the wide range of possible tissue parameters, and in the absence of sensitivity tests with respect to these, the particular choice of values may be seen as a scaling factor to ensure global agreement between the computational model and the experimental results. This demonstrates a weakness of CFD models of CSF flow: MRI is used to acquire boundary conditions in areas where the corresponding measurements are possible, but MRI does not provide high enough effective resolution to validate the calculated flow field in detail. Hence, if CFD calculations are not carried out entirely wrong, there will be necessarily a global agreement of flows between the CFD and MRI data, but no statement can be made regarding the accuracy of the local flows. It is the ability to provide information on local flows that distinguishes CFD models from bulk models.

### 8.3.2 Subarachnoid Space

#### 8.3.2.1 Spinal Subarachnoid Space

CFD models that focus on the SAS started in 2001 with the work of Loth et al. on CSF flow in the spinal canal [44]: the authors obtained a series of cross-sections of the spinal CSF space from imaging data of the Visual Human Project's Visible Man

[45] and set up a 2D model to assess the effects of spinal cord eccentricity and cross-sectional geometry on CSF flow. A 1D circular annulus model was further used to investigate the effects of flow area and cord motion. The substructure of the spinal canal including nerves and ligaments was not considered. Inertial effects were found to dominate the flow field under normal physiologic flow rates. A peak Reynolds number of 450 and Womersley number of up to 17 was observed. The authors suggested that a 3D model should be used to investigate secondary flows that are likely to occur in the cervical area, since lower dimensional models cannot capture these. In 2006, Stockman presented a 3D lattice Boltzmann model of a subsection of the spinal canal [46]. He was not concerned with obtaining the flow field (including secondary flows) along the entire spine, but rather with the effect of SAS substructure on CSF flow, which he investigated using a simplified geometry of the length of one vertebra. Stockman concluded that while the substructure has a limited effect on averaged CSF flow, it does influence the local flow field markedly. The limited effect on averaged flow is a somewhat surprising finding, as localized flow patterns such as re-circulations will dissipate energy, necessitating a larger axial pressure gradient to drive the flow. The same year, Bilston et al. presented a cylindrical 2D axisymmetric model of the spinal canal and cord to investigate whether a substantial CSF pressure increase could be induced by arachnoiditis in the SAS, which would support the hypothesis that syrinx formation in the spinal cord may be driven by CSF influx from the spinal canal [47]. The authors modeled arachnoiditis by defining a segment of the spinal canal as a porous medium region and performed finite-volume CFD calculations with prescribed temporal inflow profile based on MRI flow measurements at the superior end of the domain and a constant pressure boundary condition at the inferior end. They used the maximum calculated pressure as an input to a structural finite-element model of the spinal cord, obtained its deformations, updated the CFD model accordingly, and recalculated the pressure in the fluid domain. Depending on permeability and porosity of the porous region, CSF pressure was calculated to be 1–20 times higher than in the model without arachnoiditis, leading the authors to conclude that this elevated pressure may be involved in syrinx formation or enlargement. The authors cited the simplification of the domain geometry, the unknown structural characteristics of the arachnoiditis, as well as the linear elastic material properties used for the spinal cord as limitations of the study. In 2010, three CFD studies on CSF flow in the spinal SAS were published [48–50]. Among these, the work of Kuttler et al. on the analysis of drug distribution after intrathecal drug administration (i.e. drug delivery into the spinal SAS) was notable [50]. The authors generated a simplified 3D spinal domain based on data from the Visible Human Project [45] and imposed temporal flow profiles obtained via velocimetric MRI at the superior end of the domain. Lower-frequency CSF pulsation due to breathing was superimposed onto this flow by compression and decompression of the computational grid. The velocity field was calculated for one cardiac cycle and a steady streaming velocity field was derived therefrom (see [51] for a review on steady streaming). In order to obtain an initial drug distribution, a finer meshed domain of the lumbar and lower thoracic regions was generated, and drug administration as slow infusion or fast bolus injection was simulated using a turbulence model. The resulting drug concentration field was fed back into the larger scale model, where drug transport

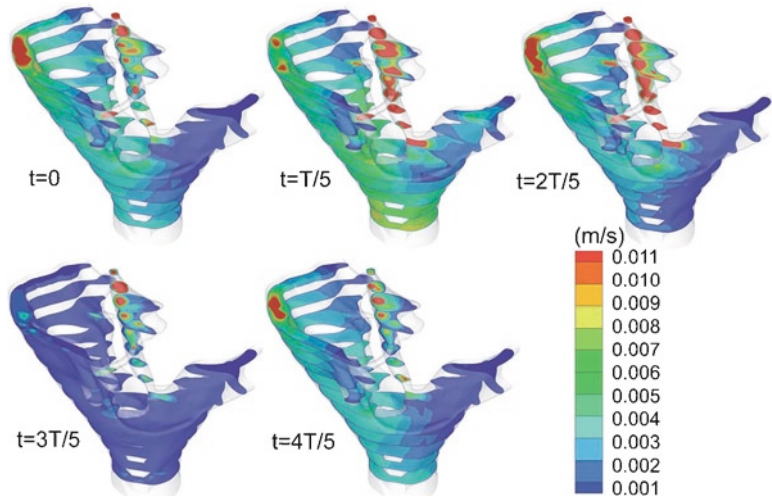


**Fig. 8.5** Velocity magnitude contours during one complete cardiac cycle in the inferior cranial subarachnoid space according to our 2009 model [3]

was studied via the steady streaming field and diffusion modeling. The authors observed that there was no clear difference in the distribution range between bolus injection and slow infusion. More important than this result is the creative approach that Kuttler and co-workers showed in this study: By using different models for phenomena occurring at different time scales, they were able to progress towards a clinically relevant CFD application in the CSF space.

### 8.3.2.2 Cranial Subarachnoid Space

Some CFD models that include the cranial SAS were mentioned in Sect. 8.3.1 [41–43]. In a pair of papers published in 2009 and 2010, my group investigated flow in an anatomically accurate representation of a healthy cranial SAS and fourth ventricle [3, 4]. We imposed CSF flow velocities obtained through MRI at the pontine and cerebellomedullary cisterns and at the foramen magnum in the spinal canal. A constant pressure boundary condition was applied at the superior end of the fourth ventricle, and a mass source with zero initial momentum was introduced in the fourth ventricle to account for the production of CSF therein, whereas other production sources were included implicitly in the measured flow profiles. The SAS was modeled as an anisotropic homogeneous porous medium. CSF outflow was assumed to take place exclusively through AG, which were taken into account through a constant pressure boundary condition in the area of the superior sagittal sinus that did not allow for CSF reflux into the SAS. The domain boundaries were considered rigid. To ensure mass conservation, virtual CSF flux across the representation of the pia mater was allowed. We saw large variations in the spatial distribution of flow velocities (Figs. 8.5 and 8.6). Our main finding,

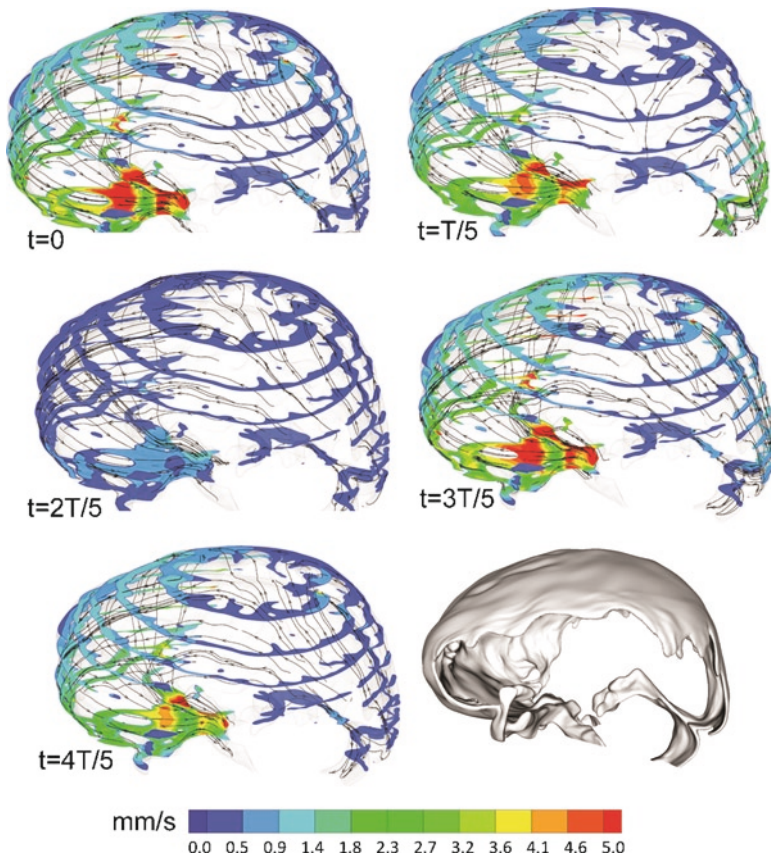


**Fig. 8.6** Velocity magnitude contours at cross-sections in the superior cranial SAS at selected points in time within one cardiac cycle according to our 2010 model originally published in Gupta et al. [4]. Also shown are the stream traces of virtual massless particles injected arbitrarily within the domain at different points in time

however, was that the substructure of the SAS clearly contributes to the pressure drop across the domain, and that the characteristics of this structure need to be better quantified to allow for accurate flow computations.

### 8.3.3 Perivascular Space

Little work has been done thus far on modeling of perivascular flows. The first CFD study on this topic was published in 2003 by Bilston and co-workers [52]. They considered a 2D rectangular domain with no slip boundary conditions at the walls and prescribed pressures at inlet and outlet. Transient deformation was prescribed on the wall representing the boundary closer to the artery lumen. The outer wall was

considered rigid. The authors reported that fluid transport occurs in the direction of arterial wave propagation up to a specific pressure gradient determined by pulse wave velocity and amplitude. For the same conditions, Wang and Olbricht reported a lower maximal adverse pressure gradient based on a theoretical analysis against which fluid could be transported [53]. Using a different theoretical approach [59], demonstrated that fluid transport in the opposite direction of wave propagation could be possible under certain conditions. This reverse transport cannot occur in the model of Wang and Olbricht. In 2010, Bilston and co-workers expanded their original CFD model to take into account a time-varying pressure gradient along the perivascular domain, reflecting the pulsation of CSF in the SAS and showing that the relative timing of the arterial pulse wave and subarachnoid pressure wave could influence perivascular fluid flow [54].

## 8.4 Conclusion

CFD as such is not a novel method, but its history with regard to application in the cerebrospinal fluid space is comparably short. Most of the early CFD models of CSF dynamics placed emphasis on the development of the respective method rather than on answering specific questions. Results in the form of velocity and pressure data were produced almost as a by-product. Now that the basic CFD methodology is well defined, more emphasis needs to be placed on hypotheses to be tested. One could argue that detailed velocity and pressure fields provided by CFD are valuable by themselves without answering specific questions, since there is no other way of obtaining such spatially resolved data in a non-invasive manner. However, these raw data usually stay within the respective research group, providing no benefit to the scientific community as a whole. This is not to say that the development of CFD methods is obsolete, as major efforts are still needed in the description of cerebrospinal fluid flow without discounting the respective substructures and transient tissue deformations. Most importantly, coupling of the ventricular, subarachnoid, interstitial, vascular and perivascular fluid spaces needs to be achieved, and steps in this direction are being taken [55].

Given the reliance of CFD models on MRI for boundary conditions, the lack of agreement on key parameters such as the physiological flow rate in the aqueduct of Sylvius is a reason for concern: It is imperative that reference standards be established for commonly used CFD boundary conditions. Attention should be paid to the accuracy of data derived from MRI modalities that are comparably new with respect to their use in CFD models, such as elastography and diffusion tensor imaging [56]. When accurate boundary conditions are used, CFD is a well-established and reliable method for the investigation of fluid dynamics in the cerebral and spinal fluid spaces.

**Acknowledgment** Swiss National Science Foundation through SmartShunt – The Hydrocephalus Project.

## References

- Jacobson, E.E., Fletcher, D.F., Morgan, M.K., et al.: Fluid dynamics of the cerebral aqueduct. *Pediatr. Neurosurg.* **24**(5), 229–236 (1996)
- Ballester, M.A.G., Zisserman, A., Brady, M.: Segmentation and measurement of brain structures in MRI including confidence bounds. *Med. Image Anal.* **4**(3), 189–200 (2000)
- Gupta, S., Soellinger, M., Boesiger, P., et al.: Three-dimensional computational modeling of subject-specific cerebrospinal fluid flow in the subarachnoid space. *J. Biomech. Eng.* **131**(2), 021010 (2009). doi:10.1115/1.3005171
- Gupta, S., Soellinger, M., Grzybowski, D.M., et al.: Cerebrospinal fluid dynamics in the human cranial subarachnoid space: an overlooked mediator of cerebral disease. I. Computational model. *J. R. Soc. Interface* **7**(49), 1195–1204 (2010). doi:rsif.2010.0033 [pii]10.1098/rsif.2010.0033
- Allen, D.J., Low, F.N.: Scanning electron microscopy of the subarachnoid space in the dog. III. Cranial levels. *J. Comp. Neurol.* **161**(4), 515–539 (1975). doi:10.1002/cne.901610404
- Cloyd, M.W., Low, F.N.: Scanning electron microscopy of the subarachnoid space in the dog. I. Spinal cord levels. *J. Comp. Neurol.* **153**(4), 325–368 (1974). doi:10.1002/cne.901530402
- Killer, H.E., Laeng, H.R., Flammer, J., et al.: Architecture of arachnoid trabeculae, pillars, and septa in the subarachnoid space of the human optic nerve: anatomy and clinical considerations. *Br. J. Ophthalmol.* **87**(6), 777–781 (2003)
- Vandenwesthuizen, J., Duplessis, J.P.: Quantification of unidirectional fiber bed permeability. *J. Compos. Mater.* **28**(7), 619–637 (1994)
- Chai, Z.H., Shi, B.C., Lu, J.H., et al.: Non-Darcy flow in disordered porous media: a lattice Boltzmann study. *Comput. Fluids* **39**(10), 2069–2077 (2010). doi:10.1016/j.compfluid.2010.07.012
- Kang, Q.J., Zhang, D.X., Chen, S.Y.: Unified lattice Boltzmann method for flow in multiscale porous media. *Phys Rev E* **66**(5), 056307 (2002). doi:10.1103/Physreve.66.056307
- Lesage, D., Angelini, E.D., Bloch, I., et al.: A review of 3D vessel lumen segmentation techniques: models, features and extraction schemes. *Med. Image Anal.* **13**(6), 819–845 (2009). doi:10.1016/j.media.2009.07.011
- Hjelle, Ø., Dæhlen, M.: Triangulations and Applications. Mathematics and Visualization. Springer, Berlin (2006)
- De Boor, C.: A Practical Guide to Splines. Applied Mathematical Sciences, vol 27, Rev. edn. Springer, New York (2001)
- Hadaczek, P., Yamashita, Y., Mirek, H., et al.: The “perivascular pump” driven by arterial pulsation is a powerful mechanism for the distribution of therapeutic molecules within the brain. *Mol. Ther.* **14**(1), 69–78 (2006). doi:S1525-0016(06)00113-4[pii]10.1016/j.mtthe.2006.02.018
- Mittal, R., Iaccarino, G.: Immersed boundary methods. *Annu. Rev. Fluid Mech.* **37**, 239–261 (2005). doi:10.1146/annurev.fluid.37.061903.175743
- Spiegel, M., Redel, T., Zhang, Y.J., et al.: Tetrahedral vs. polyhedral mesh size evaluation on flow velocity and wall shear stress for cerebral hemodynamic simulation. *Comput. Meth. Biomed. Eng.* **14**(1), 9–22 (2011). doi:10.1080/10255842.2010.518565
- Haslam, M., Zamir, M.: Pulsatile flow in tubes of elliptic gross sections. *Ann. Biomed. Eng.* **26**(5), 780–787 (1998)
- Gupta, S., Poulikakos, D., Kurtcuoglu, V.: Analytical solution for pulsatile viscous flow in a straight elliptic annulus and application to the motion of the cerebrospinal fluid. *Phys. Fluids* **20**(9), 093607 (2008). doi:10.1063/1.2988858
- Kurtcuoglu, V., Soellinger, M., Summers, P., et al.: Computational investigation of subject-specific cerebrospinal fluid flow in the third ventricle and aqueduct of Sylvius. *J. Biomech.* **40**(6), 1235–1245 (2007). doi:S0021-9290(06)00215-6[pii]10.1016/j.jbiomech.2006.05.031
- Boutsianis, E., Gupta, S., Boomsma, K., et al.: Boundary conditions by Schwarz-Christoffel mapping in anatomically accurate hemodynamics. *Ann. Biomed. Eng.* **36**(12), 2068–2084 (2008). doi:10.1007/s10439-008-9571-3

21. Soellinger, M., Rutz, A.K., Kozerke, S., et al.: 3D cine displacement-encoded MRI of pulsatile brain motion. *Magn. Reson. Med.* **61**(1), 153–162 (2009). doi:10.1002/mrm.21802
22. Shannon, C.E.: Communication in the presence of noise. *Proc. Inst. Radio Eng.* **37**(1), 10–21 (1949)
23. Luke, H.D.: The origins of the sampling theorem. *IEEE Commun. Mag.* **37**(4), 106–108 (1999)
24. Greitz, D., Greitz, T., Hindmarsh, T.: A new view on the CSF-circulation with the potential for pharmacological treatment of childhood hydrocephalus. *Acta Paediatr.* **86**(2), 125–132 (1997)
25. Koh, L., Zakharov, A., Johnston, M.: Integration of the subarachnoid space and lymphatics: is it time to embrace a new concept of cerebrospinal fluid absorption? *Cerebrospinal Fluid Res.* **2**, 6 (2005). doi:10.1186/1743-8454-2-6
26. Grzybowski, D.M., Herderick, E.E., Kapoor, K.G., et al.: Human arachnoid granulations. Part I: a technique for quantifying area and distribution on the superior surface of the cerebral cortex. *Cerebrospinal Fluid Res.* **4**, 6 (2007). doi:10.1186/1743-8454-4-6
27. Holman, D.W., Kurtcuoglu, V., Grzybowski, D.M.: Cerebrospinal fluid dynamics in the human cranial subarachnoid space: an overlooked mediator of cerebral disease. II. In vitro arachnoid outflow model. *J. R. Soc. Interface* **7**(49), 1205–1218 (2010). doi:rsif.2010.0032 [pii]10.1098/rsif.2010.0032
28. Bateman, G.: Hyperemic hydrocephalus: a new form of childhood hydrocephalus analogous to hyperemic intracranial hypertension in adults. *J. Neurosurg. Pediatr.* **5**(1), 20–26 (2010). doi:10.3171/2009.8.PEDS09204
29. Knight, J., Olgac, U., Saur, S.C., et al.: Choosing the optimal wall shear parameter for the prediction of plaque location-A patient-specific computational study in human right coronary arteries. *Atherosclerosis* **211**(2), 445–450 (2010). doi:10.1016/j.atherosclerosis.2010.03.001
30. Bloomfield, I.G., Johnston, I.H., Bilston, L.E.: Effects of proteins, blood cells and glucose on the viscosity of cerebrospinal fluid. *Pediatr. Neurosurg.* **28**(5), 246–251 (1998)
31. Brydon, H.L., Hayward, R., Harkness, W., et al.: Physical properties of cerebrospinal fluid of relevance to shunt function. 1: the effect of protein upon CSF viscosity. *Br. J. Neurosurg.* **9**(5), 639–644 (1995)
32. Chen, S., Doolen, G.D.: Lattice Boltzmann method for fluid flows. *Annu. Rev. Fluid Mech.* **30**, 329–364 (1998)
33. Jacobson, E.E., Fletcher, D.F., Morgan, M.K., et al.: Computer modelling of the cerebrospinal fluid flow dynamics of aqueduct stenosis. *Med. Biol. Eng. Comput.* **37**(1), 59–63 (1999)
34. Fin, L., Grebe, R.: Three dimensional modeling of the cerebrospinal fluid dynamics and brain interactions in the aqueduct of sylvius. *Comput. Methods Biomed. Engin.* **6**(3), 163–170 (2003). doi:10.1080/1025584031000097933016C8J55KCLQF4JT[pii]
35. Kurtcuoglu, V., Poulikakos, D., Ventikos, Y.: Computational modeling of the mechanical behavior of the cerebrospinal fluid system. *J. Biomech. Eng.* **127**(2), 264–269 (2005)
36. Du Boulay, G., O'Connell, J., Currie, J., et al.: Further investigations on pulsatile movements in the cerebrospinal fluid pathways. *Acta Radiol. Diagn. (Stockh.)* **13**, 496–523 (1972)
37. Kurtcuoglu, V., Soellinger, M., Summers, P., et al.: Mixing and modes of mass transfer in the third cerebral ventricle: a computational analysis. *J. Biomech. Eng.* **129**(5), 695–702 (2007). doi:10.1115/1.2768376
38. Tricoire, H., Locatelli, A., Chemineau, P., et al.: Melatonin enters the cerebrospinal fluid through the pineal recess. *Endocrinology* **143**(1), 84–90 (2002)
39. Cheng, S., Tan, K., Bilston, L.E.: The effects of the interthalamic adhesion position on cerebrospinal fluid dynamics in the cerebral ventricles. *J. Biomech.* **43**(3), 579–582 (2010). doi:S0021-9290(09)00566-1[pii]10.1016/j.jbiomech.2009.10.002
40. Howden, L., Giddings, D., Power, H., et al.: Three-dimensional cerebrospinal fluid flow within the human ventricular system. *Comput. Methods Biomed. Engin.* **11**(2), 123–133 (2008). doi:785046036[pii]10.1080/10255840701492118
41. Linninger, A.A., Xenos, M., Zhu, D.C., et al.: Cerebrospinal fluid flow in the normal and hydrocephalic human brain. *IEEE Trans. Biomed. Eng.* **54**(2), 291–302 (2007). doi:10.1109/TBME.2006.886853
42. Sweetman, B., Linninger, A.A.: Cerebrospinal fluid flow dynamics in the central nervous system. *Ann. Biomed. Eng.* **39**(1), 484–496 (2011). doi:10.1007/s10439-010-0141-0

43. Sweetman, B., Xenos, M., Zitella, L., et al.: Three-dimensional computational prediction of cerebrospinal fluid flow in the human brain. *Comput. Biol. Med.* **41**(2), 67–75 (2011). doi:10.1016/j.combiomed.2010.12.001
44. Loth, F., Yardimci, M.A., Alperin, N.: Hydrodynamic modeling of cerebrospinal fluid motion within the spinal cavity. *J. Biomech. Eng.* **123**(1), 71–79 (2001)
45. The Visible Human Project. 1997. [http://www.nlm.nih.gov/research/visible/visible\\_human.html](http://www.nlm.nih.gov/research/visible/visible_human.html). Accessed February 2011
46. Stockman, H.W.: Effect of anatomical fine structure on the flow of cerebrospinal fluid in the spinal subarachnoid space. *J. Biomech. Eng.* **128**(1), 106–114 (2006)
47. Bilston, L.E., Fletcher, D.F., Stoodley, M.A.: Focal spinal arachnoiditis increases subarachnoid space pressure: a computational study. *Clin. Biomech. (Bristol, Avon)* **21**(6), 579–584 (2006)
48. Hentschel, S., Mardal, K.A., Lovgren, A.E., et al.: Characterization of cyclic CSF flow in the foramen magnum and upper cervical spinal canal with MR flow imaging and computational fluid dynamics. *AJNR Am. J. Neuroradiol.* **31**(6), 997–1002 (2010). doi:ajnr.A1995 [pii] 10.3174/ajnr.A1995
49. Linge, S.O., Haughton, V., Lovgren, A.E., et al.: CSF flow dynamics at the craniocervbral junction studied with an idealized model of the subarachnoid space and computational flow analysis. *AJNR Am. J. Neuroradiol.* **31**(1), 185–192 (2010). doi:ajnr.A1766 [pii] 10.3174/ajnr.A1766
50. Kuttler, A., Dimke, T., Kern, S., et al.: Understanding pharmacokinetics using realistic computational models of fluid dynamics: biosimulation of drug distribution within the CSF space for intrathecal drugs. *J. Pharmacokinet. Pharmacodyn.* **37**(6), 629–644 (2010). doi:10.1007/s10928-010-9184-y
51. Riley, N.: Steady streaming. *Annu. Rev. Fluid Mech.* **33**, 43–65 (2001)
52. Bilston, L.E., Fletcher, D.F., Brodbelt, A.R., et al.: Arterial pulsation-driven cerebrospinal fluid flow in the perivascular space: a computational model. *Comput. Methods Biomed. Engin.* **6**(4), 235–241 (2003)
53. Wang, P., Olbricht, W.L.: Fluid mechanics in the perivascular space. *J. Theor. Biol.* (2011). doi:10.1016/j.jtbi.2011.01.014
54. Bilston, L.E., Stoodley, M.A., Fletcher, D.F.: The influence of the relative timing of arterial and subarachnoid space pulse waves on spinal perivascular cerebrospinal fluid flow as a possible factor in syrinx development. *J. Neurosurg.* **112**(4), 808–813 (2010). doi:10.3171/2009.5.JNS08945
55. Tully, B., Ventikos, Y.: Coupling poroelasticity and CFD for cerebrospinal fluid hydrodynamics. *IEEE Trans. Biomed. Eng.* **56**(6), 1644–1651 (2009). doi:10.1109/TBME.2009.2016427
56. Sarntinoranont, M., Chen, X., Zhao, J., et al.: Computational model of interstitial transport in the spinal cord using diffusion tensor imaging. *Ann. Biomed. Eng.* **34**(8), 1304–1321 (2006). doi:10.1007/s10439-006-9135-3
57. Tillmann, B.: *Atlas der Anatomie des Menschen*. Springer, Berlin (2005)
58. Schmid Daners, M., Knobloch, V., Soellinger, M., et al.: Age-specific characteristics and coupling of cerebral arterial inflow and cerebrospinal fluid dynamics (2011)
59. Schley, D., Carare-Nnadi, R., Please, C.P., et al.: Mechanisms to explain the reverse perivascular transport of solutes out of the brain. *J Theor Biol.* **238**(4), 962–974 (2006). doi:10.1016/j.jtbi.2005.07.005

# Chapter 9

## Algorithms for Computational Biomechanics of the Brain

A. Wittek, G. Joldes, and K. Miller

### 9.1 Introduction

Modeling of the brain responses due to injury-causing transients and surgery is a problem of continuum mechanics that involves irregular geometry, complex loading and boundary conditions, non-linear materials, and large deformations (see Chaps. 5 and 6). Finding a solution for such a problem requires computational algorithms of non-linear continuum mechanics.

As stated in Chap. 5, modeling for brain injury simulation has been driven by the idea that numerical surrogates of the human brain can be used in the design of countermeasures mitigating the traumatic brain injury. Such modeling has been done with significant contribution and involvement of the automotive manufacturers [1] and participation of organizations responsible for traffic safety (e.g. National Highway Traffic Safety Administration NHTSA) [2]. Because of these industrial links, modeling of the brain for injury simulation has been dominated by the explicit dynamics (i.e. utilizing explicit integration in time domain) non-linear finite element algorithms available in commercial finite element codes, such as LS-DYNA [3], PAM-SAFE [4], RADIOSS [5], that are routinely used by the automotive industry.

In computational biomechanics for medicine, on the other hand, significant research effort has been directed into the development of specialized algorithms that can provide the results within the real-time constraints of surgery. For instance, great interest was given to mass-spring method [6, 7] in which the analyzed continuum is modeled as a discrete system of nodes (where the mass is concentrated) and springs. Due to its simplicity and low computational complexity, this method was applied in simulation software for virtual reality training systems for

---

A. Wittek (✉)

Intelligent Systems for Medicine Laboratory, School of Mechanical and Chemical Engineering, The University of Western Australia,  
35 Stirling Highway, Crawley, WA 6009, Australia  
e-mail: adwit@mech.uwa.edu.au

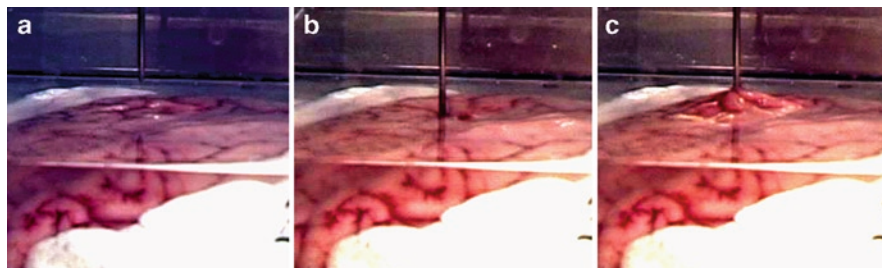


**Fig. 9.1** Swine brain deformation during needle insertion. (a) Before insertion; (b) during the insertion (note the deformation in the insertion area); (c) during the needle removal. The experiments were conducted at the laboratory of the Surgical Assist Technology Group, Group, Institute for Human Science and Biomedical Engineering, National Institute of Advanced Industrial Science and Technology (AIST), Tsukuba, Ibaraki, Japan. For the experiment description, see [31]

minimally invasive surgery [8]. However, the behavior of the mass-spring models strongly depends on the topology of the spring network and spring parameters are difficult to identify and express in terms of the soft tissue constitutive parameters (such as Young's modulus and Poisson's ratio) that are used in continuum mechanics [9]. Therefore, in recent years, more interest has been given to the finite element method [10] that utilizes the principles of continuum mechanics and does not suffer from the limitations of the mass-spring method.

Traditionally, real-time computations for biomechanics for medicine relied on linear finite element algorithms that assume infinitesimally small deformations [9, 11–14]. However, this assumption is not satisfied in surgical procedures where large deformations of the organ undergoing surgery occur. Examples include the brain deformations due to craniotomy (referred to in the literature as brain shift [15]) (see Fig. 6.1 in Chap. 6) and needle insertion (Fig. 9.1 above). Therefore, we focus on the algorithms that utilize fully non-linear (i.e. accounting for finite deformations and non-linear stress-strain relationships of soft tissues) formulation of solid mechanics that can be applied to any situation. In such a formulation, the current volume and surface of the modeled body organ (over which the integration of equations of continuum mechanics is to be conducted) are unknown. They are part of the solution rather than input data (Fig. 9.2). The literature indicates that taking into account geometric non-linearity (through finite deformation formulation of the equations of continuum mechanics) is needed to ensure accuracy of prediction of soft organ deformations even for applications that do not involve very large strains (e.g. brain shift) [16, 17].

In the subsequent sections of this chapter, we discuss the following topics:

- Section 9.2: Non-linear explicit dynamics finite element algorithms implemented in commercial finite element codes applied to modeling brain injury biomechanics.
- Section 9.3: A specialized non-linear finite element algorithm for surgery simulation that utilizes explicit integration in time domain and Total Lagrangian incremental formulation of continuum mechanics.
- Section 9.4: A specialized non-linear finite element algorithm that utilizes Dynamic Relaxation and Total Lagrangian formulation for computation of steady-state brain deformation within the real-time constraints of image-guided neurosurgery.

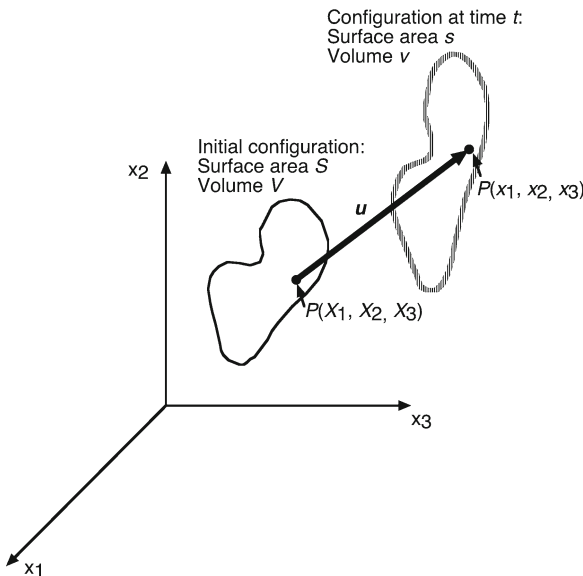


**Fig. 9.2** Computational biomechanics as a non-linear problem of continuum mechanics. During impact and surgery, human body organs undergo large displacements (composed of rigid body motions and local deformations). Consequently, the equations of continuum mechanics governing the organ behavior need to be integrated over the current surface  $s$  and volume  $v$

- Section 9.5: Element formulation for the specialized algorithms for surgery simulation and neurosurgery modeling. This includes non-locking tetrahedral element and efficient hourglass control for hexahedral element.
- Section 9.6: An efficient sliding contact algorithm for modeling of brain–skull interaction for image-guided neurosurgery.
- Section 9.7: Meshless algorithms that utilize a computational grid in the form of a cloud of points as one possible remedy for the limitations of finite element algorithms (including time-consuming generation of patient-specific computation grids as well as deterioration of the computation accuracy and instability due to very large strains induced by surgery).
- Section 9.8: Implementation of the specialized non-linear finite element algorithms for neurosurgery modeling on graphics processing units (GPUs) for real-time solution of the brain models for computer-assisted neurosurgery.
- Section 9.9: Algorithm verification.

## 9.2 Algorithms for Injury Simulation

Impact/injury biomechanics of the brain deals with events of very short duration (hundreds of milliseconds) in which the head is subjected to transient loading due to either direct impact or rapid acceleration that results in large deformation (or even

mechanical damage) of the brain tissue. As indicated in [10, 18, 19], non-linear finite element procedures with explicit integration in time domain outperform other algorithms in modeling of three-dimensional continua in such events. Therefore, they have been a preferable choice in brain injury biomechanics (see also Chap. 5) and implemented in numerous finite elements codes (such as e.g. LS-DYNA, PAM-CRASH, ABAQUS, RADIOSS) industrially applied in impact injury simulation.

In impact injury simulation and other transient dynamics problems, the global system of finite element equations to be solved at each time step is:

$$\mathbf{M}\ddot{\mathbf{u}}_{n+1} + \mathbf{K}(\mathbf{u}_{n+1}) \cdot \mathbf{u}_{n+1} = \mathbf{R}_{n+1}, \quad (9.1)$$

where  $\mathbf{u}$  is a vector of nodal displacements,  $\mathbf{M}$  is a mass matrix,  $\mathbf{K}$  is a stiffness matrix non-linearly dependent on the deformation (because of the non-linear material model), and  $\mathbf{R}$  is a vector of nodal (active) forces. The product of the stiffness matrix and nodal displacements vector gives the nodal reaction forces vector  $\mathbf{F}$ . In explicit dynamics finite element procedures, the accelerations determined from equation of motion (9.1) are integrated to calculate the displacements using difference methods. Although many difference methods exist [10], the central difference method is the most commonly used due to its efficiency [10, 18]:

$$u_{n+1} = u_n + \Delta t_{n+1} \dot{u}_n + \frac{1}{2} \Delta t_{n+1}^2 \ddot{u}_n, \quad (9.2)$$

$$\dot{u}_{n+1} = \dot{u}_n + \frac{1}{2} \Delta t_{n+1} (\ddot{u}_{n+1} + \ddot{u}_n). \quad (9.3)$$

Combining the central difference method given by (9.2) to (9.3) with the global system of finite element (9.1) yields the following formula for the vector of nodal displacements  $\mathbf{u}_{n+1}$  at integration step  $n+1$ :

$$\mathbf{M}\mathbf{u}_{n+1} = \Delta t^2 \left( \mathbf{R}_n - \sum_i \mathbf{F}_n^{(i)} \right) - \mathbf{M}(\mathbf{u}_{n-1} - 2\mathbf{u}_n). \quad (9.4)$$

Formally (9.4) represents a system of equations. This system can be decoupled by using a lumped mass matrix  $\mathbf{M}$ . For lumped mass matrices, all non-diagonal components equal zero (i.e. the mass distribution is discretized by placing the particle masses at the nodes of an element). For such matrices, (9.4) becomes an explicit formula for the unknown nodal displacements  $\mathbf{u}_{n+1}$ :

$$\mathbf{u}_{n+1}^j = \Delta t^2 \left( \mathbf{R}_n^j - \sum_i \mathbf{F}_n^{(i)j} \right) / m_{jj} - (\mathbf{u}_{n-1}^j - 2\mathbf{u}_n^j), \quad (9.5)$$

where  $\mathbf{u}_{n+1}^j$  is a vector of nodal displacements at node  $j$  at intergation step  $n+1$ ,  $m_{jj}$  is the component of the lumped mass matrix corresponding to node  $j$  (i.e. mass lumped to node  $j$ ),  $\mathbf{R}_n^j$  is the vector of external forces applied to node  $j$ ,  $\sum_i \mathbf{F}_n^{(i)j}$  is

the vector of nodal reaction forces at node  $j$  (sum of the contribution of the elements  $i$  to which the node belongs), and  $\Delta t$  is the integration step.

In (9.5), the computations are done at element level eliminating the need for assembling the stiffness matrix of the entire analyzed continuum. The mechanical properties of the analyzed continuum are accounted for in the constitutive model and included in the calculation of nodal reaction forces  $\mathbf{F}$ . Thus, computational cost of each time step and internal memory requirements are very low. It is worth noting that there is no need for iterations anywhere in the algorithm summarized in (9.5), even for non-linear problems. This implies the following advantages of non-linear finite element procedures utilizing explicit integration in time domain and mass lumping:

- Straightforward treatment of non-linearities
- No iterations required for a time step
- No need to solve a system of equations
- Low computational cost for each time step
- Low internal memory requirements

However, explicit methods are only conditionally stable. A restriction (Courant criterion [20]) on the time step size has to be included in order to obtain stable simulation results. The time step (referred to as a critical time step) that ensures the computation stability is equal to the smallest characteristic length of an element in the mesh divided by the dilatational (acoustic) wave speed [18, 20, 21]:

$$\Delta t \leq \frac{L_e}{c}, \quad (9.6)$$

where  $L_e$  is the smallest characteristic element length in the model and  $c$  is the dilatational (acoustic) wave speed. The formulae for calculating  $L_e$  for various commonly used elements are given in [22].

Equation (9.6) is equivalent to setting the condition that the time step cannot be longer than the travel time of the wave across the smallest element in the mesh [18]. Based on [22], the acoustic wave speed can be expressed as

$$c = \sqrt{\frac{E}{\rho} \frac{(1-v)}{(1+v)(1-2v)}}, \quad (9.7)$$

where  $E$  is the Young's modulus,  $\rho$  is the density, and  $v$  is the Poisson's ratio.

It should be noted that the stability limit given in (9.6) has been derived for linear problems. However, according to [18], there is considerable empirical evidence that it is also valid for non-linear problems.

Equations (9.6) and (9.7) imply that the critical time step can be increased by increasing the density (and hence the mass) of the smallest elements (as determined by the characteristic length  $L_e$ ) in the mesh. This process is referred to as mass scaling [3, 23]. Moderate mass scaling does not significantly change the responses of the analyzed continuum and is regarded as a powerful method for decreasing the

computation time [24]. However, it is also acknowledged that too severe scaling can introduce non-physical inertia effects [24]. Formal guidelines for determining permissible mass scaling limits for injury simulation have not yet been formulated and the quantitative information about the scaling that is used is rarely provided in the biomechanical literature. Majumder et al. [25] reported a significant reduction in computation time for scaling resulting in the total model mass increase as low as 0.016%. ABAQUS finite element solver manual [26] recommends that, after applying mass scaling, the kinetic energy of the system should not exceed 5% of the total energy over most of the analysis.

Stress calculation for obtaining the nodal forces  $\mathbf{F}$  is the major computation cost of the explicit dynamic finite element procedures summarized in (9.4) and (9.5). This implies that the complexity of the elements and the number of integration points per element are the key factors determining the number of computations in these procedures. Therefore, as mentioned in Chap. 5, in injury simulation utilizing non-linear finite element procedures with explicit integration in time domain, 8-noded hexahedron [27, 28] and 4-noded tetrahedron [27, 28] with linear shape functions and one integration (Gauss) point are the most commonly used elements.

The 8-noded hexahedron with one integration point is an under-integrated element (or low-order Gauss quadrature element), i.e. an element for which the stiffness matrix rank is lower than the number of element's degrees of freedom minus the number of rigid body modes [29]. Under-integrated elements exhibit an instability known as hourgassing or zero-energy modes, i.e. there are nodal displacement vectors which produce no strain energy, but do not define a rigid body motion [27, 29].

The 4-noded tetrahedral elements with linear shape functions and one Gauss point do not suffer from hourgassing. However, for incompressible (or nearly incompressible) continua, such as soft tissues, 4-noded tetrahedral elements exhibit artificial stiffening known as volumetric locking [20, 30]. A more detailed discussion on algorithms for hourglass control and volumetric locking reduction is provided in Sect. 9.3.

### 9.3 Algorithms for Surgery Simulation

As discussed in Chap. 6, surgical simulation systems are required to provide visual and haptic feedback to a surgeon or trainee. Such systems must provide a time accurate prediction of the deformation field within an organ and interaction force between the surgical tool and the tissue at frequencies of at least 500 Hz. From the perspective of continuum mechanics, such prediction requires solving the problem involving large deformations, non-linear constitutive properties and non-linear boundary conditions within the very strict time constraints of haptic feedback.

For relatively slow varying loads, such as those that occur due to interactions between tissue and surgical tool, non-linear finite element algorithms utilizing implicit integration in time domain are traditionally recommended in the literature for solving non-linear problems of solid mechanics [10]. Such procedures rely on solving systems of algebraic equations and require computationally expensive iterations. In contrast, the algorithms for injury simulation lead to an explicit formula for unknown nodal

displacements (9.5). For such algorithms, the number of operations per integration step is typically three orders of magnitude smaller than for the ones relying on implicit integration [18]. Despite the fact that surgical simulations involve phenomena with durations that are orders of magnitude longer than those that are of interest in injury simulation, the restrictions on the time step size (Courant criterion) required for solution stability (9.6) do not compromise efficiency of explicit time integration in such simulations. This is because the acoustic wave speed is proportional to the square root of the analyzed continuum Young's modulus (9.7) which is very low (under  $10^4$  Pa) for brain tissue. For instance, in the simulation of needle insertion into brain conducted using non-linear explicit dynamics finite element procedures reported in [31], the time step was over  $1.5 \times 10^{-2}$  ms. In contrast, typical engineering applications, such as metal forming, use integration steps that are of an order of  $10^{-5}$  ms [32].

In commercial finite element codes utilizing explicit time integration, the calculated variables (such as displacement, strain and stress) are incremented by referring them to the current configuration of the analyzed continuum. This method is known as the Updated Lagrangian formulation [10]. However, for surgical simulation, we advocate the Total Lagrangian (TL) formulation of the finite element method in which all variables are referred to the original configuration of the system [33]. The decisive advantage of this formulation is that all derivatives with respect to spatial coordinates are calculated with respect to the original configuration and therefore can be pre-computed as shown in the flowchart of the Total Lagrange Explicit Dynamics (TLED) algorithm presented in Fig. 9.3 (a detailed description of the algorithm is given in [33]).

Following the approach typically applied in explicit dynamics finite element analysis, for computational efficiency of our TLED algorithm we used single point integration for all elements of the mesh (improved linear tetrahedrons [34] and under-integrated linear hexahedrons). Therefore, the nodal forces for each element are computed as:

$${}^t_0 \mathbf{F}_{\text{int}} = {}^t_0 \mathbf{X} \cdot {}^t_0 \mathbf{S} \cdot \mathbf{B}_0 \cdot V_0, \quad (9.8)$$

where, according to the notation used in [10], the left superscript represents the current time, the left subscript represents the time of the reference configuration,  $\mathbf{F}_{\text{int}}$  is the matrix of nodal forces,  $\mathbf{B}_0$  is the matrix of shape function derivatives,  $\mathbf{S}$  is the second-Piola Kirchoff stress matrix,  $\mathbf{X}$  is the deformation gradient and  $V_0$  is the initial volume. In (9.8), the matrix of shape function derivatives  $\mathbf{B}_0$  and the initial volume  $V_0$  are constant and therefore can be pre-computed (see Fig. 9.3).

The main benefits of the TLED algorithm in comparison to the explicit dynamics algorithms using Updated Lagrangian formulation are:

- Allows pre-computing of many variables involved (e.g. derivatives with respect to spatial coordinates), Fig. 9.3
- No accumulation of errors – increased stability for quasi-static solutions
- Second-Piola Kirchoff stress and Green strain are used – appropriate for handling geometric non-linearities
- Easy implementation of the material law for hyperelastic materials using the deformation gradient

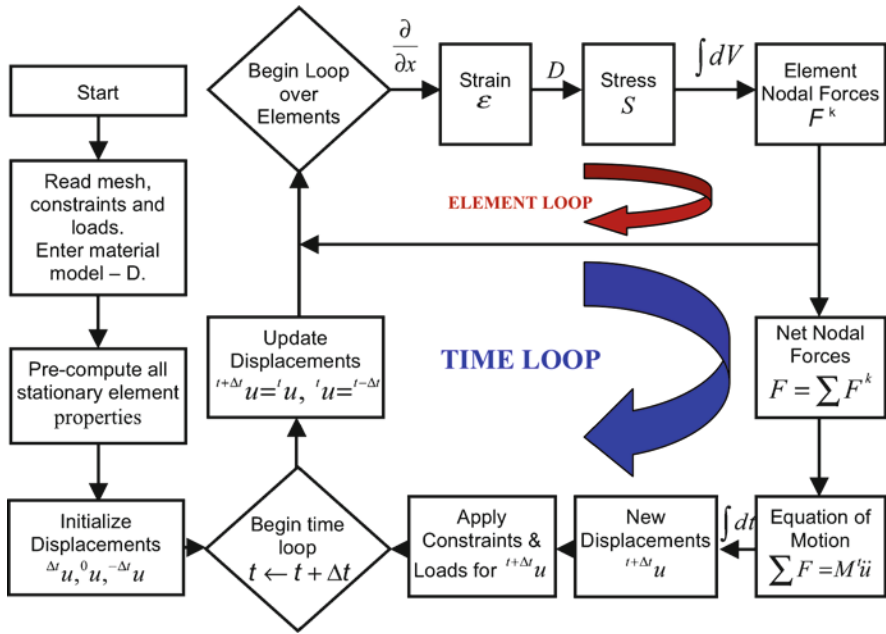


**Fig. 9.3** Flowchart of the total lagrange explicit dynamics (TLED) finite element algorithm for surgery simulation. Detailed description of the algorithm is given in [33]

The fact that many quantities involved in the computation of nodal forces can be pre-computed leads to a significant decrease in the computational effort. For instance, the TLED algorithm using eight-noded hexahedral under-integrated elements requires approximately 35% fewer floating-point operations per element, per time step than the Updated Lagrangian explicit algorithm using the same elements [33].

## 9.4 Algorithms for Neurosurgery Modeling

As explained in Chap. 6, accurate warping of high-quality pre-operative radiographic images to the intra-operative (i.e. deformed) brain configuration in a process known as non-rigid registration is a key element of image-guided neurosurgery. In order to perform such warping, only the final (deformed during surgery) state of the brain needs to be predicted. This requires algorithms for determining steady-state solution for the brain deformations. The deformations at the steady-state must be obtained within the real-time constraints of image-guided neurosurgery, which practically means that the results should be available in 40–80 s.

As stated in Chap. 6, neuroimage registration is a non-linear problem of computational mechanics as it involves large deformations, non-linear material properties and non-linear boundary conditions. However, it is a less demanding problem than surgery simulation as only the steady-state solution for deformations is of interest,

i.e. the time history of forces and deformations does not have to be obtained. Therefore, for image registration, we advocate Dynamic Relaxation (DR), which is an explicit iterative algorithm that relies on the introduction of an artificial mass-dependent damping term in the equation of motion. The damping attenuates the oscillations in the transient response, increasing the convergence towards the steady-state solution. Because of DR's explicit nature, there is no need for solving large systems of equations. All quantities can be treated as vectors, reducing the implementation complexity and the memory requirements. Although the number of iterations to obtain convergence can be quite large, the computation cost of each iteration is very low, making it a very efficient solution method for non-linear problems.

#### 9.4.1 Dynamic Relaxation Algorithm

The basic Dynamic Relaxation (DR) algorithm is presented in [35]. The main idea is to include a mass-proportional damping in the equation of motion (9.1) (see Sect. 9.2), which will increase the convergence speed towards the steady-state. The obtained damped equation is then solved using the central difference method (explicit integration). After the inclusion of mass-proportional damping, the equation of motion (9.1) becomes

$$\mathbf{M}\ddot{\mathbf{u}} + c \cdot \mathbf{M}\dot{\mathbf{u}} + \mathbf{F}(\mathbf{u}) = \mathbf{R}, \quad (9.9)$$

where  $c$  is the damping coefficient.

By applying the central difference integration method to the damped equation of motion (9.9), the equation that describes the iterations in terms of displacements becomes:

$$\mathbf{u}_{n+1} = \mathbf{u}_n + \beta(\mathbf{u}_n - \mathbf{u}_{n-1}) + \alpha \mathbf{M}^{-1}(\mathbf{R} - \mathbf{F}), \quad (9.10)$$

$$\alpha = 2h^2/(2+ch), \quad \beta = (2-ch)/(2+ch) \quad (9.11)$$

where  $h$  is a fixed time increment.

The iterative method defined by (9.10) is explicit as long as the mass matrix is diagonal. As the mass matrix does not influence the deformed state solution, a lumped mass matrix can be used that maximizes the convergence of the method.

In [35], the convergence of the DR algorithm is studied for linear structural mechanics equations, when the nodal forces can be written as

$$\mathbf{F}(\mathbf{u}) = \mathbf{K} \cdot \mathbf{u}, \quad (9.12)$$

with  $\mathbf{K}$  being the stiffness matrix.

We extend this study to the non-linear case. We propose to use the linearization of the nodal forces obtained by expanding them in a Taylor series and keeping the first two terms:

$$\mathbf{F}(\mathbf{u}_n) = \mathbf{F}(\mathbf{u}_k) + \mathbf{K}_k \cdot (\mathbf{u}_n - \mathbf{u}_k), \quad (9.13)$$

where  $\mathbf{u}_k$  is a point close to  $\mathbf{u}_n$  and  $\mathbf{K}_k$  is the tangent stiffness matrix evaluated at point  $\mathbf{u}_k$ .

By substituting  $\mathbf{F}$  from (9.13) into (9.10), we obtain the equation that advances to a new iteration for a non-linear problem as:

$$\mathbf{u}_{n+1} = \mathbf{u}_n + \beta(\mathbf{u}_n - \mathbf{u}_{n-1}) + \alpha\mathbf{b} - \alpha\mathbf{A}\mathbf{u}_n \quad (9.14)$$

with

$$\mathbf{b} = \mathbf{M}^{-1}(\mathbf{R} - \mathbf{F}(\mathbf{u}_k) + \mathbf{K}_k\mathbf{u}_k), \quad \mathbf{A} = \mathbf{M}^{-1}\mathbf{K}_k. \quad (9.15)$$

It is worth noting that (even if (9.14) has the same form as in the linear case) the point  $\mathbf{u}_k$  is not fixed during the iteration process (as it must be close to  $\mathbf{u}_n$  in order for the Taylor series expansion to be accurate). Therefore, the tangent stiffness matrix (and matrix  $\mathbf{A}$ ) changes.

The error after the  $n$ th iteration is defined as:

$$\mathbf{e}_n = \mathbf{u}_n - \mathbf{u}^*, \quad (9.16)$$

where  $\mathbf{u}^*$  is the solution. Substituting (9.16) in (9.14) gives the error equation (valid only close to the solution):

$$\mathbf{e}_{n+1} = \mathbf{e}_n - \alpha\mathbf{A}\mathbf{e}_n + \beta(\mathbf{e}_n - \mathbf{e}_{n-1}) \quad (9.17)$$

and by assuming that

$$\mathbf{e}_{n+1} = \boldsymbol{\kappa} \cdot \mathbf{e}_n \quad (9.18)$$

the following relation is obtained for computing the eigenvalues  $\boldsymbol{\kappa}$  of matrix  $\boldsymbol{\kappa}$ :

$$\boldsymbol{\kappa}^2 - (1 + \beta - \alpha A)\boldsymbol{\kappa} + \beta = 0, \quad (9.19)$$

where  $A$  denotes any eigenvalue of matrix  $\mathbf{A}$ .

The fastest convergence is obtained for the smallest possible spectral radius  $\rho = |\boldsymbol{\kappa}|$ . The optimum convergence condition is obtained when:

$$\rho^* = |\boldsymbol{\kappa}^*| = \beta^{1/2} \approx \sqrt{1 - 2\sqrt{\frac{A_0}{A_m}}}, \quad (9.20)$$

$$h \approx 2/\sqrt{A_m} = 2/\omega_{\max}, \quad (9.21)$$

$$c \approx 2\sqrt{A_0} = 2\omega_0, \quad (9.22)$$

where  $A_0$  and  $A_m$  are the minimum and maximum eigenvalues of matrix  $\mathbf{A}$  and therefore  $\omega_0$  and  $\omega_{\max}$  are the lowest and highest circular frequencies of the un-damped equation of motion [35].

The effect of eigenvalue estimation accuracy on the convergence of the method is presented in [36]. To ensure convergence, it is critical that the maximum

eigenvalue  $A_m$  is over-estimated, even if this will lead to a decreased convergence speed. If, at the same time, the minimum eigenvalue  $A_0$  is under-estimated, then uniform convergence will be obtained for all eigenvalues, with a further decrease in convergence speed. If  $A_0$  is over-estimated then it is possible to increase the convergence speed for all eigenvalues except a very narrow range of small eigenvalues.

#### 9.4.1.1 Dynamic Relaxation Algorithm: Maximum Eigenvalue $A_m$ and Mass Matrix

Using the Rayleigh quotient, it has been demonstrated that the maximum eigenvalue of an assembled finite element mesh is bounded by the maximum eigenvalue of any of the elements in the mesh [10]:

$$A_m \leq \max(\lambda_{\max}^e). \quad (9.23)$$

Therefore, an estimation of the maximum eigenvalue can be obtained by estimating the maximum eigenvalue of each element in the mesh. Such estimations for different element types are presented in [37].

In the case of a non-linear problem, the maximum eigenvalue changes during the simulation as the geometry of the elements changes and therefore it must be estimated after every iteration step.

Because the mass matrix has no influence on the steady-state (as the time derivatives in (9.9) become zero), a fictitious mass matrix that improves the convergence rate can be used. The mass matrix can be chosen such that it reduces the condition number of matrix  $\mathbf{A}$ , leading to a decrease in the spectral radius  $\rho$  (see (9.20)).

In order to reduce the condition number, we propose to align the maximum eigenvalue of all elements in the mesh to the same value by changing the density of each element. By doing this, we can still use (9.23) for estimating the maximum eigenvalue, and the condition number is at least preserved and generally decreased, as shown in [35]. This process guarantees that the selected maximum eigenvalue  $A_m$  is an over-estimation of the actual maximum eigenvalue during the simulation, therefore ensuring the convergence.

#### 9.4.1.2 Dynamic Relaxation Algorithm: Estimation of the Minimum Eigenvalue $A_0$

Estimating the minimum eigenvalue is difficult, especially for non-linear problems, where an adaptive procedure should be used in order to obtain the optimum convergence parameters. An overview of the procedures proposed by different authors in the context of DR (including an adaptive one) is presented in [35].

The adaptive method proposed in [35] is based on Rayleigh's quotient and the use of a local diagonal stiffness matrix. The elements of this matrix are computed using finite differences, which can be very difficult to do for degrees of freedom which have small displacement variation.

In this section, we propose a new adaptive method for computing the minimum eigenvalue, which is also based on Rayleigh's quotient, but does not have the shortcomings of the method proposed in [35].

We consider a change of variable:

$$\mathbf{z}_n = \mathbf{u}_n - \mathbf{u}_k, \quad (9.24)$$

where  $\mathbf{u}_k$  is the point used for linearization of the nodal forces in (9.13). The linearised nodal forces can therefore be expressed as:

$$\mathbf{F}(\mathbf{u}_n) = \mathbf{F}(\mathbf{u}_k) + \mathbf{K}_k \cdot \mathbf{z}_n. \quad (9.25)$$

After replacing (9.24) and (9.25) in (9.1), the linearized equation of motion becomes:

$$\mathbf{M} \cdot \ddot{\mathbf{z}} + \mathbf{K}_k \cdot \mathbf{z} = \mathbf{R} - \mathbf{F}(\mathbf{u}_k). \quad (9.26)$$

We can now rely on (9.26) to estimate  $A_0$  using Rayleigh's quotient and the current value of the displacements:

$$A_0 \leq \frac{(\mathbf{z}_n)^T \mathbf{K}_k \mathbf{z}_n}{(\mathbf{z}_n)^T \mathbf{M} \mathbf{z}_n}. \quad (9.27)$$

We consider the right-hand side of (9.27) as an estimate of the minimum eigenvalue. Using (9.24) and (9.25), this estimate becomes:

$$A_0 \approx \frac{(\mathbf{u}_n - \mathbf{u}_k)^T (\mathbf{F}(\mathbf{u}_n) - \mathbf{F}(\mathbf{u}_k))}{(\mathbf{u}_n - \mathbf{u}_k)^T \mathbf{M} (\mathbf{u}_n - \mathbf{u}_k)}, \quad (9.28)$$

where  $\mathbf{u}_k$  is a fixed point that must be close to  $\mathbf{u}_n$ . We choose the solution from a previous iteration as the fixed point  $\mathbf{u}_k$  and update it after a number of steps in order to keep it close to the current solution  $\mathbf{u}_n$ . No additional information (such as estimates of the stiffness matrix) is required and only vector operations are performed (as  $\mathbf{M}$  is a diagonal lumped mass matrix).

During the iterative dynamic relaxation DR procedure, the high frequencies are damped out and the system will eventually oscillate on its lowest frequency. Therefore, (9.28) will converge towards the minimum eigenvalue. This estimation process, combined with our parameter selection process, leads to an increased convergence rate, because it always offers an over-estimation of the minimum eigenvalue. The higher the over-estimation of the minimum eigenvalue, the higher the reduction of the high frequency vibrations (see [36]), and therefore (9.28) will converge faster towards the real minimum eigenvalue.

### 9.4.1.3 Dynamic Relaxation Algorithm: Termination Criteria

One very important aspect of any finite element (FE) algorithm is the termination criterion used. If the criterion is too coarse, then the solution might be too inaccurate and if the criterion is too tight, then time is lost for unnecessary computations.

The criteria used by commercial FE software are usually based on residual forces, displacements or energy. None of these criteria gives any information about the absolute error in the solution and selecting any of these termination criteria is very difficult.

We propose a new termination criterion that gives information about the absolute error in the solution, particularly suited for our solution method. Because DR iterations lead to a strong reduction of the high frequencies, the displacement vector will oscillate around the solution vector with a frequency that converges towards the smallest oscillation frequency. This implies that the error vector  $\mathbf{e}$  will converge toward the eigenvector corresponding to the lowest eigenvalue. Therefore, we can make the following approximation:

$$\mathbf{A} \cdot \mathbf{e}_n \approx A_0 \cdot \mathbf{e}_n. \quad (9.29)$$

By substituting (9.29) in (9.17) and considering relations given in (9.19) and (9.20), we obtain:

$$\mathbf{u}_{n+1} - \mathbf{u}^* \approx \rho \cdot (\mathbf{u}_n - \mathbf{u}^*). \quad (9.30)$$

Therefore, after each iteration step, the error is reduced by a ratio equal to  $\rho$ . We can now obtain an approximation of the absolute error in the solution by applying the infinity norm to (9.30):

$$\|\mathbf{u}_{n+1} - \mathbf{u}^*\|_{\infty} \approx \rho \cdot \|\mathbf{u}_n - \mathbf{u}^*\|_{\infty} \leq \rho \cdot (\|\mathbf{u}_{n+1} - \mathbf{u}^*\|_{\infty} + \|\mathbf{u}_{n+1} - \mathbf{u}_n\|_{\infty}), \quad (9.31)$$

$$\|\mathbf{u}_{n+1} - \mathbf{u}^*\|_{\infty} \leq \frac{\rho}{1-\rho} \cdot \|\mathbf{u}_{n+1} - \mathbf{u}_n\|_{\infty}. \quad (9.32)$$

Therefore, the convergence criterion can be defined as:

$$\frac{\rho}{1-\rho} \cdot \|\mathbf{u}_{n+1} - \mathbf{u}_n\|_{\infty} \leq \varepsilon, \quad (9.33)$$

where  $\varepsilon$  is the imposed absolute accuracy. This convergence criterion gives an approximation of the absolute error based on the displacement variation norm from the current iteration.

Because our parameter estimation procedures over-estimate the maximum eigenvalue  $A_m$  and under-estimate the minimum eigenvalue  $A_0$ , the value of the computed spectral radius  $\rho_c$  we use in (9.33) can be lower than the real value of the spectral radius (see (9.20)). This can lead to an early termination of the iteration process. Therefore, in (9.33) we use a corrected value of the computed spectral radius:

$$\rho_{co} = \rho_c + \zeta \cdot (1 - \rho_c), \quad (9.34)$$

where  $\zeta$  is a correction parameter with values between 0 and 1, defining the maximum under-estimation error for the spectral radius  $\rho$ . In our simulations we use  $\zeta=0.2$ .

## 9.5 Element Formulation for Finite Element Algorithms for Surgery Simulation and Neurosurgery Modeling

### 9.5.1 Volumetric Locking

As stated in Chap. 6, due to stringent computation time requirements, the finite element meshes for models applied in surgery simulation and image registration must be constructed using low-order elements that are computationally inexpensive. Mixed meshes consisting of tetrahedral and hexahedral element are most convenient from the perspective of automation of simulation process. However, the standard formulation of the tetrahedral element exhibits volumetric locking, especially in case of soft tissues such as the brain, which are modeled as almost incompressible materials [38–44]. There are a number of improved linear tetrahedral elements already proposed by different authors [45–48]. The average nodal pressure (ANP) tetrahedral element proposed by Bonet and Burton in [45] is computationally inexpensive and provides much better results for nearly incompressible materials than the standard tetrahedral element. Nevertheless, one problem with the ANP element and its implementation in a finite element code is the handling of interfaces between different materials. In [34], we extended the formulation of the ANP element so that all elements in a mesh are treated in a similar way, requiring no special handling of the interface elements.

### 9.5.2 Stability of Under-Integrated Hexahedral Elements; Hourgassing

As stated in Chap. 6, low-order hexahedral elements with one Gauss point (referred to in Chap. 1 as a linear under-integrated hexahedral elements) are the preferred choice for explicit dynamics-type algorithms from the perspective of computational efficiency. However, such elements exhibit unphysical zero-energy deformation modes (hourgassing). The hourglass modes can be controlled by calculating hourglass forces that oppose the hourglass deformation modes. We have shown in [49] that the hourglass control forces for each element can be computed (in matrix form) as:

$${}^t_0\mathbf{F}^{Hg} = k \cdot {}^t_0\mathbf{Y} \cdot {}^t_0\mathbf{Y}^T \cdot {}^t_0\mathbf{u}, \quad (9.35)$$

where  $k$  is a constant that depends on the element geometry and material properties,  ${}_0\mathbf{Y}$  is the matrix of hourglass shape vectors and  $\mathbf{u}$  is the matrix of current displacements. In (9.35), all quantities except  $\mathbf{u}$  are constant and can be pre-computed, which makes the hourglass control mechanism very efficient.

## 9.6 Modeling of the Brain–Skull Interactions for Image-Guided Neurosurgery: Efficient Finite Sliding Contact Algorithm

Modeling of interactions between continua (e.g. soft organs) undergoing deformations is a challenging task. To facilitate such modeling, many sophisticated contact algorithms have been proposed in the literature (e.g. [50–53]) and implemented in commercial finite element codes such e.g. ABAQUS [26] and LS-DYNA [3]. Application of such algorithms tends to consume significant computing resources, which substantially increases the solution time.

When computing the brain deformation for neuroimage registration, we are interested in the interactions between the brain and the rigid skull that provide constraints for the brain tissue deformation and brain rigid body motion. Accurate modeling of such interactions can be done using a very efficient algorithm that treats these interactions as a finite sliding, frictionless contact between a deformable object (the brain) and a rigid surface (the skull) [54]. The main parts of such a contact algorithm (for detailed description see [54]) are, first, the detection of nodes on the brain surface (also called the slave surface) which have penetrated the skull surface (master surface) and second, the displacement of each slave node that has penetrated the master surface to the closest point on the master surface.

An efficient penetration detection algorithm can be formulated based on the closest master node (nearest neighbor) approach [3]. As the surfaces of the anatomical structures of the segmented neuroimages are typically discretized using triangles, the skull surface can be treated as a triangular mesh. We refer to each triangular surface as a “face”, to the vertices – “nodes” and to the triangles’ sides – “edges”. Using this terminology, the basic brain–skull contact algorithm is described as follows:

- For each slave node P:
  - Find the closest master node C (global search).
  - Check the faces and edges surrounding C for penetration (local search).
  - Check additional faces and edges that might be penetrated by P (identified in the master surface analysis stage – because the master surface is rigid, this analysis can be done pre-operatively).

Further improvement of efficiency of the penetration detection algorithm and computation speed is done by implementing bucket sort [3, 53] in the global search phase.

## 9.7 Alternatives to Finite Element Method for Image-Guided Neurosurgery and Surgery Simulation: Meshless Algorithms

There are two important factors limiting the application of finite element methods for predicting brain responses in image-guided neurosurgery and surgery simulation:

1. Time-consuming generation of patient-specific finite element meshes of the brain and other body organs (more detailed discussion on generation of patient-specific computational grids is provided in Chap. 6).
2. Deterioration of the solution accuracy and instability as the elements undergo distortion (inversion) when surgical tools induce large deformations [31].

Meshless algorithms [55], in which the analyzed continuum is discretized by nodes (where forces and displacements are calculated) with no assumed structure on the interconnection of the nodes and integration points (where stresses and strains are calculated) (Fig. 9.4), have been proposed in the literature for generating computational grids of domains of complex geometry and providing reliable results for large deformations [56–58].

Smoothed particle hydrodynamics SPH is regarded as the first meshless method. It utilizes a strong form of equations of continuum mechanics, and the nodes are also the integration points [59]. SPH and other particle methods (such as material point method in which a weak form of equations of continuum mechanics is used) were applied in injury biomechanics [60, 61]. However, the literature indicates several important shortcomings of the SPH method. These include instabilities in tension and accuracy inferior to that of the finite element method [55]. Therefore, we

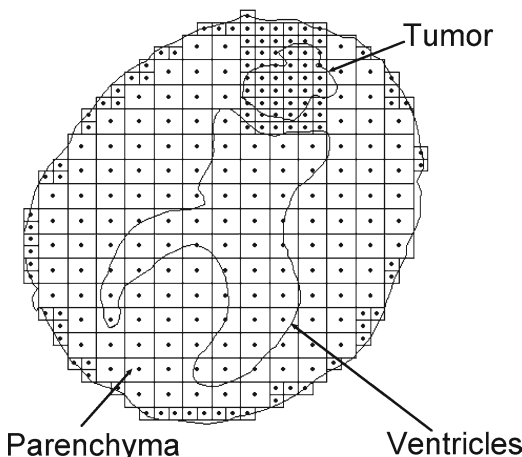


**Fig. 9.4** Background regular integration grid for a patient-specific meshless model of the brain with tumor. The integration points are indicated as *black dot*. Note that the background grid does not conform to the geometry boundary. Adapted from [69]

focus on meshless methods that utilize the weak form of the equations of continuum mechanics and background integration grid. As an example, we discuss the Meshless Total Lagrangian Explicit Dynamics algorithm [56] which is motivated by the need for simple, automatic model creation for real-time simulation.

### 9.7.1 *Meshless Total Lagrangian Explicit Dynamics (MTLED): Algorithm Description*

In the Meshless Total Lagrangian Explicit Dynamics (MTLED) algorithm, the integration of equations of continuum mechanics is done over a background grid of hexahedral cells with a single integration point per cell (the idea similar to the one used in under-integrated hexahedral elements described in Sect. 9.2) [56] (Fig. 9.4). As this grid does not have to conform to the boundary of the analyzed continuum, it can be generated automatically even for complicated geometry. The nodes where the displacements are calculated are independent of the background integration grid. Almost arbitrary placement of the nodes throughout the analyzed continuum can be used, which is well suited for complicated geometry. However, restrictions (discussed later) on the ratio of the number of integration points and nodes apply.

Construction of the shape functions is the crucial difference between the MTLED algorithm and the Total Lagrangian Explicit Dynamics (TLED) finite element algorithm described in Sect. 9.3. In the MTLED algorithm, we use Moving Least-Squares shape functions that were initially applied in the Diffuse Element Method by Nayroles et al. [62]:

$$\mathbf{u}^h(\mathbf{x}) = \mathbf{p}^T(\mathbf{x}) \cdot \mathbf{a}(\mathbf{x}), \quad (9.36)$$

where  $\mathbf{u}^h$  is the approximation of the displacement  $\mathbf{u}$ ,  $\mathbf{p}(\mathbf{x})$  is the vector of monomial basis function,  $\mathbf{a}(\mathbf{x})$  is the vector of coefficients that need to be calculated, and  $\mathbf{x}$  is the point belonging to the analyzed continuum but not located at the node. In the MTLED algorithm, low-order (up to quadratic order) monomial basis functions are used [56]:

$$\mathbf{p}^T(\mathbf{x}) = (1 | x \ y \ z | xy \ xz \ yz | x^2 \ y^2 \ z^2). \quad (9.37)$$

It has been shown that for a stable solution, the nodal support domains need to overlap (i.e. a given node must belong to more than one support domain) and that the number of nodes in a given support domain should be approximately twice the length of the vector of basis functions [56] (for (9.37) the possible vector lengths are 4 for linear basis functions and 10 for quadratic ones). Therefore, from the perspective of solution accuracy, stability and computation efficiency, a trade-off exists between the number of nodes and the total number of integration points. Through parametric study, it has been estimated in [56] that the number of integration points should be twice the number of nodes to ensure accuracy and convergence. According to [56], increasing the number of integration points beyond this ratio exerts negligible effects on the results.

## 9.8 Real-Time Computations without Supercomputers: Increasing Computation Speed Through Algorithm Implementation on Graphics Processing Unit (GPU)

The algorithms for surgery simulation and image-guided surgery discussed in this chapter facilitate efficient and robust computations. For instance, they make it possible to compute the deformation field within the brain for an image registration problem in under 40 s on a standard personal computer for non-linear finite element models consisting of around 30,000 elements. However, predicting the time history of the force between the soft tissue and the surgical tool at a frequency of 500 Hz (required for haptic feedback) poses a challenge even for very efficient non-linear algorithms deployed on a personal computer.

For hardware-based increase of computation speed, we advocate the implementation of our algorithms on graphics processing units (GPUs). This is done by using a GPU as a coprocessor for the computer's central processing unit (CPU) for executing sections of the code that can be run in parallel. Before the introduction of NVIDIA's Compute Unified Device Architecture (CUDA), general-purpose computations on GPUs were done by recasting the computations in graphic terms and using the graphics pipeline [63]. Therefore, a scientific or general-purpose computation often required a concerted effort by experts in both computer graphics and in the particular scientific or engineering domain. With the introduction of CUDA, in November 2006, NVIDIA proposed a new parallel programming model and instruction set for their GPUs that can be used for performing general-purpose computations. CUDA comes with a software environment that allows developers to use C as a high-level programming language. A minimum set of keywords are used to extend the C language in order to: identify the code that must be run on the GPU as parallel threads, identify each thread (and the block of threads it belongs to) and to organize and transfer the data in the different GPU memory spaces. CUDA also exposes the internal architecture of the GPU and allows direct access to its internal resources. The programmer has more control over the internal hardware resources of the GPU, but this comes at the expense of an increased programming effort compared to a CPU implementation.

The GPU has a highly parallel, multithreaded, many core processor architecture and its cost (under US\$3,000 for a general-purpose GPU) is orders of magnitude smaller than that of a supercomputer with a comparable number of parallel threads. GPU architecture is well suited for problems that can be expressed as data-parallel computations with high arithmetic intensity, where the same program is executed on many data elements in parallel. CUDA is a general purpose parallel computing architecture that allows the development of application software that transparently scales with the number of processor cores in the GPU.

Because it only uses vectors, an explicit integration algorithm is perfectly suited for parallel implementation on a GPU. We implemented the Dynamic Relaxation algorithm presented in Sect. 9.4 – on GPU using CUDA. We transferred all the computationally intensive parts of the algorithm (element force computation, displacement vector computation, contact handling, parallel reduction – including infinity norm computation and scalar product of vectors) to the GPU, to take advantage

of its massive parallelism. The code was run on a NVIDIA Tesla C870 computing board, which has 16 multiprocessors with eight scalar processor cores each and single-precision floating-point operations. A detailed description of the implementation can be found in [64]. The GPU implementation performs 2,000 iterations of the brain shift simulation in 1.8 s, offering real-time computation capabilities.

## 9.9 Algorithm Verification

The general guidelines for verification in computational solid mechanics have been proposed by the American Society of Mechanical Engineers ASME in [65]. These guidelines underscore the importance of establishing confidence through collection of evidence that the solution algorithms are working correctly. As for non-linear problems of computational solid mechanics, analytical solutions typically do not exist. Therefore, we advocate collecting such evidence by comparing the results obtained through new algorithms with the solutions from established algorithms (such as those implemented in commercial finite element codes).

In the following sections, we will present verification results for some of the algorithms described in this chapter: hourglass control, volumetric locking, dynamic relaxation and brain–skull interaction (contact).

### 9.9.1 Hourglass Control

This verification experiment was artificially designed to compound difficulties associated with hourglass control: large deformations, bending and rigid body motions. A column having a height of 1 m and a square section with the side size 0.1 m was meshed using hexahedral elements (Fig. 9.5a). The mesh has 496 nodes and 270 elements. A Neo-Hookean almost incompressible material model was used, having the mechanical properties similar to those of the brain (mass density of 1,000 kg/m<sup>3</sup>, Young's modulus in undeformed state equal to 3,000 Pa and Poisson's ratio 0.49).

The deformation was imposed by constraining the lower face and displacing the upper face of the column, with maximum displacements of 0.5 m in the  $x$  direction and 0.3 m in the  $z$  direction.

The deformed shape obtained using the TLED algorithm is presented in Fig. 9.5b for the under-integrated hexahedral elements with no hourglass control. The influence of the presented hourglass control mechanism can be clearly seen in Fig. 9.5c.

The displacements of a line of nodes from the side of the column (in the plane  $y=0$ ) are presented in Fig. 9.6. These displacements are compared with the results obtained using the commercial finite element software ABAQUS (fully integrated linear hexahedral elements with hybrid displacement-pressure formulation).

The displacement maximum relative error, defined as the ratio between the maximum displacement difference and the imposed displacement, was 1.4% in the case of column deformation. This demonstrates the good accuracy of the elements using the proposed hourglass control mechanism.

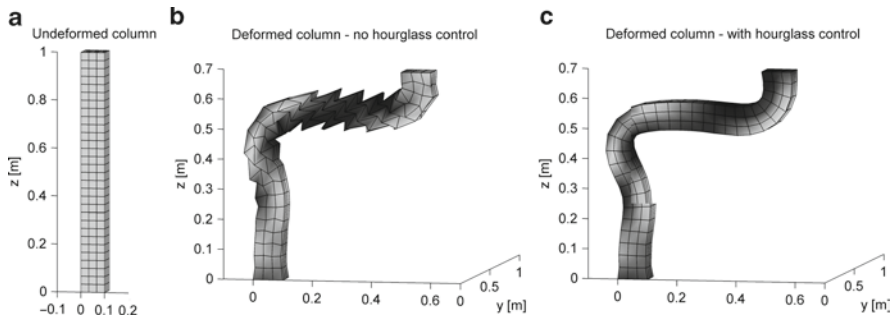


**Fig. 9.5** Verification of hourglass control algorithm using deformation of a column as an example. (a) Undeformed shape; (b) deformed shape with no hourglass control; and (c) deformed shape with successful hourglass control. Copied from [49]

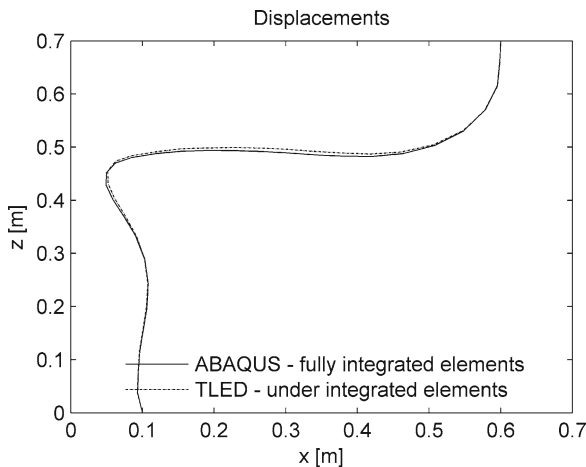


**Fig. 9.6** Deformation of a column (*middle line displacements*). Comparison of results between TLED and ABAQUS finite element solver. Copied from [49]

### 9.9.2 Volumetric Locking

Because the only difference between our improved ANP (IANP) element and the standard ANP element consists in the way interfaces between different materials are handled, we designed a simulation experiment that highlights these differences. We considered a cylinder with a diameter of 0.1 m and a height of 0.2 m made out of alternating sections with two different material properties, as shown in Table 9.1. We used a Neo-Hookean material model for both materials.

Half of the nodes on the upper face of the cylinder were displaced in order to create a complex deformation field at different material interfaces (Fig. 9.7a).

Using the cylindrical geometry, we created a hexahedral mesh (13,161 nodes and 12,000 elements) and a tetrahedral mesh (11,153 nodes and 60,030 elements). The behavior of the following elements was compared:

**Table 9.1** Material properties

Property	Material 1	Material 2
Young's modulus $E$ [Pa]	3,000	30,000
Poisson ratio $\nu$	0.49	0.48
Density $\rho$ ( $\text{kg}/\text{m}^3$ )	1,000	1,000

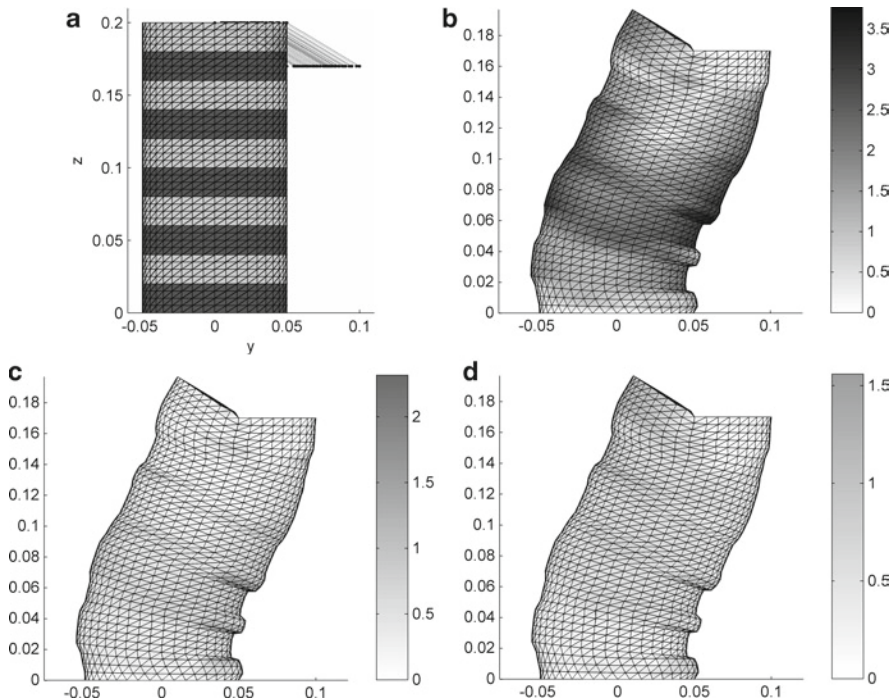


**Fig. 9.7** Deformation of a cylinder made out of sections with different material properties. (a) The undeformed configuration and the nodal displacements applied. The color bars show the difference in positions of the surface nodes, in millimeters, between the models using hexahedral elements and models using (b) locking tetrahedral elements (c) ANP elements and (d) IANP elements. Copied from [34]

1. Fully integrated linear hexahedra, with selectively reduced integration of the volumetric term (Hexa), which should offer a benchmark solution [66]
2. Standard average nodal pressure elements (ANP)
3. Our improved average nodal pressure elements (IANP)
4. Linear standard tetrahedron (Tetra)

All the computations were done using the TLED algorithm. Based on the displacement differences presented in Fig. 9.7, we note that the usage of standard locking tetrahedral elements can lead to errors of up to 3.8 mm in the deformation field. The use of ANP elements reduces the maximum error to 2.3 mm, while the use of IANP elements leads to a maximum error of 1.5 mm (all errors are considered relative to the results of the model that uses Hexa elements).

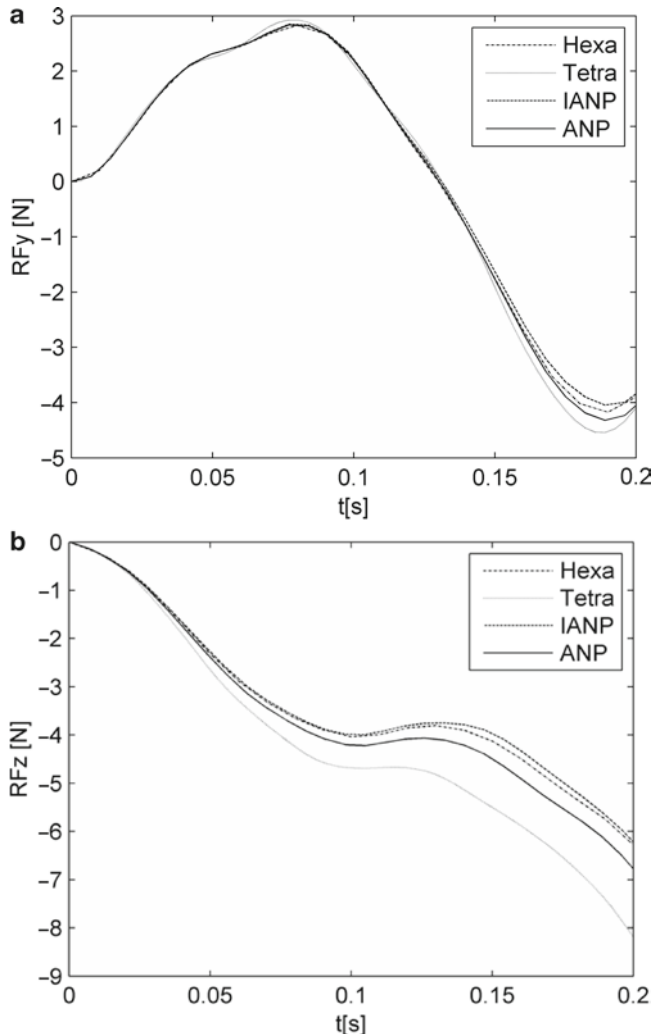


**Fig. 9.8** Reaction forces on the displaced face (a) in the  $y$  direction (b) in the  $z$  direction. Adapted from [34]

The reaction forces computed on the displaced face are presented in Fig. 9.8. The results obtained using the IANP elements are the closest to the benchmark results given by the Hexa elements. Therefore, the IANP elements offer the best performances both in terms of displacements and reaction forces, while the standard tetrahedral element offers the worst performances, as expected.

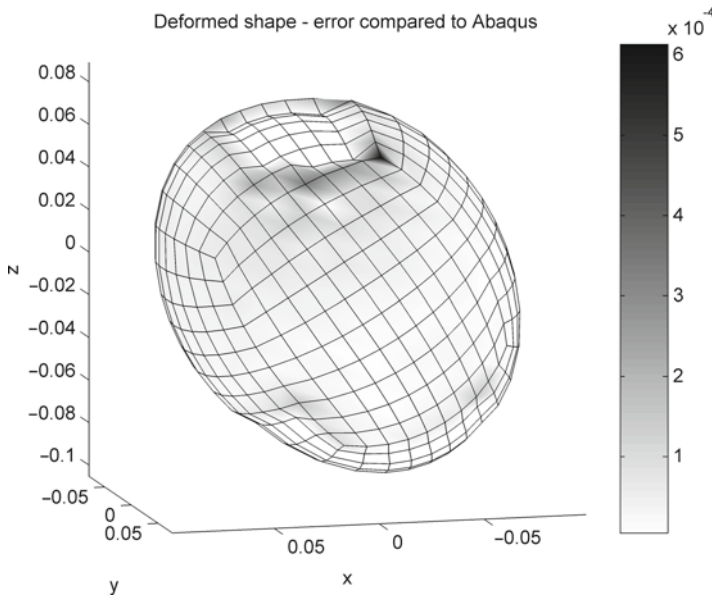


**Fig. 9.9** Absolute difference (gray-scale coded) in nodal positions between our algorithm and ABAQUS. Dimensions are in meters. Copied from [36]

### 9.9.3 Dynamic Relaxation: Steady-State Computation

We use this verification example to demonstrate the accuracy of our steady-state computation method. For an ellipsoid having approximately the size of the brain, we fixed a set of nodes (at the bottom) and displaced another set of nodes (at the top) in order to obtain a deformation field similar to what happens in brain shift. The mesh was created using hexahedral elements and has 2,200 elements and 2,535 nodes. We used an almost incompressible Neo-Hookean material model and a large displacement value (2 cm).

We performed the displacement computation first by using our algorithm and second by using ABAQUS [26]. For computational efficiency, we use under-integrated hexahedral elements with the hourglass control implementation based on the relations presented in [49]. In ABAQUS, we used hybrid displacement-pressure hexahedral elements, which are the “gold standard” for almost incompressible materials. We used the static solver with the default configuration and assumed that the ABAQUS simulation provides accurate results.

The error distribution (absolute difference in nodal position between the two simulations) is presented in Fig. 9.9. The maximum error magnitude of 0.6 mm is obtained at the edge of the displaced area and it is mainly an artifact of using under-integrated elements. Nevertheless, the average error is 0.025 mm which demonstrates that our simulation results are more than acceptable (as the error is much smaller than the accuracy of image-guided neurosurgery).

### 9.9.4 Brain–Skull Interface: Contact Algorithm

In order to assess the performance of our brain–skull interface algorithm, we performed simulations using our implementation of the contact algorithm (combined with Dynamic Relaxation as a solution method) and the commercial finite element solver LS-DYNA [3], and compared the results. The same loading conditions and material models were used for both solvers. The loading consisted of displacements applied to the nodes in the craniotomy area using a smooth loading curve. Neo-Hookean material models were used for the brain and tumor tissues, and a linear elastic model was used for the ventricles. In order to obtain the steady-state solution, the oscillations were damped using both mass and stiffness proportional damping in LS-DYNA.

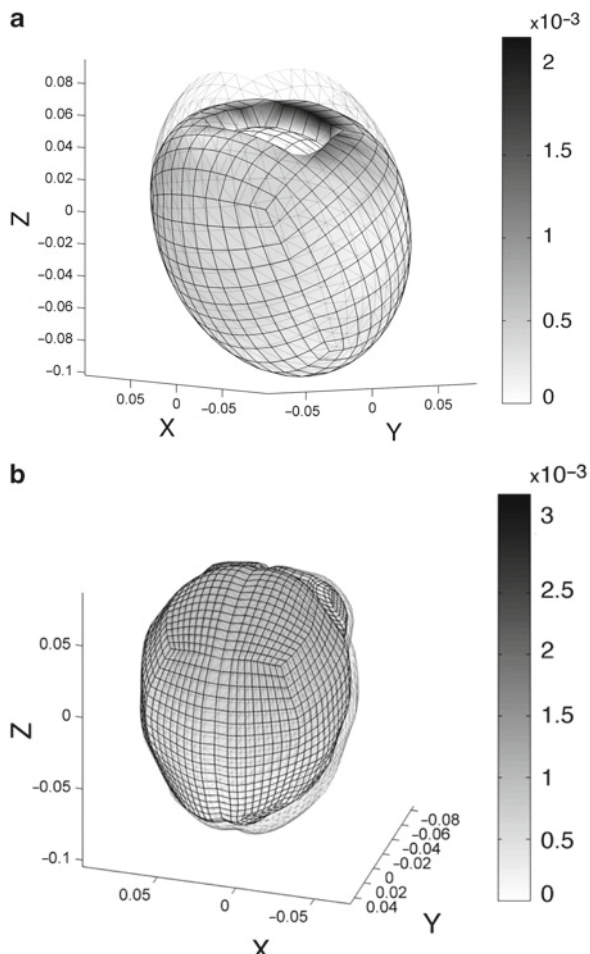


**Fig. 9.10** Displacement differences (in millimeters) between our results and LS-DYNA simulations are presented using color codes. The transparent mesh is the master contact. **(a)** Ellipsoid model; **(b)** brain model. Adapted from [54]

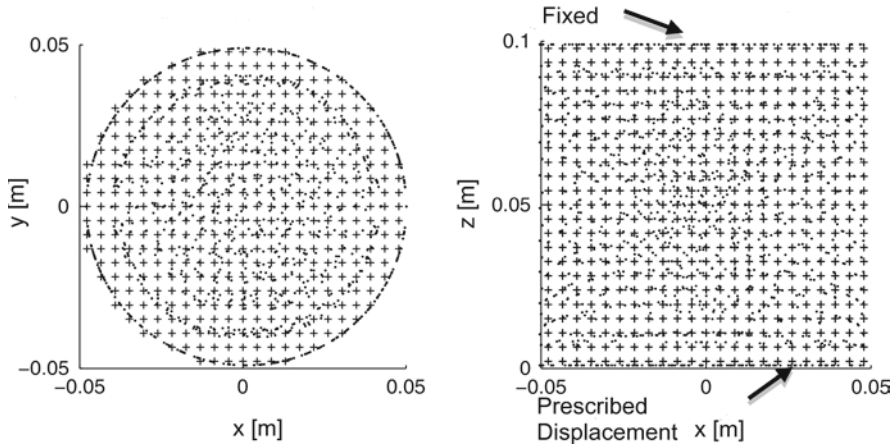


**Fig. 9.11** Meshless model of a cylinder used in verification of the MTLED algorithm by Horton et al. [56]. The nodes are indicated as *dot* and integration points as *plus*. Note almost arbitrary node placement. The integration points do not conform to geometry. The boundary conditions are shown in the *right-hand side* figure: the nodes on the *top boundary* were constrained and the prescribed displacement was applied to the nodes on the *bottom boundary*. Adapted from [56]

In a first simulation experiment, we displaced an ellipsoid (made of a hyperelastic Neo-Hookean material) with the approximate size of a brain inside another ellipsoid simulating the skull. The maximum displacement applied was 40 mm. The average difference in the nodal displacement field between our simulation and the LS-DYNA simulation was less than 0.12 mm (Fig. 9.10a).

In the second simulation experiment, we performed the registration of a patient-specific brain shift. The LS-DYNA simulations for this case have been done previously and the results were found to agree well with the real deformations [67]. We performed the same simulations using Dynamic Relaxation and our contact algorithm. The average difference in the nodal displacement field was less than 0.2 mm (Fig. 9.10b).

### 9.9.5 Meshless Total Lagrangian Explicit Dynamics (MTLED) Algorithm

The MTLED algorithm has been verified by comparing the results obtained using this algorithm with those of an established finite element code (ABAQUS implicit nonlinear solver was used) when modeling semi-confined uniaxial compression and shear of a cylinder made from a very soft (shear modulus of 1 kPa) hyperelastic (Neo-Hookean) material. In meshless discretization of the cylinder, almost arbitrary node placement and integration points non-conforming to geometry were used (Fig. 9.11).

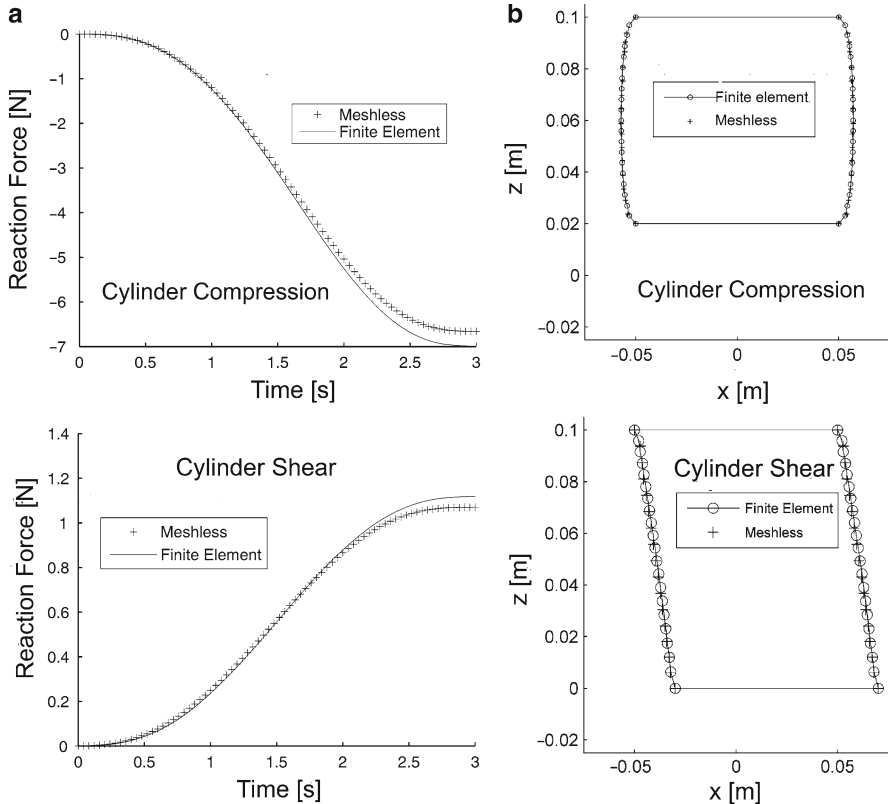


**Fig. 9.12** Comparison of the results obtained when modeling 20% compression and shear of a cylinder using meshless (MTLED) and finite element (ABAQUS implicit solver) algorithms. (a) Reaction force vs. time; (b) contour of the deformed cylinder at time of 3 s. The displacement  $u$  was enforced over a period  $T=3$  s using a 3-4-5 polynomial that ensures zero velocity and acceleration at time  $t=0$  and time  $t=T$  [70]. The displacement magnitude was 0.02 in  $z$  direction for compression and 0.02 in  $x$  direction for shear.  $x$  and  $z$  directions are defined in Fig. 9.11. Adapted from [56]

For 20% compression and shear of the cylinder, the difference in the total reaction force on the displaced cylinder surface between MTLED and ABAQUS implicit finite element solver was no more than 5% (Fig. 9.12a). The forces obtained using the meshless algorithm were qualitatively similar to those of the finite element method. The maximum relative difference in displacement between MTLED and ABAQUS was around 3.5% (it can be seen in Fig. 9.12b that some of the meshless nodes do not sit exactly on the deformed finite element boundary).

The MTLED algorithm produces stable results even for very large deformations as indicated by the energy – time histories obtained when modeling the cylinder compressed to 20% of its original height (Fig. 9.13). For such large compression, no verification against the ABAQUS finite solver could be done as the finite element solution became unstable.

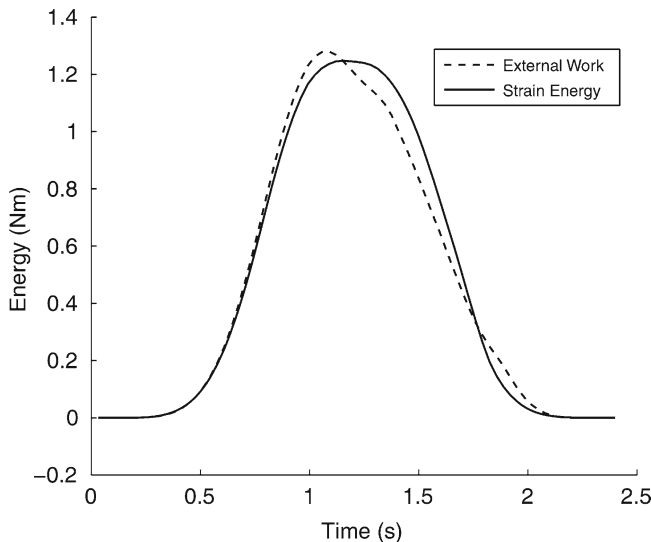


**Fig. 9.13** MTLED algorithm. External work and strain energy when compressing a cylinder to 20% of its original height (and returning to the initial state). The displacement was enforced using a 3-4-5 polynomial [70]. Adapted from [56]

## 9.10 Conclusions

Modeling of the brain for injury simulation and computer-assisted neurosurgery is a non-linear problem of continuum mechanics and involves large deformations, very large strains, non-linear material models, complex loading and boundary conditions and complex geometry. Various finite element (FE) algorithms have been applied for solving this problem.

Modeling of the brain for injury simulation has been often conducted with the idea in mind that numerical surrogates of the human head can be used in the design of countermeasures for traumatic brain injury mitigation. Such modeling has been almost exclusively conducted using non-linear explicit dynamics (i.e. utilizing explicit integration in time domain) finite element algorithms implemented in commercial finite element codes that are routinely used in the automotive industry for transient dynamics problems involving rapid (impact-type) loading such as car structure responses during collision and metals sheet forming.

However, the computational efficiency of the algorithms available in commercial finite element codes is insufficient for computer-integrated neurosurgery where the solution needs to be provided within the real-time constraints of neurosurgery. This led to development of specialized non-linear finite element algorithms aiming at satisfying these constraints. We advocate the application of non-linear finite element algorithms utilizing explicit integration in the time domain (and therefore requiring no iteration for non-linear problems) and Total Lagrangian incremental

formulation of continuum mechanics (as it allows pre-computing of the derivatives with respect to the spatial coordinates):

- Total Lagrangian explicit dynamics (TLED) finite element algorithm for time accurate solution for surgery simulation.
- Dynamic Relaxation (DR) Total Lagrangian algorithm for computing steady-state deformations for neurosurgical modeling.

For hardware-based increase of computation speed, we propose the implementation of these algorithms on graphics processing units (GPUs) by using a GPU as a coprocessor for the computer's CPU. It has been shown in [64] that the implementation of the finite element Dynamic Relaxation algorithm on NVIDIA Tesla C870 GPU performs 2,000 iterations of the brain shift simulation in under 2 s, offering real-time computation capabilities at a fraction of a traditional supercomputer or PC cluster cost. It can be expected that for newer generation of GPUs this already excellent performance would appreciably improve due to significant increase in the number of streaming processor cores (e.g. NVIDIA Tesla C870 GPU had 128 cores while NVIDIA Fermi GPUs released in 2009 have 512 cores [68]) and available shared memory (e.g. 16 kb for NVIDIA Tesla and 48 kb for NVIDIA Fermi).

Application of the most efficient finite element algorithms in surgery simulation and neurosurgery modeling is limited by time-consuming generation of patient-specific finite element meshes and deterioration of the solution accuracy when the elements undergo distortion induced by large deformations. As a solution for overcoming these limitations, we advocate meshless algorithms in which the computational grid has the form of a “cloud” of points. The Meshless Total Lagrangian Explicit Dynamics (MTLED) algorithm described in this chapter has been proven to be capable of providing a stable solution in situations (such as compressing of a cylinder made of soft hyperelastic material to 20% of its original height) where the well-established and extensively verified non-linear finite element algorithms fail.

The instabilities due to element distortion are not limited to simulation and neurosurgery modeling using finite element algorithms. They are even more pronounced in modeling for injury simulation where the brain is exposed to transient loads due to rapid acceleration and/or direct impact to the head. Therefore, although the Meshless Total Lagrangian Explicit Dynamics algorithm described in this chapter was developed in the context of real-time patient-specific surgery simulation, its ability to provide a stable solution for very large strains is relevant also for injury simulation. Development of meshless algorithms that facilitate modeling of surgical dissection and injury-related rupture of soft tissues provides the next challenge in injury and surgery simulation.

**Acknowledgements** The financial support of the Australian Research Council (grants no. DP0343112, DP0664534, DP1092893 and LX0560460) and NIH (grant no. R03-CA126466-01A1) is greatly acknowledged.

We thank our collaborators Dr Ron Kikinis and Dr Simon K. Warfield of Harvard Medical School (Boston, MA, USA), and Dr Kiyoyuki Chinzei and Dr Toshikatsu Washio of Surgical Assist Technology Group of AIST (Tsukuba, Japan) for help in various aspects of this work.

## References

1. Fressmann, D., Munz, T., Graf, O., et al.: FE human modelling in crash – aspects of the numerical modelling and current applications in the automotive industry. LS-DYNA Anwenderforum. DYNAmore GmbH, Frankenthal, Germany, pp. F-I-23–F-I-34 (2007)
2. Takhounts, E.G., Eppinger, R.H., Campbell, J.Q., et al.: On the development of the SIMon finite element head model. *Stapp Car Crash J.* **47**, 107–133 (2003)
3. Hallquist, J.O.: LS-DYNA Theory Manual. Livermore Software Technology Corporation, Livermore (2005)
4. PSI: Pam-System Programs in Applied Mechanics. PAM-CRASH, PAM-SAFE Version 1998. Release Note. ESI Group Software Product Company (1998)
5. Mecalog: RADIOSS Users' Manual, Paris, France (1994)
6. Baumann, R., Glauser, D., Tappy, D., et al.: Force feedback for virtual reality based minimally invasive surgery simulator. *Stud. Health Technol. Inform.* **29**, 564–579 (1996)
7. Cover, S.A., Ezquerra, N.F., O'Brien, J.F., et al.: Interactively deformable models for surgery simulation. *IEEE Comput. Graph. Appl.* **13**, 68–75 (1993)
8. Kühnapfel, U., Çakmak, H.K., Maaß, H.: Endoscopic surgery training using virtual reality and deformable tissue simulation. *Comput. Graph.* **24**, 671–682 (2000)
9. Cotin, S., Delingette, H., Ayache, N.: A hybrid elastic model for real-time cutting, deformations, and force feedback for surgery training and simulation. *Vis. Comput.* **16**, 437–452 (2000)
10. Bathe, K.-J.: Finite Element Procedures. Prentice-Hall, New Jersey (1996)
11. Bro-Nielsen, M.: Finite element modeling in surgery simulation. *Proc. IEEE* **86**, 490–503 (1998)
12. Bro-Nielsen, M., Cotin, S.: Real-time volumetric deformable models for surgery simulation using finite elements and condensation. *Comput. Graphics Forum* **15**, 57–66 (1996)
13. DiMaio, S.P., Salcudean, S.E.: Interactive simulation of needle insertion models. *IEEE Trans. Biomed. Eng.* **52**, 1167–1179 (2005)
14. Warfield, S.K., Talos, F., Tei, A., et al.: Real-time registration of volumetric brain MRI by biomechanical simulation of deformation during image guided neurosurgery. *Comput. Vis. Sci.* **5**, 3–11 (2002)
15. Roberts, D.W., Hartov, A., Kennedy, F.E., et al.: Intraoperative brain shift and deformation: a quantitative analysis of cortical displacement in 28 cases. *Neurosurgery* **43**, 749–758 (1998)
16. Miller, K., Wittek, A.: Neuroimage registration as displacement – zero traction problem of solid mechanics (lead lecture). In: Miller, K., Poulikakos, D. (eds.) *Proc. of Computational Biomechanics for Medicine I. Workshop affiliated with Medical Image Computing and Computer-Assisted Intervention MICCAI 2006*, Copenhagen, Denmark, 1st October p. 2–13, Samfunds litteratur Grafik, Copenhagen, ISBN 10: 87-7611-149-0 (2006)
17. Wittek, A., Hawkins, T., Miller, K.: On the unimportance of constitutive models in computing brain deformation for image-guided surgery. *Biomech. Model. Mechanobiol.* **8**, 77–84 (2009)
18. Belytschko, T.: A survey of numerical methods and computer programs for dynamic structural analysis. *Nucl. Eng. Des.* **37**, 23–34 (1976)
19. Bathe, K.-J.: Crush simulation of cars with FEA. Mechanical engineering <http://www.memagazine.org/backissues/november98/features/crushcar.html> (1998)
20. Cook, R.D., Malkus, D.S., Plesha, M.E.: Finite elements in dynamics and vibrations. In: Concepts and Applications of Finite Element Analysis, pp. 367–428. Wiley, New York (1989)
21. Hallquist, J.O.: LS-DYNA Theoretical Manual. Livermore Software Technology Corporation, Livermore (1998)
22. Belytschko, T.: An overview of semidiscretization and time integration procedures. In: Belytschko, T., Hughes, T.J.R. (eds.) *Computational Methods for Transient Analysis*, vol. 1, pp. 1–66. North-Holland, Amsterdam (1983)
23. Dassault Systèmes Simulia Corp.: ABAQUS Theory Manual Version 6.5, Providence, RI, USA (2010)
24. Olovsson, L., Simonsson, K., Unosson, M.: Selective mass scaling for explicit finite element analyses. *Int. J. Numer. Methods Eng.* **63**, 1436–1445 (2005)

25. Majumder, S., Roychowdhury, A., Subrata, P.: Three-dimensional finite element simulation of pelvic fracture during side impact with pelvis-femur-soft tissue complex. *Int. J. Crashworthiness* **13**, 313–329 (2008)
26. Hibbit, D., Karlsson, B., Sorensen, P.: Abaqus Analysis User's Manual Version 6.5. ABAQUS Inc., Providence, RI (2005)
27. Flanagan, D.P., Belytschko, T.: A uniform strain hexahedron and quadrilateral with orthogonal hourglass control. *Int. J. Numer. Methods Eng.* **17**, 679–706 (1981)
28. Cifuentes, A.O., Kalbag, A.: A performance study of tetrahedral and hexahedral elements in 3-D finite element structural analysis. *Finite Elem. Anal. Des.* **12**, 313–318 (1992)
29. Cook, R.D., Malkus, D.S., Plesha, M.E.: Concepts and Applications of Finite Element Analysis. Wiley, New York (1989)
30. Hughes, T.J.R.: The Finite Element Method: Linear Static and Dynamic Finite Element Analysis. Dover, Mineola (2000)
31. Wittek, A., Dutta-Roy, T., Taylor, Z., et al.: Subject-specific non-linear biomechanical model of needle insertion into brain. *Comput. Methods Biomed. Eng.* **11**, 135–146 (2008)
32. Rojek, J., Oñate, E., Postek, E.: Application of explicit FE codes to simulation of sheet and bulk metal forming processes. *J. Mater. Process. Technol.* **80–81**, 620–627 (1998)
33. Miller, K., Joldes, G., Lance, D., et al.: Total Lagrangian explicit dynamics finite element algorithm for computing soft tissue deformation. *Commun. Numer. Methods Eng.* **23**, 121–134 (2007)
34. Joldes, G.R., Wittek, A., Miller, K.: Non-locking tetrahedral finite element for surgical simulation. *Commun. Numer. Methods Eng.* **25**, 827–836 (2009)
35. Underwood, P.: Dynamic relaxation. In: Belytschko, T., Hughes, T.J.R. (eds.) Computational Methods for Transient Analysis, vol. 1, pp. 245–265. New-Holland, Amsterdam (1983)
36. Joldes, G.R., Wittek, A., Miller, K.: Computation of intra-operative brain shift using dynamic relaxation. *Comput. Meth. Appl. Mech. Eng.* **198**, 3313–3320 (2009)
37. Hughes, T.J.R.: Analysis of transient algorithms with particular reference to stability behavior. In: Belytschko, T., Hughes, T.J.R. (eds.) Computational Methods for Transient Analysis, vol. 1, pp. 67–155. New-Holland, Amsterdam (1983)
38. Miller, K.: Biomechanics of the Brain for Computer Integrated Surgery. Publishing House of Warsaw University of Technology, Warsaw (2002)
39. Miller, K., Chinzei, K.: Mechanical properties of brain tissue in tension. *J. Biomech.* **35**, 483–490 (2002)
40. Miller, K., Chinzei, K., Orssengo, G., et al.: Mechanical properties of brain tissue in-vivo: experiment and computer simulation. *J. Biomech.* **33**, 1369–1376 (2000)
41. Miller, K.: Constitutive modelling of abdominal organs. *J. Biomech.* **33**, 367–373 (2000)
42. Miller, K., Chinzei, K.: Constitutive modelling of brain tissue; experiment and theory. *J. Biomech.* **30**, 1115–1121 (1997)
43. Bilston, L.E., Liu, Z., Phan-Tien, N.: Linear viscoelastic properties of bovine brain tissue in shear. *Biorheology* **34**, 377–385 (1997)
44. Margulies, S.S., Thibault, L.E., Gennarelli, T.A.: Physical model simulations of brain injury in the primate. *J. Biomech.* **23**, 823–836 (1990)
45. Bonet, J., Burton, A.J.: A simple averaged nodal pressure tetrahedral element for incompressible and nearly incompressible dynamic explicit applications. *Commun. Numer. Methods Eng.* **14**, 437–449 (1998)
46. Bonet, J., Marriott, H., Hassan, O.: An averaged nodal deformation gradient linear tetrahedral element for large strain explicit dynamic applications. *Commun. Numer. Methods Eng.* **17**, 551–561 (2001)
47. Zienkiewicz, O.C., Rojek, J., Taylor, R.L., et al.: Triangles and tetrahedra in explicit dynamic codes for solids. *Int. J. Numer. Methods Eng.* **43**, 565–583 (1998)
48. Dohrmann, C.R., Heinstein, M.W., Jung, J., et al.: Node-based uniform strain elements for three-node triangular and four-node tetrahedral meshes. *Int. J. Numer. Methods Eng.* **47**, 1549–1568 (2000)
49. Joldes, G.R., Wittek, A., Miller, K.: An efficient hourglass control implementation for the uniform strain hexahedron using the total Lagrangian formulation. *Commun. Numer. Methods Eng.* **24**, 315–323 (2008)

50. Hallquist, J.O., Goudreau, G.L., Benson, D.J.: Sliding interfaces with contact-impact in large-scale Lagrangian computations. *Comput. Meth. Appl. Mech. Eng.* **51**, 107–137 (1985)
51. Doghri, I., Muller, A., Taylor, R.L.: A general three-dimensional contact procedure for implicit finite element codes. *Eng. Comput.* **15**, 233–259 (1998)
52. Stewart, J.R., Gullerud, A.S., Heinstein, M.W.: Solution verification for explicit transient dynamics problems in the presence of hourglass and contact forces. *Comput. Meth. Appl. Mech. Eng.* **195**, 1499–1516 (2006)
53. Sauvé, R.G., Morandin, G.D.: Simulation of contact in finite deformation problems – algorithm and modelling issues. *Int. J. Mech. Mater. Des.* **1**, 287–316 (2004)
54. Joldes, G., Wittek, A., Miller, K., et al.: Realistic and efficient brain-skull interaction model for brain shift computation. In: Miller, K., Nielsen, P.M.F. (eds.) *Proceedings of Computational Biomechanics for Medicine III*. Workshop affiliated with International Conference on Medical Image Computing and Computer-Assisted Intervention MICCAI 2008, New York, USA, pp. 95–105, September 2008
55. Belytschko, T., Krongauz, Y., Organ, D., et al.: Meshless methods: an overview and recent developments. *Comput. Meth. Appl. Mech. Eng.* **139**, 3–47 (1996)
56. Horton, A., Wittek, A., Joldes, G.R., et al.: A meshless total Lagrangian explicit dynamics algorithm for surgical simulation. *Int. J. Numer. Methods Biomed. Eng.* **26**, 977–998 (2010)
57. Doblaré, M., Cueto, E., Calvo, B., et al.: On the employ of meshless methods in biomechanics. *Comput. Meth. Appl. Mech. Eng.* **194**, 801–821 (2005)
58. Horton, A., Wittek, A., Miller, K.: Subject-specific biomechanical simulation of brain indentation using a meshless method. *Proc. of International Conference on Medical Image Computing and Computer-Assisted Intervention MICCAI 2007*; In *Lect. Notes Comput. Sci.* **4791**, 541–548 (2007)
59. Monaghan, J.J.: Smoothed particle hydrodynamics. *Annu. Rev. Astron. Astrophys.* **30**, 543–574 (1992)
60. Lee, S.-H., Darvish, K., Lobovsky, L.: Fluid-structure interaction in finite element modeling of traumatic aortic rupture. *ASME Conference Proceedings ASME 2004, Advances in Bioengineering*, Anaheim, CA, USA, pp. 337–338, 13–19 November 2004
61. Ionescu, I., Guilkey, J., Berzins, M., et al.: Computational simulation of penetrating trauma in biological soft tissues using the material point method. *Stud. Health Technol. Inform.* **111**, 213–218 (2005)
62. Nayroles, B., Touzot, G., Villon, P.: Generalizing the finite element method: diffuse approximation and diffuse elements. *Comput. Mech.* **10**, 307–318 (1992)
63. Owens, J.D., Luebke, D., Govindaraju, N., et al.: A survey of general-purpose computation on graphics hardware. *Comput. Graphics Forum* **26**, 80–113 (2007)
64. Joldes, G.R., Wittek, A., Miller, K.: Real-time nonlinear finite element computations on GPU – Application to neurosurgical simulation. *Comput. Meth. Appl. Mech. Eng.* **199**, 3305–3314 (2010)
65. ASME PTC 60/V&V 10: Guide for Verification and Validation in Computational Solid Mechanics. The American Society of Mechanical Engineers (ASME) Standards Committee on Verification and Validation in Computational Solid Mechanics PTC 60/V&V 10. <http://cstools.asme.org/csconnect/pdf/CommitteeFiles/24816.pdf> (2006)
66. ABAQUS: ABAQUS Theory Manual, Version 5.8. Hibbit, Karlsson & Sorensen, Inc., Rhode Island (1998)
67. Wittek, A., Miller, K., Kikinis, R., Warfield, S.K.: Patient-specific model of brain deformation: application to medical image registration. *J. Biomech.* **40**, 919–929 (2007)
68. NVIDIA: NVIDIA's Next Generation CUDA Compute Architecture: Fermi. NVIDIA. [http://www.nvidia.com/content/PDF/fermi\\_white\\_papers/NVIDIA\\_Fermi\\_Compute\\_Architecture\\_Whitepaper.pdf](http://www.nvidia.com/content/PDF/fermi_white_papers/NVIDIA_Fermi_Compute_Architecture_Whitepaper.pdf) (2009)
69. Horton, A., Wittek, A., Miller, K.: Computer simulation of brain shift using an element free Galerkin method. In: Middleton, J., Jones, M. (eds.) *7th International Symposium on Computer Methods in Biomechanics and Biomedical Engineering CMBEE 2006*, Antibes, France (2006)
70. Waldron, K.J., Kinzel, G.L.: *Kinematics, Dynamics, and Design of Machinery*. Wiley, New York (1999)



# Index

## A

Accuracy, 44, 49, 54, 59, 97, 99, 101, 107, 112, 114, 115, 122–124, 128, 130, 150, 174, 177, 180, 181, 185, 190, 191, 198, 201, 204, 205, 207, 211, 216  
Acquisition paradigms, 49, 59  
Almansi strain, 119  
Amygdala (amygdaloid body), 13, 35  
Anatomical landmarks, 41, 44, 48, 50, 57, 119  
Anatomy, 2, 5–36, 42, 49, 50, 106, 112, 175, 180  
Angular gyrus, 11, 53, 56  
Anisotropy, 44, 47, 56, 83  
Anterior commissure, 15, 16, 18, 32, 34  
Anterior communicating artery, 26, 32  
Aqueduct, 13, 138, 160, 161, 163, 171, 174, 176, 177, 179, 180, 185  
Arterial system, 22, 24–29  
Association tracts, 30, 33–35  
Atay, S.M., 75  
Atrium (or trigon), 14  
Auditory radiations, 34, 35  
Axons, 8, 69, 96

## B

Baledent, O., 137  
Bandak, F.A., 103  
Basal ganglia (nuclei)  
  caudate nucleus, 13, 34  
  lentiform nuclei  
    globus pallidus  
    lateral (or outer) segment, 13, 34–35  
    medial (or inner) segment, 13, 15, 34–35  
  putamen, 13, 34

Basilar artery, 24, 25, 171, 181

Berger, M.S., 44  
Bilston, L.E., 69, 72, 73, 75, 77–80, 182, 184, 185

Biological variability,

Biomechanics, 1–3, 69, 92, 93, 113–123, 189–216

Biorheology,

Body (or central portion), 5, 13, 14, 32, 69, 86, 101, 104, 117–119, 159, 170, 190, 191, 194, 203, 204, 207

Bonet, J., 202

Boundary conditions, 92, 93, 101, 112–114, 116–117, 119, 125–127, 174–181, 184, 185, 189, 194, 196, 213, 215

Brain

  atrophy, 154–155  
  injury, 3, 69–71, 86, 91, 93, 102, 104–107, 123, 138, 189, 190, 192, 215  
  parcellation, 6–10  
  swelling, 102  
  tumor, 41, 46–58, 86, 116

Brainstem, 6, 9, 30, 34, 35, 97

Burton, A.J., 202

## C

Callosomarginal artery, 24  
Cardiovascular system, 169, 170, 178  
Caudate nucleus, 13, 34  
Central sulcus, 8, 50  
Cerebellum, 6, 9, 30, 34, 3595  
Cerebral blood flow, 55, 137, 169–185  
Cerebral cortex, 6, 8, 34, 44  
Cerebral hemispheres, 6–8, 30, 34

- Cerebral veins  
  deep veins, 27, 30, 35  
  superficial veins, 27–31, 35
- Cerebrospinal fluid (CSF), 3, 13, 69, 96, 127, 137–163, 169–185  
  absorption, 177  
  circulation, 137, 139–143, 155  
  flow, 69, 137, 139, 147–150, 153, 160, 161, 170–174, 177–183  
  production, 138, 177
- Cerebrum, 6, 34
- Cheng, S., 78–80
- Chen, W.W., 78
- Chinzei, K., 78, 79, 82, 127
- Cingulate gyrus, 11
- Cingulate sulcus, 8, 11
- Cingulum, 33
- Circle of Willis, 24, 26, 29, 32, 35, 171
- Clinical applications, 41, 43, 45–59, 137–163
- Cloots, R.J., 96
- Cognitive systems, 51–52
- Commissural tracts, 30, 32, 34, 35
- Computational fluid dynamic (CFD), 3, 169–185
- Computational fluid mechanics,
- Computational methods, 3
- Computational solid mechanics, 207
- Computer-assisted surgery, 111–132, 191, 215  
  Found as Computer-assisted neurosurgery)
- Computer simulation, 3, 122, 124–130
- Constitutive models, 70, 77, 79, 81–83, 85, 86, 119, 120, 123, 125–127, 131, 193
- Contact algorithm, 191, 203, 212–213
- Contact model, 117
- Continuity equation, 170
- Corpus callosum, 32, 34, 35, 97, 104
- Cortico-bulbar tract, 34, 35
- Cortico-pontine tract, 34, 35
- Cortico-spinal (pyramidal) tract, 34, 35
- Cortico-thalamic tract, 34, 35
- Craniosynostosis, 138
- Czosnyka, M., 137
- Czosnyka, Z., 137
- D**
- Davson, H., 138
- Deep gray nuclei, 6, 13–15, 34
- Deep nuclei,
- Diencephalon, 6, 8, 34
- Diffusion tensor imaging (DTI), 43–44, 46–48, 51, 55–59, 185
- Du Boulay, G., 180
- Dural sinuses (DS), 22, 23, 26–28, 30, 31, 35
- Dynamic relaxation (DR), 190, 197–202, 206, 207, 211–213, 216
- Dynamics of cerebrospinal fluid, 3, 137–166, 169
- E**
- Elastance, 140, 141, 143–144, 152, 154, 166
- Elastography, 72, 75, 84–86, 122, 185
- Electric field, 44, 45
- Electroencephalography (EEG), 44–46, 48, 57–59
- Element-free methods, 116
- Engineering, 1–3, 77, 123, 195, 206
- Epilepsy, 15, 41, 46–58
- Eppinger, R.H., 103
- Estes, M.S., 78
- Explicit dynamics, 189, 190, 192, 194, 195, 202, 215
- F**
- Fallenstein, G.T., 79
- Finite element method, 3, 92, 116, 131, 173, 179, 190, 195, 204–205, 214
- Flow, 3, 42, 55, 69, 79, 86, 101, 114, 137–139, 146–153, 160–163, 169–185
- Fluid mechanics,
- Fourth ventricle, 13, 35, 96, 171, 177, 183
- Franceschini, G., 84
- Frieden, H., 144
- Frontal lobe, 8, 10, 11, 32–34, 102, 103
- Frontal veins, 28
- Frontopolar veins, 28
- Functional imaging, 48
- Functional mapping, 46, 49–52, 54–55
- Functional maps, 43, 44
- functional MRI (fMRI), 42–59
- G**
- Galerkin method, 116
- Garo, A., 85
- Gefen, A., 84, 85
- Gennarelli, T.A., 71, 103
- Geometry, 92, 93, 97, 105, 107, 112–116, 124, 126, 128, 172, 174, 177, 179, 180, 182, 189, 199, 203–205, 208, 213, 215
- Globus pallidus interna, 15, 20, 21
- Gray matter, 6, 8, 13, 55, 69, 96, 97, 106
- Gurdjian, E.S., 102, 105
- Gyri, 8, 10, 11, 13, 33, 34, 41, 45, 53, 56, 96, 102

**H**

- Haines, D.E., 95, 96  
Haptic feedback, 111–113, 123, 194, 206  
Haptic interface, 111, 123  
Harder, R.L., 98  
Hardy, W.N., 92, 104–106  
Hexahedral elements, 98, 99, 124, 125, 127, 174, 191, 202–203, 205, 207, 209, 211  
Hippocampus, 13, 35, 47, 53, 58, 96, 115  
Ho, J., 97  
Holbourn, A., 71  
Horns  
  frontal (anterior), 14  
  occipital (posterior), 14, 128, 130, 171  
  temporal (inferior), 14  
Horton, A., 213  
Hourglass control, 125, 191, 194, 202, 203, 207–208, 211  
Howden, L., 181  
Hughes, T.J.R., 101  
Hussey, F., 142  
Hydrocephalus, 70, 79, 80, 83, 84, 86, 137–139, 149, 153–157, 160–166, 169, 178, 180  
Hyperelasticity, 80–83, 127, 195, 213, 216  
Hyper-viscoelasticity, 79  
Hypothalamus, 8, 32, 35, 180

**I**

- ICP monitoring, 143–147, 153, 157, 163  
ICP waveform, 144–146  
Idiopathic intracranial hypertension, 137–139  
Image-guided surgery, 3, 111, 123, 128, 206  
Image registration, 112–114, 117, 124, 131, 197, 202, 206  
Incompressibility, 84, 122, 124, 179  
Inferior frontal gyrus, 10  
Inferior longitudinal fasciculus, 33, 35, 56  
Inferior occipital gyrus, 11  
Inferior occipito-frontal fasciculus, 33, 35  
Inferior parietal gyrus (lobule), 11  
Inferior peduncle, 30  
Inferior sagittal sinus, 28  
Inferior temporal gyrus, 11, 13  
Infinitesimal deformations, 130, 190  
Infusion test, 138, 142–147, 157, 163  
Injury, 1, 3, 57, 69–71, 83, 86, 91–108, 116, 123, 138, 189–195, 204, 215, 216  
Insula, 8  
Internal carotid arteries, 24–26, 35, 150, 171  
Interventricular foramina, 13

- Intracranial pressure, 3, 55, 91, 92, 94, 102, 104–105, 146, 148, 152, 163–178  
Isthmus (of cingulate gyrus), 11

**J**

- Jacobsen, 170  
Jin, X., 101  
Joldes, G.R., 111, 189

**K**

- Kasprowicz, M., 137  
Katzman, R., 142  
King, A.I., 91  
Kleiven, S., 97  
Kurtcuoglu, V., 169  
Kuttler, A., 182, 183

**L**

- Laminar flow, 150, 178  
Lateral occipitotemporal gyrus/fusiform gyrus, 13  
Left and right cerebellar hemispheres, 9  
Left and right lateral ventricles, 13, 96  
Left and right sigmoid sinuses, 28  
Left and right transverse sinuses, 28  
Liebenthal, E., 41  
Limbic lobe, 8, 11, 35  
Lingual gyrus, 11, 13  
Lippert, S.A., 74  
Liu, Z., 85  
Loading, 69–73, 75–83, 85, 86, 92–94, 99, 101, 103, 105, 107, 113, 114, 117–122, 125–127, 130, 131, 189, 191, 212, 215  
Loth, F., 181  
Lump-parameter model,  
Lymphatic pathways, 177, 178

**M**

- MacNeal, R.H., 98  
Magnetic field, 44–46, 149  
Magnetic resonance imaging (MRI), 42–49, 57–59, 112, 114, 115, 119, 123, 125, 129, 137, 147, 149–154, 160–163, 169–171, 173–175, 177–183, 185  
Magnetoencephalography, 44–45  
Margulies, S.S., 84, 85  
Marmarou, A., 139  
Maxeiner, H., 104

- M**
- McElhaney, J.H., 78
  - Mechanical properties, 1, 3, 69–86, 96, 97, 113–115, 117, 119–122, 125, 127, 130, 131, 193, 207
  - Medial occipitotemporal gyrus, 13
  - Medicine, 3, 42, 131, 189, 190
  - Medulla, 9, 30, 35
  - Meshless methods, 113, 115, 116, 131, 204, 205
  - Meshless total lagrangian explicit dynamics (MTLED) algorithm, 205, 213–216
  - Midbrain, 9, 30, 32, 35, 97
  - Middle frontal gyrus, 10, 53, 56
  - Middle longitudinal fasciculus, 33, 35
  - Middle occipital gyrus, 11
  - Middle peduncle, 30
  - Middle temporal gyrus, 11, 53, 56
  - Midline vermis, 9, 35
  - Miller, K., 1, 78, 79, 82, 120, 127, 189
  - Modelling, 113–123
  - Motor systems, 50–51
  - Multimodal imaging, 45–46
  - Muttupillai, R., 74
- N**
- Nahum, A.M., 92, 105
  - Nakaji, P., 112
  - Navier-Stokes (NS) equations, 169, 170, 172, 174, 179
  - Neo-Hookean model, 122, 127, 207, 208, 211, 212
  - Nerve cell, 8
  - Nerve fibers, 8, 69
  - Neural activity, 42, 44, 59
  - Neurosurgery, 2, 5, 15, 46–58, 111–131, 190, 191, 196–205, 211, 215, 216
  - Non-communicating and acute communicating hydrocephalus, 155–156
  - Non-locking tetrahedra, 191
  - Nowinski, W.L., 5
  - Numerical algorithms, 113
- O**
- Occipital lobe, 8, 11, 13, 32–34, 95
  - Occipital veins, 28
  - Ogden model, 82
  - Olbricht, W.L., 185
  - Ommaya, A.K., 1
  - Operation planning, 111–114
  - Orbital gyri, 11, 34
- P**
- Parahippocampal gyrus, 11
  - Parietal lobe, 8, 11
  - Parietal veins, 28
  - Parieto-occipital fissure, 8, 11
  - Pericallosal artery, 24
  - Perivascular space, 173, 179, 184–185
  - Permeability, 171, 172, 182
  - Pervin, F., 78
  - Phase contrast MRI, 147, 149–153
  - Physiology and pathophysiology, 138–139
  - Pickard, J.D., 137
  - Pons, 9, 30, 35
  - Postcentral gyrus, 11
  - Posterior commissure, 15, 18, 32, 34, 35
  - Posterior communicating arteries, 26, 32
  - Prange, M.T., 84
  - Precentral gyrus, 10
  - Prefrontal veins, 28
  - Presurgical mapping, 41, 46, 48–58
  - Prisms, 174
  - Projection tracts, 30, 34–36
  - Pyramids, 174
- R**
- RAP index, 146–147, 154, 163
  - Rowson, S., 92
- S**
- Sack, I., 84
  - Schiavone, P., 80
  - Sensory systems, 45, 50–51
  - Shear modulus, 71, 72, 74–76, 84, 103, 122, 213
  - Shen, F., 72
  - Shenkin, H.A., 104
  - Shunt, 70, 138, 142, 153, 156–160
  - Shunt failure, 138
  - Skill assessment, 111–112
  - Smielewski, P., 137
  - Soft tissue mechanics, 2
  - Solid mechanics, 82, 112, 117, 190, 194, 207
  - Spatial discretization, 170, 173–174
  - Speltzer, R.F., 112
  - Spinal cord, 6, 35, 85, 96, 101, 104, 117, 138, 182
  - Stability, 193, 195, 202–203, 205
  - Stockman, H.W., 182
  - Straight gyrus, 11
  - Straight sinus, 28
  - Strain, 71–74, 76–83, 85, 86, 92–94, 97, 100,

- 102, 103, 107, 111, 119, 121, 122, 130, 131, 137, 190, 191, 194, 195, 204, 215, 216
- Strain rate, 73, 78, 80, 81, 83, 85, 86, 107, 121, 131
- Stress, 46, 71–73, 77, 78, 81, 82, 96, 100, 102, 103, 111, 112, 120–123, 130, 131, 137, 178, 190, 194, 195, 204
- Structural imaging, 41–48
- Subarachnoid space (SAS), 96, 101, 138, 139, 147, 148, 161, 163, 171–173, 181–185
- Subcallosal gyrus (areas), 11
- Subcortical structures, 15, 34, 35
- Subthalamic nucleus, 8, 15, 20
- Subthalamus, 8
- Sulci, 8, 10, 11, 13, 41, 45, 96, 163
- Superior frontal gyrus, 10, 11
- Superior longitudinal fasciculus, 33, 35, 56, 57
- Superior occipital gyrus, 11
- Superior occipito-frontal fasciculus, 33, 35
- Superior parietal gyrus (lobule), 11
- Superior peduncle, 30
- Superior sagittal sinus, 28, 138, 171, 177, 183
- Superior temporal gyrus, 11
- Supramarginal gyrus, 11
- Surgeon training, 111–113
- Surgical simulation, 2, 3, 83, 111–113, 117, 131, 194–196
- Sweetman, B., 181
- Sylvian (lateral) fissure, 8
- T**
- Takhounts, E., 105
- Tamura, A., 78, 79
- Temporal lobe, 8, 11, 32–34, 52–54, 58, 102
- Tetrahedra, 174
- Thalamus, 8, 13, 15, 20, 32, 34–36, 96, 97
- Theoretical models, 137–163
- Thibault, L.E., 71, 84
- Third ventricle, 13, 96, 128, 129, 160, 161, 173, 180
- Tisell, M., 143
- Total Lagrangian formulation, 131, 190
- Traumatic brain injury (TBI), 69–71, 86, 91–93, 102, 104–108, 138, 189, 215
- Trosseille, X., 92
- U**
- Uncinate fasciculus, 33, 35
- V**
- Validation, 74, 75, 93, 104–106, 108, 122–123, 128–130
- Vappou, J., 74
- Velocity, 74, 86, 146, 149, 150, 163, 170, 174, 178, 181–185, 214
- Venous system, 22, 26–32, 35
- Ventricular system, 6, 13–15, 34, 35, 96, 163, 176
- Ventrointermediate nucleus  
of the thalamus, 15, 20
- Verification, 191, 207–215
- Vertebral arteries, 24, 25, 35, 150, 171, 176, 177
- Viscoelasticity, 86
- Viscosity, 82, 170, 178
- Visualization, 42, 44, 46, 47, 172
- Volumetric locking, 124, 194, 202, 207–211
- W**
- Wang, P., 185
- Weaver, J.B., 84
- Webster, J.E., 102
- Weerakkody, R., 137
- White matter, 5, 6, 8, 30, 33, 43, 44, 46, 56, 58, 69, 83, 96, 97, 102, 104, 106, 122, 163
- Wittek, A., 111, 189
- Wolff, M., 104
- Y**
- Yang, K.H., 91, 92
- Z**
- Zhang, L., 92, 97